Assessing long-term carbonation resistance of blended concretes from short-term natural exposure

A thesis submitted in fulfilment of the requirements for the degree of

Doctor of Philosophy and Diploma of Imperial College London

by

Kai Zhang

Concrete Durability Group, Department of Civil and Environmental Engineering

Imperial College London

March 2022

Declaration

I hereby declare that this thesis, submitted for the degree of Doctor of Philosophy and Diploma of Imperial College London is the result of my own study. Any information from the work of others, whether published or unpublished, has been acknowledged in the text and a list of the reference is provided. I hereby certify that the work presented in this thesis has not been submitted in any form to any other institution, for any degree, diploma or other qualification.

The copyright of this thesis rests with the author and is made available under a Creative Commons Attribution Non-Commercial No Derivatives licence. Researchers are free to copy, distribute or transmit the thesis on the condition that they attribute it, that they do not use it for commercial purposes and that they do not alter, transform or build upon it. For any reuse or redistribution, researchers must make clear to others the licence terms of this work.

Kai Zhang

March 2022

Abstract

The use of blended cements by partially replacing ordinary Portland cement (CEM I) with supplementary cementitious materials (SCMs) is a major approach for mitigating the massive CO_2 emissions from the concrete industry. Such cements usually have better engineering properties but are more vulnerable to carbonation. Most standard carbonation studies involve carbonating cementitious samples in an accelerated environment. However, such accelerated tests distort the carbonation mechanism in relation to natural carbonation, providing results that are not ideal for service life prediction modelling for cement-based materials. Demonstrating that novel blended cements are durable is a major barrier to their commercial adoption. As such, there is an urgent need to develop new approaches for rapidly assessing the durability of blended cements.

This thesis aims to assess the long-term carbonation resistance of cement-based materials from short-term exposure to natural carbonation. The main methodology involves exposing blended samples to short-term natural carbonation, characterising the evolution of shallow carbonation depth through high-resolution techniques, and extrapolating to longer-term carbonation resistance. Another major focus of this research is to understand the effects of natural carbonation on the microstructure and mass transport properties of concretes containing blended cements. It is expected that the research will lead to improved service life prediction models and facilitate the development of low-carbon sustainable cementitious materials.

Confocal Raman microscopy (CRM) was explored as a novel method for high-resolution characterisation of shallow carbonation depth after relatively short-term natural exposure. To enable this, a parametric optimisation of CRM for spectral mapping of cement-based materials was performed. The effects of sample preparation and various operating parameters on data quality were examined. Microstructural changes and damage induced by prolonged laser irradiation were also investigated. Recommendations on optimal settings were made based on the obtained results.

The feasibility of CRM for monitoring early surface carbonation of hardened cement pastes was studied in real-time for up to 7 d. Samples were exposed to natural carbonation (440 ppm CO_2) and accelerated carbonation (4% CO_2), and the evolution of calcium carbonate ($CaCO_3$) polymorphs, portlandite, ettringite, C-S-H gel and unreacted cement particles was followed. Results demonstrated that CRM is a valuable tool for non-destructive real-time imaging of surface carbonation in cement-based materials.

The reliability of CRM for determining carbonation depth was investigated by comparing with the conventional phenolphthalein spray testing and various profile-grinding analysis methods such as

thermogravimetric analysis, X-ray diffraction, Fourier transform infrared spectroscopy, and Raman spectroscopy. Results showed that the carbonation fronts observed with CRM were distinct and matched well with those observed with the phenolphthalein method under accelerated carbonation conditions. However, the difference in the measured carbonation depths by the two methods was increased after short-term (1-3 months) natural carbonation due to the ambiguous colouration of phenolphthalein when measuring shallow carbonation depth in some samples. Furthermore, profile-grinding analysis measures only the 'apparent' maximum carbonation depth, which is larger than the depths measured with CRM profiles. The discrepancies were found to be related to the spatial variation of the carbonation front and sampling interval adopted. A simple method was proposed to estimate the average carbonation depth from the carbonation profile, and the results obtained for profile-grinding analysis agreed well with those determined by CRM image analysis, with the average difference being only 1.1%. Overall, this chapter demonstrates that CRM is a reliable technique for measuring the true carbonation depth of cement-based materials and is especially powerful for measuring shallow carbonation depth (e.g. < 3 mm) after short-term natural carbonation.

Using CRM and phenolphthalein, the evolution of average carbonation depth in CEM I and blended cements paste, mortar and concrete samples after short-term (1-3 months) and longer-term (6-24 months) natural exposure was studied. The main variables include water/binder ratio (0.45 and 0.6), curing duration (3d and 122d), aggregate content (0% for paste, 20% and 50% for mortar, and 70% for concrete), and binder type (CEM I, CEM I + 30% fly ash and 50% slag). The effect of these variables on natural carbonation was examined, and the changes in mass transport properties and microstructure with the progress of carbonation were investigated. The derived results were employed to assist the carbonation modelling study in the next chapter.

Artificial neural networks (ANNs) were applied to model the long-term carbonation depths in concrete exposed to natural exposure for up to 20 years. Approximately 3300 pieces of data records were compiled from 33 papers, including this study. Thirty-three influential variables were selected as input neurons to the ANN model. Two critical parameters relating to the architecture of ANNs were optimised to reduce the errors in the prediction. By fitting the required input variables to the trained ANN algorithm, prediction of carbonation depths can be conveniently obtained. Results show a good correlation between the predicted and measured carbonation depths in the test dataset with an average root mean squared error of 1.97 and an average percentage error of 19.2%. The prediction accuracy is much higher for larger carbonation depths and the obtained error was reduced to merely 4.3% when predicting a carbonation depth of 50 mm. Since larger carbonation depth is usually detected in blended cements due to their higher vulnerability to carbonation, ANNs are thus deemed suitable for rapidly assessing the long-term carbonation resistance of blended cements with good accuracy.

Acknowledgements

I am forever grateful to my supervisors, Dr Hong Wong and Professor Nick Buenfeld for their continuous encouragement, guidance and support throughout the study. I am greatly honoured to have the opportunity to pursue this PhD under their supervision. I also wish to acknowledge the China Scholarship Council for covering part of my tuition fees and living costs in London.

I would also like to thank the following individuals, as without their support this thesis would not have been possible.

Dr Marcus Yio for his valuable ideas, comments and discussions, for showing me to use the Fiji ImageJ software and training me the many experimental techniques in the laboratory;

Mr Andrew Morris for his dedicated help with the laboratory work;

Undergraduate and MSc students for assisting me with the experiments and data collection: Deema Abu-Salma and Awni Abdullah for their help with some of the mass transport tests, and Cyril Crawford for sharing his ideas of Python coding for the artificial neural network analyses;

My colleagues, teammates, and friends in the section: Fadhilah, Alalea, He, Xi, Sam, Roshni, Shiying, Jia Xiang, Alexander, Barnaby, Adam, Kaine, Terry, Tiejun, Meng, Caitlin, John, Runzi, Yixiu and Jack, for the ideas, discussions, lab help and funny jokes; Friends in department and college: Hanyu, Wenjie, Zhan, Fangce, Ying, Xiang, Xin, Mamon, Ding, Mayue, Shawn, Ruizhi, Luai, Xi, Qiming, Heather, and many others, for their motivation and companionship with lots of enjoyable breaks and talks;

Sarah Willis, Fionnuala Ni Dhonnabhain, Angela Frederick and other staffs from the Department of Civil and Environmental Engineering, Centre for Academic English, Central Library, International Office, and Student Hub for their assistance.

My father and mother for their unconditional love, continuous encouragement, and unlimited support with every decision I have made in my life.

Notation

Abbreviations

a.u.	Arbitrary unit
AFt	Ettringite
AFm	Monosulphate
AH	Unreacted cement
ANN	Artificial neural network
ATR	Attenuated Total Reflectance
BSE	Backscattered electron
C_2S	Dicalcium silicate
C_3A	Tricalcium aluminate
C_3S	Tricalcium silicate
C_4AF	Tetracalcium aluminoferrite
CCD	Charged-coupled device
CCUS	Carbon capture, utilisation and storage
CH	Calcium hydroxide
CRM	Confocal Raman microscopy
C-S-H	Calcium silicate hydrate
DR	Diffuse Reflectance
EDS	Energy dispersive X-ray spectroscopy
FTIR	Fourier transform infrared spectroscopy
GGBS	Ground granulated blastfurnace slag
HP	Hydration product
ITZ	Interfacial transition zone
LS	Limestone filler
MS	Microsilica
NA	Numerical aperture
Na_2O_{eq}	Sodium oxide equivalent
NMR	Nuclear magnetic resonance
PFA	Fly ash
pH	Potential of hydrogen
RH	Relative humidity
RMSE	Root mean square error

ROI	Region of interest
RS	Raman spectroscopy
S.D.	Standard deviation
SCM	Supplementary cementitious material
SEM	Scanning electron microscopy
SiC	Silicon carbide
SNR	Signal-to-noise ratio
SSD	Saturated and surface dry condition
TGA	Thermogravimetric analysis
w/b	Water/binder ratio
w/c	Water/cement ratio
XRD	X-ray diffraction

Roman letters

A	Cross-sectional area (m^2)
a	Fitting constant
b_n	Biases in artificial neural network
C_1	Mean concentration of O_2 in the N_2 stream at 1 bar (m^3/m^3)
C_2	Concentration of O_2 in the O_2 stream (m^3/m^3) at 1 bar
C_A	Concentration of oxygen (mol/m^3)
C_c	Contention of calcium carbonate in the carbonated zone
C_{nc}	Contention of calcium carbonate in the non-carbonated zone
D	Intrinsic diffusion coefficient of a bulk system (m^2/s)
d_n	Carbonation depth at location n (mm)
G_0	Concentration of O_2 in the initial N_2 stream (%)
G_1	Concentration of O_2 in the outflow stream (%)
i	Water absorbed per unit area of inflow surface (g/m^2)
J_A	Flux of the gas A (mol/m^2s)
k_g	Apparent gas permeation coefficient(m^2)
k_{int}	Intrinsic gas permeability (m^2)
L	Sample thickness (m)
m	Mass of sample at preconditioned state at 55% RH, 21 ºC (g)
m_d	Mass of sample at 105ºC oven-dried condition (g)
m_s	Mass of sample at SSD condition (g)

n	Number of data facts in artificial neural network
P_1	Pressure of O_2 stream (bar)
P_1^*	Absolute inlet gas pressure (N/m^2)
P_2	Pressure difference between the O_2 and N_2 streams (bar)
P_2^*	Absolute outlet gas pressure (N/m^2)
P_m	Mean value of the inlet and outlet pressure (N/m^2)
Q	Oxygen diffusion rate at 1 bar (m^3/s)
Q^*	Oxygen permeation rate at 1 bar (m^3/s)
R_1	Flow rate of N_2 stream (mL/min)
R_2	Flow rate of O_2 stream (mL/min)
R^2	Correlation coefficient
S_n	Electronic energy levels
S	Sorptivity coefficient ($g/m^2min^{0.5}$)
t	Elapsed time (min)
t_i	Predicted results in artificial neural network
V	Volume of samples (m^3)
w_n	Connection strength in artificial neural network
x	Distance of gas diffusion (m)
y_i	Correct results in artificial neural network

Greek letters

β	Klinkenberg constant (N/m^2)
η	Dynamic viscosity of the permeating fluid (Ns/m^2)
η_g	Dynamic viscosity of permeating gas (Ns/m^2)
φ	Accessible porosity (%)
φ_t	Total porosity (%)
ν	Vibrational energy sublevels
ρ	The density of water (g/mm^3)
$\emptyset$	Diameter (mm)

Contents

Declaration 2
Abstract 3
Acknowledgements 5
Notation 6
Contents 9
List of Tables 13
List of Figures 14

1 Introduction 21
1.1 Background 21
1.2 Aim and objectives 23
1.3 Thesis outline 24

2 Literature Review 26
2.1 Blended cements and SCMs 26
2.2 Carbonation of cementitious materials 26
2.3 Changes in hardened cement paste after carbonation 27
2.3.1 Chemical reactions 27
2.3.2 Microstructural changes 28
2.4 Influence of carbonation on transport properties 31
2.5 Accelerated carbonation 32
2.6 Techniques to measure carbonation 34
2.6.1 pH indicator 34
2.6.2 Thermogravimetric analysis (TGA) 35
2.6.3 X-ray diffraction (XRD) 37
2.6.4 Fourier transform infrared spectroscopy (FTIR) 38
2.6.5 Scanning electron microscopy (SEM) 39
2.6.6 Raman spectroscopy 41
2.7 Mathematical modelling of carbonation 42
2.8 Summary 43

3 Methodology 45
3.1 Materials and mix proportion 45

3.1.1 Materials 45
3.1.2 Mix proportions 46
3.2 Development of a natural carbonation chamber 47
3.2.1 Unsuccessful attempts 48
3.2.2 Employed method using a pond air pump (100 L/min) 51
3.3 Confocal Raman microscopy 53
3.3.1 Principle 53
3.3.2 Confocal Raman microscopy (CRM) 54
3.4 Backscattered electron microscopy (BSE) 56
3.4.1 Sample preparation for BSE 56
3.4.2 Instrument 57
3.5 Phenolphthalein spray test 58
3.6 Mass transport tests 58
3.6.1 Oxygen diffusion 59
3.6.2 Oxygen permeation 60
3.6.3 Water absorption 62
3.7 Summary 63

4 Optimising confocal Raman microscopy for spectral mapping of cement-based materials 64
4.1 Introduction 64
4.2 Experimental 66
4.2.1 Materials and sample preparation 66
4.2.2 Conditioning and carbonation 67
4.2.3 Confocal Raman microscopy 67
4.2.4 Backscattered electron microscopy 69
4.3 Results 70
4.3.1 Effect of laser wavelength, fluorescence background and scan accumulation 70
4.3.2 Effect of laser power and exposure time 72
4.3.3 Effect of surface moisture and roughness 74
4.3.4 Effect of prolonged laser irradiation during mapping 77
4.3.5 Comparison between BSE images and confocal Raman maps 81
4.4 Discussion 84
4.5 Conclusion 86

5 Real-time monitoring of carbonation of hardened cement pastes using confocal Raman microscopy 88
5.1 Introduction 88
5.2 Experimental 90

5.2.1 Materials and sample preparation 90
5.2.2 Carbonation 90
5.2.3 Confocal Raman microscopy 90
5.3 Results 91
5.3.1 Raman maps 91
5.3.2 Raman spectra 94
5.3.3 Quantification by image analysis 95
5.4 Discussion 96
5.5 Conclusion 97

6 Confocal Raman microscopy for measuring carbonation depth in cement-based materials: a comparison with other techniques 98
6.1 Introduction 98
6.2 Experimental 103
6.2.1 Materials and sample preparation 103
6.2.2 Conditioning and carbonation 104
6.2.3 Confocal Raman microscopy 105
6.2.4 Phenolphthalein spray method 106
6.2.5 Profile-grinding analysis 107
6.2.6 Backscattered electron microscopy 108
6.3 Results 108
6.3.1 CRM vs. phenolphthalein spray method 108
6.3.2 CRM vs. profile-grinding analysis 110
6.3.3 Spatial variation of carbonation front and sampling interval 114
6.3.4 Estimating average carbonation depth from profile analysis 117
6.3.5 Application of CRM to measure short-term natural carbonation depth 119
6.4 Discussion 122
6.5 Conclusion 125

7 Experimental investigation of natural carbonation and its influence on microstructure and transport properties 127
7.1 Introduction 128
7.2 Experimental 129
7.2.1 Materials and sample preparation 129
7.2.2 Conditioning and carbonation 130
7.2.3 Average carbonation depth 131
7.2.4 Mass transport tests and vacuum saturation 132
7.2.5 Backscattered electron microscopy 133

7.3 Results 133
7.3.1 Carbonation resistance 133
7.3.2 Mass transport properties and porosity after curing 139
7.3.3 Mass transport properties and porosity after carbonation 142
7.3.4 Effect of carbonation on microstructure 145
7.4 Discussion 150
7.4.1 Factors influencing carbonation resistance 150
7.4.2 Effect of natural carbonation on porosity and mass transport properties 152
7.4.3 Effect of natural carbonation on microstructure 153
7.5 Conclusion 154

8 Predicting carbonation with artificial neural network analyses 156
8.1 Introduction 156
8.2 ANN model development 157
8.2.1 General 157
8.2.2 Data compilation 159
8.2.3 Input variables 161
8.2.4 Parametric optimisation and ANN training 165
8.3 Results 166
8.3.1 Parametric optimisation for ANN models 166
8.3.2 Prediction of carbonation depth 167
8.3.3 Effect of variables on carbonation 170
8.4 Discussion 174
8.5 Conclusions 175

9 Conclusions and further research 177
9.1 Conclusions 177
9.2 Recommendations for further research 180

References 183
Appendix - Publications arising from this research 202

List of Tables

Table 2.1 Properties of the minerals involved in carbonation reaction (Arandigoyen et al., 2006). 29

Table 3.1 Oxide composition and loss of ignition of CEM I, PFA and GGBS. 45

Table 3.2 Specific gravity at SSD, 24-hour absorption and moisture content of sand and gravel. 46

Table 4.1 Mix proportions. 67

Table 6.1 Experimental studies using pH indicators and profile-grinding techniques to measure the carbonation depths of neat CEM I and blended cement. Technique: PHP: phenolphthalein, TYP: thymolphthalein, AYR: alizarin yellow R, TGA: thermogravimetry, XRD: X-ray diffraction, FTIR: Fourier transform infrared spectroscopy, PP: pH profile method, Gamma: gammadensimetry, OM: optical microscopy. Sample type: P: paste, M: mortar, C: concrete, SCC: self-compacting concrete. Binder: PC: Portland cement, LS: limestone filler, MK: metakaolin, LDHs: layered double hydroxides, CSA: calcium sulfoaluminate cement. 101

Table 6.2 Mix proportions. 104

Table 7.1 Mixture proportions for paste, mortar and concrete samples 130

Table 8.1 Summary of the literature compiled in this study 160

Table 8.2 Summary of input variables. 164

List of Figures

Figure 2.1 Profiles of $CaCO_3$ and $Ca(OH)_2$ against depth by TGA of CEM I concrete subjected to accelerated carbonation at 20% CO_2 concentration for 8 weeks (Ji et al., 2014). 37

Figure 2.2 BSE image showing the two rims in the inner C-S-H, adopted from Shah et al. (2018). ... 40

Figure 2.3 Raman spectra for calcite, aragonite and vaterite (Ševčík & Mácová, 2018)..... 41

Figure 3.1 Grading curves for Thames valley sand and gravel..... 46

Figure 3.2 Sample designation..... 47

Figure 3.3 Change of CO_2 concentration in CO_2 incubator when testing airtightness (a), and setting 0.1% CO_2 (b)..... 49

Figure 3.4 Variation of CO_2 concentration in CO_2 incubator after installing an electric air inflator (400 L/min) (a), and an aquarium air pump (11.2 L/min) (b). 50

Figure 3.5 Connection of the aquarium air pump to the CO_2 incubator 51

Figure 3.6 Variation of CO_2 concentration for 5 hours (a), and average monthly CO_2 concentration (b), temperature (c), and RH (d) from 2019 quarter 3 to 2021 quarter 2 in CO_2 incubator after installing the pond air pump. Error bars mark standard deviation. 52

Figure 3.7 Pond air pump (100 L/min) (a) and the schematic set-up of climate chamber for long-term natural carbonation (b). 53

Figure 3.8 Schematic energy level diagram of a molecule for fluorescence (a), Rayleigh scattering (b), Raman scattering Stokes (c), and Raman scattering anti-Stokes (d). Image was adopted from Masilamani et al. (2017). 54

Figure 3.9 Schematic set up of CRM, from Leng (2013). 55

Figure 3.10 Renishaw inVia Qontor confocal Raman microscope. 56

Figure 3.11 Hitachi TM4000 Plus scanning electron microscope. 58

Figure 3.12 Schematic of oxygen diffusion test set-up (Wong, 2006). 60

Figure 3.13 Schematic of oxygen permeation test set-up (Wong, 2006), and an example plot for Klinkenberg correction for non-carbonated C-0.45-PC-70%/3d. 62

Figure 3.14 Schematic of water absorption test set-up (Wong, 2006), and an example plot for non-carbonated C-0.45-PC-70%/3d. 63

Figure 4.1 Example Raman spectra of calcite (from carbonated zone), unreacted cement and portlandite acquired with 532 and 758 nm lasers before (a) and after (b) background removal. Asterisks mark the photoluminescence bands. 71

Figure 4.2 Effect of laser wavelength on SNR of calcite (from carbonation and limestone filler), unreacted cement and portlandite peaks after single scan (a) and multiple scan (b) accumulation. Analysis was carried out at 4.15 mW laser power and 1s exposure time. Dotted lines show best-fit power law relations ($R^2 > 0.96$). Error bars represent standard deviation. 72

Figure 4.3 Effect of laser power and exposure time on the SNR of the main Raman peaks of calcite (from carbonation and limestone filler), alite + belite, portlandite and ettringite. Analysis was carried out with 532 nm laser at scan accumulation of 1. Dotted lines show best-fit power law relations ($R^2 > 0.95$). Error bars represent standard deviation. 73

Figure 4.4 Effect of exposure time on the quality of Raman spectra for calcite (from carbonated zone) (a) and unreacted cement (from non-carbonated zone) (b). The SNR of the weak peaks of AFt and CH are shown. Analysis was carried out with 532 nm laser, 4.15 mW laser power and scan accumulation of 1 74

Figure 4.5 Evolution of the main Raman peaks (a-c) and SNR (d) of calcite, alite + belite and portlandite with ambient drying at ~45% RH, 21ºC (for less than 9 minutes) from a freshly cut surface and at 33% RH, 21ºC until mass equilibrium (for 1 month). Analysis was carried out with 532 nm laser, 4.15 mW laser power, 2s exposure time and scan accumulation of 2. 75

Figure 4.6 Colour-coded Raman maps of alite + belite and calcite from the carbonated zone at different surface roughness after grinding and polishing. Colour scale bar indicates peak intensities (a.u.). Optical and BSE images show the microstructure of the matching area after polishing. Analysis was carried out with 532 nm laser, 4.15 mW laser power, 2s exposure time, scan accumulation of 2 and 1 μm step size. AH: unreacted cement; HP: hydration product. 76

Figure 4.7 Effect of surface roughness (indicated by the measured mean surface height S_a from SEM) on the average map intensity of alite + belite and/or calcite at carbonated (A & B) and non-carbonated (C & D) locations. 77

Figure 4.8 Evolution of SNR of the main Raman peaks for calcite (from carbonation and limestone filler), alite + belite and portlandite as a function of scan accumulation by spot analysis, at 0.55 mW (filled symbol) and 4.15 mW (empty symbol) laser power. Analysis was carried out with 532 nm laser and 2s exposure time. Error bars represent standard deviation. 78

Figure 4.9 Area-matching BSE images showing the appearance of microcracks on the as-cut (non-epoxy impregnated) surface and impregnated/polished surface before and after Raman mapping at

step sizes of 1 and 0.3 μm. Both locations were from the carbonated zone. Microcracks were extracted for quantification via image analysis. 79

Figure 4.10 Crack density observed in carbonated and non-carbonated areas (120 × 90 mm^2) subjected to varying laser power (a), exposure time (b) and step size (c) with 532 nm laser and scan accumulation of 2. 80

Figure 4.11 Area-matching BSE images showing epoxy-impregnated cement paste in the carbonated zone (a-b) and plain epoxy (c-d) before and after Raman mapping with high laser power of 37 mW (2s exposure time, accumulation scan of 2 and 1μm step size). 81

Figure 4.12 Comparison between BSE images and Raman maps of portlandite (CH) and calcite in carbonated and non-carbonated regions. Asterisks in (c, f) mark the spots analysed by EDS. Arrows mark the presence of portlandite and calcite in the non-carbonated region. (532 nm laser, 4.15 mW laser power, 2s exposure time and 0.3 μm step size). 83

Figure 4.13 Comparison of the summed Raman spectra between non-carbonated and carbonated areas, obtained from the Raman maps shown in Figure 4.12. 84

Figure 5.1 Area-matching optical and BSE micrographs of the selected ROIs for Raman analysis to be exposed to natural (a) and accelerated (b) carbonation. AH: unreacted cement; HP: hydration product 92

Figure 5.2 Raman maps showing the evolution of calcite, portlandite and C_2S & C_3S under natural (a) and accelerated (b) carbonation. 93

Figure 5.3 Raman spectra showing the evolution of the peaks of different phases under natural (a) and accelerated (b) carbonation. 95

Figure 5.4 Evolution in the volume fractions of calcite, C_2S + C_3S and portlandite quantified by image analysis of the Raman maps. 96

Figure 6.1 Carbonation depths measured using profile-grinding techniques (TGA, FTIR and XRD) vs. those measured using pH indicators from literature (Table 6.1). Solid and dashed lines mark 1:1 correspondence and ±10 mm boundaries respectively. 102

Figure 6.2 Overview of the experimental procedure. Extraction of two adjacent blocks (Blocks A and B) of 6 × 21 × 50 mm^3 from the main sample (a-b) for CRM and phenolphthalein spray test (c), profile-grinding analysis (d), and BSE image analysis (e) respectively. 105

Figure 6.3 Raman maps of $CaCO_3$ polymorphs (1085 + 1090 cm^{-1}) (a, e) and $Ca(OH)_2$ (356 cm^{-1}) (b, f), and corresponding phenolphthalein spray results (c, g) and carbonation profiles (d, h) for P-

0.45-PC and M-0.45-PC exposed to accelerated carbonation (4% CO_2) for 2 months. The horizontal cyan lines mark the width of the carbonation fronts. 109

Figure 6.4 Comparison of the average carbonation depths measured with phenolphthalein and with Raman maps of $CaCO_3$ for all CEM I samples exposed to 1-3 months accelerated carbonation (4% CO_2). Error bars represent standard deviation. The solid line represents 1:1 correspondence. 110

Figure 6.5 Example TGA-DTG curves (a), as well as FTIR (b), XRD (c) and RS (d) spectra of ground powders sampled at increasing depths from P-0.45-PC exposed to accelerated carbonation (4% CO_2) for 2 months. CH: portlandite, AFt: ettringite, A: aragonite, V: vaterite..... 111

Figure 6.6 Carbonation profiles of $CaCO_3$ and $Ca(OH)_2$ produced by profile-grinding analysis with different techniques for P-0.45-PC exposed to accelerated carbonation (4% CO_2) for 2 months. 112

Figure 6.7 Profiles of $CaCO_3$, $Ca(OH)_2$ and porosity measured by CRM, profile-grinding analysis, and BSE for all CEM I samples after 1-3 months accelerated carbonation (4% CO_2). Vertical red lines represent the carbonation depth measured by CRM image analysis. Red and black arrows represent the carbonation depth measured from carbonation profile obtained with CRM and profile-grinding analysis respectively. 113

Figure 6.8 Illustration of three scenarios where 'apparent' maximum carbonation depth measured by profile-grinding increases with the variation of carbonation front and sampling position. White dotted lines represent profiles measured by profile-grinding, superimposed on CRM maps of $CaCO_3$ divided into five equal-distanced sampling layers. The right-hand side for each dotted line represents high $CaCO_3$ concentration. 114

Figure 6.9 Effect of spatial variation of carbonation front indicated by the width of the transition zone (a) and standard deviation of the carbonation depths (b) on overestimation of 'apparent' maximum carbonation depths measured by profile-grinding for all CEM I samples exposed to 1-3 months accelerated carbonation (4% CO_2). 115

Figure 6.10 Evolution of $CaCO_3$ profiles with successively larger step size resampled from the Raman map of $CaCO_3$ for M-0.6-PC exposed to accelerated carbonation (4% CO_2) for 1 month. Red dots mark the 'apparent' maximum carbonation depths. 116

Figure 6.11 Effect of sampling interval on overestimation of 'apparent' maximum carbonation depth obtained following the approach shown in Figure 6.10 for all CEM I systems exposed to 1-3 months accelerated carbonation (4% CO_2) (a), and data extracted from the literature showing a similar trend (b). 117

Figure 6.12 Proposed method to estimate average carbonation depth from profile analysis. The depth at which the carbonation front is split into two equal areas is taken as the average carbonation depth..... 118

Figure 6.13 Determining the average carbonation depth of M-0.45-PC (3-month accelerated carbonation) from its $CaCO_3$ profile derived from CRM map (a), and average carbonation depths estimated with the proposed method vs. those measured by CRM image analysis for all accelerated carbonated samples (b). The solid and dashed lines represent 1:1 correspondence and ±5 mm boundaries respectively..... 119

Figure 6.14 Example CRM-$CaCO_3$ images for w/b 0.45 paste containing different binder types after 1-3 months natural carbonation..... 120

Figure 6.15 Average carbonation depths measured by CRM image analysis for all samples exposed to natural carbonation. Error bars represent standard deviation..... 121

Figure 6.16 Comparison of the average carbonation depths measured with phenolphthalein and with CRM image analysis for all naturally carbonated samples..... 122

Figure 6.17 Images after spraying phenolphthalein for P-0.45-PC after 1 month (a) and 2 months (b) natural carbonation showing ambiguous coloration at the carbonation front..... 122

Figure 7.1 Measurement of carbonation depths (marked by the cyan bars) at 31 equally distanced (interval of 1 mm) locations on the surface sprayed with phenolphthalein of M-0.45-V-50% after 9 months of natural carbonation (average carbonation depth = 3.4 mm)..... 132

Figure 7.2 Average carbonation depth of CEM I (a), CEM I blended with 30% PFA (b) and 50% GGBS (c) samples (3d curing) after 1-24 months natural carbonation, and the corresponding plots against square-root-of-exposure duration (d-f). P, M and C represent paste, mortar and concrete respectively. The percentage values represent the aggregate volume fraction. Error bars represent standard deviation. The dotted lines represent the best fit linear regression ($R^2 > 0.84$)..... 135

Figure 7.3 Carbonation coefficients of samples containing CEM I (PC), 30% PFA (V) and 50% GGBS (S) grouped according to the mix design and w/b after 3d (a) and 122d moist curing (b). Error bars represent standard deviation..... 136

Figure 7.4 Normalised carbonation coefficients showing the effect of w/b (3d curing) (a) and curing duration (b). The same y-axis scale is used for better comparison. Error bars represent standard deviation. Note that the lines are indicative and do not represent a relationship, thus should not be used for interpolation or extrapolation..... 137

Figure 7.5 Normalised carbonation coefficients showing the effect of aggregate volume fraction on carbonation coefficients in samples moist cured for 3d (a) and 122d (b). 138

Figure 7.6 Correlation of carbonation coefficients between blended cements and CEM I (a), and correlation between carbonation coefficients and $w/CaO_{reactive}$ for all samples (b). 139

Figure 7.7 Mass transport properties: O_2 diffusivity (a), O_2 permeability (b), and sorptivity (c) of all concrete samples after 3d and 122d curing. Error bars represent standard deviation. 140

Figure 7.8 Changes of total (a) and accessible (b) porosity of all concrete samples after 3d and 122d curing. Error bars represent standard deviation. 140

Figure 7.9 Correlation between accessible porosity and O_2 diffusivity (a), O_2 permeability (b), and sorptivity (c) for all concrete samples (3d and 122d curing). Error bars represent standard deviation. The dotted lines represent the best fit linear regression. 141

Figure 7.10 Correlations between carbonation coefficient and O_2 diffusivity for all concrete samples (3d and 122d curing). Error bars represent standard deviation. 142

Figure 7.11 Evolution of mass transport properties: O_2 diffusivity (a), O_2 permeability (b), and sorptivity (c) with carbonation duration for 3d cured concrete samples. Error bars represent standard deviation. 143

Figure 7.12 Evolution of total (a) and accessible (b) porosity with carbonation duration for 3d cured concrete samples. Error bars represent standard deviation. 144

Figure 7.13 Correlation between O_2 diffusivity, O_2 permeability, sorptivity, total porosity and accessible porosity for 3d cured concrete samples after natural carbonation for up to 2 years. Arrows mark the progress of carbonation. 145

Figure 7.14 Example BSE images of the non-carbonated and carbonated paste in CEM I, CEM I + 30% PFA, and CEM I + 50% GGBS concrete samples (w/b 0.6, 3d curing) after 0 and 24 months of natural carbonation. Arrows mark the belite grains appearing as dark relicts. 147

Figure 7.15 Example binary images showing the extent of detectable microcracks in the non-carbonated and 24-month naturally carbonated concrete samples (3d curing) containing different binder types. Microcracks were extracted for quantification via image analysis. 149

Figure 7.16 Average crack density observed in non-carbonated (NC) and 24-month naturally carbonated (C) concrete samples (3d curing) containing different binder types. Error bars represent standard deviation. 149

Figure 8.1 Schematic diagram of an ANN. 158

Figure 8.2 Effect of the number of neurons in the (first and only) hidden layer on the average RMSE (a) and average percentage error (b). 166

Figure 8.3 Effect of the number of neurons in the second hidden layer on the average RMSE (a) and percentage error (b). 167

Figure 8.4 Correlation between predicted and measured carbonation depths for the training (a), validation (b), and testing (c) datasets. Solid and dashed lines represent 1:1 and ±5 mm boundaries respectively. 168

Figure 8.5 Correlation of absolute error (a) and percentage error (b) with the measured carbonation depth 169

Figure 8.6 Correlation of measured carbonation depth and square-root-of-carbonation duration for the entire dataset (a), and percentage error obtained with the prediction (b). 170

Figure 8.7 Effect of different exposure types (a) and Na_2O_{eq} content in cement (b) on carbonation depth. 171

Figure 8.8 Effect of PFA replacement level (a) and different SCMs (b) on carbonation depth. 172

Figure 8.9 Effect of cement content (a), w/b (b), and durations for moist curing (c) on carbonation depth. 173

Figure 8.10 Effect of RH and temperature in the exposure environment (a), and exposure locations (b) on carbonation depth. 174

1 Introduction

1.1 Background

Concrete is the most heavily used manufactured material in the world. Although concrete itself is believed to have a low environmental impact, it contributes to approximately 8% of man-made CO_2 because of the vast consumption of ordinary Portland cement (CEM I or PC) (Stemmermann et al., 2010). In cement manufacturing, around 60% of the CO_2 emission stems from the decomposition of limestone (Gartner, 2004), and the rest is mainly associated with the energy consumed in kilns to heat the raw materials to a temperature of 1450°C. To curb the huge CO_2 emission, the cement industry has already improved kiln efficiency and switched to low-carbon fuels, but because of the large unavoidable process emissions, further reduction in CO_2 emission is unlikely to occur through this approach. Thus, the industry has to shift to other approaches; the most practical one at present time is by partially substituting Portland cement with supplementary cementitious materials (SCMs), such as fly ash (PFA), ground granulated blastfurnace slag (GGBS), microsilica (MS), calcined clays etc. These materials are usually by-products of other industries and have lower embodied carbon than CEM I. Additionally, SCMs directly participate in cement hydration, and the concrete produced by blended cements usually achieves improved engineering properties and long-term durability.

Carbonation of cement-based materials involves the reaction between atmospheric CO_2 and calcium-bearing constituents, mainly portlandite ($Ca(OH)_2$) and calcium silicate hydrate (C-S-H), to form calcium carbonate ($CaCO_3$). This process leads to a pH drop in the pore solution, thereby depassivating any embedded rebar in the carbonated zone and enabling corrosion when water and oxygen are present (Bentur et al., 1997). Thus, the evolution of carbonation depth and extent needs to be accurately assessed in order to predict time to carbonation-induced corrosion for service-life modelling of concrete structures. The ability to predict progress of carbonation is also important for maintenance of existing structures and durability design/assessment of new concrete materials. Furthermore, carbonation is also relevant to research on developing carbon capture, utilisation and storage (CCUS) strategies such as accelerated CO_2 curing of concrete and carbonation of waste concrete fines. This is considered a viable solution to reduce CO_2 emission in cement industries and stabilise atmospheric CO_2 concentration (Kashef-Haghighi & Ghoshal, 2013).

Natural carbonation of concrete is a very slow process which can take decades to penetrate the concrete cover. Therefore, accelerated carbonation involving high CO_2 concentrations (1% to 100%) is often preferred for laboratory investigations of carbonation resistance (Groves et al., 1991; Castellote et al., 2009; Bernal et al., 2012; BS 1881-210, 2013; Morandeau et al., 2014; Shi et al.,

2016; Leemann et al., 2017). However, previous studies have found that the decalcification process involved, and the carbonates formed under accelerated carbonation are different from those under natural carbonation (Groves et al., 1990; Goñi et al., 2002; Auroy et al., 2018). For example, elevated CO_2 concentration from natural level to > 10% can significantly enhance the carbonation rate of not only C-S-H, but also other calcium-bearing phases like ettringite and unreacted cement (Castellote et al., 2009). Although accelerated carbonation at lower CO_2 concentration (e.g. 3%) was found to be somewhat representative of natural carbonation in terms of mineralogical and microstructural changes in cement pastes (Castellote et al., 2009; Auroy et al., 2018), this is not applicable to all binding systems. For example, it was reported to underestimate the service life prediction for alkali-activated binders when exposed to 1% CO_2 concentration (Bernal et al., 2012). Furthermore, the conversion from accelerated carbonation results to natural carbonation using some established empirical equations are still not accurate enough and was found to underestimate the true carbonation rate for mortars with 50% PFA exposed to 1% CO_2 concentration (Van Den Heede & De Belie, 2019). As such, accelerated carbonation is not ideal for service life prediction modelling for cement-based materials.

Carbonation is a diffusion-controlled reactive transport process. Transport is closely dependent on the microstructure, while the chemical reactions of different phases in turn affect the microstructure in different manners, making the process highly complex. For example, it is known that the carbonation of portlandite is volumetrically expansive and refines the pore structure (Arandigoyen et al., 2006), while C-S-H carbonation forms silica gel and undergoes shrinkage (Chen et al., 2006). Overall in neat CEM I cement samples, the extent of $Ca(OH)_2$ carbonation tends to be stronger than C-S-H carbonation, leading to reduced total porosity (Houst & Wittmann, 1994; Ngala & Page, 1997; Villain & Thiery, 2006; Leemann et al., 2017). However, for blended cement concrete, the findings from previous studies are inconsistent, some showing a decrease (Ngala & Page, 1997; Fabbri et al., 2009; Chindaprasirt & Rukzon, 2009; Gruyaert et al., 2013) while others an increase (Šavija & Luković, 2016; Shi et al., 2016; Wu & Ye, 2017) in total porosity after carbonation. The variation in microstructure can significantly affect the transport properties, whereas again, observations are inconsistent in literature (Martin, 1986; Borges et al., 2010; Bernal et al., 2012). Furthermore, the understanding of the effect of carbonation on microstructure and transport properties under natural conditions are still limited for assessing the carbonation resistance of cement-based materials.

Since accelerated carbonation testing is not ideal for modelling carbonation-induced corrosion in cement-based materials, a more promising alternative involves exposing specimens to natural carbonation, characterising carbonation profile with time and extrapolating the data to longer-term performance. However, natural carbonation is a slow process and for the most practical exposure periods, the achieved carbonation depth will only be a few mm or less. Such depths are too shallow to

be adequately measured with the commonly used, well-characterised methods, such as the phenolphthalein indicator test due to the potential 'underestimation' of the carbonation depth, or more 'accurate' profile-grinding analysis techniques involving thermogravimetric analysis (TGA) X-ray diffraction (XRD), Fourier transform infrared spectroscopy (FTIR) due to the destructive nature in sample preparation and the limit in sampling resolution. Therefore, alternative high-resolution techniques are required to detect and measure these limited changes in carbonation due to short-term natural carbonation.

Raman spectroscopy is a powerful technique capable of providing chemical and structural information of various phases in cement-based materials. Combining Raman spectroscopy with confocal microscopy enables high-resolution chemical imaging of phase distribution, hence, confocal Raman micro-spectroscopy or microscopy (CRM) could be a suitable technique for characterising short-term natural carbonation and for measuring shallow carbonation depths. However, several issues need to be addressed before this technique can be implemented confidently. These include the effect of sample preparation and various operating parameters on data quality, as well as the feasibility and reliability of CRM for studying microstructural changes during the carbonation of cementitious materials.

1.2 Aim and objectives

The overall aim of this research is to develop a reliable methodology to assess the long-term carbonation resistance of cement-based materials and to understand the effect of carbonation on the microstructure, mass transport properties and durability of blended cementitious materials. This will be based on short-term exposure to natural carbonation, high-resolution characterisation of carbonation with time, and extrapolation to longer-term carbonation resistance.

This will be achieved by the following objectives:

- Optimise and validate CRM for studying carbonation in cement-based materials.
- Characterise phase evolution of cementitious materials in real-time when exposed to natural and accelerated carbonation.
- Determine the reliability of CRM for measuring shallow carbonation depth after relatively short-term natural exposure.
- Investigate the evolution of natural carbonation in cement-based materials containing SCMs; examine the effect of different influential factors of carbonation (water/binder ratio, curing duration, aggregate content, and binder type), and the influence of natural carbonation on microstructure and transport properties.
- Establish a database for natural carbonation of cement-based materials and model long-

term carbonation resistance from short-term measurements.

1.3 Thesis outline

This thesis is composed of nine chapters. Chapter 1 discusses the background, objectives and scope of the study. Chapter 2 presents a literature review on the subjects relevant to the scope of this research. Chapter 3 introduces the experimental methodology including the materials, sample preparation and instrumentation. The main findings of this research are presented in the following five chapters (4-8).

CRM has shown a huge potential to characterise microstructural changes during carbonation, however, the effect of sample preparation and various operating parameters on data quality has not been fully understood. In Chapter 4, a parametric optimisation of CRM for spectral mapping of cement-based materials is presented. The effects of drying, sample preparation, surface roughness, and operating parameters such as laser power, exposure time, scan accumulation and mapping step size on data quality and signal-noise-ratio were examined. Microstructural changes and damage induced by prolonged laser irradiation were also investigated. Some recommendations were made based on the obtained results.

Following parametric optimisation, the viability of CRM as a non-destructive technique to monitor early surface carbonation and to study in real-time, phase evolution that occurs during natural and accelerated carbonation was investigated. In Chapter 5, hardened CEM I cement pastes exposed to continuous carbonation at 440 ppm and 4% CO_2 levels were analysed at designated time points up to 7 d. The evolution of various cementitious phases was analysed qualitatively and quantitatively using the collected Raman maps and spectra.

In Chapter 6, carbonation depths in cement-based pastes and mortars were measured with the optimised CRM approach from Chapter 4. The results were compared with conventional phenolphthalein spray test and various profile-grinding analysis techniques to assess the reliability of the optimised approach. Porosity changes induced by carbonation were characterised via backscattered electron microscopy (BSE) image analysis as supporting evidence. The application of CRM to measure shallow carbonation depth exposed to short-term natural carbonation was explored.

Using CRM and phenolphthalein, Chapter 7 studied the evolution of natural carbonation depth in paste, mortar and concrete samples for 1- 24 months, focusing on four important influential factors: water/binder ratio, curing duration, aggregate content, and binder type (SCMs). The effects of natural carbonation on mass transport properties and microstructure of blended cementitious systems were

also investigated. The obtained results were employed to assist the carbonation modelling study in the next chapter.

Several models to predict carbonation exist, however the majority are based on empirical relationships derived from a limited number of datasets. As such, the implementation of these models for practical service life prediction of concrete structures in real environment remains questionable. One obstacle is the limited reliability in coping with a wide range of variables. In Chapter 8, artificial neural networks (ANNs) were employed to address this problem. Approximately 3300 sets of natural carbonation data were compiled from 33 studies, including Chapter 7, and were classified in 33 concrete- and environmental-related input parameters to train, validate and test the ANN model. The performance of the trained ANN to predict long-term carbonation depths for up to 20 years was studied and the effects of several important factors on carbonation resistance were analysed.

Finally, Chapter 9 summarises the main findings in this thesis and gives various recommendations for future work.

2 Literature Review

This chapter provides a review of literature on topics relevant to the scope of this research. First, the chemical and physical changes that occur with carbonation are assessed. Next, the effect of carbonation on mass transport properties is discussed. Existing approaches for measuring carbonation depth and extent are then evaluated. Finally, carbonation prediction models are reviewed.

2.1 Blended cements and SCMs

Blended cements are cements that contain SCMs as partial replacements of Portland clinker. The SCMs contribute to the properties of the hardened composite medium through either a pozzolanic reaction (e.g. microsilica) or combined hydraulic and pozzolanic reactions (e.g. GGBS) depending on their chemical compositions. Typically, microsilica contains over 90% of amorphous silica and is highly pozzolanic, while GGBS contains over 30% calcium oxide and exhibits hydraulic properties. The reaction rate of SCMs at the early stage is significantly retarded by the formation of a Si-rich layer on their particle surface when mixed with water (Thomas, 2013). Gradually, the build-up of alkalinity up to a pH of 12-13 in the surrounding pore solution induces the breakdown of this layer and allows the reaction to proceed. The increase in alkalinity is due to cement hydration forming portlandite, which later participates in the pozzolanic reaction producing additional C-S-H. This process refines capillary pores, densifies the microstructure of hardened cement paste, and improves certain engineering and durability properties of concrete. However, blended cements are low lime systems and their pozzolanic reaction consumes portlandite, reducing further the alkalinity and pH buffer capacity in the hardened cement paste and thus making concrete more susceptible to carbonation.

2.2 Carbonation of cementitious materials

The process of carbonation involves: ingress of atmospheric CO_2 in concrete through the pore structure; dissolution of CO_2 in the pore water and formation of carbonic acid; ionisation to produce carbonic ions in pore solution; reaction with calcium ions and precipitation of $CaCO_3$ solid. As carbonation proceeds, calcium ions will be supplied by the solid hydration products including portlandite, C-S-H, unreacted cement particles and ettringite.

Carbonation in plain concrete is usually not a concern because $CaCO_3$ precipitates in pores and reduces overall porosity. This densifies concrete microstructure, improves compressive strength, and

reduces further penetration. However, carbonation is problematic to reinforced concrete. Steel reinforcement is protected from corrosion by a passive layer and the maintenance of this layer requires a highly alkaline environment in the surrounding pore solution (Neville, 2011). A pH in the vicinity of steel lower than 11.5 triggers the breakdown of this layer (Bentur et al., 1997), which is regarded as the threshold value for depassivation. Carbonation is known as a neutralisation process, which consumes portlandite and reduces the alkalinity in the carbonated region to a pH below 9. Once the carbonation front reaches the reinforcement, the passive layer breaks down, and corrosion can be initiated when oxygen and water are present. The presence of cracks in concrete aggravates the carbonation process, leading to a locally deeper carbonation front (Parrott & Killoh, 1989).

However, carbonation is not always problematic as it is also relevant to research on developing carbon capture, utilisation and storage (CCUS) strategies, which are considered as a viable solution for the reduction in the CO_2 emission in cement industries and stabilisation of atmospheric CO_2 concentration (Kashef-Haghighi & Ghoshal, 2013). Understanding of the carbonation process developed in this thesis could be valuable for further research in this application area.

2.3 Changes in hardened cement paste after carbonation

2.3.1 Chemical reactions

C-S-H and $Ca(OH)_2$ are the main hydration products that make up 50-60 vol. % and 20-25 vol.% of the total solid volume respectively in a completely hydrated cement paste. Carbonation primarily involves portlandite, which forms $CaCO_3$ and releases free water (Equation 2.1). $CaCO_3$ has three polymorphs, calcite, aragonite and vaterite in the order of decreasing thermodynamic stability. Initially, hydrated forms of $CaCO_3$ involving amorphous $CaCO_3$ and monohydrocalcite can form, acting as precursors and gradually transforming into other more stable polymorphs by dissolution-precipitation (Ogino et al., 1987; Black et al., 2007; López-Arce et al., 2011; Al Omari et al., 2016). The carbonation of $Ca(OH)_2$ causes a drop in the pH of the pore solution. This subsequently reduces the stability of other phases such as C-S-H, ettringite, and monosulfate, enabling them to carbonate. According to thermodynamics, the carbonation of these more stable phases can occur after all portlandite has reacted. However, in real systems, all of these phases may carbonate simultaneously (Slegers & Rouxhet, 1976).

Carbonation of C-S-H causes the leaching of calcium from the interlayer, precipitation of $CaCO_3$ and formation of a porous silica gel (Equation 2.2). This is accompanied by the reduction of Ca/Si ratio in C-S-H. The $CaCO_3$ formed during C-S-H carbonation has been found to be aragonite and vaterite

according to Morandeau et al. (2014) who also confirmed that this process does not release physical water but results in a highly hydrated silica gel.

Compared with $Ca(OH)_2$ and C-S-H, ettringite and monosulfate are minor phases in hydrated CEM I and their carbonation produces $CaCO_3$, alumina gel, gypsum, and water (Equation 2.3 and 2.4). Additionally, unreacted cement (alite and belite) can also react with CO_2 and water converting these to $CaCO_3$ and C-S-H. The $CaCO_3$ formed contains both calcite and aragonite, and the structure of the C-S-H formed from carbonation is similar to that from cement hydration (Ashraf & Olek, 2016). However, further carbonation results in decalcification of C-S-H (Equation 2.5 and 2.6). Ashraf & Olek (2016) witnessed a similar carbonation reactivity of C_3S and C_2S, though C_3S hydrates much faster than C_2S. Other minor phases such as Na_2O and K_2O mainly stay in the pore solution in the form of NaOH and KOH can also react with CO_2. Most phases in the hardened cement paste can potentially carbonate, especially those containing CaO.

$$Ca(OH)_2 + CO_2 \rightarrow CaCO_3 + H_2O \qquad \text{Equation 2.1}$$

$$x(CaO) \cdot (SiO_2) \cdot n(H_2O) + xCO_2 \rightarrow xCaCO_3 + SiO_2 \cdot (H_2O)_n \qquad \text{Equation 2.2}$$

$$3CaO \cdot Al_2O_3 \cdot 3CaSO_4 \cdot 32H_2O + 3CO_2 \rightarrow 3CaCO_3 + 3(CaSO_4 \cdot 2H_2O) + Al_2O_3 \cdot (H_2O)_n + (26-n)H_2O \qquad \text{Equation 2.3}$$

$$3CaO \cdot Al_2O_3 \cdot CaSO_4 \cdot 12H_2O + 3CO_2 \rightarrow 3CaCO_3 + CaSO_4 \cdot 2H_2O + Al_2O_3 \cdot (H_2O)_n + (10-n)H_2O \qquad \text{Equation 2.4}$$

$$3CaO \cdot SiO_2 + 3CO_2 + nH_2O \rightarrow 3CaCO_3 + SiO_2 \cdot (H_2O)_n \qquad \text{Equation 2.5}$$

$$2CaO \cdot SiO_2 + 2CO_2 + nH_2O \rightarrow 2CaCO_3 + SiO_2 \cdot (H_2O)_n \qquad \text{Equation 2.6}$$

2.3.2 Microstructural changes

2.3.2.1 Pore structure in hardened cement paste

Hardened cement paste contains multiple phases including various hydration products, unreacted cement particles, and pores, resulting in a complicated microstructure. Pores are inevitable in

concrete, and their presence facilitates mass transport and carbonation. The ingress of gaseous CO_2 occurs via the pore structure and the penetrated CO_2 react with cement components when dissolved in the pore solution. Thus, the pores govern both the transport of CO_2 and the carbonation reactivity. The four major pore types with sizes increasing from nanometres to millimetres are gel pores, capillary pores, entrained and entrapped air voids. Gel pores are the interstitial spaces residing in the C-S-H structure with a characteristic dimension of approximately 1-3 nm (Neville, 2011), which is too small to have a practical influence on transport of ions. Gel pores make up around 30% of the C-S-H volume and have the capacity to hold a large amount of evaporable water. Capillary pores are spaces that are originally filled with water and are progressively occupied by hydration products; the dimension of these pores is approximately 0.01 to 10 μm. Air voids can be entrapped due to incomplete compaction or entrained intentionally by means of air-entraining admixture for frost protection. Entrapped air voids make up approximately 1-2 vol. % of a typical concrete while entrained air voids are usually specified at 5-8 vol. % with void dimensions larger than 10 μm and spacing factor of ~200 μm to ensure adequate freeze-thaw resistance. Capillary pores and air voids are usually interconnected, providing continuous paths for mass transport (Wong et al., 2011).

2.3.2.2 Microstructural changes due to $Ca(OH)_2$ carbonation

Carbonation is accompanied by microstructural changes within the hardened cement paste because of volumetric differences between the solid reactants and products of carbonation. As one of the main carbonation processes, the conversion from $Ca(OH)_2$ to $CaCO_3$ is volumetrically expansive by 2.9% to 18.7% depending on the polymorphs formed (Table 2.1). $CaCO_3$ precipitates preferentially in smaller pores because of their better water condensation (Arandigoyen et al., 2006); this process refines the pore structure and increases the proportion of pores with smaller diameters. Therefore, $Ca(OH)_2$ carbonation leads to a reduction in overall porosity, decreasing further transport of CO_2 into concrete. However, $Ca(OH)_2$ carbonation is also believed to be one of the reasons for carbonation shrinkage due to the loss of water formed in $Ca(OH)_2$ carbonation; this drying process is caused by the moisture gradient between the environment and the pore, and the latter is believed to be saturated with water when the carbonation rate is high in the locality (Swenson & Sereda, 1968).

Table 2.1 Properties of the minerals involved in carbonation reaction (Arandigoyen et al., 2006).

Mineral	Molar volume (cm^3/mol)	Crystal shape	Variation of volume (%)
Portlandite	33.20	Laminar	/
Calcite	36.93	Prismatic	11.2
Aragonite	34.16	Fibrous	2.9
Vaterite	39.40	Spherical	18.7

2.3.2.3 Microstructural change due to C-S-H carbonation

C-S-H carbonation involves two main processes: decalcification of C-S-H and formation of silica gel; the latter usually occurs in the later stage. C-S-H decalcification refers to leaching of calcium ions from the C-S-H interlayer to surrounding pore solution and subsequent reaction with carbonic ions to form $CaCO_3$. Solid $CaCO_3$ precipitates on the pore walls outside of the C-S-H and the Ca/Si ratio of the C-S-H is reduced (Shah et al., 2018). The precipitation of solid $CaCO_3$ reduces the surrounding pore size (Groves et al., 1990) and the extent of reduction is dependent on the Ca/Si ratio in C-S-H: vaterite is detected for Ca/Si ratios > 1.0, whereas aragonite has been reported for Ca/Si ratios < 0.5 (Nishikawa & Suzuki, 1994). The decrease of Ca/Si ratio also changes the C-S-H morphology from a fractal structure at Ca/Si = 1.7 to a sheet-like structure for Ca/Si < 1.1 (Šavija & Luković, 2016). At Ca/Si ratios < 1, C-S-H transforms into a highly deformable structure with very limited cohesion (Heukamp et al., 2003). Eventually, C-S-H can decompose completely when fully carbonated.

Calcium is gradually removed from the C-S-H interlayer as carbonation proceeds. This removal causes negative charges in the C-S-H structure, which are readily balanced by the formation of Si-OH groups. The neighbouring Si-OH groups tend to condense to form Si-O-Si linkage causing an increase of attraction between neighbouring regions; total volume within the C-S-H area is subsequently reduced resulting in capillary pore coarsening. The formation of silica gel is another reason for carbonation shrinkage (Chen et al., 2006).

In comparison to $Ca(OH)_2$ carbonation, the effect of C-S-H carbonation on porosity is more complicated. The solid volume is increased in the area outside of C-S-H due to the precipitation of $CaCO_3$, but decreased within the C-S-H structure due to the formation of amorphous silica gel. Thus, the overall volume variation due to C-S-H carbonation is governed by the molar volume change of both processes. Since water formed during C-S-H carbonation is all bonded in silica gel ($SiO_2 \cdot xH_2O$), its molar volume can vary significantly from 12 to 34 cm^3/mol depending on the amount of water (Wolery, 1992; Morandeau et al., 2014). Thiery et al. (2011) witnessed an increase in the overall volume after C-S-H carbonation where the silica gel contains approximately two water molecules (x closes to 2 in $SiO_2 \cdot xH_2O$). In addition, C-S-H carbonation is also accompanied by the morphology change of C-S-H structure due to the reduction of Ca/Si ratio.

2.3.2.4 Overall microstructural changes in hardened cement paste

The overall porosity and pore size distribution variations in hardened cement paste after carbonation are dependent on the extent of carbonation of both $Ca(OH)_2$ and C-S-H phases.

In CEM I concrete, $Ca(OH)_2$ carbonation is likely to dominate over C-S-H carbonation and a reduction of overall porosity is normally witnessed (Houst & Wittmann, 1994; Ngala & Page, 1997; Villain & Thiery, 2006; Thiery et al., 2011; Leemann et al., 2017). However, for blended cement concrete, the findings from previous studies are inconsistent; these include decreased total porosity (Ngala & Page, 1997; Fabbri et al., 2009; Chindaprasirt & Rukzon, 2009; Gruyaert et al., 2013) and increased total porosity (Leemann et al., 2015; Shi et al., 2016; Wu & Ye, 2017). The variation in total porosity is reported to be relevant to the substitution levels of SCMs (Ngala & Page, 1997), the initial $Ca(OH)_2$ content (Auroy et al., 2015), the type of the SCMs (Leemann et al., 2017) and the amount of carbonated C-S-H (Neville, 2011; Wu & Ye, 2017).

For the change of pore size distribution after carbonation, the precipitation of $CaCO_3$ refines the pore structure and increases the proportion of small pores, while the formation of silica gel coarsens the pores and increases the proportion of large pores. Again, this variation is dependent on the blending systems. The filling of small pores is more profound in CEM I systems, however, the extent of pore coarsening can increase with the water/cement (w/c) ratio (Villain & Thiery, 2006). In comparison, significant pore coarsening was reported in blended cements irrespective of the SCMs types (Litvan & Meyer, 1986; Morandeau et al., 2015; Auroy et al., 2015; Leemann et al., 2017). Additionally, the change in pore size distribution is also dependent on CO_2 concentration. Thiery et al. (2012) reported the occurrence of large pores (diameter > 100 nm) when exposing CEM I to 50% CO_2, but this was considerably reduced when applying a lower concentration of 10%. This was attributed to excessive carbonation of C-S-H triggered by unrealistically high CO_2 concentration.

2.4 Influence of carbonation on transport properties

Transport properties are important indicators of concrete durability and they govern the rate of carbonation. The three major transport mechanisms are gas diffusion, gas permeation and water absorption. These refer to the transport of substances as a result of concentration difference, pressure gradient and capillary suction respectively. Transport properties are dependent on the total porosity and pore size distribution of the material. Processes like carbonation that change the phase composition and microstructure can affect the transport properties of concrete. Among the mentioned transport properties, gas diffusion is the most tested one as the CO_2 diffusion coefficient is the decisive factor of the carbonation process (Houst, 1996). However, since CO_2 is reactive with cement-based materials, O_2 is often used instead because it is also relevant to steel corrosion.

Ngala & Page (1997) mentioned that the influence of carbonation on O_2 diffusivity is more profound on blended systems than on CEM I systems. The effect is also dependent on the SCM type. Leemann et al. (2017) witnessed a decrease in O_2 diffusivity in CEM I and blended cements (containing 15%

limestone powder or portlandite) due to the dominance of porosity reduction over pore coarsening. In contrast, blended mortars containing 15% microsilica and 66% slag showed increased diffusivity due to predominant pore coarsening. Similarly, decreased O_2 diffusivity was also reported in concretes cast with CEM I and cement blended with 30% PFA after carbonation in Bertin et al. (2018), while increased O_2 diffusivity was found in concrete containing 60% GGBS. These authors also observed an increase in both gas and moisture permeability for all samples due to the coarser pore structure with higher interconnectivity.

Microcracks can also affect transport properties. Drying-induced microcracking is found to have a more profound influence on permeability than on diffusivity and sorptivity, because permeation is more size-dependent, while diffusion and water absorption are more relevant to total porosity (Wong et al., 2009). In terms of carbonation-induced microcracking, a similar phenomenon was reported by Borges et al. (2010) who found a significant increase in O_2 permeability in samples blended with up to 90% of slag after carbonation, and by Lin et al. (2013) who exposed cement slurry samples to supercritical conditions. However, reduced permeability was also reported in previous studies (Martin, 1986; Dewaele et al., 1991; Song & Kwon, 2007). Nevertheless, available studies on the effect of carbonation-induced microcracks are limited.

2.5 Accelerated carbonation

In natural environments, carbonation is a slow process that would normally take several years to obtain a detectable carbonation area. This is mainly because of the low CO_2 concentration in the atmosphere (around 0.04%). To study carbonation within a practically short duration, accelerated tests are normally used in previous studies by applying unrealistically high CO_2 concentrations. Some studies employed 1% (BS EN 13295, 2004; Bernal et al., 2012; Shi et al., 2016), mostly 2-4% (Ho & Lewis, 1983; DuraCrete, 1999; FIB 34, 2006; Castellote et al., 2009; Visser, 2012; Bernal et al., 2012; BS 1881-210, 2013; Cui et al., 2015; Leemann et al., 2017), 10% (Morandeau et al., 2014), 20% (Chang & Chen, 2006; GB/T 50082-2009, 2010; Liu et al., 2016), even up to 50% (Papadakis et al., 1991a) and 100% (Groves et al., 1991; Phung et al., 2015). Accelerated carbonation dramatically increases the carbonation rate and is increasingly involved in the research on developing carbon capture, utilisation and storage strategies such as accelerated CO_2 curing of concrete and carbonation of waste concrete fines. Nevertheless, when used for assessing the carbonation depth and extent of a cement-based material, such short-term accelerated carbonation test distorts the deterioration mechanism in relation to natural carbonation, providing results that are not representative of the actual carbonation in service.

First of all, the carbonation mechanism of different phases involved can be distorted. Groves et al. (1991) reported that the carbonation rate of portlandite can be significantly enhanced under pure CO_2. This can lead to the rapid precipitation of $CaCO_3$ directly on the portlandite crystals, forming a dense layer that inhibits the further carbonation of CH. This dense layer was also detected by Chen et al. (2006), Galan et al. (2015) and Šavija & Luković (2016). Apart from portlandite, carbonation of other cementitious constituents is also affected. For example, Castellote et al. (2009) found that increasing CO_2 concentration from a natural level to > 10% significantly increases the carbonation rate of unreacted cement, C-S-H and ettringite. As has been mentioned, the microstructural change after carbonation is mainly governed by $Ca(OH)_2$ and C-S-H carbonation. Accelerated carbonation distorts the carbonation of $Ca(OH)_2$ and C-S-H, thus, the change in microstructure is also affected.

Furthermore, elevated CO_2 concentration also alters the $CaCO_3$ polymorphs formed during carbonation. Calcite was found the only $CaCO_3$ when exposing PC paste to pure CO_2, while all three polymorphs were developed under natural conditions (Goñi et al., 2002). A similar observation was made by Anstice et al. (2005) who found the abundance of aragonite than the other two polymorphs under natural carbonations. However, Auroy et al. (2018) reported that 3% CO_2 tended to promote the precipitation of vaterite and aragonite with regards to calcite. They also conclude that these three polymorphs were generated from the carbonation of C-S-H, ettringite and portlandite respectively. Even though accelerated carbonation at a low CO_2 concentration (e.g. 3%) was reported to be somewhat representative of natural carbonation in terms of mineralogical and microstructural change in cement pastes (Castellote et al., 2009; Auroy et al., 2018), this is not applicable to all binding systems and was reported to underestimate the service life prediction for alkali-activated binders when exposed to 1% CO_2 concentration (Bernal et al., 2012). Furthermore, the conversion from accelerated carbonation results to natural carbonation using established empirical equations are still not accurate enough and was found to underestimate the true carbonation rate for mortars with 50% PFA exposed to 1% CO_2 (Van Den Heede & De Belie, 2019).

In addition, accelerated carbonation distorts the carbonation rate by affecting the saturation degree of the specimen. A favouring water saturation degree is needed for carbonation; carbonation effectively stops when the specimen is too wet or too dry. Researchers usually control the water content in cementitious samples by controlling the relative humidity (RH) of the exposure environment and previous studies indicate that carbonation reaches a maximum rate when the RH is between 50 and 70% (Wierig, 1984; Saeki et al., 1991). Although favouring RH is controlled in the exposure environment, water is also produced in pores during $Ca(OH)_2$ carbonation, which could increase the local saturation degree and reduce the carbonation rate. This is not a problem for naturally carbonated specimens as water is only slowly produced due to a low carbonation rate, allowing sufficient time for the excess water to evaporate. However, in accelerated tests, rapid carbonation results in fast

saturation of the sample due to the rapid formation of water filling up capillary pores, and limited conditioning time to remove the excess water, which significantly reduces the carbonation rate (Phung et al., 2015).

The main carbonation process involves: (1) transport of CO_2 in concrete and dissolution in pore solution; (2) chemical reactions between dissolved CO_2 and constituents of concrete; and (3) microstructural changes leading to the variation in physical properties of concrete. Increasing the CO_2 concentration to accelerate one process do not accelerate the others to the same extent such that the overall carbonation mechanism is distorted in relation to natural carbonation. This could lead to unrealistically larger changes in microstructure and carbonation depth measurements, making the accelerated carbonation test not a reliable approach when modelling carbonation depths in cement-based materials. Therefore, a more promising alternative is to expose specimens to natural carbonation, characterising carbonation profile with time and extrapolating to longer-term performance. As natural carbonation is a rather slow process and for the most practical exposure periods, the carbonation depth will only be a few mm or less. To measure such small depths, a reliable methodology needs to be developed.

2.6 Techniques to measure carbonation

2.6.1 pH indicator

Carbonation is an acidification process reducing the pH of the pore solution from approximately 13 to 8. The changes in alkalinity can be detected with a pH indicator. For example, a solution of 1% phenolphthalein in 70% ethanol is recommended by RILEM Committee CPC-18 (1988) and BS EN 13295 (2004). The colouration pH range of phenolphthalein is between 8.2 and 9.8 (Vogler et al., 2020) from colourless to pink. The phenolphthalein solution is sprayed onto the freshly broken surface of the specimen, and the colour change occurs almost instantly that reveals two distinct regions. The colourless region close to the exposed surfaces is regarded as the fully carbonated zone with a $pH < 8.2$, while the region located in the core of the specimen exhibiting a bright pink colour is regarded as the non-carbonated zone with a $pH > 9.8$. The boundary between the two regions is the carbonation front. This front is approximately parallel to the exposed surface but can be irregular due to: (1) presence of aggregate that is usually dense and unreactive with CO_2 acting as a local obstacle; and (2) heterogeneity in microstructure of hardened cement paste leading to spatially varying transport rates. As such, the carbonation depth of a specimen is usually calculated by averaging the carbonation depths at multiple locations. The depth is usually measured with a ruler, which is simple and rapid, but likely to produce operational errors. To mitigate this, a more accurate approach is by image analysis (Herrera, 2011). Nevertheless, since this method is based on the visual judgment of

colouration boundary, the accuracy of the measurement is often found to be impaired by the insignificant colouration (Lo & Lee, 2002).

Despite its simplicity and convenience, this technique is often criticised to 'underestimate' the true carbonation depth. One reason is associated with the limitation in determining the extent of carbonation and in verifying the presence of partially carbonated zones, which is, however, evident when profiling the carbonation product using profile-grinding analysis techniques (Chang & Chen, 2006). As a result, the determined carbonation front by phenolphthalein is believed to be located in the partially carbonated zone, ahead of the actual carbonation front in terms of chemical reaction. Another reason for the underestimation is ascribed to the discrepancy between the colouration pH range of phenolphthalein (8.2-9.8) and the threshold pH value of passive film decomposition (11.5) of reinforcement steel (Parrott, 1987). Therefore, the underestimation could lead to a situation where corrosion of embedded steel is already initiated before the apparent carbonation front as measured by this method reaches the steel (Yoon et al., 2007; Hussain & Ishida, 2009; Hussain et al., 2011).

Furthermore, phenolphthalein is classified as carcinogenic and will be phased out for future use. Thus, alternative indicators, such as thymol blue (colouration pH 8.0-9.6 from yellow to blue), thymolphthalein (colouration pH 9.3-10.5 from colourless to blue), alizarin yellow R (colouration pH 10-12.1 from light yellow to brown), tropaeolin O (colouration pH 11.1-12.7 from yellow to red) are have been proposed as potential replacements (Sufian Badar et al., 2014; Belda Revert et al., 2018; Vogler et al., 2020). Among these indicators, thymolphthalein is recommended by Yu et al. (2010) as the best substitute for phenolphthalein as they have a close colouration range. Furthermore, a combination of these indicators including phenolphthalein can increase the accuracy as it exhibits several colour changes over a wider colouration range, for example, a universal indicator shows blue when pH lies between 8 and 11, and violet when pH is higher than 11.

2.6.2 Thermogravimetric analysis (TGA)

TGA is a widely applied profile-grinding analysis technique for quantitative characterisation of microstructure including assessment of carbonation. This technique measures the mass fraction of hydration and carbonation products via continuous monitoring of the mass of a powdered sample at gradually increasing temperature at a constant rate (10-20°C/min) from < 30°C to > 1000°C under an N_2 flow (Villain et al., 2007). Thermal decomposition of different phases occurs at different temperatures, which acts like a fingerprint to help distinguish their identities. The relationship between weight and temperature is depicted in a TG curve. The first derivative of this is known as a DTG curve, and it indicates the percentage weight loss in the temperature range of the TG curve (Chang & Chen, 2006).

For a carbonated sample, four peaks are generally recognised in a DTG curve. The first peak located at approximately 100℃ (Chang & Chen, 2006) or in a range of 25-105℃ (Huijgen et al., 2005) corresponds to the loss of free water physically absorbed in large pores. The next peak appears at about 130℃, corresponding to the loss of bound water (Valenti & Cioffi, 1985). The third peak located between 425 and 550℃ is ascribed to the disassociation of CH, which forms CaO and H_2O (Chang & Chen, 2006). The final peaks are located between 550℃ and 950℃ due to decomposition of $CaCO_3$, releasing CaO and CO_2. Regarding the polymorphs of $CaCO_3$, vaterite and aragonite decompose at a lower temperature due to their lower thermodynamic stability compared with calcite (Borges et al., 2010), though they cannot be clearly differentiated (Shah et al., 2018). Nevertheless, Torres-Carrasco et al. (2017) mentioned that the 530-650ºC, 650-800ºC, and 800-900ºC regions are correspondent to the decarbonisation of vaterite, aragonite and calcite respectively. Based on the peaks of $Ca(OH)_2$ and $CaCO_3$, the proportions of these phases can be measured, and their profile as a function of depth can be plotted to estimate carbonation depth, which is defined as the depth beyond which the phase profiles become stable (Chang & Chen, 2006).

The depth determined by TGA is believed to be more accurate than the phenolphthalein spray test. Previous studies have found that carbonation depths obtained from TGA were two times larger than those obtained using phenolphthalein (Chang & Chen, 2006). A twofold result was also obtained when using alternative indicators such as alizarin yellow R and a mixed indicator (Vogler et al., 2020). In addition to this, the profiles of different phases at different depths determined by TGA also reveals that carbonation does not produce a sharp front, but a partially carbonated zone exhibiting a transition of the contents of $Ca(OH)_2$ and $CaCO_3$. It has been observed that the increase in the amount of $CaCO_3$ at a certain carbonation depth is larger than the decrease in the amount of $Ca(OH)_2$ at the same depth (Fig. 2.1). This indicates that the carbonation of other phases, e.g., C-S-H, also occur in addition to CH.

Despite its advantages, this technique is destructive and requires substantial sample preparation including cutting, crushing, powder grinding, and sieving to increase the total surface area for sufficient thermal decomposition. The powders are usually collected directly using an electric drill at consecutive depths following a small interval of typically several mm. However, this process can suffer from operational error and powder contamination when drilling the sample, and the limited sampling locations may be insufficient to achieve a truly representative analysis of the entire sample. To mitigate this, an alternative approach was employed by first slicing the sample into several layers and then grinding into powder. Nevertheless, additional carbonation can occur when the fine powders are exposed to atmospheric CO_2 (Morandeau et al., 2014). Furthermore, the measurement can be affected by the presence of aggregate, so they are less suitable for mortar and concrete samples (Villain et al., 2007; Witkowski & Koniorczyk, 2018). Some disassociation peaks can overlap and

disturb the measurement, hence, TGA is sometimes supplemented with mass spectrometry to differentiate the decomposition products (Villain et al., 2007).

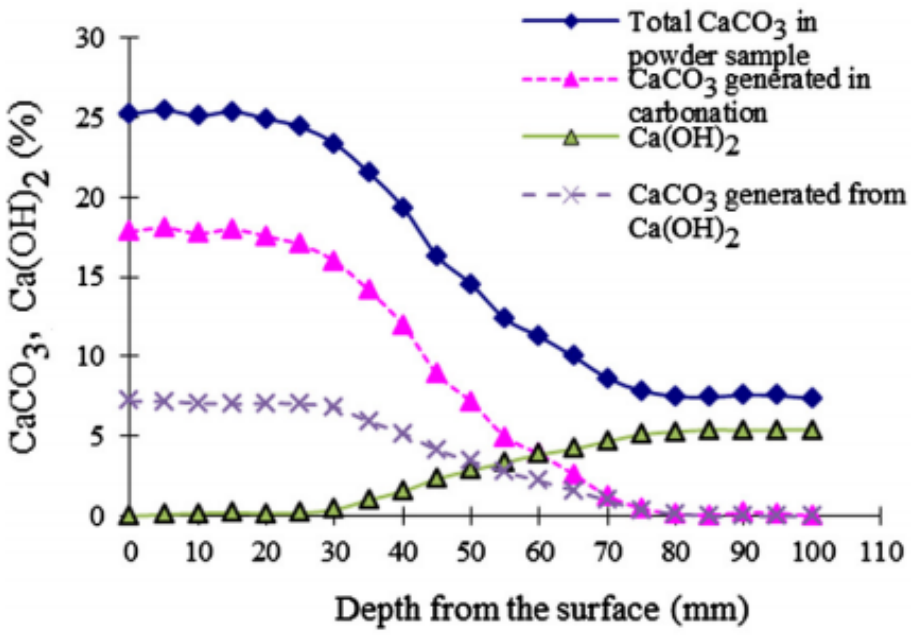


Figure 2.1 Profiles of $CaCO_3$ and $Ca(OH)_2$ against depth by TGA of CEM I concrete subjected to accelerated carbonation at 20% CO_2 concentration for 8 weeks (Ji et al., 2014).

2.6.3 X-ray diffraction (XRD)

XRD is another profile-grinding analysis technique for characterising the crystalline phases in cement-based materials. This relies on the detection of diffraction patterns when an X-ray beam interacts with the sample. By interpreting the XRD patterns combined with Rietveld analysis, the type and amount of a particular crystalline phase can be determined. This technique has been used to characterise the hydration and carbonation products in hardened cement paste (Phung et al., 2015; Khan et al., 2017; Shah et al., 2018; Liu et al., 2019), especially $Ca(OH)_2$ (identified by peaks at 2θ of 18.1°) and $CaCO_3$ polymorphs (Fukushima et al., 1998; Cultrone et al., 2005; Liu et al., 2019). By profiling the content of these phases against depth, the partially carbonated zone can be determined (Lee et al., 2017; Rafiq et al., 2018). The measured carbonation depth agrees well with the results from other profile-grinding analysis techniques, e.g., TGA (Chang & Chen, 2006). This technique has another advantage in terms of its ability to differentiate polymorphs of $CaCO_3$ based on their unique peaks, for instance, at 2θ of 29.4º, 45.8º, and 24.9º corresponding to basal planes of (104) for calcite, (221) for aragonite, and (110) for vaterite (Kontoyannis & Vagenas, 2000; Chong et al., 2014).

Even though XRD is believed to be a reliable method for detecting carbonation, this technique is destructive, and the spatial distribution of the measured phases is thus lost. Substantial sample

preparation is required, and the process suffers from the same issues as those discussed in TGA. XRD can only detect well-crystallised components but some amorphous components, such as C-S-H and amorphous $CaCO_3$, are difficult to be identified. To mitigate this, researchers (Castellote et al., 2009; Liu et al., 2019) have suggested the application of NMR to detect changes in C-S-H gel after carbonation.

2.6.4 Fourier transform infrared spectroscopy (FTIR)

FTIR is a vibrational spectroscopic technique that detects the presence of certain phases by their corresponding molecular bonds. The bonds are vibrating constantly in two motions, stretching and bending, and both can be symmetrical or asymmetrical, in-plane or out-of-plane. The four most general vibrational modes are in-plane symmetric stretching (ν1), out-of-plane bending (ν2), in-plane asymmetric stretching (ν3) and in-plane bending (ν4). These vibrations are unique and can absorb the infrared radiation of the matching frequency. Thus, the identification of the bond can be achieved via an FTIR spectrometer by plotting absorbance or transmittance (%) against wavenumber. For cement-based materials, this technique has been used to characterise cement clinkers, C-S-H, AFt/AFm (Horgnies et al., 2013) and the interfacial transition zone (ITZ) between cement paste and aggregate (Ševula et al., 1994).

Carbonation involves the conversion from a C=O bond in CO_2 to a C-O bond in $CaCO_3$, which can be characterised by its unique peak between wavenumber of 1410 and 1510 cm^{-1} in the FTIR spectrum (Chang & Chen, 2006). When examining samples at increasing depths, the intensity of the characteristic peak for the C-O bond decreases until a baseline is reached. This depth corresponds to the depth reaching a steady state in the phase profiling plot, and is regarded as the carbonation depth. In contrast, $Ca(OH)_2$ is detected by the characteristic peak of the O-H bond at 3640 cm^{-1} (Horgnies et al., 2013) and shows an increasing trend until the carbonation front is reached (Chang & Chen, 2006). Similar observations were made by Lo & Lee (2002) and Lee et al. (2012). In addition, Chang & Chen (2006) believed that FTIR is capable of detecting $CaCO_3$ from a pH of 8.3 to 11.5, and Lo & Lee (2002) extended this range to a pH of 12.5. These pH ranges are larger than the phenolphthalein solution, suggesting a better accuracy for FTIR. When comparing the carbonation depths determined by the two techniques, Lo & Lee (2002) found a 23.9% larger depth determined by FTIR, while Chang & Chen (2006) obtained a twofold result in agreement with those from TGA and XRD.

FTIR can also distinguish $CaCO_3$ polymorphs, based on their unique bands at 877 cm^{-1} (ν2) and 713 cm^{-1} (ν4) for calcite, 1083 cm^{-1} (ν1), 858 cm^{-1} (ν2), 713 cm^{-1} and 700 cm^{-1} (ν4) for aragonite, and 1087 cm^{-1} (ν1), 876 cm^{-1} (ν2), and 745 cm^{-1} (ν4) for vaterite (Chakrabarty & Mahapatra, 1999; Vagenas et al., 2003; Xu & Poduska, 2014). Furthermore, FITR can yield very fast measurements. It

only requires several minutes to obtain a result compared to several hours for other techniques such as TGA.

Despite the simplicity in FTIR measurement, the traditional transmittance mode requires the mixing of powder with KBr to produce a pellet before each measurement. Although this procedure is no longer needed for the other sampling modes, such as Diffuse Reflectance (DR) and Attenuated Total Reflectance (ATR), the powder preparation is still tedious and suffers from the same issues as TGA. Similar to TGA and XRD, the accuracy of FTIR can also be compromised by the presence of carbonaceous aggregate and this would require careful calibration (Herrera, 2011). The presence of capillary water could also disturb the interpretation of certain phases (Horgnies et al., 2013) and pre-conditioning will be needed.

2.6.5 Scanning electron microscopy (SEM)

SEM is an imaging technique commonly used to characterise the microstructure of concrete. This technique is often used in the backscattered electron (BSE) mode and supplemented with energy dispersive X-ray Spectroscopy (EDS). BSE are high-energy incident electrons that undergo elastic scattering and re-emerge from the sample surface. The intensity of BSE is proportional to the local mean atomic number, and a greater value results in a brighter pixel. Therefore, the grey levels in a BSE image can be used to discern different phases. A more detailed explanation can be found in Wong (2006), Stutzman (2004) and Stutzman et al. (2016). For a typical cement paste, the unreacted cement grains appear the brightest, while pores and microcracks appear the darkest as they are filled with epoxy. Other phases, such as unreacted slag, aggregate, hydration products and reacted slag shows decreasing brightness following unreacted cement. BSE has been extensively applied to study cementitious materials both qualitatively and quantitatively, for example, studies on estimating water-cement ratio, water content, cement content and degree of hydration (Wong & Buenfeld, 2009; Wong et al., 2013), the fraction of SCMs in hydrated blended cement (Feng et al., 2004; Yio et al., 2014), as well as the porosity and pore size distribution (Wong et al., 2006; Zeng et al., 2012; Yio, 2017).

SEM-BSE-EDS has also been applied to characterise carbonation. For example, Galan et al. (2015) studied portlandite carbonation in humid CO_2 gas (25%-90% RH) at high magnification and observed the growth of the dense $CaCO_3$ layer on the surface of portlandite crystals reducing the further leaching of Ca^{2+} and OH^-. C-S-H carbonation was reported by Shah et al. (2018) who observed the presence of two rims in the inner C-S-H with distinct brightness (Fig. 2.2): the inner darker rim with decreased Ca/Si ratio indicates C-S-H decalcification, and the surrounding brighter rim with elevated Ca content indicates the leaching of Ca^{2+} and the precipitation of $CaCO_3$. Furthermore, SEM is also capable of differentiating $CaCO_3$ polymorphs by their morphology. Under high magnification, calcite,

aragonite and vaterite typically exhibit layered and rhombohedral, spherical, and needle morphology respectively (Wang et al., 2013; Al Omari et al., 2016). $CaCO_3$ in an amorphous state can also be observed under SEM appearing as small spheres.

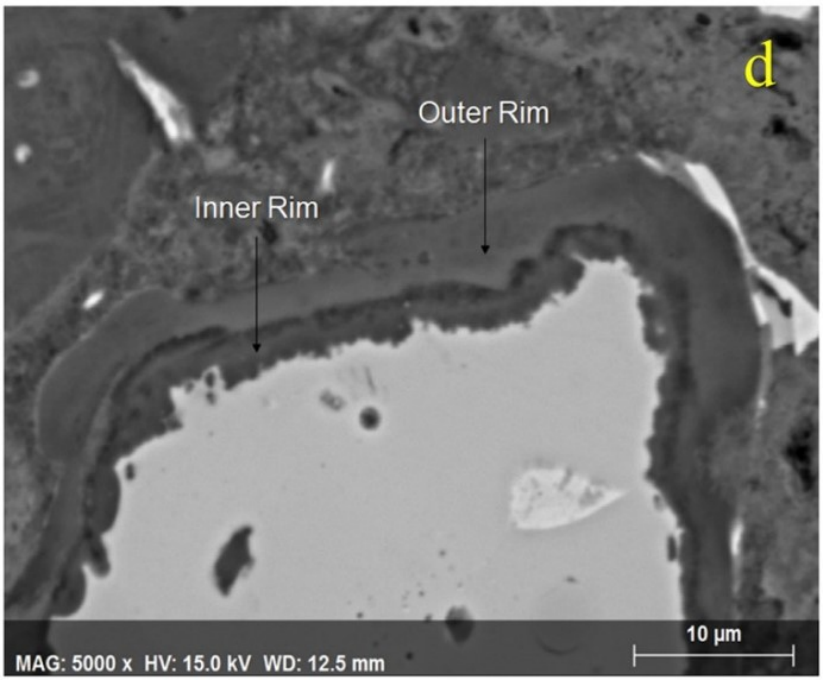


Figure 2.2 BSE image showing the two rims in the inner C-S-H, adopted from Shah et al. (2018).

In contrast, SEM is rarely used for determining carbonation depth or the spatial distribution of $CaCO_3$. The main obstacle is because phases like $CaCO_3$ and some hydration products have limited brightness contrast (Stutzman, 2004) and hence remain difficult to detect and isolate. Even though porosity change is often used instead to evaluate the extent of carbonation (Rimmelé et al., 2008), it can be affected by the heterogeneity in the cement paste or the ITZ introduced by aggregate. As a result, the porosity difference can be insignificant for visual justification. In such situation, EDS can be used to facilitate the differentiation. Since EDS is not reliable in measuring light elements such as carbon, oxygen and nitrogen, Branch et al. (2016) mapped the spatial distribution of Ca/(Al+Si) ratio and stated that the region with a high ratio is regarded to be dominated by $CaCO_3$, otherwise is dominated by decalcified C-S-H. However, the carbonation depth still cannot be clearly distinguished. Even though $CaCO_3$ can be detected to some extent by analysing carbon with better accuracy via wavelength dispersive X-ray spectroscopy (Kashef-Haghighi & Ghoshal, 2013), the type of polymorphs cannot be determined. Furthermore, the measurement of carbon can be disturbed by the carbon that exists in the impregnated epoxy resin. BSE imaging requires the sample to be fully dried, epoxy-impregnated, ground and polished, which is also time-consuming and requires expertise.

2.6.6 Raman spectroscopy

Raman spectroscopy is another vibrational spectroscopic technique capable of providing chemical and structural information of organic and mineral phases. It is based on the excitation of chemical bonds with a laser to produce Raman scattering. The frequency difference between the incident and scattered light, registered in the form of a spectrum, provides fingerprint information on chemical structure. Raman spectroscopy can detect oxides, carbonates, sulphates and silicates, and hence is particularly suitable for analysing cement-based materials. Since its first application on white cements by Bensted (1976), Raman spectroscopy has seen increasing use in the characterisation of various cements (Torréns-Martín et al., 2013), supplementary cementitious materials (Guedes et al., 2008; Yue et al., 2018), alkali-activated materials (Caggiani et al., 2021) and corrosion products (Marcotte & Hansson, 2007; Larroumet et al., 2007; Criado et al., 2015; Dang et al., 2015). This technique is also capable of distinguishing $CaCO_3$ polymorphs (Ibáñez et al., 2007; Corvisier et al., 2010; Martinez-Ramirez et al., 2013; Ševčík et al., 2016) and the respective Raman spectrum can be found in Fig. 2.3.

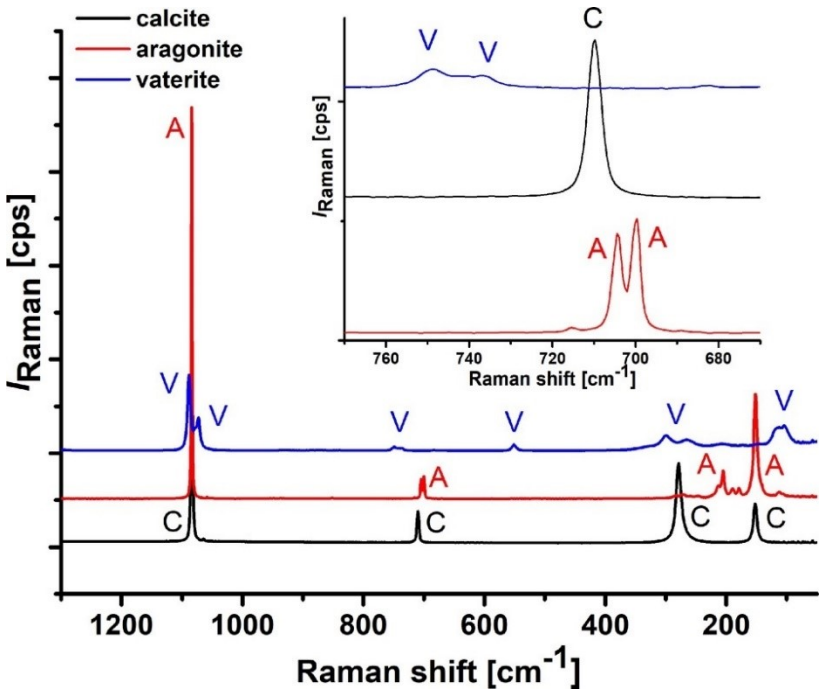


Figure 2.3 Raman spectra for calcite, aragonite and vaterite (Ševčík & Mácová, 2018).

Combining Raman spectroscopy with confocal microscopy enables high-resolution chemical imaging of phase distribution. The use of laser, confocal pinhole and high-power objective enables a very small sampling volume (~ 1 μm^3), thus achieving high spatial resolution analysis of local features. Confocal Raman micro-spectroscopy or microscopy (CRM) has been used to image clinker remnants and aggregates in historic cement stone (Schmid & Dariz, 2013) and hydration of cement pastes (Higl

et al., 2016; Mikhailova et al., 2019; Torres-Carrasco et al., 2019). Upon carbonation, Corvisier et al. (2010) mapped the spatial distribution of $CaCO_3$ polymorphs on samples exposed to supercritical CO_2 and concluded that vaterite is the first polymorph to crystalise in the carbonation process. Ševčík et al. (2016) studied the evolution of carbonation depth in lime pastes and observed the formation of amorphous $CaCO_3$ in the partial carbonated zone. The weathering of anhydrous cement was studied by Torres-Carrasco et al. (2017) who found the coexistence of carbonate and amorphous carbon. Most recently, Mi et al. (2021) assessed the correlation between the Raman intensity and the content of $CaCO_3$ and the quantified carbonation degree of the cement paste agreed with that obtained with TGA. These studies have shown the ability of CRM to map $CaCO_3$, however, the reliability of CRM to determine carbonation depth is still not confirmed as the comparison with other well-characterised techniques has not been systematically studied. In addition, previous studies focused more on the hardened CEM I paste and the effect of SCMs and aggregate remains under-explored.

CRM is non-destructive and does not require complicated sample preparation compared to the abovementioned techniques. This technique can also provide insightful information on phase composition. However, it probes only the sample surface, thus the sample still needs to be sectioned to measure carbonation depth. The cross section should be flat and smooth to generate good Raman images even though live tracking (autofocusing) is available in some equipment. The scanning process can be time-consuming, especially when imaging a large area.

2.7 Mathematical modelling of carbonation

Carbonation is one of the main causes for steel corrosion in reinforced concrete, and this problem has led to a huge economic burden, estimated to account for 3–5% of the national gross domestic product (Ekolu, 2016). Therefore, a comprehensive understanding of the carbonation process for modelling long-term carbonation resistance is required.

In the past decades, many mathematical models for predicting concrete carbonation have been developed. Most of these are semi-empirical and developed by fitting mass transport theory, for instance, Fick's first law of diffusion, to the experimental results to determine the required parameters. The most general expression of these mathematical models is the square-root-of-time law to determine the carbonation coefficient (Ho & Lewis, 1987b; Papadakis et al., 1991a). This model is simple to use in conventional cement-based materials, and has shown some good correlations with experimental results (Papadakis et al., 1991a; Köliö et al., 2016; Omikrine Metalssi et al., 2020; Zhang et al., 2020). In addition to the carbonation duration, many other models were developed by incorporating the effect of other influential factors for the carbonation process, such as CO_2 concentration, temperature, RH, concrete quality, etc. (Kobayashi & Uno, 1990; Papadakis et al.,

1991b; Jiang et al., 2000; Khunthongkeaw et al., 2006; Hyvert et al., 2010; Zhang & Xiao, 2018; Carević et al., 2019). These models assume a steady state of diffusion, while in real carbonation, the diffusion rate of CO_2 in concrete changes over time. This fact was taken into consideration in another simple model established by changing the exponent value of the carbonation duration in the basic square-root-of-time law. Such model was found to fit the carbonation data from samples blended with high content of SCMs or subjected to long-term loading (Sisomphon & Franke, 2007; Ekolu, 2018).

Despite the simplicity and convenience, the most general square-root-of-time model considers solely the carbonation duration to calculate the carbonation coefficient, neglecting the effect from other influential factors of the carbonation process. Even though these are involved in some more sophisticated models, such models are generally established with limited amount of experimental data from certain carbonation conditions, thus their applicability in wide applications is still limited to some extent. Some of the models are based on results from accelerated carbonation with the assumption that the observed mechanism can be directly transferred to natural carbonation (FIB 34, 2006; Wang & Lee, 2009; Zhang et al., 2013; Ta et al., 2016; Wang et al., 2020). However, this is not the case as has been discussed in Section 2.5. Therefore, utilising natural carbonation data from long-term exposure trials and carbonation surveys would be a more rational approach for carbonation modelling. Unfortunately, such data generally involves a large number of relevant variables, missing data and non-linearity, which can be highly difficult to utilise with conventional empirical modelling methods.

2.8 Summary

Carbonation is a highly complex phenomenon that involves mass transport and chemical reaction of atmospheric CO_2 with calcium-bearing phases, mainly $Ca(OH)_2$ and C-S-H, in cement-based materials. The carbonation of these phases alters the microstructure and transport properties in different manners, and such changes can in turn affect the subsequent carbonation process. Since natural carbonation is a very slow process, accelerated carbonation with elevated CO_2 concentration is often applied in laboratory studies. Such tests dramatically increase the carbonation rate and are increasingly involved in research on developing carbon capture, utilisation and storage strategies such as accelerated CO_2 curing of concrete and carbonation of waste concrete fines. However, accelerated carbonation distorts the real carbonation mechanism in relation to natural carbonation, resulting in unrealistic measurement of microstructural change as well as the carbonation depth and extent, and the application of results from such tests is not ideal for carbonation-modelling. A promising alternative is by carbonating the samples in natural conditions, characterising the carbonation depth

with time, and extrapolating to long-term carbonation resistance. The most critical part here is the ability to measure the shallow carbonation depth after short-term natural exposure.

The most widely used method for characterising carbonation depth in concrete is the phenolphthalein spray test. Despite its simplicity and convenience, this technique is often said to 'underestimate' the true carbonation extent in concrete due to the uncertainties caused by partial carbonation. Moreover, phenolphthalein is classified as a carcinogen, and will be phased out for future use. More advanced profile-grinding analysis techniques including TGA, XRD and FTIR have been adopted to provide more accurate measurements of $CaCO_3$ formed and therefore the extent of carbonation. However, such techniques are not suitable for measuring shallow carbonation depth due to their destructive sample preparation and limited sampling resolution. The presence of aggregate particles in concrete further complicates data analysis. BSE has been widely applied to study microstructural changes induced by carbonation in concrete at high magnification, while successful application for measuring carbonation depth is still limited. In contrast, CRM is able to study the spatial distribution of $CaCO_3$ with high resolution and is believed to be a suitable technique to detect and measure shallow carbonation depths. However, several unclear aspects need to be addressed before it can be used confidently.

In the past decades, many mathematical models for predicting carbonation have been developed and most of these are semi-empirical. Despite the simplicity, these models are generally established with limited amount of experimental data from certain carbonation conditions, thus their general applicability remains questionable. Some of the models are based on results from accelerated carbonation, where results are distorted in relation to natural carbonation. The other issue is the large number of factors influencing the carbonation process that cannot be modelled comprehensively using conventional approaches.

3 Methodology

This chapter describes the materials and experimental procedures applied in this thesis. Details involving materials, sample preparation and instrumentation are introduced.

3.1 Materials and mix proportion

3.1.1 Materials

The cementitious materials used were CEM I 52.5 N, CEM I blended with 30% Class F PFA, and 50% GGBS. The oxide compositions and the properties of CEM I, PFA, and GGBS are given in Table 3.1. The mineral composition of CEM I was 62.4% C_3S, 10.3% C_2S, 10.6% C_3A, 2.2% C_4AF and 4.9% calcite as limestone filler, and the specific gravity and loss on ignition were 3.06 and 2.1 respectively. Thames Valley sand (< 5 mm) and gravel (< 10 mm) were used as fine and coarse aggregate, respectively. The particle size distributions are given in Fig. 3.1. Physical properties involving specific gravity at saturated and surface dry condition (SSD), 24-hour absorption, and moisture content of the sand and gravel are shown in Table 3.2.

Table 3.1 Oxide composition and loss of ignition of CEM I, PFA and GGBS.

Material	Oxide composition: %								Loss of ignition (%)
	CaO	SiO_2	Al_2O_3	Fe_2O_3	MgO	Na_2O	K_2O	SO_3	
CEM I	63.4	20.8	5.4	2.4	1.5	0.3	0.7	2.7	2.1
PFA	5.0	52.7	25.9	6.2	1.6	0.5	1.4	0.3	2.6
GGBS	41.5	34.7	11.5	0.5	6.1	0.2	0.7	2.9	1.0

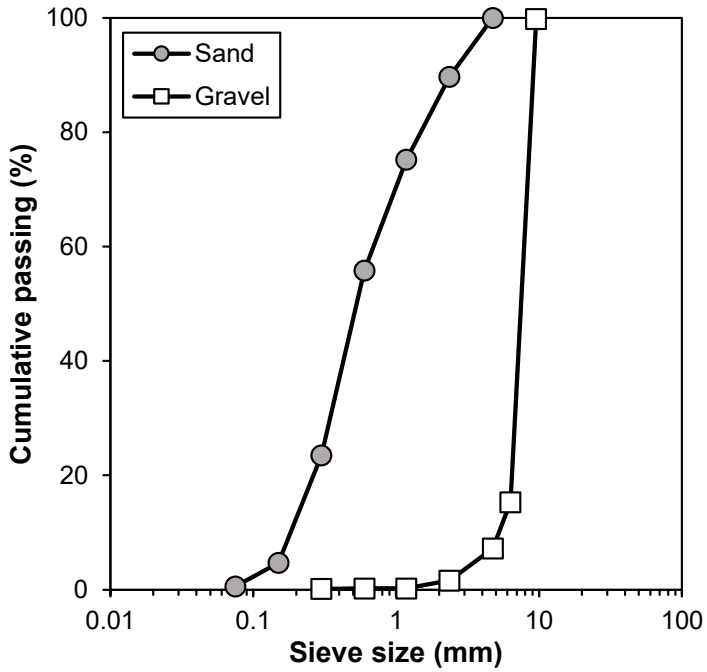


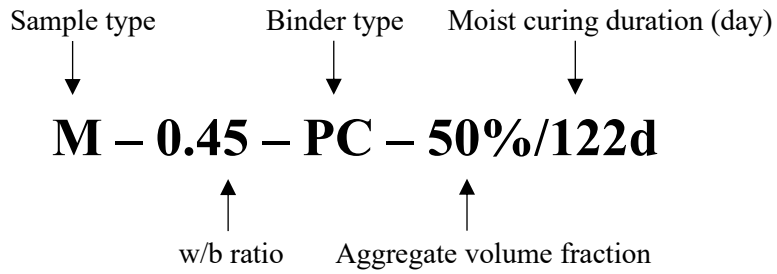
Figure 3.1 Grading curves for Thames valley sand and gravel.

Table 3.2 Specific gravity at SSD, 24-hour absorption and moisture content of sand and gravel.

Aggregate type	Specific gravity	24-hour absorption (%)	Moisture content (%)
Sand	2.54	0.52	0.22
Gravel	2.71	0.87	0.48

3.1.2 Mix proportions

Absolute volume method was employed to calculate the proportions of CEM I, SCMs, tap water, and aggregates. Different samples were prepared based on the purpose of the study. In general, paste, mortar and concrete samples were cast at water/binder (w/b) ratios of 0.45 and 0.6 to obtain a low and high porosity material. The aggregate volume fractions were 20% and 50% for mortar, and 70% for concrete. Since aggregates were stored open in the laboratory and were relatively dry, the additional water, taken as the difference between the 24-hour absorption and moisture content (Table 3.2), was added to the batch water, to obtain the designed free w/b ratio in the hardened cement paste. The samples were exposed to moist curing in a fog room at > 95% RH and 21 ºC for 3 and 122 days. All samples follow the designation format shown in Fig. 3.2. The specific mix proportions, casting, curing, conditioning and carbonation procedures were slightly different and will be introduced separately in the respective chapters.



Notation:

Sample type	P	= Paste
	M	= Mortar
	C	= Concrete
Binder type	PC	= CEM I
	V	= CEM I blended with 30% PFA
	S	= CEM I blended with 50% GGBS

Figure 3.2 Sample designation.

3.2 Development of a natural carbonation chamber

Carbonation was carried out in two Panasonic incubators (MCO-230ACI-PE) with an internal volume of 230 L. This incubator was equipped with a built-in CO_2 sensor capable of controlling CO_2 concentration between 0.1 and 20%. 4% CO_2 was used for accelerated carbonation conforming with BS 1881-210, (2013). However, the lowest achievable concentration was still too high compared with natural conditions as the desired CO_2 level for natural carbonation should be kept within the range of 0.04%-0.05% (400-500 ppm) with limited fluctuation. Therefore, the existing incubator was modified so that a natural carbonating environment can be achieved and maintained in the lab for at least a 2-year period. The main factors to be controlled were the CO_2 concentration, temperature, and RH. Their changes in the incubator were verified by a CO_2 meter (CO2Meter CM-0016). This meter provided testing ranges for CO_2 concentration of 0-1% with an accuracy of ±3% of the measured value, temperature of-40 to 120°C with an accuracy of ±0.5°C, and relative humidity (RH) of 0-100% with an accuracy of ±3%. Real-time data were stored in the internal memory and then processed in a GasLab Data Logging Software v.2.3. Several methods to develop the natural carbonation chamber were tested. Some of the unsuccessful attempts are briefly presented followed by the description of the employed method in the following sections.

3.2.1 Unsuccessful attempts

3.2.1.1 Airtightness of incubator

The first attempt studied the airtightness of the incubator to detect potential air exchange between incubator and lab air. To verify this, the incubator was switched off and a tray of saturated NaOH solution was placed to absorb CO_2. Prior to the test, the incubator door was left open for 10 min to ensure CO_2 equilibrium with the natural level was reached. The change of CO_2 concentration was monitored every minute using the CO_2 sensor consecutively for 24 hours. The result (Fig. 3.3a) shows that CO_2 in the incubator was rapidly absorbed by the NaOH solution and was maintained at a low level (< 50 ppm) for almost 15 hours. After approximately 24 hours, the incubator door was opened, and the CO_2 concentration increased dramatically to 440 ppm (arrowed). This result verifies the airtightness of the incubator and that very limited gas exchange can occur when the incubator is sealed, and that the internal CO_2 concentration cannot be maintained within 400-500 ppm.

3.2.1.2 Incubator set at 0.1% CO_2

The next attempt was carried out by setting the target CO_2 level at 0.1% in the incubator. This was tried because 0.1% is the lowest setting achievable by the incubator and thereby the closest value the incubator can provide to an ambient level of ~ 400 ppm. Because the incubator has a larger fluctuation at this low setting, it might end up providing a CO_2 concentration close to 400 ppm. The CO_2 concentration in the incubator was logged by the CO_2 sensor for 24 hours. Result (Fig. 3.3b) shows that the average CO_2 concentration was around 1580 ppm (0.158%), which was around 4 times larger than the required ambient value. A large fluctuation can also be observed in the graph indicating that the concentration achieved at the lowest setting is unstable and excessively high to be suitable for natural carbonation.

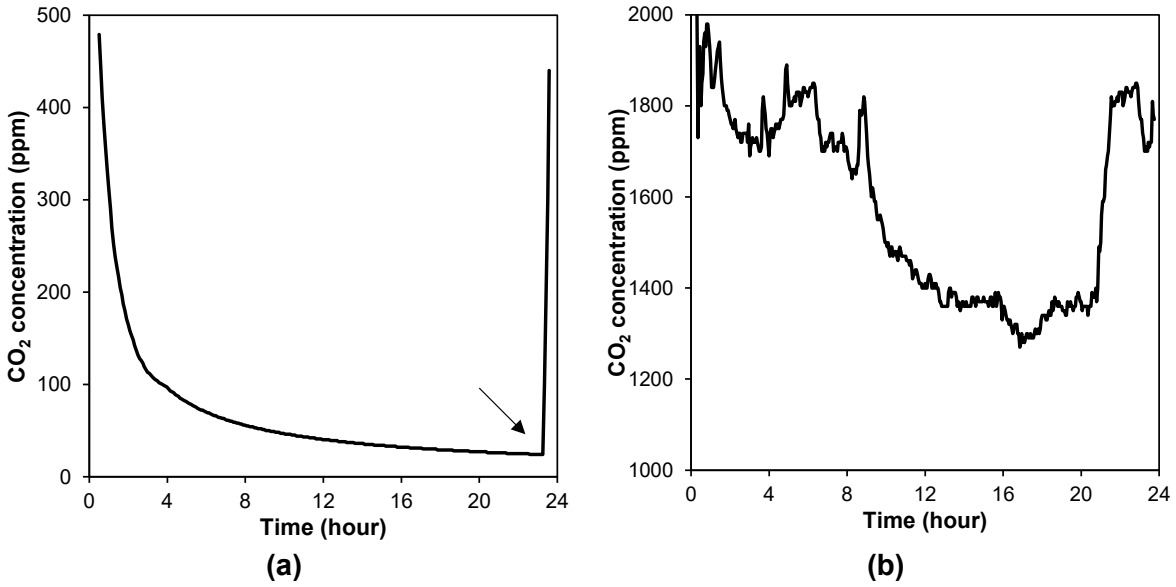


Figure 3.3 Change of CO_2 concentration in CO_2 incubator when testing airtightness (a), and setting 0.1% CO_2 (b).

3.2.1.3 Electric air inflator (400 L/min)

Since the CO_2 control on the incubator cannot meet the requirement for natural carbonation, the CO_2 channel of the incubator was hereby isolated (switched off). As the internal space of the incubator is in a sealed condition once the incubator door is closed, fresh air is needed to be injected into the incubator from outside via an air pump in order to maintain an ambient CO_2 concentration. The first pump selected was an electric air inflator that is capable of providing a high airflow of 400 L/min. Air was inflated from the top left corner at the back of the incubator and deflated from the sampling port at the bottom right corner close to the incubator door. Theoretically, this pump should be sufficient to refresh the air in the incubator within 1 min. After connecting the air pump to the incubator, cementitious samples were loaded into the incubator to initiate carbonation and the change of CO_2 level was monitored. Fig. 3.4a shows that the CO_2 in the incubator was consumed very fast that its concentration was below 400 ppm after merely 5 min of exposure. This indicates that in order to maintain a natural CO_2 concentration, air needs to be injected every 5 min, however, the tested air inflator was not designed to work at this high frequency.

3.2.1.4 Aquarium air pump (11.2 L/min)

Another air pump selected was an aquarium air pump. This pump has four gas outlets (Fig. 3.5), and each provides a maximum flow rate of 2.8 L/min. Although this pump has a much lower flow rate than the air inflator, it is able to work continuously. The maximum flow rate provided by the pump is 11.2 L/min when all four ports are connected to the manifold. Fig. 3.4b shows the results of the

changes of CO_2 concentration in the incubator when only 1 port (dashed) and all 4 ports (solid) were connected to the incubator. Within the first 1 hour, the CO_2 concentrations dropped rapidly and reached below 400 ppm at around 18 min regardless of the number of ports connected. This time has been significantly delayed compared with the electric air inflator (5 min). The CO_2 stabilised at 186 ppm when 1 port was connected to the incubator and 300 ppm when all 4 ports were connected. Although an increase of 300% inflow rate only generates an increase of 61% in the stabilised CO_2 concentration, these results verify that increasing the flow rate could increase and stabilise the CO_2 concentration, ensuring the potential to reach the target range of 400-500 ppm using this type of pump.

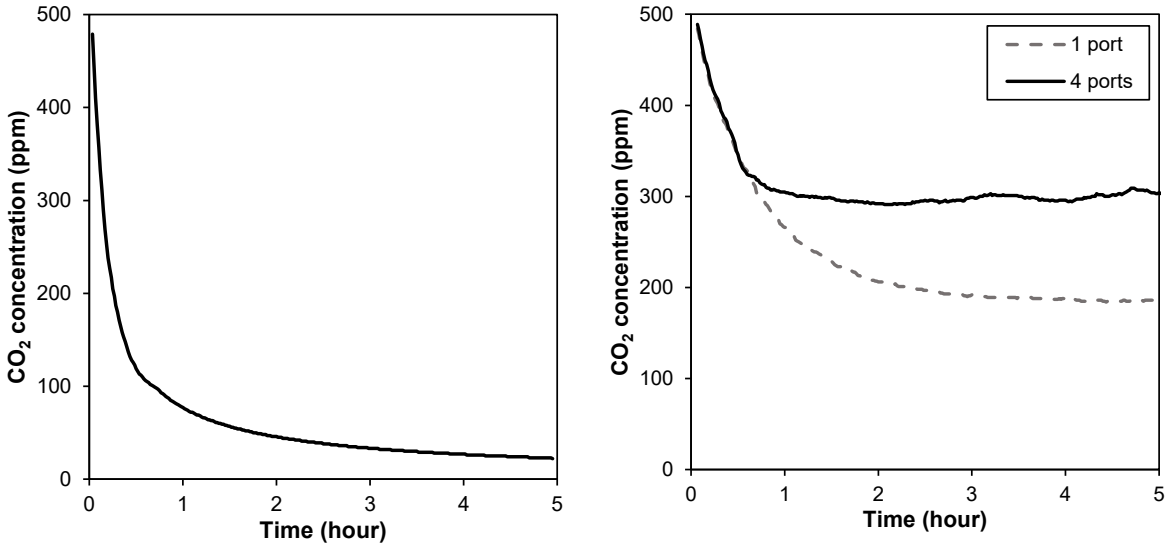


Figure 3.4 Variation of CO_2 concentration in CO_2 incubator after installing an electric air inflator (400 L/min) (a), and an aquarium air pump (11.2 L/min) (b).

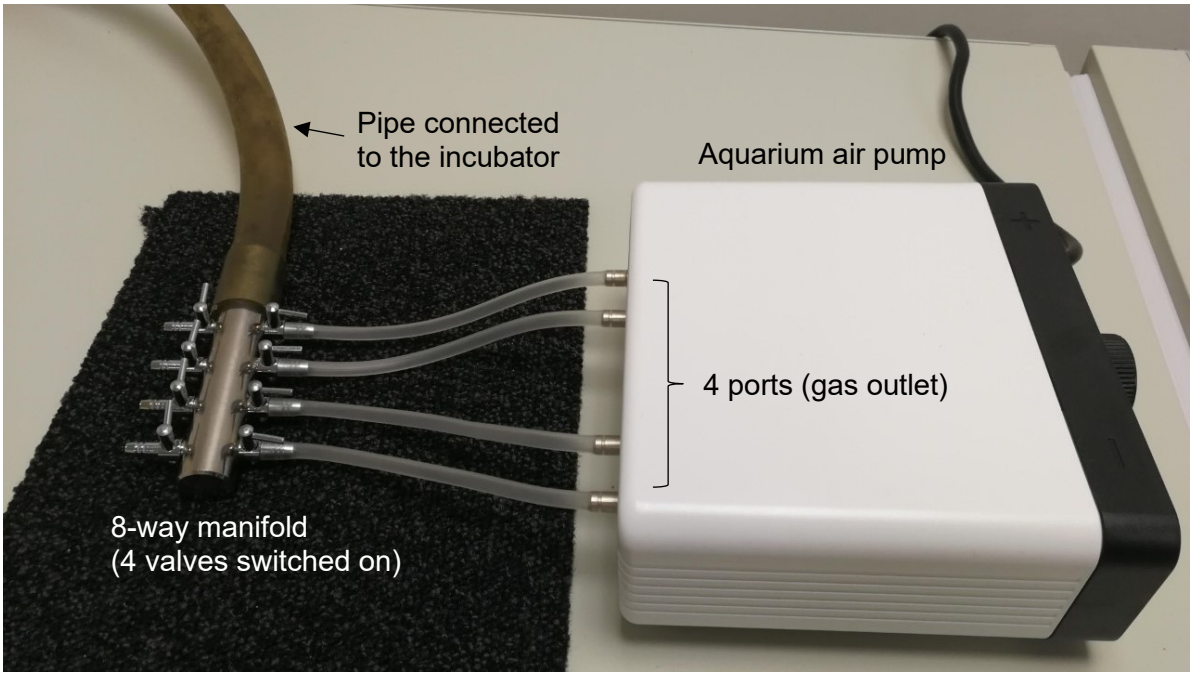


Figure 3.5 Connection of the aquarium air pump to the CO_2 incubator

3.2.2 Employed method using a pond air pump (100 L/min)

The selected pond air pump can consistently provide a high flow rate at 100 L/min at the maximum setting. When connected to the incubator, the CO_2 concentration was maintained within the range of 400-500 ppm with very low fluctuation. Fig. 3.6a shows an example of the monitored CO_2 data for 5 hours. The CO_2 stabilised at 435.9 ppm with a standard deviation (S.D.) of 3.1 ppm. CO_2 monitored for up to two years confirms that this pump is capable of maintaining a natural CO_2 concentration for a longer term (Fig. 3.6b). The average CO_2 concentration was 440.2 ppm with limited fluctuation (S.D. 5.9 ppm). Thus, this set-up was selected to modify the incubator for long-term natural carbonation. The schematic set-up of the climate chamber is illustrated in Fig. 3.7. Note that a natural carbonation chamber, applying the similar CO_2 monitoring and injection system used in the incubator mentioned in Section 3.2.1 (Unsuccessful attempts), was developed in Newlands (2001). However, by implementing a more accurate CO_2 sensor (0-2000 ppm ± 5% of the measured value), the CO_2 concentration can be controlled at on average 350 ppm ± 20 ppm.

Apart from CO_2 concentration, the other two key parameters for carbonation are temperature and RH. In a natural environment, the CO_2 concentration generally lies in a steady state, but temperature and RH can be different daily, monthly, and yearly. This could cause a complicated situation to accurately understand carbonation in a natural condition. Thus, to maintain a relatively high but also steady carbonation rate, the temperature and RH must be controlled to be within the desired ranges for carbonation. Regarding temperature, the incubator and air pump are placed in the lab controlled at a

temperature of approximately 21°C. The temperature monitored throughout the 2-year period (Fig. 3.6c) shows that temperature ranged between 20.5°C and 21.5°C, averaging at 21.2°C (S.D. 0.18°C). Although the lab is temperature-controlled, the temperature was slightly higher during warm weather between May and October than between November and April.

As mentioned previously, the desired RH for carbonation lies within the range of 50-70%. To maintain this, several trays of tap water were placed in the incubator to humidify the gas from approximately 45% RH in the lab air to 65%. The RH monitored for 2 consecutive years (Fig. 3.6d) had an average result of 64.7% (S.D. 1.14%). Contrary to temperature, RH was slightly higher between November and April than between May and October.

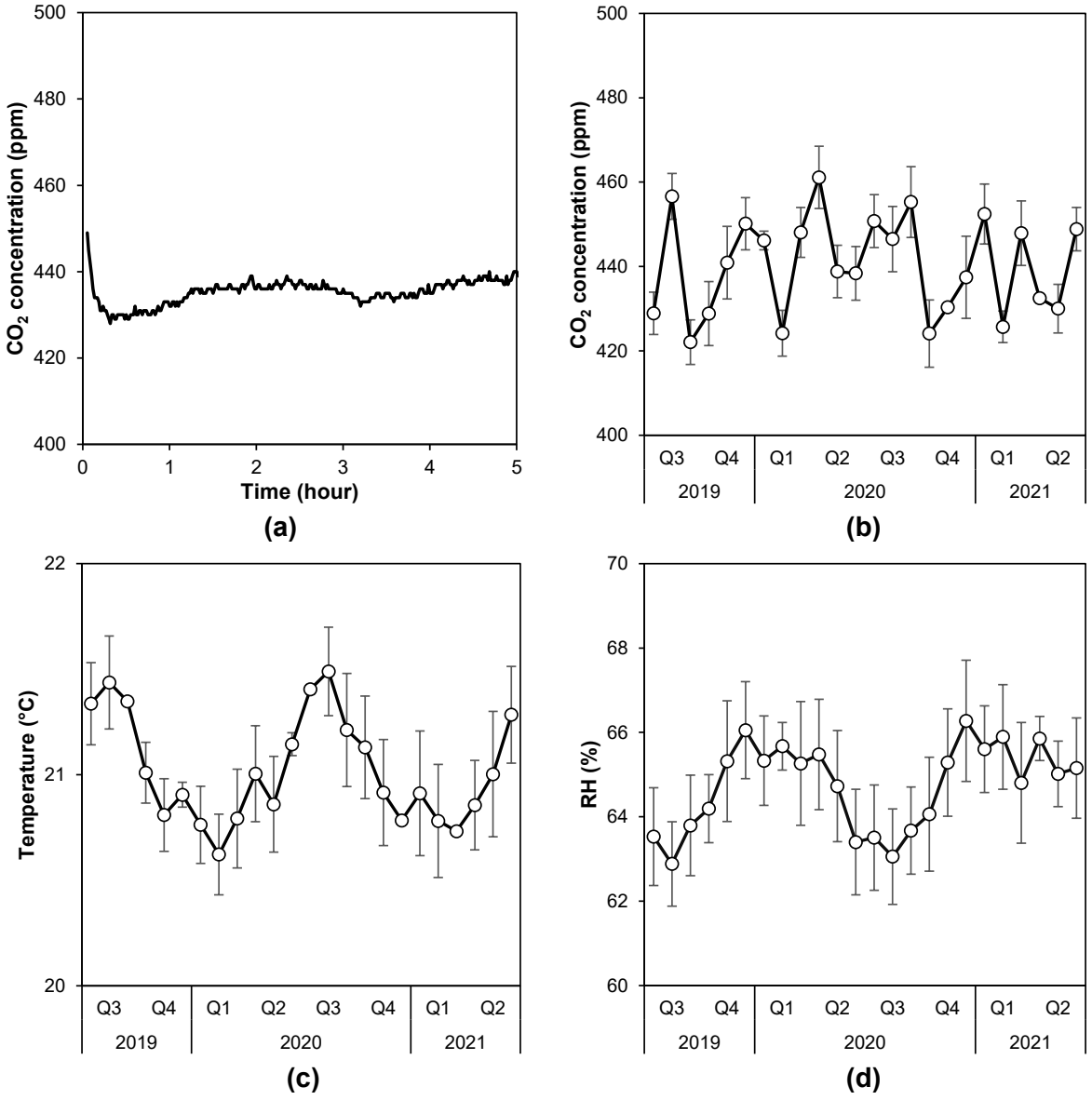


Figure 3.6 Variation of CO_2 concentration for 5 hours (a), and average monthly CO_2 concentration (b), temperature (c), and RH (d) from 2019 quarter 3 to 2021 quarter 2 in CO_2 incubator after installing the pond air pump. Error bars mark standard deviation.

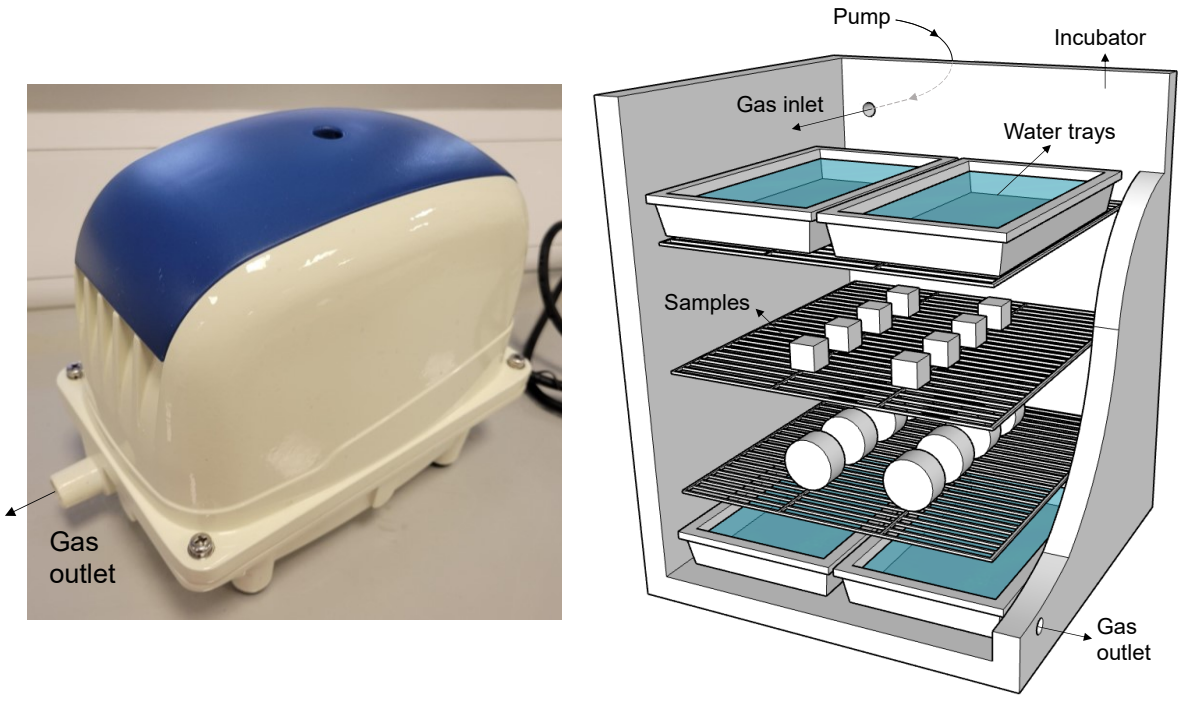


Figure 3.7 Pond air pump (100 L/min) (a) and the schematic set-up of climate chamber for long-term natural carbonation (b).

3.3 Confocal Raman microscopy

3.3.1 Principle

Raman spectroscopy determines the vibrational modes of molecules relying on the detection of inelastic scattering of photons. Molecules are composed of atoms with electrons orbiting around the nuclei at different energy levels in an electric field. A molecule can have more than one electronic energy levels (S_0 and S_1 in Fig. 3.8), and each consists of several different vibrational energy sublevels (ν = 0-2). When an incident photon interacts with the molecule at the ground state (S_0, ν_0), the molecule can be excited to a virtual state and return back to the original state. This process does not lose any energy and another photon is re-emitted at the same frequency in a different direction, which is known as Rayleigh scattering. Occasionally, the molecule can return to the ground state but at a vibrationally excited level (S_0, ν_1) so that the scattered photon has lower energy and frequency, which is known as Stokes scattering. An even rare possibility is that the vibrationally excited molecule (S_0, ν_1) can be excited to another virtual state and then return to the S_0, ν_0 state. The scattered photon can gain energy and have a higher frequency, which is known as anti-Stokes scattering. The latter two are the so-called Raman scattering, and the shift in the frequencies between

the incident and scattered lights is unique for a specific molecular vibration mode that enables the identification of the composition of materials.

In addition to scattering, some molecules can produce fluorescence when absorbing photons. Different from the scattering process that occurs between a real electronic energy state and a virtual state, fluorescence occurs between real electronic energy states (e.g. S_0 and S_1), thus can be 10-100 times stronger (Masilamani et al., 2017).

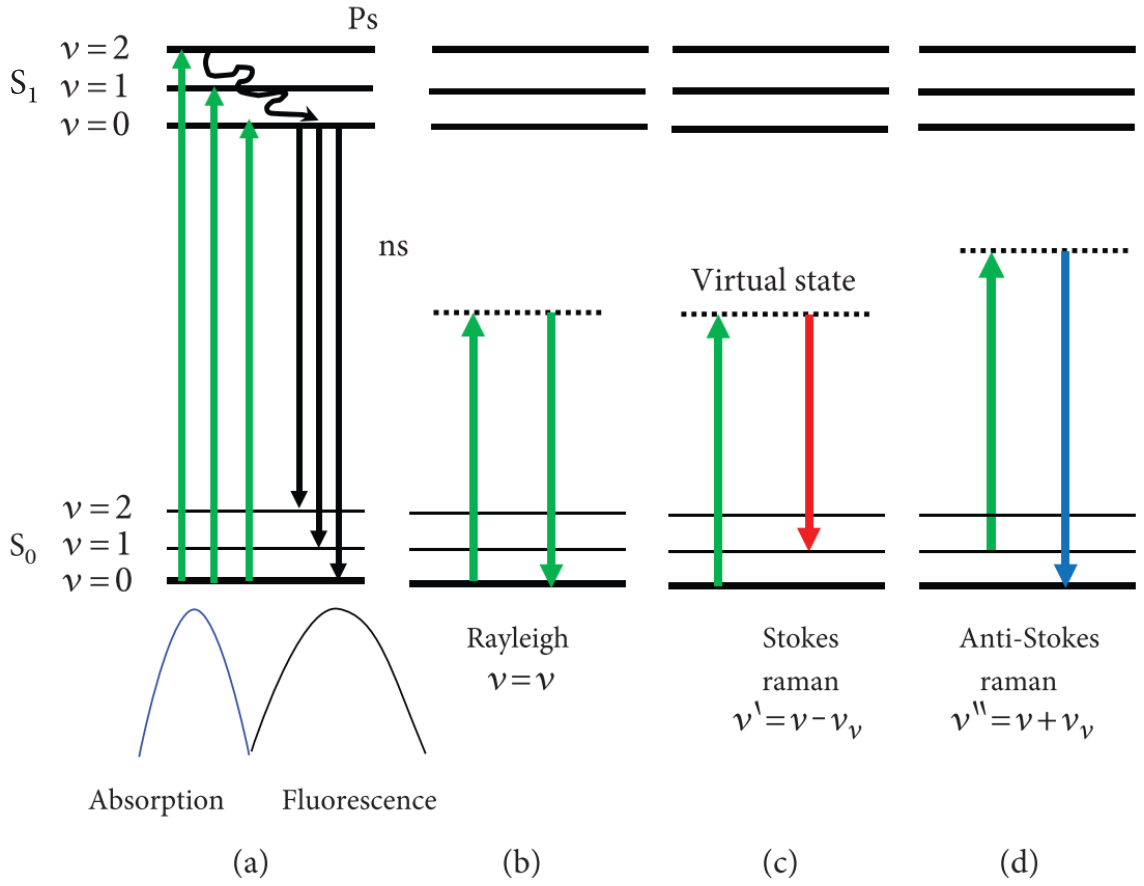


Figure 3.8 Schematic energy level diagram of a molecule for fluorescence (a), Rayleigh scattering (b), Raman scattering Stokes (c), and Raman scattering anti-Stokes (d). Image was adopted from Masilamani et al. (2017).

3.3.2 Confocal Raman microscopy (CRM)

CRM is developed by combining Raman spectroscopy and confocal microscopy, and a schematic set-up of CRM is presented in Fig. 3.9. A laser beam is transferred in the apparatus first to the holographic notch filter to direct the laser to the microscope and block any incident laser from entering the detector. The objective lens focuses the laser onto the sample surface and collects the resultant scatterings. The collected signal is passed through a Rayleigh rejection filter to remove

Rayleigh scattering and focused through a confocal pinhole. The focused scatterings are then diffracted by a grating, and analysed by a detector, for example, a charged-coupled device (CCD) camera.

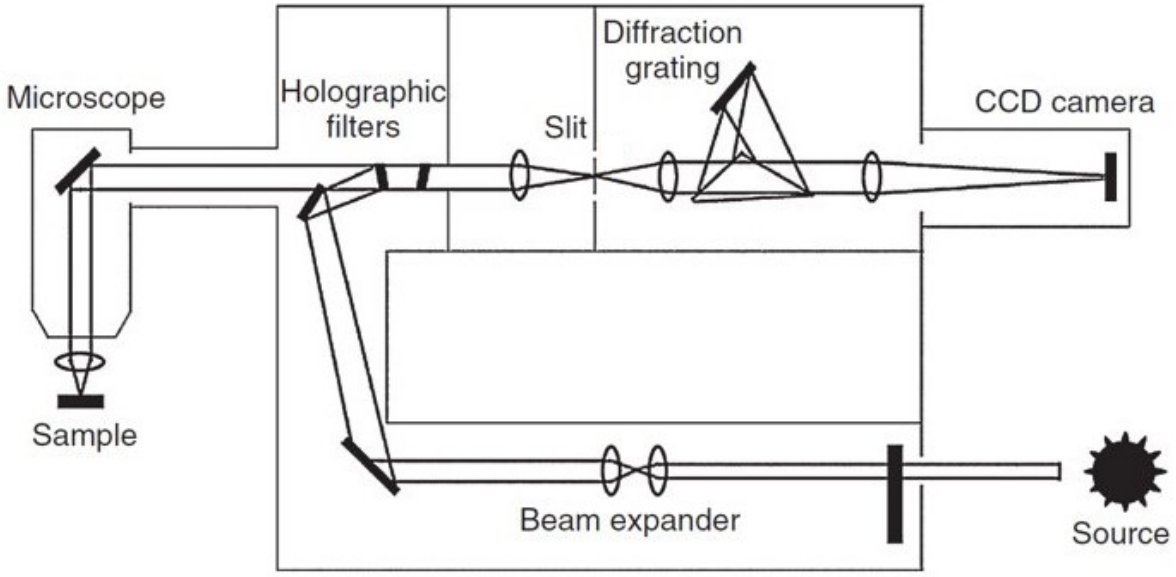


Figure 3.9 Schematic set up of CRM, from Leng (2013).

A Renishaw inVia Qontor confocal Raman microscope (Wotton-under-Edge, UK) equipped with 50 mW 532 nm and 300 mW 785 nm diode lasers was employed. The maximum laser power at the sampling level was 37 mW and 250 mW, respectively. The diffraction gratings for 532 nm and 785 nm lasers were 2400 and 1200 lines/mm. The system was installed with four objective lenses: Leica N PLAN EPI 5× NA 0.12, N PLAN EPI 20× NA 0.4, N PLAN L 50× (long working distance) NA 0.5, and N PLAN 100× NA 0.75. The apparatus was equipped with a motorised, optically encoded, scanning stage MS30 with a minimum achievable step size (resolution) of 0.1 μm. A picture of the CRM is shown in Fig. 3.10.



Notation:

1. Viewing screen
2. Control panel
3. Objective lenses
4. MS30 motorised scanning stage
5. Focus control
6. Eyepieces
7. Main unit
8. CCD array detector

Figure 3.10 Renishaw inVia Qontor confocal Raman microscope.

3.4 Backscattered electron microscopy (BSE)

3.4.1 Sample preparation for BSE

The samples for BSE microscopy were prepared following the method developed by Wong & Buenfeld (2006), which is summarised as follows:

1. **Cutting and conditioning.** Blocks with a size of 50 × 21 × 6 mm^3 were extracted from the carbonated or non-carbonated samples using a high precision cutter (Buehler) at a low speed of 200 rpm to ensure a good quality cut. Then the blocks were preconditioned (at 33% RH in most cases) until equilibrium to remove water from pores. Some blocks for characterising the microstructure of the matching area for Raman scanning in Chapter 4 and 5 were imaged under BSE right after this procedure.
2. **Encasing.** The block was encased with epoxy resin in a silicon rubber mould to protect the block from damage in the following steps. The surface of interest was preserved from encasing by sealing with one layer of water-proof tape and another layer of double-sided tape. The resin was allowed to harden for 24 hours. After demoulding, the tapes were removed, and any residual

epoxy on the surface of interest was carefully ground using a silicon carbide (SiC) paper (grit size of 500) on a Struers LaboForce-Mi grinding machine. The encased block with a flat surface of interest was then cleaned in acetone in an ultrasonic water bath to remove the dust from grinding.

3. **Impregnation.** The block was transferred to a separate chamber under vacuum for 1h to remove air in the pores. At the end of vacuuming, a low viscosity epoxy resin was produced by mixing Struers EpoFix resin with hardener at a mass ratio of 22:3 and adding 5 wt.% toluene of the total mass. The mixture was allowed to de-air in the vacuum chamber prior to being poured onto the sample surface. The vacuum was then released to force the resin into pores and cracks. After this, samples were transferred to a pressure chamber at 3 bars to achieve a deep impregnation. After two hours, the excessive epoxy was removed, and the remaining epoxy was allowed to set under pressure for 1 day.
4. **Grinding and polishing.** The impregnated surface was ground using SiC papers of successively finer grit size of 220, 500, 1000 and 1200 to remove excessive resin, and polished with non-woven cloth containing diamond abrasives of 6, 3, 1 and 0.25 μm to obtain a scratch-free surface. After each step, samples were cleaned in acetone in an ultrasonic bath. The surface finish after each grinding step was regularly monitored with an optical microscope (Olympus BX 51). After grinding and polishing, the samples were stored in a desiccator at 3% RH (silica gel), 21°C for 2 days to remove excessive moisture prior to SEM-BSE characterisation.

3.4.2 Instrument

A Hitachi TM4000 Plus scanning electron microscope was used to characterise the microstructural change due to Raman scanning and carbonation. The system was equipped with an Oxford Instruments Aztec Advanced X-Act Compact energy dispersive X-ray detector (EDS) to perform elemental analysis. BSE images were captured using a 4-segment BSE detector in low vacuum mode to avoid charging artefacts and the need for carbon-coating. The SEM was operated at 15 kV in the BSE mode and the working distance was set to 7 mm to achieve optimal spatial resolution according to Monte Carlo simulations (Yio et al., 2016). A picture of the SEM is shown in Fig. 3.11.



Notation:

1. Main unit
2. Sample chamber
3. Viewing screen
4. X-ray detector

Figure 3.11 Hitachi TM4000 Plus scanning electron microscope.

3.5 Phenolphthalein spray test

To study the evolution of carbonation depth after a certain period of carbonation, the samples were removed from the carbonation chamber and sectioned. Phenolphthalein solution, prepared by dissolving 1 g of phenolphthalein in a mixture of 30 ml deionised water and 70 ml ethyl alcohol, was sprayed onto the fresh cross section. Note that phenolphthalein is classified as a carcinogen, and personal protective equipment involving gloves, masks, and goggles should be worn when using phenolphthalein. Images of the treated surfaces were then captured using a stereoscope (Olympus SZX10) at a magnification of 0.63× to achieve a large field of view. The carbonation depths at 21 equally spaced locations (interval 0.5 mm) were measured by an image processing software, ImageJ (v.1.8.0) and the results averaged. The same method was employed for measuring average carbonation depth on Raman mappings. The approaches to determine carbonation depth using various profile-grinding analysis techniques will be presented in Chapter 6.

3.6 Mass transport tests

After a certain period of carbonation, samples were subjected to three mass transport tests following the order of oxygen diffusion, oxygen permeation and water absorption. Oxygen was selected because it does not react with cement, while it is relevant to the corrosion of reinforcement. Three replicate discs were tested, and the results averaged.

3.6.1 Oxygen diffusion

Oxygen diffusion under the influence of concentration gradient involves both ordinary diffusion and Knudsen diffusion. The combined flux can be approximated by Equation 3.1 based on Fick's first law of diffusion (Kobayashl & Shuttoh, 1991).

$$J_A = -D\frac{dC_A}{dx} \qquad \text{Equation 3.1}$$

Where J_A is the flux of the gas A (mol/m^{2}s), D is the diffusion coefficient (m^2/s), C_A is the concentration of oxygen (mol/m^3), and x is the distance (m).

The test set-up is shown in Fig 3.12. The sample was sealed in a silicone rubber ring to prevent gas leakage through the side. The opposite surfaces were exposed to a flow of N_2 and a flow of O_2 at equal pressure to generate a concentration gradient across the disc. The two gasses counter diffuse through the sample and the O_2 concentration in the outflow N_2 gas stream was monitored with a zirconia oxygen analyser until a steady concentration was achieved. The mass of the sample before and after diffusion testing was measured to check for loss of moisture, which was usually very small. The O_2 diffusivity is then calculated following Equation 3.2.

$$D = \frac{QL}{A(C_2 - C_1)} \qquad \text{Equation 3.2}$$

Where Q is the oxygen diffusion rate (m^3/s) at 1 bar, calculated by:

$$Q = \frac{R_1(G_1 - G_0)}{60 \times 10^6} \times \frac{P_1 - P_2}{100} \qquad \text{Equation 3.3}$$

Where R_1 is the flow rate of N_2 stream (mL/min), G_1 is the concentration of O_2 in the outflow stream (%), G_0 is the concentration of O_2 in the initial N_2 stream (%), P_1 is the pressure of O_2 stream (bar), P_2 is the pressure difference between the O_2 and N_2 streams (bar), A is the cross-sectional area (m^2), L is the sample thickness (mm), C_2 is the concentration of O_2 in the O_2 stream (m^3/m^3) at 1 bar, expressed as Equation 3.4.

$$C_2 = \{100 - [\frac{R_1}{R_2} \times \frac{(G_1 - G_0)}{2} \times \frac{\sqrt{32}}{\sqrt{28}}]\} \times \frac{P_1}{100}$$ Equation 3.4

Where R_2 is the flow rate of O_2 stream (mL/min) and C_1 is the mean concentration of O_2 in the N_2 stream at 1 bar (m^3/m^3), expressed as Equation 3.5.

$$C_1 = \frac{(G_1 + G_0)}{2} \times \frac{P_1 - P_2}{100}$$ Equation 3.5

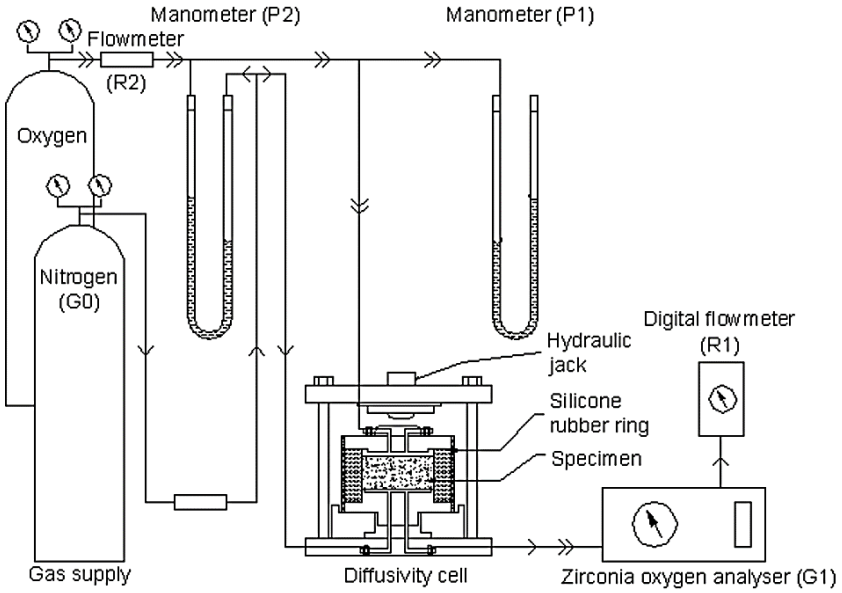


Figure 3.12 Schematic of oxygen diffusion test set-up (Wong, 2006).

3.6.2 Oxygen permeation

Permeation refers to flow of a fluid that occurs as a result of pressure gradient. For an incompressible fluid in a laminar flow regime at a steady-state condition, Darcy's law can be employed to calculate flow rate (m^3/s):

$$Q^* = -\frac{kA\Delta P}{\eta L}$$ Equation 3.6

Where k is the permeation coefficient (m^2), $\Delta P/L$ is the pressure gradient (N/m^3) across the sample thickness L, and η is the dynamic viscosity of the permeating fluid (Ns/m^2).

Since O_2 is a compressible fluid, flow would change with pressure in a nonlinear fashion; hence Equation 3.6 is no longer valid. However, Darcy's law can be modified for this effect (Equation 3.7) by considering that the pressure-velocity product is constant throughout the sample at a steady-state condition (Dullien, 1992).

$$Q^* = -k_g \frac{A}{2\eta_g L}\left(\frac{P_1^{*2} - P_2^{*2}}{P_2^*}\right) \qquad \text{Equation 3.7}$$

Where k_g is the apparent gas permeation coefficient (m^2), η_g is the dynamic viscosity of gas (for O_2 at 20°C, η_g=2.02 × 10^{-5} Ns/m^2), P_1^* and P_2^* are the absolute inlet and outlet pressures (N/m) respectively.

The test set-up for O_2 permeation is presented in Fig. 3.13a. O_2 permeation was carried out on a permeation cell of a similar design to the diffusion cell. O_2 flows at different pressures (0.5, 1.5, and 2.5 bar above atmospheric pressure) were applied to one surface of the sample to generate pressure gradient. The flow rate of the outflow gas was measured by a series of bubble flow meters at steady-state conditions. For each applied inflow pressure, four readings of the outflow rate were taken to calculate the average flow rate. The permeability was calculated using Equation 3.7 for each applied pressure. However, the obtained permeability is an apparent value that is dependent on the applied pressure. This is because gas slippage can occur at the walls of pore channels, and this becomes profound when the mean free path of the gas molecules is of comparable size to the pore channel. Consequently, in very fine pore channels, gas slippage can occur frequently and thus the flow rate of the gas is higher than expected. To address this issue, Klinkenberg method has been applied to obtain an intrinsic gas permeability that is not pressure-dependent (Klinkenberg, 1941).

$$k_g = -k_{int}\left(1 + \frac{\beta}{P_m}\right) \qquad \text{Equation 3.8}$$

Where k_{int} is the intrinsic gas permeability (m^2), β is a constant (N/m^2), and P_m is the mean value of the inlet and outlet pressure. The three calculated apparent permeation coefficients were plotted against the reciprocal of the corresponding P_m values ($1/P_m$) as is presented in Fig. 3.13b. The linear relationship (generally $R^2 > 0.99$) was extrapolated to the infinite mean pressure ($1/P_m \approx 0$) to determine k_{int}.

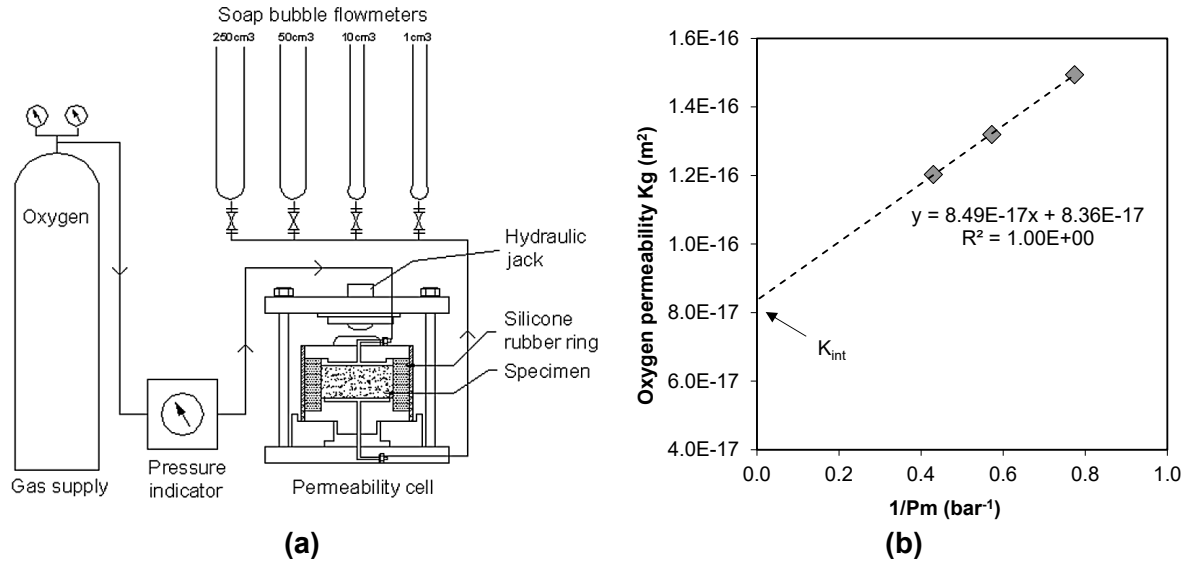


Figure 3.13 Schematic of oxygen permeation test set-up (Wong, 2006), and an example plot for Klinkenberg correction for non-carbonated C-0.45-PC-70%/3d.

3.6.3 Water absorption

Water absorption describes the transport of water due to capillary suction in an unsaturated porous media. This capillary suction is caused by the unequal surface tension between the fluid-solid and fluid-fluid interfaces (Martys & Ferraris, 1997). Water absorption is an important transport mechanism because most concrete structures in service are in an unsaturated state. Considering unidirectional absorption, the cumulative mass of absorbed water per unit area of the inflow surface, i (g/m^2), over time can be expressed as Equation 3.9.

$$i = a + S\sqrt{t} \qquad \text{Equation 3.9}$$

Where a is fitting constant accounting for minor edge and surface effects (Hall & Hoff, 2012), S is the sorptivity coefficient (g/m^{2}min$^{0.5}$), and t is the elapsed time (min).

The water absorption test set-up is shown in Fig. 3.14a. Samples were placed on plastic rods with the bottom 2 to 3 mm immersed in a tray of shallow water to allow free water access. The amount of water absorbed was monitored by weighing the samples periodically from the first 5 min to several hours and days until a saturation state was achieved. Prior to each measurement, surface water was wiped off with dampened cloth and the weighing was completed within 30s. The cumulative mass gain per inflow area was then plotted against square-root-of-elapsed time. The slope of the best fit line

drawn across the first ten readings was determined as the sorptivity coefficient as is exampled in Fig. 3.14b.

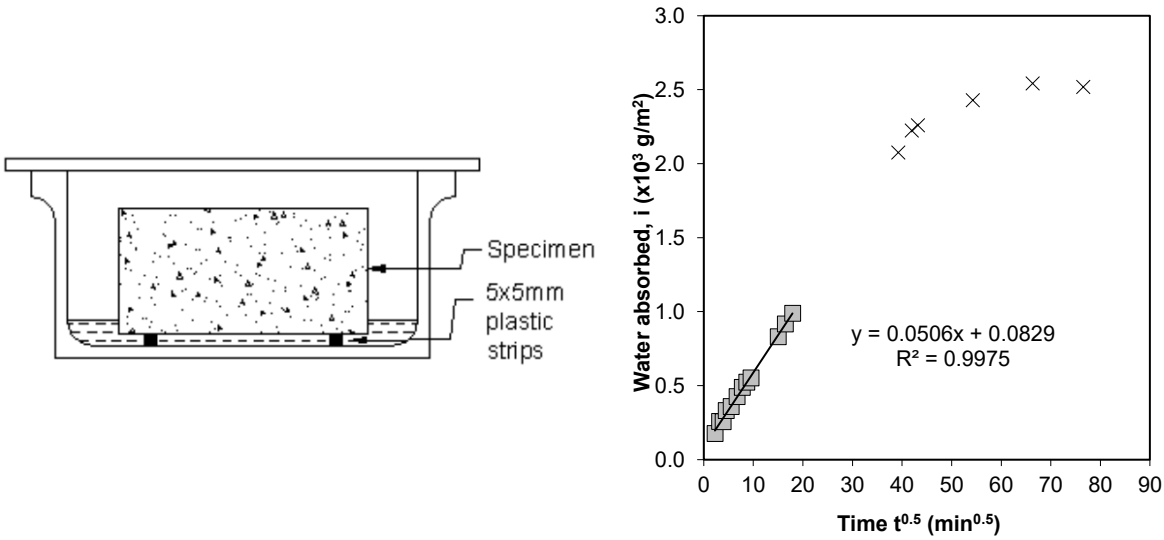


Figure 3.14 Schematic of water absorption test set-up (Wong, 2006), and an example plot for non-carbonated C-0.45-PC-70%/3d.

3.7 Summary

The materials, experimental methods and instrumentation used in this thesis were described. The mix design, curing regime, sample preparation, conditioning, and carbonation were slightly different depending on the purpose of the study and will be presented in the respective result chapters. The development of a natural carbonation chamber was described, and the exposure condition can be maintained at ~440 ppm (S.D. 5.9 ppm) CO_2 concentration, 21°C (S.D. 0.18°C) and 65% (S.D. 1.14%) RH. The instrumentation of the main techniques employed in this thesis, i.e. CRM and BSE imaging, and some of the operating parameters were introduced. Further optimisation for CRM will be presented in the next chapter. Test methods to study the effect of carbonation on mass transport properties of concrete such as oxygen diffusion, permeation, and water absorption were described.

4 Optimising confocal Raman microscopy for spectral mapping of cement-based materials

Confocal Raman microscopy (CRM) is a relatively new technique with huge potential for high-resolution chemical mapping to characterise the composition and spatial distribution of different phases in cement-based materials. However, the effect of sample preparation and various operating parameters on the data quality for spectral mapping has not been systematically studied. This chapter optimises CRM for high-resolution spectral mapping of carbonated and non-carbonated cement-based materials. The effects of sample preparation and various scanning parameters on the detection of four main phases (calcite, portlandite, ettringite and unreacted cement) were investigated. Results show that a freshly cut sample surface can be analysed as-is but the Raman signals improve with drying and flat-polished surface. Increasing the laser power is more effective than increasing the exposure time and scan accumulation to achieve adequate Raman signals. Point-by-point scanning with step sizes < 20 μm can induce microcracking, especially in carbonated systems. However, such damage can be limited by impregnating the sample with epoxy to protect the microstructure. This chapter show for the first time that CRM can be used to quantify the volume fraction of calcium carbonate and portlandite at high resolution when combined with SEM. The advantages and limitations of CRM for mapping carbonation in cement-based materials are discussed.

4.1 Introduction

The phase assemblage of hardened cement-based materials is highly complex, consisting of capillary pores, unreacted cement and various hydration products including amorphous calcium-silicate-hydrate (C-S-H) and minerals such as portlandite (CH), ettringite (AFt), gypsum, etc. Depending on the curing and exposure conditions, the phase assemblage evolves over time, influencing the mechanical properties and durability of concrete. When exposed to carbonation, calcium-bearing phases (particularly portlandite and C-S-H) react with atmospheric CO_2 in the pore solution to form various calcium carbonate ($CaCO_3$) polymorphs including calcite, vaterite and aragonite (Morandeau et al., 2014). This leads to a pH drop in concrete, causing depassivation and corrosion initiation of steel reinforcement (Bentur et al., 1997). Carbonation is also relevant to research on developing carbon capture, utilisation and storage (CCUS) strategies such as accelerated CO_2 curing of concrete and carbonation of waste concrete fines. Therefore, the ability to map the phase assemblage composition and characterise its spatio-temporal distribution is highly valuable for many fundamental research applications.

X-ray diffraction (XRD), thermogravimetric analysis (TGA) and Fourier transform infrared spectroscopy (FTIR) are techniques commonly used to characterise phase composition of hardened cement pastes (Matsushita et al., 2000; Chang & Chen, 2006; Villain et al., 2007; Shah et al., 2018). However, these techniques are mainly for bulk analysis of powdered samples. They require destructive sample preparation and hence are unable to provide spatial information on the microstructural level, which is important for understanding, monitoring and predicting concrete deterioration and carbon capture. For example, knowledge on the spatial distribution of portlandite and $CaCO_3$ enables precise profiling of carbonation in concrete. However, these techniques are impractical for analysing mortar or concrete due to the presence of aggregate particles, in particular limestone aggregates that are difficult to separate out (Villain et al., 2007).

Petrographic examination with optical microscopy has long been employed for direct characterisation of the physical and mineralogical properties of concrete (Walker et al., 2006; Poole & Sims, 2016; Wong et al., 2020). Different phases can be distinguished based on their colour, morphology and optical properties under normal, fluorescent or polarised light. For example, portlandite and $CaCO_3$ can be readily distinguished from C-S-H under polarised light based on their high birefringence (Erlin & Stark, 1990; Çopuroğlu, 2016; Sahu et al., 2019). This technique however requires laborious sample preparation to produce thin sections for analysis, and extensive knowledge and experience to interpret the images obtained. Achieving quantitative analysis is difficult.

Backscattered electron (BSE) microscopy is another technique widely used for examining the microstructure and constituent phases of cement-based materials. Different phases are distinguishable based on their grey levels, which increase with the mean atomic number. However, phases such as $CaCO_3$ and hydration products share similar grey levels and hence remain difficult to detect and isolate (Stutzman, 2004). Although the use of energy or wavelength-dispersive X-ray spectroscopy can facilitate the segmentation process to some extent, the exact type of polymorphs present cannot be determined (Kashef-Haghighi & Ghoshal, 2013; Branch et al., 2016). BSE also requires substantial sample preparation including drying, epoxy-impregnation, grinding and polishing.

Raman spectroscopy is a powerful technique capable of providing chemical and structural information of organic and mineral phases. It is based on the excitation of chemical bonds with a laser to produce Raman scattering. The frequency difference between the incident and scattered light, registered in the form of a spectrum, provides fingerprint information on chemical structure. Raman spectroscopy can detect oxides, carbonates, sulphates and silicates, and hence is particularly suitable for analysing cement-based materials. Since its first application on white cements by Bensted (1976), Raman spectroscopy has seen increasing use in the characterisation of various cements (Torréns-Martín et al., 2013), supplementary cementitious materials (Guedes et al., 2008; Yue et al., 2018), alkali-activated

materials (Caggiani et al., 2021) and corrosion products (Marcotte & Hansson, 2007; Larroumet et al., 2007; Criado et al., 2015; Dang et al., 2015). Combining Raman spectroscopy with confocal microscopy enables high-resolution chemical imaging of phase distribution. The use of laser, confocal pinhole and high-power objective enables a very small sampling volume (~ 1 μm^3), thus achieving high spatial resolution analysis of local features. Confocal Raman micro-spectroscopy or microscopy (CRM) has been used to image clinker remnants and aggregates in historic cement stone (Schmid & Dariz, 2013), hydration of cement pastes (Higl et al., 2016; Mikhailova et al., 2019; Torres-Carrasco et al., 2019), weathering of anhydrous cements (Torres-Carrasco et al., 2017), alkali-silica reaction (Ling et al., 2018), and carbonation of hardened cement pastes (Corvisier et al., 2010; Mi et al., 2021) and lime paste (Ševčík et al., 2016).

Despite the huge potential applications, there has been no systematic study published on understanding the effects of sample preparation and various operating parameters on data quality, and on optimising CRM for spectral mapping of cement-based materials. Previous studies have used different sample preparation protocols, drying and sample types including cast, cut, fractured and polished surfaces for analysis. Scan settings also varied significantly between studies, with laser wavelength ranging from 488 nm to 1064 nm, laser power from 0.025 mW to 400 mW, exposure time from 0.1 to 60 s and mapping step size from 0.2 to 150 μm. These parameters are expected to influence results, but the magnitude of the effects on different phases in cement-based materials is unclear.

The aim of this chapter is to understand these effects and to optimise confocal Raman microscopy for spectral mapping of cement-based materials. Four main phases were focused: unreacted cement (alite, belite), portlandite, calcium carbonate and ettringite, in naturally carbonated and non-carbonated cement paste samples. The effects of drying, sample preparation, surface roughness, and operating parameters such as laser power, exposure time, scan accumulation and mapping step size on data quality and signal-noise-ratio were examined. Microstructural changes and damage induced by prolonged laser irradiation were also investigated. Finally, some recommendations were made based on the obtained results.

4.2 Experimental

4.2.1 Materials and sample preparation

Cement pastes with a water/cement ratio (w/c) of 0.45 were prepared. Portland cement CEM I 52.5N was used. The chemical compositions and physical properties of the cement were specified in Section 3.1. Mix proportions are given in Table 4.1. The cement was mixed with tap water in a Hobart mixer

for 3 min and then compacted in two equal layers into a steel mould of 50 mm cube on a vibration table. Immediately after casting, the compacted samples were covered with plastic sheet and wet hessian for the first 24 h, and then demoulded and cured in a chamber at > 95% relative humidity (RH) and 21 ºC for 3 days.

Table 4.1 Mix proportions.

Mix ID	Free w/c	Water: kg/m^3	CEM I: kg/m^3
P-0.45-PC	0.45	582.5	1294.4

4.2.2 Conditioning and carbonation

After curing, the samples were transferred to a separate chamber for drying at 65% RH, 21ºC until mass equilibrium. The chamber contained saturated sodium nitrite to maintain the RH, soda lime to keep the CO_2 level at < 10 ppm and a motorised fan to circulate air. The samples were then transferred to a CO_2 incubator for natural carbonation at the same humidity and temperature (65% RH, 21ºC) for 3 months. All except one cast surface were sealed with two layers of waterproof tape to ensure unidirectional carbonation. The environment inside the incubator was continuously refreshed using an air pump to maintain the CO_2 level at ~440 ppm (Section 3.2.2). Phenolphthalein spray test confirmed that an average carbonation depth of ~2 mm was achieved. After carbonation, each sample was diamond-sectioned using tap water as a coolant to produce four blocks of 50 × 21 × 6 mm^3. One of the blocks was surface-dried with paper towel and analysed immediately (Section 4.2.3.3) whereas the remaining blocks were pre-conditioned at 33% RH, 21 ºC in a conditioning chamber containing saturated magnesium chloride, soda lime and motorised fan for 1 month to achieve mass equilibrium for other analyses.

4.2.3 Confocal Raman microscopy

4.2.3.1 Overview and general considerations

The set-up of the Renishaw inVia Qontor confocal Raman microscope, equipped with 50 mW 532 nm and 300 mW 785 nm diode lasers, and a charged-coupled device (CCD) array detector, was shown in Section 3.3.2. For the 785 nm laser, a pinhole was inserted into the beam path to produce a circular excitation spot comparable to that of the 532 nm laser. The laser power at the sample surface was adjusted to range from 0.55 to 4.15 mW as part of optimisation (Section 4.3.2). The laser beam was focused onto the sample surface through a long working distance objective of 50× and 0.5 NA, providing a spatial resolution of 1.3 μm for the 532 nm laser and 1.9 μm for the 785 nm laser. Prior to each scan, spectral calibration was verified using an internal silicon standard with a Raman shift at

520.2 ± 0.5 cm^{-1}. The spectral range was set to 143 to 1385 cm^{-1} to ensure that the most intense peaks of the main phases of interest were captured, i.e. 1085 cm^{-1} for calcite, 356 cm^{-1} for portlandite, 988 cm^{-1} for ettringite, 864 cm^{-1} for belite and 835 cm^{-1} for alite (Liu et al., 2015; Torres-Carrasco et al., 2017). These phases were selected for analysis because they are the Raman-active phases involved in carbonation. All data acquisition was performed using Renishaw WiRE v.5.2 software. Spectral artefacts including cosmic rays and background were removed using the nearest neighbour method and least squares polynomial fit respectively.

4.2.3.2 Optimisation of scanning parameters

Spot analysis was performed on the cut surface of one of the pre-conditioned sample blocks to optimise the laser line (532, 785 nm), laser power (0.55, 0.72, 0.89, 2.48, 4.15 mW), exposure time (0.1, 0.5, 1, 2, 5, 10 s) and scan accumulation (1, 2, 3, 5, 10). It should be noted that the laser power here refers to the laser power at the sample surface (measured with Thorlabs Optical Power Meter) and not that of the laser beam. The exposure time represents the duration of each scan whereas scan accumulation represents the number of scans performed on the same spot repeatedly. These parameters influence the intensity of Raman scattering and in turn the overall spectral quality. The parameter ranges covered the values typically used in literature. While optimising the main parameter, the other parameters were kept constant at 532 nm laser line, 4.15 mW laser power, 1 s exposure time and 1 scan accumulation.

Both carbonated and non-carbonated regions were analysed. The phases of interest were located by visual examination combined with Raman spot analysis. Unreacted cement particles were located based on their defined morphology and relatively dark appearance under optical microscopy. Calcite and portlandite can also be distinguished visually as they were present in abundance in the carbonated and non-carbonated zones respectively. Five different locations were analysed for each phase and the results averaged. Signal-to-noise ratio (SNR) of the main peaks was quantified by dividing the signal level by the root mean square error (RMSE) of the noise on the background signal according to ASTM E579-04 (2015). Unless otherwise stated, all other analyses were carried out using the 532 nm laser line, with 4.15 mW laser power, 2 s exposure time and scan accumulation set to 2.

4.2.3.3 Sample moisture condition and surface roughness

The freshly cut surface-dried sample block was analysed as-is to investigate the effect of moisture on Raman signals and to determine whether sample drying was necessary for Raman analysis. Spot analysis was performed on the phases of interest at several time intervals to monitor any spectral changes as the sample was left to air-dry naturally in the microscope enclosure at ~45% RH, 21 ºC for up to 9 minutes. Following that, the sample was dried at 33% RH, 21 ºC for 1 month until mass

equilibrium and then reanalysed at the exact same locations to observe any differences in the collected spectra. Three different locations were analysed, and the results averaged.

The effect of surface roughness was investigated by impregnating the pre-conditioned sample blocks (33% RH, 21 ºC) with epoxy resin and then progressively grinding and polishing the impregnated surface using silicon carbide (SiC) paper at 1000 grit size (grinding) and non-woven cloth containing diamond abrasives of 6, 3 and 1 μm (polishing) to produce successively finer surfaces. Grinding and polishing were performed at low pressure and slow rotational speed (50 rpm) for 1 and 3 min respectively to avoid surface relief. Four regions of interest (ROI) of 80 × 60 μm^2, two in the carbonated zone and two in the non-carbonated zone, were analysed at a step size of 1 μm. The surface roughness (S_a) of the ROIs was measured as the average height difference between surface irregularities and the arithmetical mean height under SEM (Section 4.2.4) using the Hitachi map 3D software (v.7.4).

4.2.3.4 Prolonged laser irradiation during mapping

In another series of experiments, spot analysis was performed on calcite, unreacted cement and portlandite on the pre-conditioned sample blocks (33% RH, 21 ºC) for six successively larger number of scan accumulations (1, 5, 10, 100, 500, and 1000) to evaluate the effect of prolonged laser irradiation at 0.55 mW and 4.15 mW. Five different locations on the sample surface were analysed for each phase. Furthermore, point-by-point mapping was performed on both as-cut and epoxy-impregnated polished surfaces to determine if closely-spaced laser irradiation over an extended area (120 × 90 μm^2) would induce microstructural changes. A systematic study involving varying laser power (0.55, 0.89, 2.48, 4.15 mW), exposure time (0.1, 0.5, 1, 2 s) and step size (0.3, 1, 5, 10, 20 μm) was performed. While examining the effect of one parameter, the others were kept constant at 2 s exposure time, 4.15 mW laser power, and step size as 1 μm. Two ROIs (each in the carbonated and non-carbonated zone) were studied and duplicate accumulation was applied throughout. Immediately after Raman imaging, the same area was observed with BSE imaging to detect microstructural changes. Microcracks that existed before and after Raman imaging were extracted by manual tracing in Fiji (Schindelin et al., 2012) to calculate crack density (total crack length ÷ image area).

4.2.4 Backscattered electron microscopy

The set-up of the Hitachi TM4000 Plus scanning electron microscope (SEM) equipped with an Oxford Instruments Aztec Advanced X-Act Compact energy dispersive X-ray detector (EDS) for microstructural characterisation and elemental analysis was shown in Section 3.4.2. The SEM was operated at 15 kV in the backscattered electron (BSE) mode and the working distance was set to 7 mm to achieve optimal spatial resolution according to Monte Carlo simulations (Yio et al., 2016).

Images were captured at magnifications of 500× and 1000× at a scan format of 1280 × 960 pixels to give pixel sizes of 0.2 and 0.1 μm respectively.

4.3 Results

4.3.1 Effect of laser wavelength, fluorescence background and scan accumulation

Fig. 4.1 a-b show examples of Raman spectra for calcite (from carbonated zone), unreacted cement and portlandite obtained with 532 nm (4.15 mW) and 785 nm (4.03 mW) lasers before and after background subtraction respectively. The fluorescence background in the 532 nm spectra was markedly higher than in the 785 nm spectra (Fig. 4.1a). This is expected given that cement-based materials are prone to autofluorescence and that this effect is greater at short excitation wavelengths due to the higher excitation energy (Richardson et al., 2010). Nevertheless, the least squares polynomial subtraction was sufficient to remove the fluorescence background while retaining the Raman peaks of interest (Fig. 4.1b). The intensity of the Raman peaks for calcite, unreacted cement and portlandite were significantly higher in the 532 nm spectra. This is due to the fact that Raman scattering is inversely proportional to the fourth power of the excitation wavelength (Gierlinger et al., 2012).

Another disadvantage of long excitation wavelength (785 nm) is the introduction of broad intense photoluminescence bands (asterisked in Fig. 4.1b) caused by the presence of trace rare earth impurities in the cement mineral lattice (Dyer & Smith, 1995). Such bands are intrinsic and cannot be corrected by background subtraction. Furthermore, these photoluminescence bands can overlap with certain phases of interest including alite, belite and calcite, obscuring their detectability. Similar observations were reported by Richardson et al. (2010), Dyer et al. (1993) and Bonen et al. (1994) at higher laser wavelength of 1064 nm. This study shows that the use of 532 nm laser can avoid the formation of such photoluminescence bands.

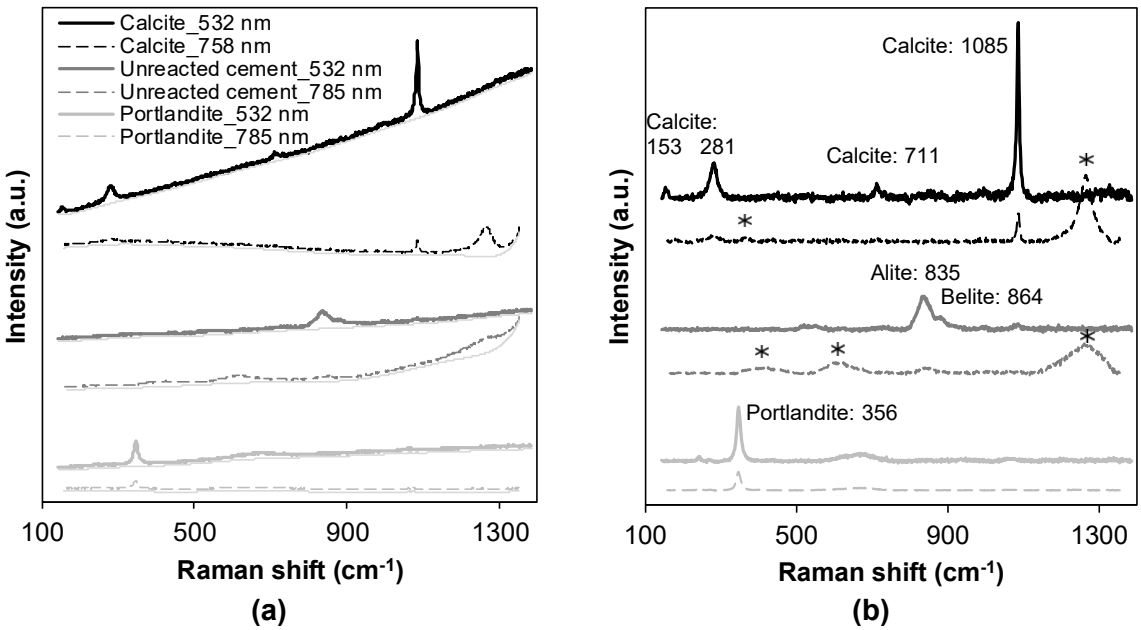


Figure 4.1 Example Raman spectra of calcite (from carbonated zone), unreacted cement and portlandite acquired with 532 and 758 nm lasers before (a) and after (b) background removal. Asterisks mark the photoluminescence bands.

Fig. 4.2a shows the calculated SNR of the Raman peaks for calcite (1085 cm^{-1}), alite + belite (835 to 864 cm^{-1}), and portlandite (356 cm^{-1}) after one scan accumulation. It can be seen that the SNR for all phases were higher when measured with the 532 nm laser compared to the 785 nm laser. Calcite gave the highest SNR, followed by portlandite, and unreacted cement (alite, belite), in line with their order of crystallinity (Torres-Carrasco et al., 2019). It is also worth noting that the spectrum and SNR for calcite are similar regardless of whether the analysis was conducted in the carbonated or non-carbonated regions (from limestone filler in the cement).

Fig. 4.2b shows the effect of scan accumulation on the SNR of the Raman peaks. Irrespective of the laser line and the measured phase, SNR increased with increase in scan accumulation following a power law trend. An accumulation of 10 scans was observed to improve the SNR by a factor of 2 to 4 compared to the SNR of one scan. However, the acquisition time was also significantly prolonged and this makes large area mapping impractical. Nevertheless, it is noted that an accumulation of 2 scans with 532 nm laser was sufficient to achieve an SNR > 10 for all phases. This is adequate for spectral mapping subtraction (e.g. AFt and CH peaks in Fig. 4.4) and therefore deemed as a good balance for achieving high SNR at relatively short testing time.

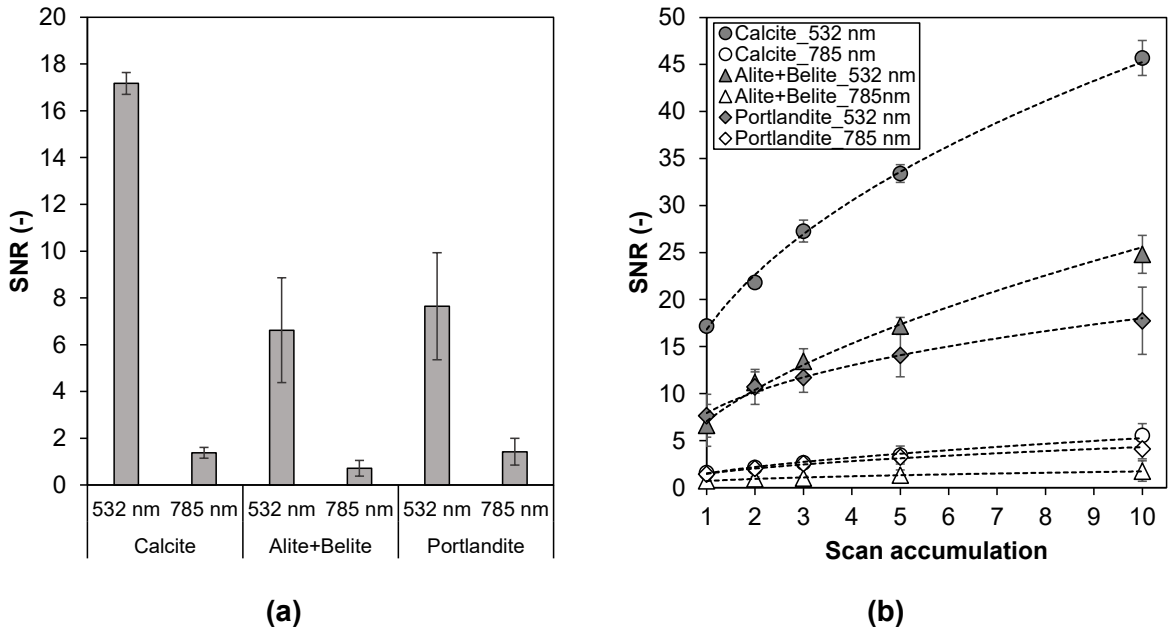


Figure 4.2 Effect of laser wavelength on SNR of calcite (from carbonation and limestone filler), unreacted cement and portlandite peaks after single scan (a) and multiple scan (b) accumulation. Analysis was carried out at 4.15 mW laser power and 1s exposure time. Dotted lines show best-fit power law relations ($R^2 > 0.96$). Error bars represent standard deviation.

4.3.2 Effect of laser power and exposure time

Fig. 4.3 shows the effect of laser power and exposure time on the SNR of the Raman peaks. It can be seen that the SNR increased with exposure time and laser power, again following a power law trend ($R^2 > 0.95$) regardless of the laser wavelength and analysed phase. Increasing the laser power was found to be more effective in improving SNR than increasing the exposure time. For example, a combination of an exposure time of 2 s and a laser power of 4.15 mW would provide an SNR comparable to that obtained with an exposure time of 10 s and a laser power of 2.48 mW, but with 80% less acquisition time.

The SNR for ettringite (988 cm^{-1}) was much lower than for other phases (Fig. 4.3d) due to its presence as a minor phase intermixed with calcite (Fig. 4.4a). Ettringite is also known to dehydrate and lose part of its chemically combined water above 100°C (Zhou & Glasser, 2001; Pourchez et al., 2006). Here, the SNR for ettringite was observed to increase with laser power and exposure time. This suggests that the largest applied laser power (4.15 mW) and exposure time (10 s) were safe and did not produce sufficient heat to cause degradation of ettringite. The effect of excessive laser exposure leading to microstructural changes and phase decomposition will be examined further in Section 4.3.4.

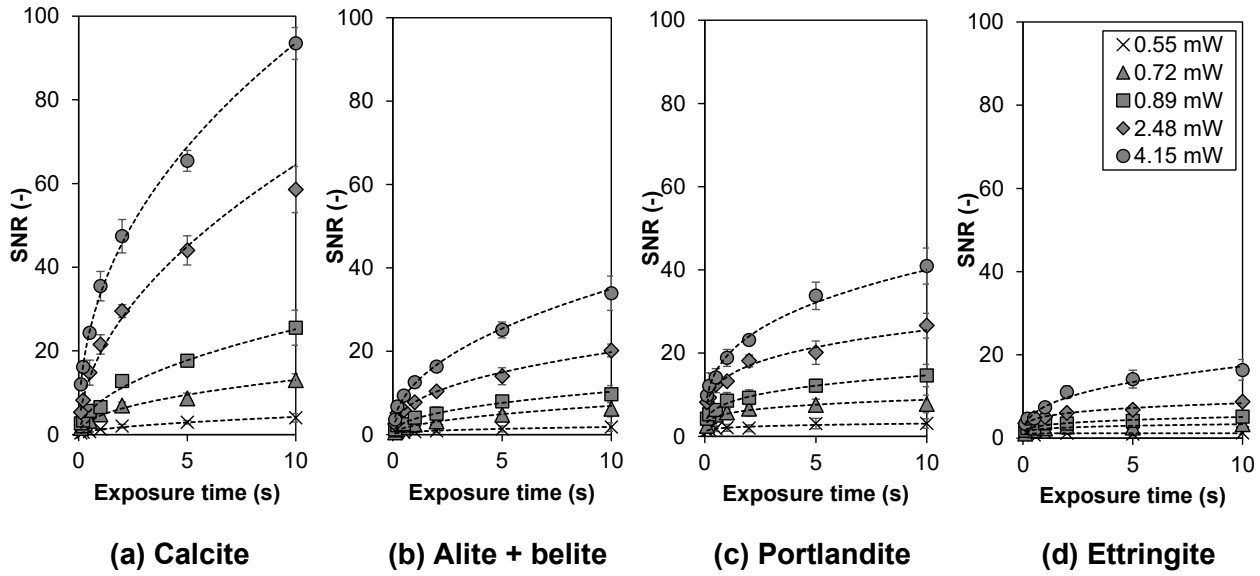


Figure 4.3 Effect of laser power and exposure time on the SNR of the main Raman peaks of calcite (from carbonation and limestone filler), alite + belite, portlandite and ettringite. Analysis was carried out with 532 nm laser at scan accumulation of 1. Dotted lines show best-fit power law relations ($R^2 > 0.95$). Error bars represent standard deviation.

Fig. 4.4 shows a series of spectra for calcite and unreacted cement from carbonated and non-carbonated zone respectively at increasing exposure time and a constant laser power of 4.15 mW. It can be clearly seen that a longer exposure time improves detectability of not only the target phases, but also the minor intermixed phases such as ettringite (AFt) and portlandite (CH). At short exposure time below 2 s, the background signal increases dramatically, and the detectability of weaker peaks diminishes.

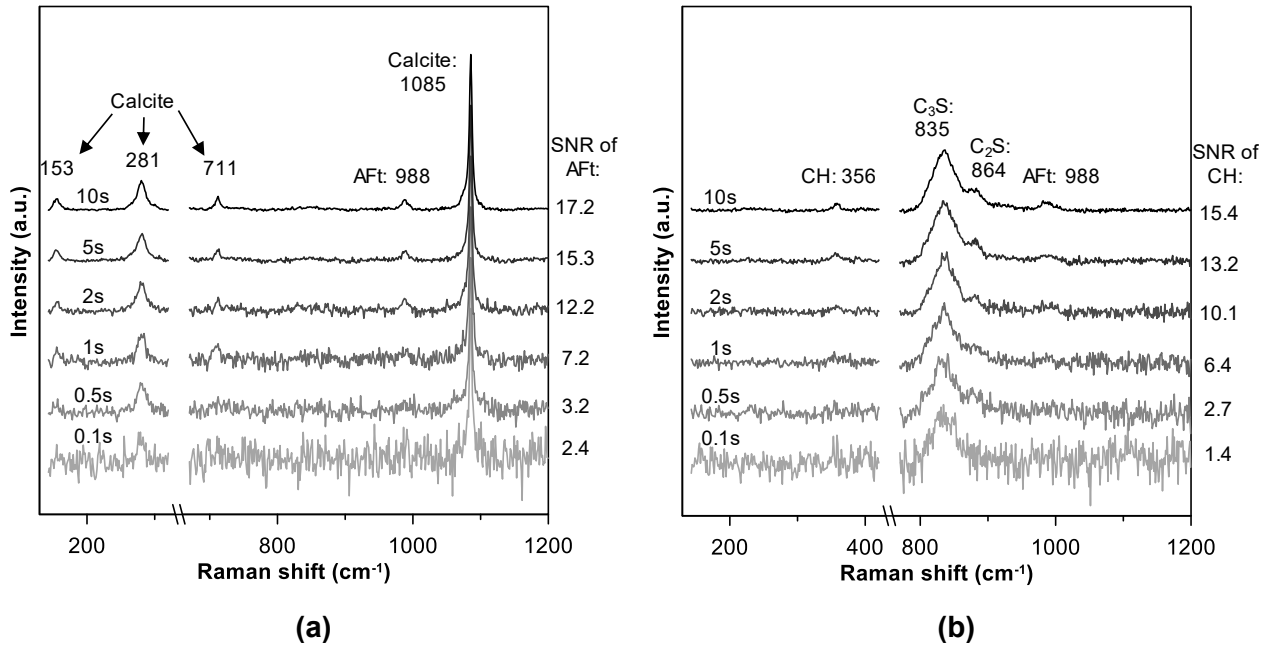


Figure 4.4 Effect of exposure time on the quality of Raman spectra for calcite (from carbonated zone) (a) and unreacted cement (from non-carbonated zone) (b). The SNR of the weak peaks of AFt and CH are shown. Analysis was carried out with 532 nm laser, 4.15 mW laser power and scan accumulation of 1.

4.3.3 Effect of surface moisture and roughness

Fig. 4.5 shows the evolution of the main Raman peaks for calcite, alite + belite and portlandite with ambient drying of the freshly-cut surface at 45% RH and 33% RH, 21ºC. It can be seen that peak intensities for all phases increased with drying. This suggests that although the sample surface was towel-dried prior to analysis, there was still a small amount of residual free water present in the pore space obscuring the detection of the solid phases. Detectability of the solid phases improved once the residual surface water was removed, and the Raman spectra gradually converged towards a stable form. Fig. 4.5d shows the evolution of the SNR of the Raman peaks as a function of drying time. The SNR improved significantly during the first 1 min of drying at 45% RH, 21ºC and stabilised after ~4 min. After ~9 min, the SNR is very similar to those obtained after long-term drying (1 month) at 33% RH, 21ºC (empty symbols) to mass equilibrium.

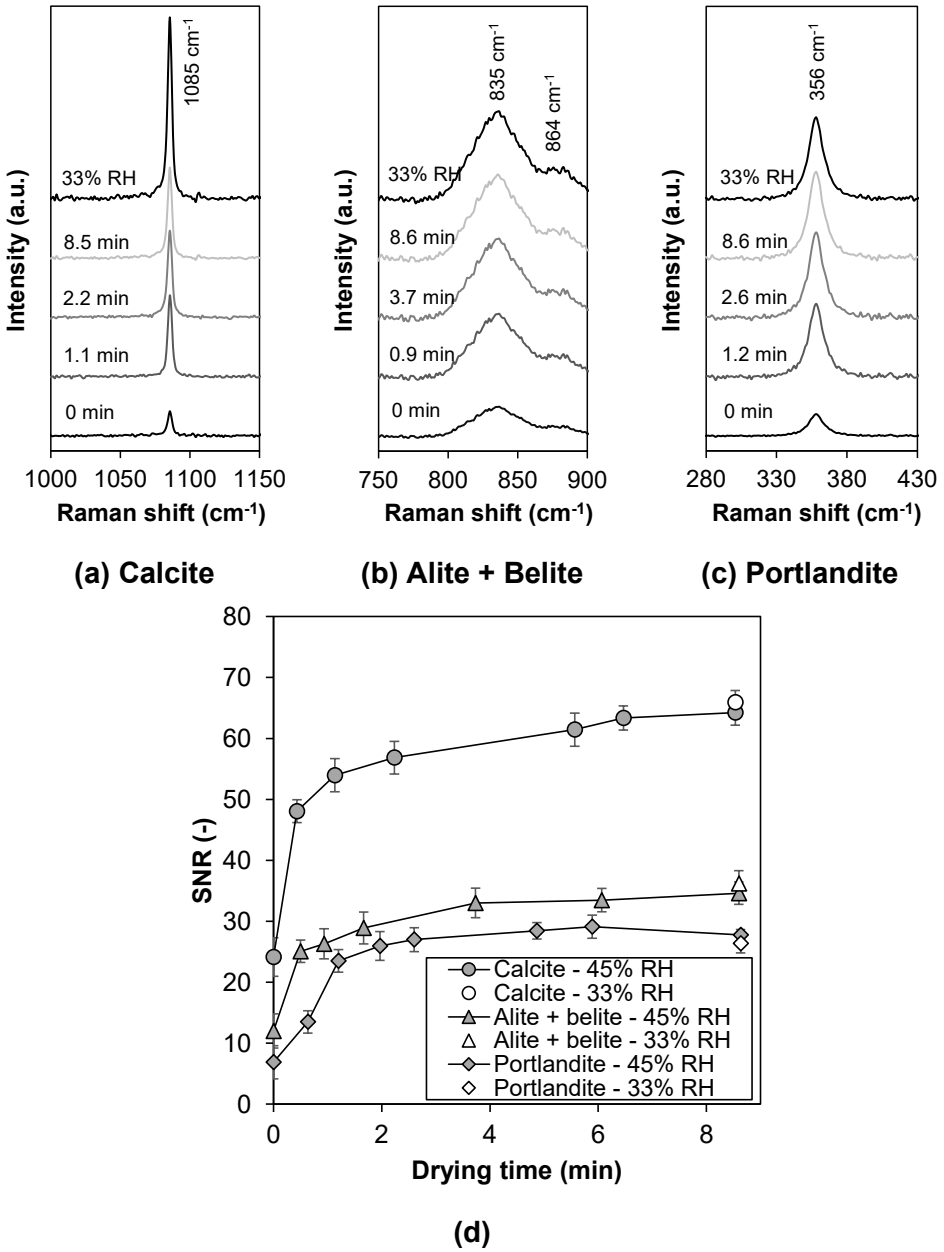


Figure 4.5 Evolution of the main Raman peaks (a-c) and SNR (d) of calcite, alite + belite and portlandite with ambient drying at ~45% RH, 21ºC (for less than 9 minutes) from a freshly cut surface and at 33% RH, 21ºC until mass equilibrium (for 1 month). Analysis was carried out with 532 nm laser, 4.15 mW laser power, 2s exposure time and scan accumulation of 2.

Fig. 4.6 shows the effect of surface roughness on the Raman maps of alite + belite and calcite acquired from the carbonated zone. Note that the sample was dried at 33% RH, 21ºC and epoxy-impregnated prior to grinding and polishing. The measured surface roughness (S_a, mean surface height from SEM) decreased from 0.41 μm after SiC grinding at 1000 grit to 0.13 μm after diamond polishing at 1 μm showing a progressively finer surface. The Raman maps were produced based on the intensity of the main Raman peaks (1085 cm^{-1} for calcite, 835-864 cm^{-1} for alite + belite). Blue

pixels indicate low intensity whereas red pixels indicate high intensity areas corresponding to the phase of interest. The same colour scales were used for different surface roughness for ease of comparison.

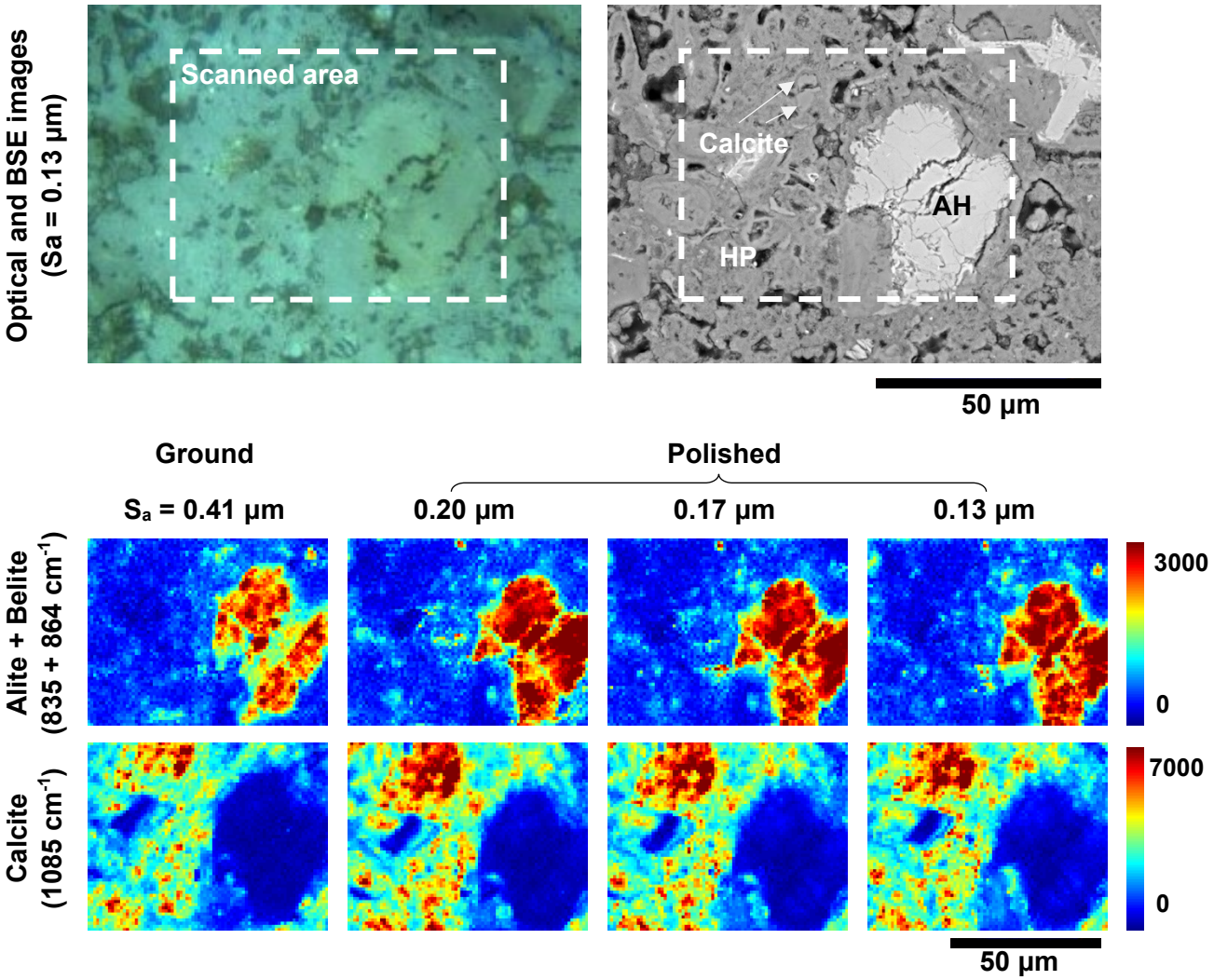


Figure 4.6 Colour-coded Raman maps of alite + belite and calcite from the carbonated zone at different surface roughness after grinding and polishing. Colour scale bar indicates peak intensities (a.u.). Optical and BSE images show the microstructure of the matching area after polishing. Analysis was carried out with 532 nm laser, 4.15 mW laser power, 2s exposure time, scan accumulation of 2 and 1 µm step size. AH: unreacted cement; HP: hydration product.

Fig. 4.7 shows the average map intensity of alite + belite and calcite in the carbonated (A & B) and non-carbonated (C & D) regions plotted against surface roughness (S_a). The results were normalised to those of the SiC ground surface. Clearly, the Raman intensity improved with decreasing surface roughness, especially after diamond polishing. Results show that decreasing surface roughness from ~0.4 to 0.1 µm improved Raman peak intensities by 5 to 30%. This is because less interference from

surface irregularities occur and thus more Raman scattering events are detectable (Giridhar et al., 2017). As such, the spatial resolution of the maps also improved with decreasing surface roughness, enabling the detection of finer features.

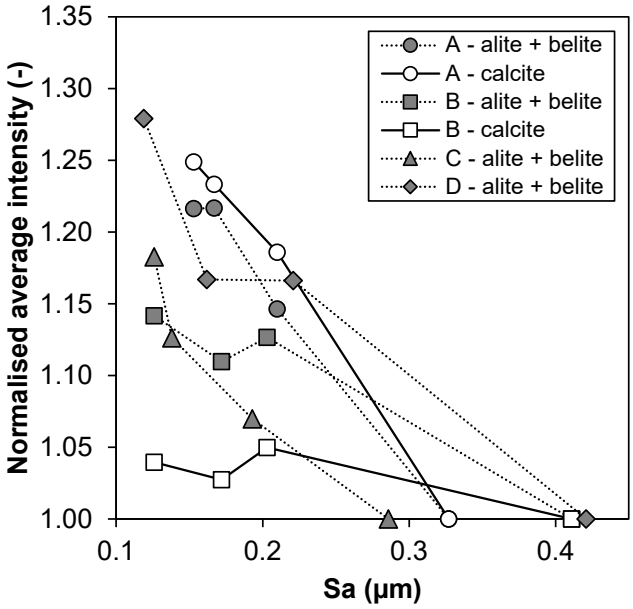


Figure 4.7 Effect of surface roughness (indicated by the measured mean surface height S_a from SEM) on the average map intensity of alite + belite and/or calcite at carbonated (A & B) and non-carbonated (C & D) locations.

4.3.4 Effect of prolonged laser irradiation during mapping

Fig. 4.8 plots the SNR, normalised to the first scan for comparison, against scan accumulation. The results showed large fluctuations at 0.55 mW laser power, presumably because the weak excitation produced insufficient signals and caused inconsistencies in the Raman spectra. The SNR at 4.15 mW laser power were more consistent, with variations no larger than 3.5%. Close inspection of the Raman spectra confirmed no occurrence of peak shift or formation of new peaks, indicating that the molecular structure and chemical composition of the phases remained unchanged.

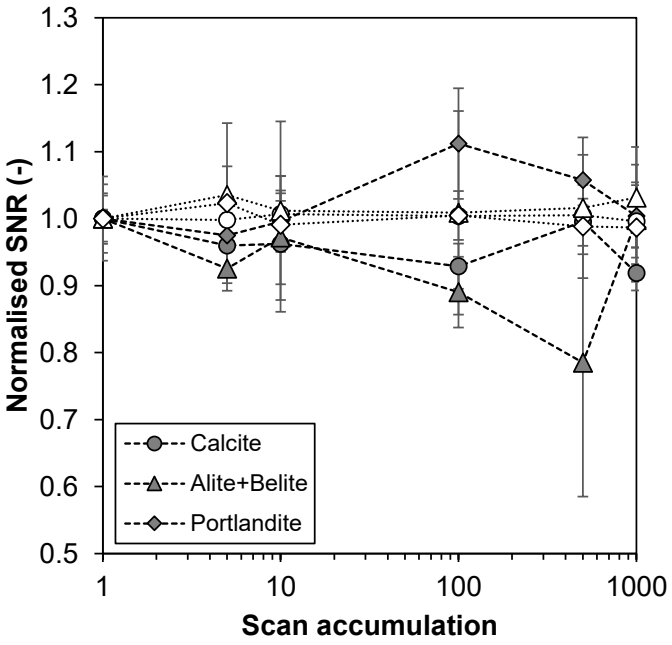


Figure 4.8 Evolution of SNR of the main Raman peaks for calcite (from carbonation and limestone filler), alite + belite and portlandite as a function of scan accumulation by spot analysis, at 0.55 mW (filled symbol) and 4.15 mW (empty symbol) laser power. Analysis was carried out with 532 nm laser and 2s exposure time. Error bars represent standard deviation.

Fig. 4.9 shows that extensive microcracking and pore coarsening appeared after Raman mapping, especially for the non-epoxy impregnated sample. The microcracks were generally < 1 μm wide, < 100 μm in length, and randomly distributed. These characteristics are reminiscent of microcracks induced by drying shrinkage (Wu et al., 2017; Wu et al., 2019). The crack density of the epoxy-impregnated sample after Raman mapping at 0.3 μm step size was 73% lower than the non-impregnated sample mapped at 1 μm step size.

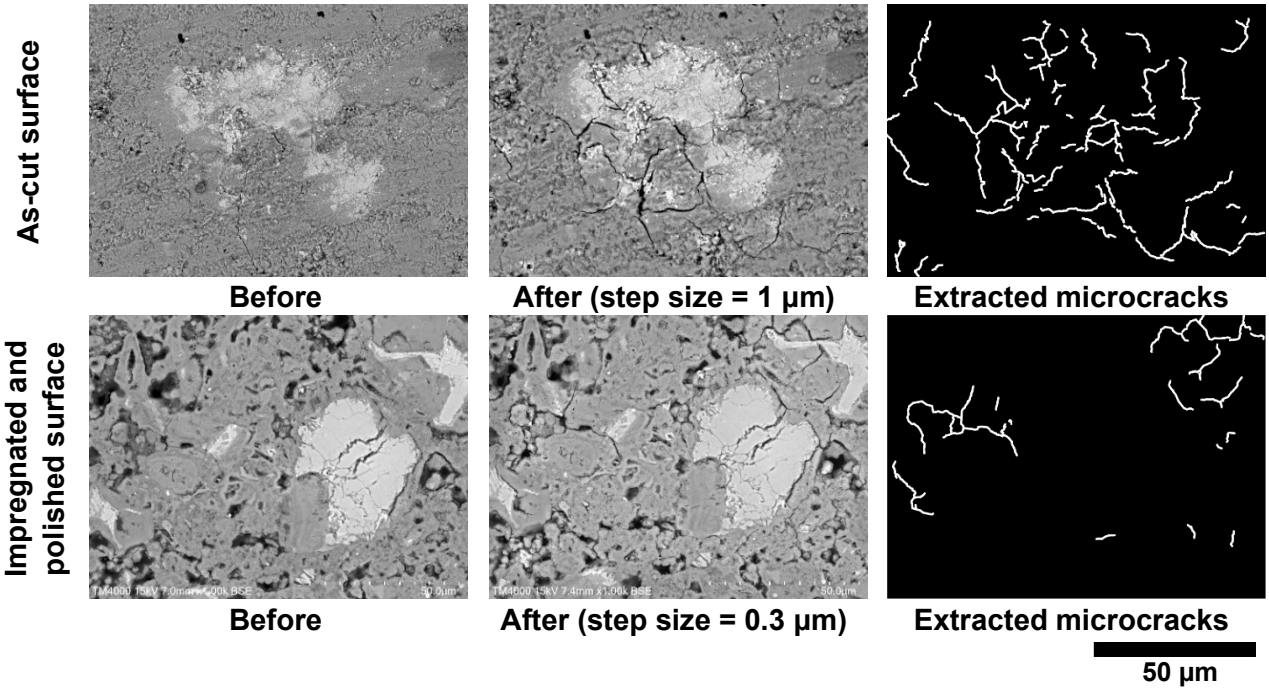


Figure 4.9 Area-matching BSE images showing the appearance of microcracks on the as-cut (non-epoxy impregnated) surface and impregnated/polished surface before and after Raman mapping at step sizes of 1 and 0.3 µm. Both locations were from the carbonated zone. Microcracks were extracted for quantification via image analysis.

Fig. 4.10 shows that the crack density increased with increase in laser power and exposure time, and with smaller step size. Therefore, extended Raman mapping on a small area (120 × 90 µm^2) can cause microstructural damage due to concentrated laser-induced heating. Carbonated areas were more susceptible to microcracking. This is perhaps unsurprising given that carbonation causes additional shrinkage, the effect of which is exacerbated by exposure to laser. However, epoxy-impregnation is very effective in protecting the microstructure. For example, Fig. 4.10c shows that crack density in the carbonated epoxy-impregnated sample was 95% lower than that of the non-impregnated sample at 1 µm step size. Microcracking in the carbonated epoxy-impregnated sample remained significantly lower than the non-impregnated sample even when the step size decreased to 0.3 µm.

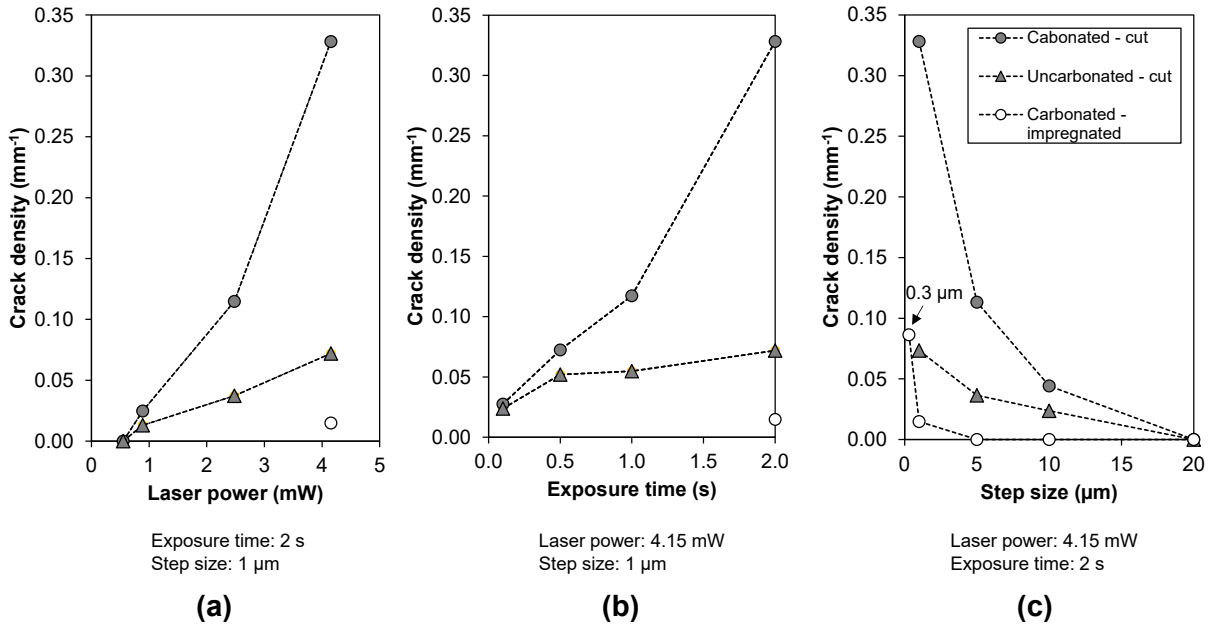


Figure 4.10 Crack density observed in carbonated and non-carbonated areas (120 × 90 mm^2) subjected to varying laser power (a), exposure time (b) and step size (c) with 532 nm laser and scan accumulation of 2.

It is interesting to note that laser power as high as 20 to 400 mW has been used in previous studies, but the potential damaging effects have not been investigated (Tarrida et al., 1995; Garbev et al., 2007; Mikhailova et al., 2019). Therefore, a further experiment was performed at 37 mW, which is the highest achievable laser power in the current setup, on the same epoxy-impregnated sample. The exposure time, scan accumulation and step size were set to 2 s, 2 and 1 µm respectively to scan an area of 256 × 192 µm^2. The obtained Raman maps (not shown) were oversaturated with signals, rendering the maps unusable. A more striking observation however, was that the microstructure of the cement paste was significantly altered with formation of many large interconnected cavities, especially in the originally porous regions (Fig. 4.11a-b). A similar observation was made on pure hardened epoxy (Fig. 4.11 c-d). This suggests that the severe damage in the cement paste was partly due to softening of the epoxy, which has a glass transition temperature of < 170ºC (Allaoui & El Bounia, 2009). It should be noted that cement hydrates, especially C-S-H and ettringite, will undergo dehydroxylation at such temperature.

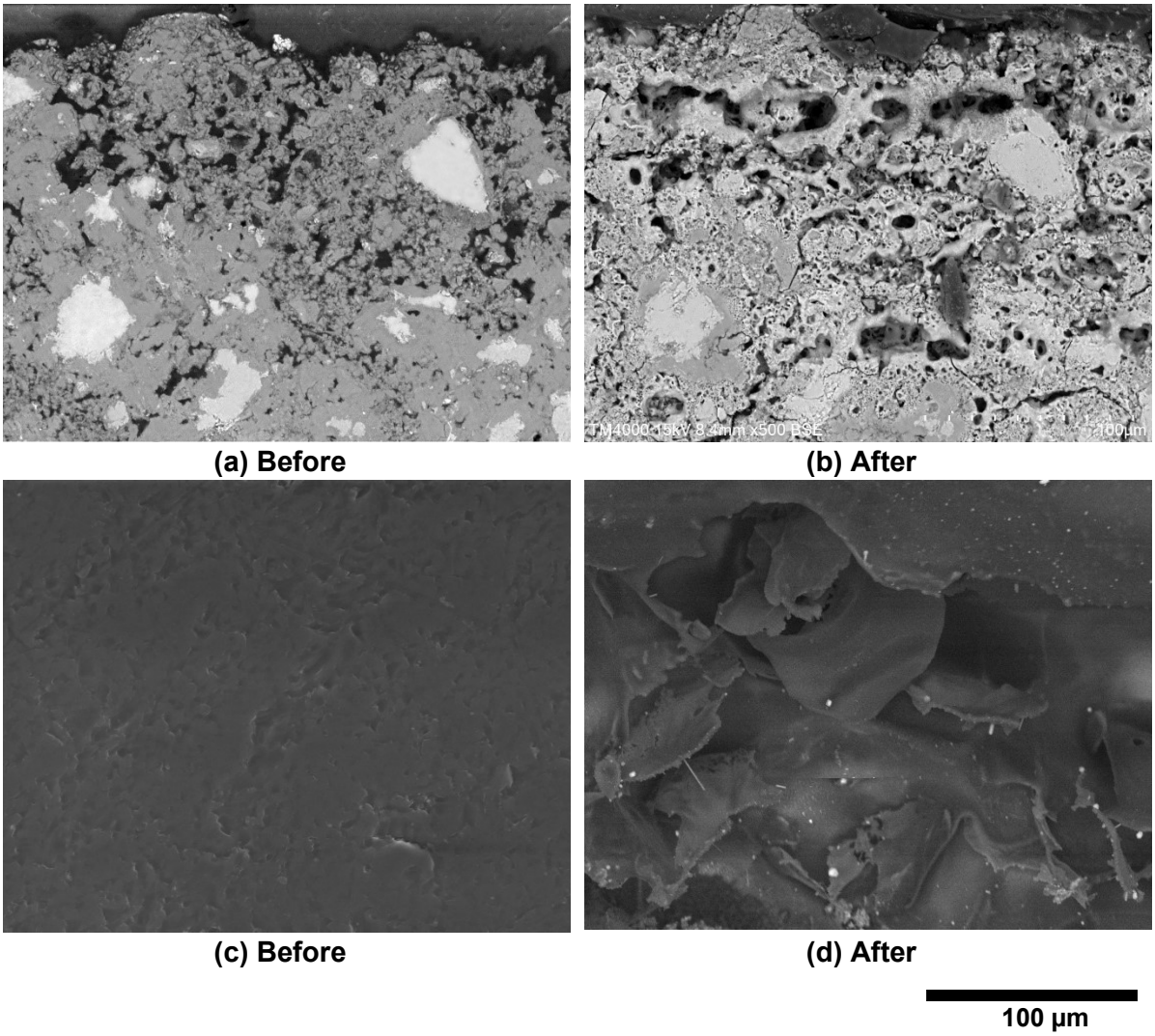


Figure 4.11 Area-matching BSE images showing epoxy-impregnated cement paste in the carbonated zone (a-b) and plain epoxy (c-d) before and after Raman mapping with high laser power of 37 mW (2s exposure time, accumulation scan of 2 and 1µm step size).

4.3.5 Comparison between BSE images and confocal Raman maps

Fig. 4.12 compares BSE images and Raman maps acquired from carbonated and non-carbonated regions of the epoxy-impregnated polished sample. The Raman maps were acquired with 532 nm laser at 4.15 mW, 2 s exposure time and a step size of 0.3 µm over an area of 160 × 110 μm^2 to be comparable with the BSE images. Both regions contained a large unreacted cement particle surrounded by a porous hydration product matrix (Fig. 4.12a-b). In the BSE images, hardly any differences can be detected between the non-carbonated and carbonated regions. With CRM however, the microstructures are clearly distinct between these two regions.

In the non-carbonated region, CRM showed a substantial amount of portlandite surrounding the unreacted cement particles (Fig. 4.12c). On close inspection, some of the large portlandite precipitates were also visible in the BSE image (arrowed in Fig. 4.12a), with spatial distribution that matched the Raman map. This is further corroborated by EDS spot analysis showing a high level of Ca, but low levels of Si and C. The corresponding calcite map (Fig. 4.12e) shows two distinct spots with high Raman intensities (arrowed), which are remnants of limestone filler from the CEM I cement. The other areas show negligible calcite, confirming that the region was non-carbonated.

In contrast, the carbonated region showed no portlandite (Fig. 4.12d) suggesting that the phase had reacted completely. This is confirmed by the corresponding calcite map (Fig. 4.12f) showing widespread distribution throughout the outer hydration product matrix. The calcite precipitates are microscopic, inter-mixed with other hydration products and not readily detectable by BSE microscopy. However, EDS spot analysis shows elevated levels of Ca, C and O, which corroborates with Raman microscopy. It is also worth noting that the unreacted cement particle remained non-carbonated.

The BSE images and Raman maps were further analysed and combined to construct composite images showing the spatial distribution of the segmented phases (Fig.4.12g-h). Unreacted cement and capillary pores were extracted from the BSE images using the Overflow method (Wong et al., 2006), whereas calcite and portlandite were extracted from the Raman maps by manual thresholding. Results show that the non-carbonated region had 7.9% portlandite and 0.1% calcite, while the carbonated region had 0% portlandite and 8.9% calcite. These findings demonstrate the potential of Raman microscopy to provide quantitative information (concentration and spatial distribution) on phases otherwise difficult to measure with BSE microscopy.

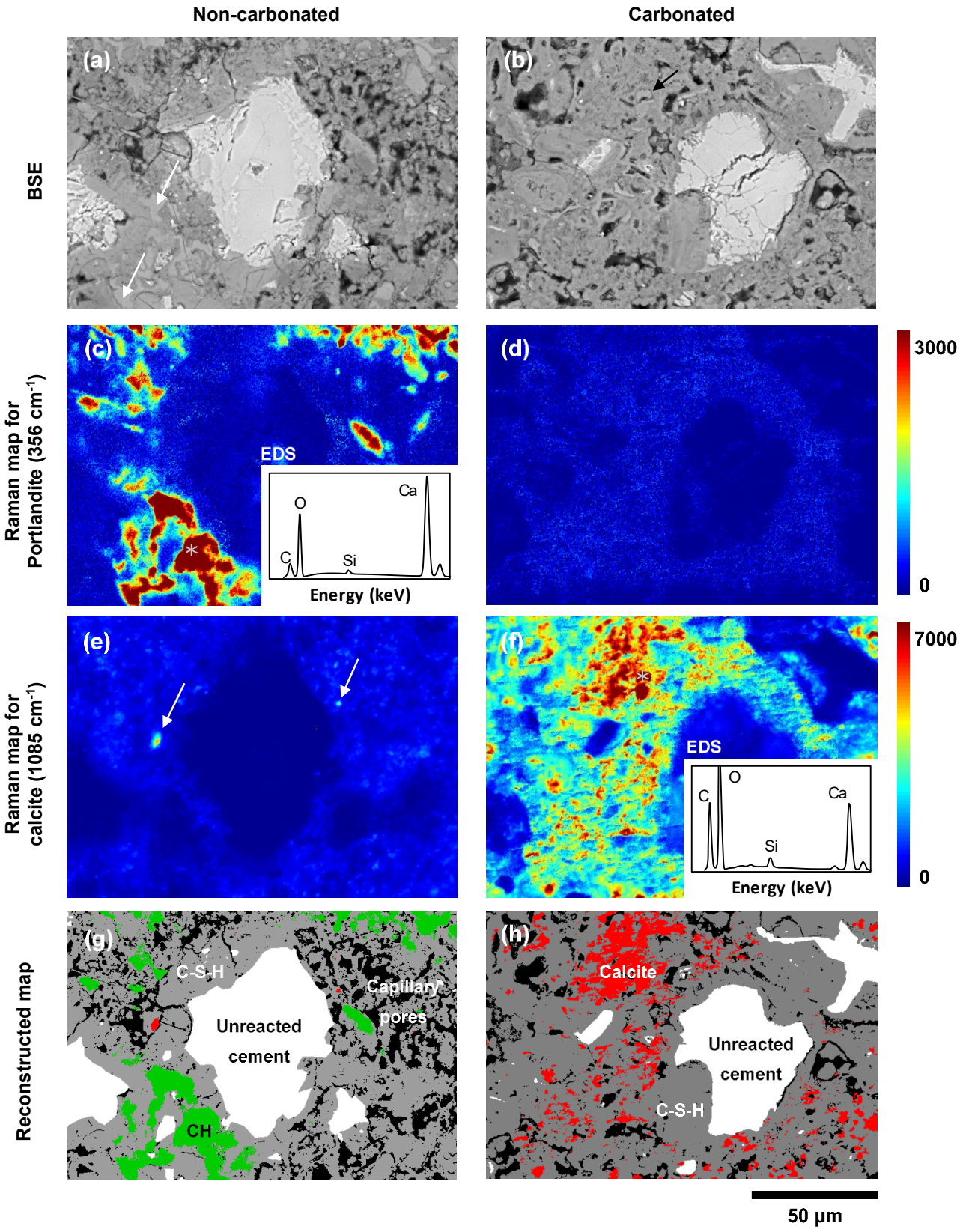


Figure 4.12 Comparison between BSE images and Raman maps of portlandite (CH) and calcite in carbonated and non-carbonated regions. Asterisks in (c, f) mark the spots analysed by EDS. Arrows mark the presence of portlandite and calcite in the non-carbonated region. (532 nm laser, 4.15 mW laser power, 2s exposure time and 0.3 µm step size).

The spectra from all pixels of the Raman maps (Fig. 4.12) were summed and are presented in Fig. 4.13. The main identifiable Raman peaks are those of calcite, alite, belite and portlandite. As expected, the calcite peaks were significantly stronger in the carbonated region. However, neither aragonite nor vaterite was detected. It is known that these polymorphs are metastable and they form mainly from the carbonation of C-S-H under high CO_2 levels (Morandeau et al., 2014). The Raman band of C-S-H (660 to 680 cm^{-1}) (Liu et al., 2015; Torres-Carrasco et al., 2017) in the carbonated region was similar to that in the non-carbonated region, indicating that the C-S-H was not carbonated. A similar observation was made for alite + belite. Portlandite appeared to be the only phase to have undergone carbonation, as indicated by the absence of its Raman peaks in the carbonated region.

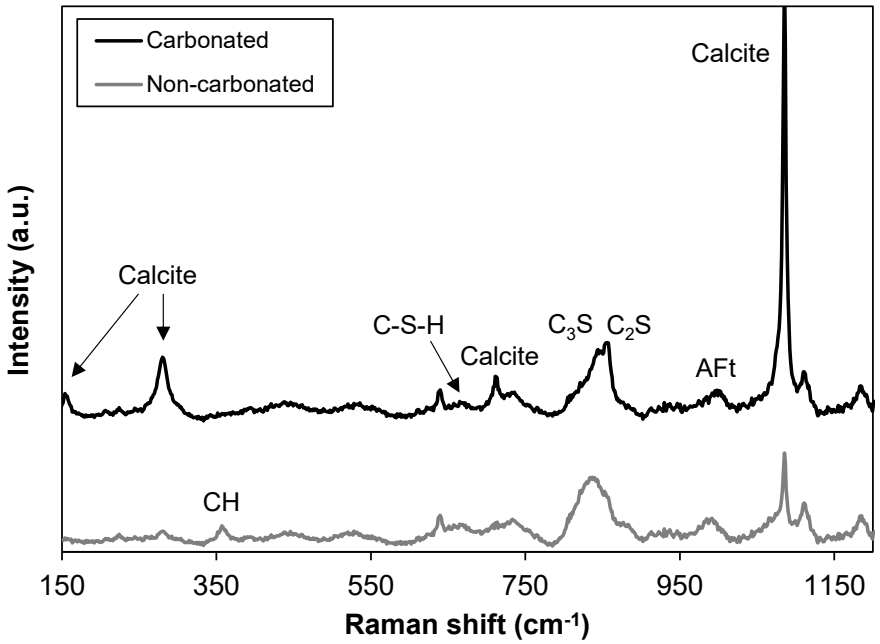


Figure 4.13 Comparison of the summed Raman spectra between non-carbonated and carbonated areas, obtained from the Raman maps shown in Figure 4.12.

4.4 Discussion

Results show that samples can be analysed as-is with Raman microscopy without requiring extensive drying. This makes the technique particularly suitable for analysis of samples that are sensitive to drying-induced changes or damage. For point-by-point mapping, however, the sample surface may carbonate during the scanning process due to the long acquisition time required. One recent study showed that surface carbonation of hardened cementitious materials can take place within an hour of exposure to ambient CO_2 level (Zhang et al., 2022). To prevent this from happening, it is recommended to keep the CO_2 level in the microscope enclosure to ≤ 10 ppm by using soda lime.

Optimisation shows that the 532 nm laser is a better option than the 785 nm laser for testing cement-based materials because it can yield higher SNR in the collected spectrum at the same parametric input, and can avoid photoluminescence bands. Another option is the 633 nm laser, which was not tested in this study but shown in an earlier work to be sufficient in avoiding photoluminescence (Richardson et al., 2010). The SNR increases with increase in laser power, exposure time and accumulation scan following a power law. However, this comes at a cost of longer analysis time and greater risk of specimen damage induced by laser exposure. The results in Fig. 4.4 indicate that a SNR of at least 10 is adequate for retaining the weaker peaks during background subtraction. Guided by this, the optimisation work suggests that a laser power of 4.15 mW, exposure time of 2s and scan accumulation of 2 is a good operating condition for Raman analysis of cement-based materials.

Prolonged laser irradiation during Raman mapping can induce localised heating, drying shrinkage and severe microcracking. To mitigate this, it is recommended to use a mapping step size of at least 20 μm, which is adequate for large-scale mapping (e.g. to determine carbonation depth). For high spatial resolution mapping (e.g. to resolve cement hydrates), a smaller step size of ~1 μm would be necessary. For such applications, it is recommended that the sample is epoxy-impregnated to protect the microstructure and flat polished to minimise signal interference from surface irregularities. Furthermore, the laser power should be kept as low as possible. In this study, 4.15 mW was found to be sufficient to yield satisfactory Raman signals without causing degradation of moisture-sensitive phases such as ettringite.

This study demonstrates that Raman microscopy can be used to characterise the spatial distribution of $CaCO_3$ in non-carbonated (limestone filler) and carbonated cement paste at the microstructural level. When combined with image analysis, precise quantification and profiling of carbonation can be performed. This is especially important for natural carbonation, where the precipitation of $CaCO_3$ is a slow process and difficult to measure with conventional profile-grinding analysis techniques such as XRD, TGA and FTIR at early stages of carbonation. Despite the fact that Raman imaging can be time consuming, mapping an area of 160 × 110 μm^2 at a step size of ~1 μm takes 19 hours with the optimised operating conditions. Further work on applying CRM for high-resolution quantification of carbonation following short-term exposure were presented in Chapter 5.

It is worth pointing out that some Raman microscopes such as the one used in this study have the capability to perform fast mapping by line scanning (Bernard et al., 2008; Corvisier et al., 2010), where the sample is illuminated with a line of laser, rather than an intense spot of laser. This enables large-area mapping in a shorter time without inducing damage. However, this function is usually proprietary and limited to specific instruments only. Moreover, the signals obtained tend to be weaker than those attainable with spot analysis especially for less Raman-active or low content phases.

Nevertheless, line scanning remains useful for highly Raman-active phases such as $CaCO_3$ polymorphs, which do not require intense laser power (Corvisier et al., 2010).

It is envisaged that the findings from this study can be applied to other minor phases in cementitious materials including C_3A, C_4AF, gypsum and monosulphate. Results in Chapter 6 show that the recommended settings are applicable to systems containing supplementary cementitious materials such as PFA and GGBS, in addition to CEM I. Furthermore, quartz is Raman active and has a fingerprint peak at 465 cm^{-1}. The recommended settings are applicable to mortars containing siliceous aggregates, even though the quartz fines are sometimes mixed with other crystalline minerals such as calcite, feldspar and mica. In any case, the presence of these phases is not expected to interfere with the detectability of cement hydrates and clinker minerals in the cement paste matrix. For mortars and concretes containing high aggregate volume fraction however, a small mapping step size should be used corresponding to the thinner cement paste regions between aggregate particles.

4.5 Conclusion

This study optimises confocal Raman microscopy (CRM) for spectral mapping of cement-based materials. The effect of sample moisture and surface roughness, and scanning parameters including laser wavelength (532, 785 nm), laser power (0.55, 0.72, 0.89, 2.48, 4.15 mW), exposure time (0.1, 0.5, 1, 2, 5, 10 s), scan accumulation (1, 2, 3, 5, 10) and mapping step size (0.3, 1, 5, 10, 20 μm) were investigated. The investigation was carried out in the naturally carbonated and non-carbonated regions of w/c 0.45 cement pastes, focusing on four main phases: calcite (from limestone filler or carbonation), portlandite, ettringite and unreacted cement. The effects of prolonged laser irradiation and mapping step size were also studied. The key findings are:

a) The use of short laser wavelength (532 nm) is advantageous over 785 nm for cement-based materials as it yields a higher signal-to-noise ratio (SNR) in the collected spectrum. Longer laser wavelength induces broad photoluminescence bands that are intrinsic and cannot be corrected by background correction. The photoluminescence bands obscure the peaks of certain phases of interest such as calcite and unreacted cement particles.
b) The SNR of the collected spectrum increases with increase in laser power, exposure time and accumulation scan following a power law trend ($R^2 > 0.95$). The optimisation work shows that a 4.15 mW laser power, 2s exposure time and scan accumulation of 2 with a 532 nm laser is a good operating condition for Raman analysis of cement-based materials. This yields an SNR of > 10 for all investigated phases at a relatively short testing time and low risk of laser-induced damage.
c) Freshly cut specimens can be analysed as-is without drying, however the presence of residual surface moisture can obscure phase detection. This problem is mitigated by short gentle drying

prior to Raman analysis. For example, drying at 45% RH, 21ºC for several minutes improves SNR significantly, achieving values that are equivalent to those obtained after long-term drying (1 month) at 33% RH.

d) Surface grinding/polishing prior to analysis increases peak intensities, improves spatial resolution of Raman maps and enables detection of finer features. For example, decreasing surface roughness from ~0.4 μm (after SiC grinding at 1000 grit) to 0.1 μm (after diamond polishing) improves Raman intensities by 5 to 30% due to the decreased interference from surface irregularities.

e) Repeated spot laser irradiation up to 1000 accumulations at 4.5 mW did not cause detectable Raman peak shifts or formation of new peaks, suggesting no changes to the chemical structure or composition of the analysed phases. However, closely spaced laser irradiation (< 20 μm step size) during Raman mapping can cause extensive microcracking due to localised heating, especially for carbonated systems. This effect can be mitigated by using a step size > 20 μm or by epoxy impregnating the specimen prior to mapping.

f) Confocal Raman microscopy has huge potential for high-resolution chemical mapping to characterise the composition and spatial distribution of various phases in cement-based materials for various applications. For example, the spatial distribution of unreacted cement (alite, belite), portlandite and calcite can be mapped at micron resolution. The obtained maps can be further processed by image analysis to extract quantitative information to complement results from BSE microscopy.

5 Real-time monitoring of carbonation of hardened cement pastes using confocal Raman microscopy

This chapter describes the research to investigate the feasibility of confocal Raman microscopy for monitoring early surface carbonation of hardened cement pastes in real-time for up to 7 d. Samples were exposed to natural carbonation (440 ppm CO_2) and accelerated carbonation (4% CO_2), and the evolution of calcium carbonate ($CaCO_3$) polymorphs, portlandite, ettringite, C-S-H gel and unreacted cement particles was followed. Results showed that calcite is the main polymorph formed under both natural and accelerated carbonation. Under accelerated carbonation, the formation of calcite on the sample surface completed within 1 d whereas under natural carbonation, the formation of calcite is expected to continue beyond 7d. The contents of portlandite and ettringite decreased rapidly under accelerated carbonation but much more gradually under natural carbonation. However, calcium silicate minerals in unreacted cement particles remained unchanged throughout the carbonation processes. Overall, this study demonstrated that confocal Raman microscopy is a valuable tool for non-destructive real-time imaging of surface carbonation in cement-based materials.

5.1 Introduction

Carbonation in cement-based materials involves the reaction between atmospheric CO_2 and calcium-bearing constituents, mainly calcium hydroxide (CH) and calcium silicate hydrate (C-S-H), to form calcium carbonate ($CaCO_3$) (Slegers & Rouxhet, 1976). Carbonation leads to a pH drop in concrete, thereby depassivating any embedded rebar in the carbonated zone and enabling corrosion. Natural carbonation of concrete is usually a very slow process, which can take decades to penetrate the concrete cover. Therefore, accelerated exposure involving high CO_2 concentrations (1% to 100%) (Groves et al., 1991; Castellote et al., 2009; Bernal et al., 2012; BS 1881-210, 2013; Shi et al., 2016; Leemann et al., 2017) are often used in laboratory. Accelerated tests have been criticised as being unrepresentative of natural carbonation as the decalcification processes involved and the carbonates that formed tend to be different (Chen et al., 2006; Castellote et al., 2009; Šavija & Luković, 2016). Nevertheless, accelerated carbonation is relevant to research on developing carbon capture, utilisation and storage (CCUS) strategies such as accelerated CO_2 curing of concrete and carbonation of waste concrete fines. The ability to observe carbonation in real-time would therefore be highly valuable to provide insights into the actual processes involved.

The most widely used method to investigate carbonation in concrete is the phenolphthalein spray test. Despite its simplicity and convenience, this technique is often criticised as underestimating the true

carbonation extent in concrete due to its dependence on colour change that occurs when pH drops to < 9.5 (Chang & Chen, 2006). Moreover, phenolphthalein is classified as a carcinogen and it could be phased out for future use to be replaced by thymolphthalein. Advanced techniques including thermogravimetric analysis (TGA), X-ray diffraction (XRD) and Fourier transform infrared spectroscopy (FTIR) have been adopted to provide more accurate measurements of $CaCO_3$ formed and therefore the extent of carbonation (Lo & Lee, 2002; Villain et al., 2007; Shah et al., 2018). NMR could be used to detect amorphous $CaCO_3$ that forms during early carbonation prior to crystallisation into vaterite and calcite. However, these techniques are destructive as they require substantial sample preparation including cutting, crushing and powder grinding, which may induce additional carbonation (Morandeau et al., 2014). The presence of aggregate particles in concrete further complicates data analysis.

Backscattered electron microscopy (BSE) has been widely applied to study microstructural changes induced by carbonation in concrete (Wang et al., 2013; Galan et al., 2015; Al Omari et al., 2016; Shah et al., 2018). However, as $CaCO_3$ cannot be readily distinguished from other solid hydration phases, porosity change is often used as an indicator to evaluate the extent of carbonation (P. Stutzman, 2004). Micro-tomography is another technique used to study changes in porosity as an indicator for carbonation. Although energy or wavelength-dispersive X-ray spectroscopy can be used to detect $CaCO_3$ to some extent, the type of polymorphs formed cannot be determined (Kashef-Haghighi & Ghoshal, 2013; Branch et al., 2016). Some techniques (e.g. SEM-BSE) requires samples to be fully dried, epoxy-impregnated, ground and polished, and therefore cannot be used for real-time monitoring purposes.

Raman spectroscopy provides a non-destructive means to characterise the phase composition of a sample based on molecular vibrations. When combined with confocal microscopy, the technique enables high resolution Raman imaging of phase distribution at a microstructural level. Furthermore, the technique can be applied to wet and uneven surfaces and therefore is suited for observing samples in their natural states. Confocal Raman microscopy (CRM) has been used to study the hydration of C_3S (Higl et al., 2016), weathering of anhydrous cements (Torres-Carrasco, del Campo, et al., 2017), and carbonation of lime paste (Ševčík et al., 2016). However, its application for real-time imaging of cement-based materials remains under-explored. Torres-Carrasco et al. (2019) and Mikhailova et al. (2019) used Raman microscopy to study the hydration of Portland cement and polymerisation of alkali-activated cement and their results show that Raman microscopy is a promising tool for *in situ* observation of phase evolution in cement-based materials.

The aim of this study is to determine the viability of confocal Raman microscopy as a non-destructive technique to monitor early surface carbonation and to study the phase evolution that occurs during

natural and accelerated carbonation. Hardened CEM I cement pastes exposed to continuous carbonation at 440 ppm and 4% CO_2 levels were analysed at designated time points up to 7 d. The evolution of $CaCO_3$ polymorphs, portlandite, ettringite, C-S-H gel and unreacted cement particles were analysed qualitatively and quantitatively using the collected Raman maps and spectra. The findings showed that Raman microscopy is a powerful tool for real-time monitoring of carbonation in cement-based materials, and provided some interesting new insights into the mechanisms involved.

5.2 Experimental

5.2.1 Materials and sample preparation

Cement paste with a water/cement ratio (w/c) of 0.45 was prepared using ordinary Portland cement CEM I 52.5N. The chemical compositions and physical properties of the cement were specified in Section 3.1. The mix proportions, casting and curing processes were the same as those in Chapter 4. After curing, the cubic sample was diamond sectioned vertically at the centre to produce two adjacent blocks (50 × 21 × 6 mm), one for natural carbonation and the other for accelerated carbonation. Prior to carbonation, the blocks were conditioned at 21°C, 65% RH in the presence of soda lime (CO_2 < 10 ppm) for 1 d to stop hydration at the surface of the sample, and then viewed with SEM-BSE at 500× magnification to identify a matching region of interest (ROI) for analysis.

5.2.2 Carbonation

Carbonation of the block samples was carried out in two separate incubators (Sectioned 3.2), one maintained at 440 ppm CO_2 for natural carbonation and the other at 4% CO_2 for accelerated carbonation. The temperature and RH of the incubators were controlled at 21°C and 65% respectively. The samples were exposed to carbonation in all directions. At each designated time point (0, 1 & 5 h, 1, 2, 3, 4 & 7 d), the samples were removed from the incubators and analysed with Raman microscopy. Each analysis took around 30 min and the samples were returned to their respective incubator immediately after analysis. Soda lime was placed in the microscope enclosure to minimise ambient carbonation during analysis.

5.2.3 Confocal Raman microscopy

Raman mapping was performed with the CRM at ambient conditions (21°C, 45% RH, 440 ppm CO_2). Measurements were made using a laser line of 532 nm, grating of 2400 lines/mm and a long-working distance objective of 50× magnification (NA = 0.5). The theoretical spot size of the laser was ~1.3 μm. A thermoelectrically-cooled charge-coupled device (CCD) with 1024 × 256 pixels was used as

the detector. Raman shift calibration was carried out using an internal silicon standard (520.2 ± 0.5 cm^{-1}) prior to each scan. The laser power at the sample surface and exposure time were set to 1.25 mW and 0.5 s respectively to minimise laser-induced damage (Tarrida et al., 1995). The spectral range was set from 143 to 1385 cm^{-1} to cover the main peaks of various $CaCO_3$ polymorphs including calcite (280 and 1085 cm^{-1}), aragonite (205 and 1085 cm^{-1}) and vaterite (300, 1080 and 1090 cm^{-1}) (S. Martinez-Ramirez et al., 2003). A total of 4675 points at a step size of 2 μm were analysed to give a Raman map of 18700 μm^2. All data acquisition was performed using the Renishaw WiRE v.5.2 software. Spectral artefacts including cosmic rays and background were removed using the nearest neighbour method and least squares polynomial fit respectively.

The Raman maps acquired were further quantified by image analysis to measure the volume fractions of calcite, portlandite and unreacted cement (C_2S + C_3S). Image segmentation was performed by manual thresholding. Since the ROIs analysed for natural and acceleration carbonation were not exactly the same, the quantified areas of the individual phases were normalised to that of the hydration product matrix (where carbonation mainly occurred) to enable a meaningful comparison.

5.3 Results

5.3.1 Raman maps

Fig. 5.1 shows the ROIs on each sample block selected for Raman mapping. Although the blocks were cut adjacent to each other, their microstructure appeared slightly different due to material loss caused by cutting. However, as confirmed by BSE, both ROIs contained a large unreacted cement particle (AH) surrounded by a porous matrix of hydration products (HP).

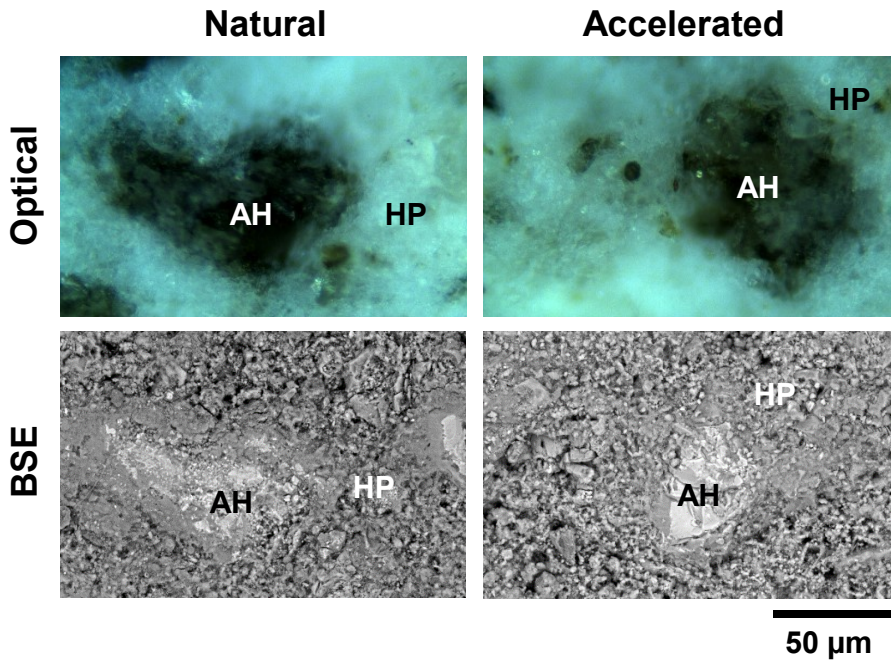


Figure 5.1 Area-matching optical and BSE micrographs of the selected ROIs for Raman analysis to be exposed to natural (a) and accelerated (b) carbonation. AH: unreacted cement; HP: hydration product

Fig. 5.2 a-b present Raman maps showing the evolution of calcite, portlandite and unreacted cement (C_2S & C_3S) under natural and accelerated carbonation respectively. The maps were produced based on the intensity of the main Raman peaks, i.e. 1085 cm^{-1} for calcite, 356 cm^{-1} for portlandite, 864 cm^{-1} for C_2S and 835 cm^{-1} for C_3S (Torres-Carrasco et al., 2019). Dark pixels indicate low content whereas bright pixels indicate high content of the respective phase. However, it should be pointed out that pixel brightness is also dependent on the crystallinity of the phases (Torres-Carrasco et al., 2019) such that more crystalline phases (e.g. calcite) tend to produce higher signals and hence brighter pixels.

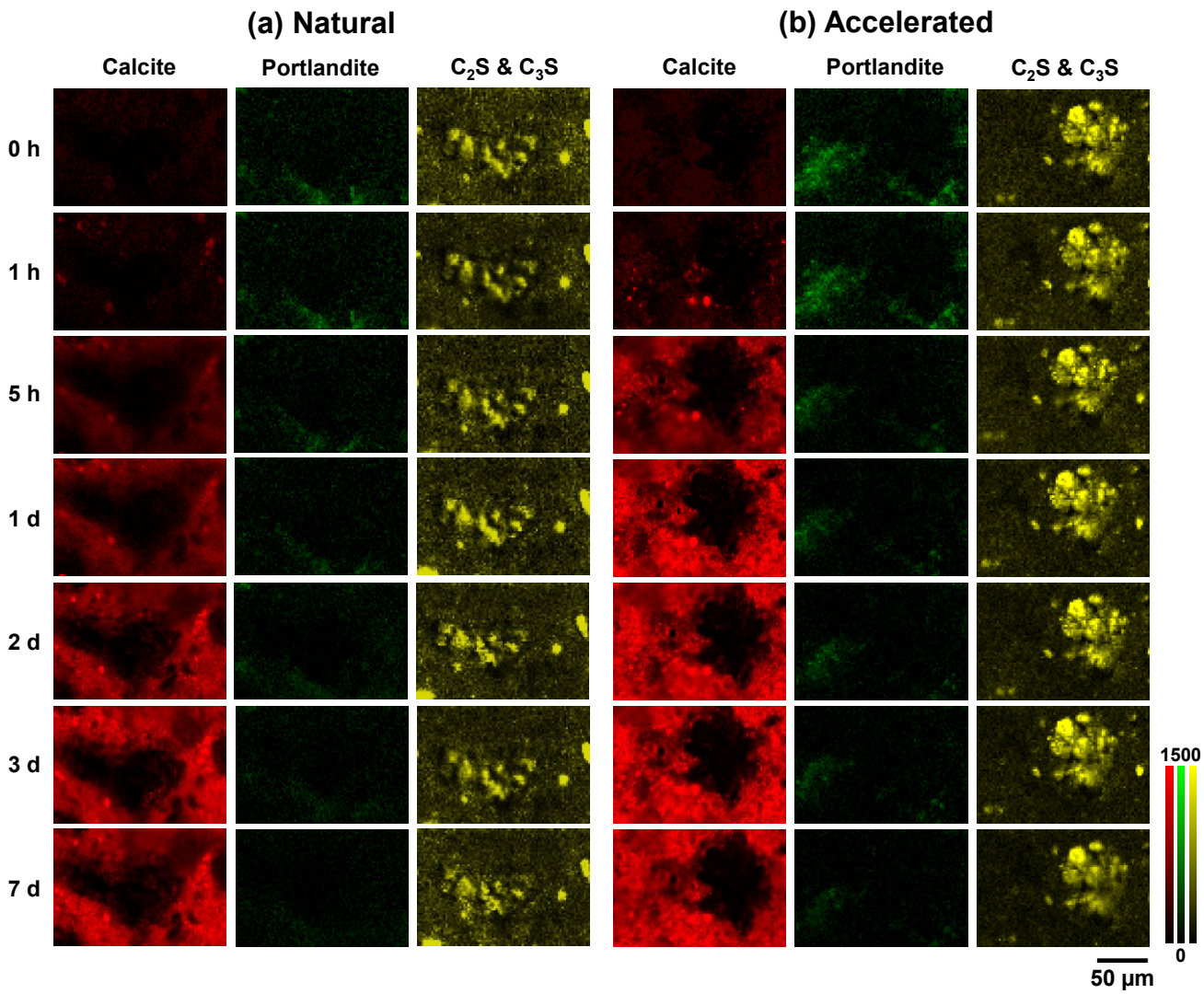


Figure 5.2 Raman maps showing the evolution of calcite, portlandite and C_2S & C_3S under natural (a) and accelerated (b) carbonation.

At 0 h, no calcite (or other polymorphs of $CaCO_3$) was detected in either sample, confirming that carbonation had not occurred during curing or conditioning. The calcium silicates present within the unreacted cement particles show relatively well-defined morphology, with the remaining areas likely to be surface irregularities. Small amounts of portlandite were observed in both samples at 0 h although the signals were relatively weak. Between 1 and 5 h of carbonation, calcite began to appear in both samples in the hydration product matrix. This confirms that carbonation occurs very rapidly on concrete surface even if it takes place naturally under ambient conditions. However, the amount of calcite formed during accelerated carbonation was clearly more than that of natural carbonation.

After 1 d, the surface of the sample exposed to accelerated carbonation appeared fully carbonated, evident by the consistent pixel brightness of calcite. This suggests that carbonation had completed at

the sample surface after 1 d and had possibly advanced into the subsurface. In contrast, the surface of the sample exposed to natural carbonation showed a gradual increase in calcite concentration and the data suggest that the formation of calcite will continue beyond 7 d. In either case, the intensity of the portlandite signal decreased with time, indicating that portlandite had reacted with CO_2 to form $CaCO_3$. However, calcite did not only form where the portlandite was located but also elsewhere in the cement paste matrix due to dissolution-precipitation process. Some C-S-H gel and perhaps also ettringite might have also carbonated to form calcite (Auroy et al., 2018). However, this was not evident from the Raman maps due to the very weak signals of these phases (hence not presented). The unreacted cement particles remained relatively unaffected throughout the exposure to CO_2. However, it is expected that with a longer period of carbonation, unreacted cement can also become decalcified (Ashraf & Olek, 2016; Siddique et al., 2020).

5.3.2 Raman spectra

The Raman spectra from each map were summed up and compared to observe all detectable phases. Results are presented in Fig. 5.3. In corroboration with Fig. 5.2, the intensity of the Raman peak for calcite (1085 cm^{-1}) increased over time and advanced more rapidly under accelerated carbonation. Correspondingly, the intensity of the Raman peak for portlandite (356 cm^{-1}) decreased with carbonation. Other polymorphs of $CaCO_3$ including aragonite (205 cm^{-1}) and possibly vaterite (300 cm^{-1}) were also detected, especially under accelerated carbonation, but their signals were very weak. These polymorphs are known to be metastable and act as precursors to the precipitation of more stable calcite (Ogino et al., 1987; Al Omari et al., 2016). It should be pointed out that amorphous $CaCO_3$ can also form prior to the formation of crystalline $CaCO_3$ (Black et al., 2007). Indeed, at 1 h carbonation, a hump attributed to the symmetric stretching of C-O bonds of different lengths (DeCarlo, 2018) was observed between 1080 and 1090 cm^{-1} in addition to the crystalline peak at 1085 cm^{-1} and a weak lattice peak at 281 cm^{-1}. It was therefore likely that both amorphous and crystalline $CaCO_3$ coexisted in the sample at early carbonation. In addition to amorphous $CaCO_3$, monohydrocalcite is another hydrated form of $CaCO_3$ (López-Arce et al., 2011) but this was not observed (1069 cm^{-1}) (Coleyshaw et al., 2003) in this study.

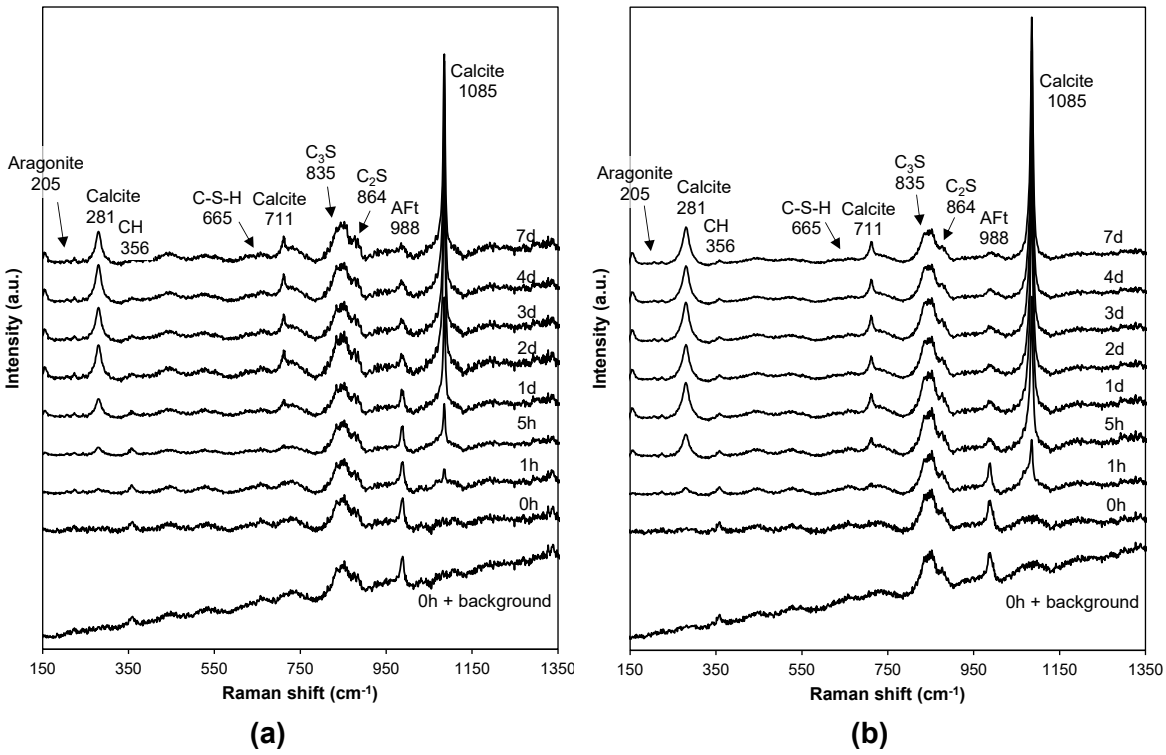


Figure 5.3 Raman spectra showing the evolution of the peaks of different phases under natural (a) and accelerated (b) carbonation.

The characteristic Raman peak of C-S-H (665 cm^{-1}) was also detected but the signals were similarly very weak due to its poor crystallinity (Torres-Carrasco et al., 2019). However, careful observation suggests that C-S-H remained relatively unchanged under natural carbonation but slightly decreased with accelerated carbonation after 1 d. This appears to be consistent with the study by Castellote et al. (2009) who reported significantly enhanced decalcification of C-S-H under accelerated carbonation. Another detectable phase worth discussing is ettringite (988 cm^{-1}). The presence of ettringite is unsurprising given the relatively young age of the sample. It is clear from the spectra that ettringite decreased with increasing carbonation, especially after 1 d of accelerated carbonation. It has been reported by Auroy et al. (2018) that pure ettringite can decalcify to form aragonite, gibbsite and either gypsum or bassanite under accelerated and natural carbonation respectively but the Raman peaks for these phases were not detected in this study.

5.3.3 Quantification by image analysis

Image analysis results show that under accelerated carbonation, nearly all calcite was formed during the first day, whereas under natural carbonation, the formation of calcite was much slower and likely to continue beyond 7 d. This corresponds with the trends of portlandite which appears to decrease rapidly under accelerated carbonation and much more gradually under natural carbonation. The

volume fraction of C_3S and C_2S, in contrast, remained stable throughout carbonation in both exposure regimes. Overall, the results appear to corroborate the qualitative observations made in Sections 5.3.1 and 5.3.2.

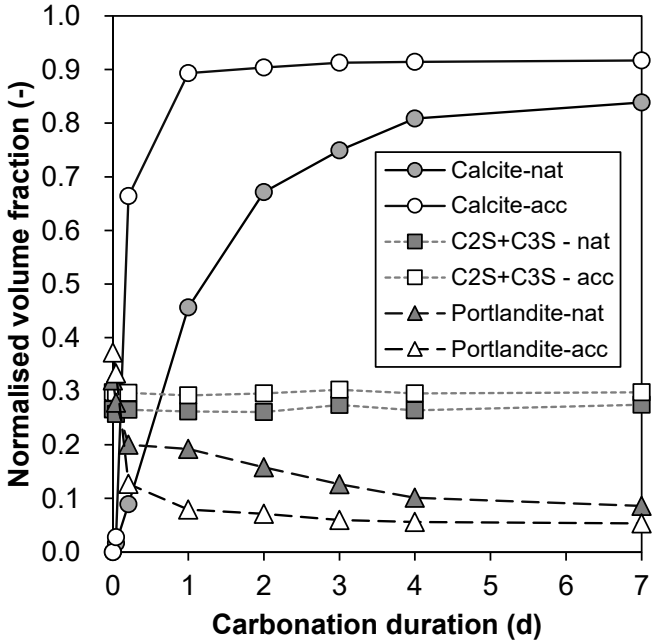


Figure 5.4 Evolution in the volume fractions of calcite, C_2S + C_3S and portlandite quantified by image analysis of the Raman maps.

5.4 Discussion

This study demonstrates the feasibility of CRM for real-time mapping of early carbonation in cementitious materials. The technique is non-destructive and requires very minimal sample preparation, and therefore is advantageous for observing hydrated samples. The high spatial resolution also enables the distribution of various phases to be observed at a microstructural level. However, Raman mapping of large surface area can be time-consuming and prolonged scanning may lead to microstructural changes as a result of drying, although this was not observed in the current study. This can be limited to some extent by keeping the laser power and exposure time low. Alternatively, an *in situ* environmental chamber may be used to maintain the atmosphere in the microscope and to avoid the need to remove the sample.

Further work is required to confirm the findings presented in this chapter. For example, the analysis of multiple locations will improve the representativeness of the results. Other techniques including XRD, infrared spectroscopy and BSE-EDS may also be used to provide additional supporting data, especially concerning phases that are less sensitive to Raman imaging such as C-S-H, vaterite and

aragonite. Given that the depth of carbonation has practical significance, work adapting the technique for depth profiling to monitor sub-surface changes and the progress of the carbonation front in cement-based materials will be presented in Chapter 6.

5.5 Conclusion

Confocal Raman microscopy (CRM) was used to study the evolution of hardened cement pastes subjected to surface carbonation. The evolution of calcium carbonate polymorphs, portlandite, unreacted cement and other phases including ettringite under natural carbonation (440 ppm CO_2) and accelerated carbonation (4% CO_2) was investigated. Results showed that surface carbonation completed within 1 d of accelerated carbonation, but the formation of calcite is expected to continue beyond 7d for natural carbonation. Portlandite and ettringite decreased rapidly under accelerated carbonation but much more gradually under natural carbonation. Unreacted cement particles remained relatively unaffected throughout the 7d exposure to carbonation. Overall, this study demonstrated that CRM is a powerful tool for non-destructive real-time monitoring of surface carbonation after short-term exposure.

6 Confocal Raman microscopy for measuring carbonation depth in cement-based materials: a comparison with other techniques

This chapter applies confocal Raman microscopy (CRM) to measure the carbonation depth of cement-based materials by mapping the spatial distributions of $CaCO_3$ polymorphs and portlandite. Neat CEM I and blended (CEM I + 30% fly ash, CEM I + 50% slag) systems exposed to accelerated (4% CO_2) and natural (440 ppm CO_2) carbonation were used for investigation. The carbonation depths measured with CRM were compared with those obtained using the phenolphthalein method and profile-grinding analysis via thermogravimetry, X-ray diffraction and Fourier transform infrared spectroscopy. Results showed that the carbonation fronts observed with CRM were distinct and matched well with those observed with the phenolphthalein method under accelerated carbonation conditions. The average difference in the carbonation depths measured with these two methods was 1.2% for accelerated carbonation. This increased to 14.3% for short-term (1-3 months) natural carbonation due to the ambiguous colouration of phenolphthalein when measuring shallow carbonation depth in some samples. The 'apparent' maximum carbonation depths determined by profile-grinding were on average 16.6% larger than those measured with CRM. The discrepancies were found to be related to the spatial variation of the carbonation front and the sampling interval used. A simple method was proposed to estimate the average carbonation depth from the carbonation profile, and the results obtained for profile-grinding analysis agreed well with those determined by CRM image analysis, with the average difference being only 1.1%. Overall, this chapter demonstrates that CRM is a reliable technique for measuring the true carbonation depth of cement-based materials and is especially powerful for measuring shallow carbonation depth (e.g. < 3 mm) after short-term natural carbonation.

6.1 Introduction

Carbonation of cement-based materials involves the reaction between atmospheric CO_2 and calcium-bearing constituents, mainly portlandite ($Ca(OH)_2$) and calcium silicate hydrate (C-S-H), to form calcium carbonate ($CaCO_3$). This phenomenon is problematic as it induces a pH drop in pore solution, which in turn depassivates the embedded rebar and initiates corrosion (Bentur et al., 1997). Accurate measurement of the carbonation depth is therefore necessary for reliable service life prediction of reinforced concrete structures.

Natural carbonation of concrete is a very slow process which can take many decades to penetrate the concrete cover. Therefore, accelerated carbonation involving high CO_2 concentrations (1% to 100%) is often preferred for laboratory investigations (Groves et al., 1991; Castellote et al., 2009; Bernal et al., 2012; Morandeau et al., 2014; Shi et al., 2016; Leemann et al., 2017). However, previous studies have found that the decalcification process involved and the carbonates formed under accelerated carbonation are different from those under natural carbonation (Chen et al., 2006; Galan et al., 2015; Šavija & Luković, 2016). For example, elevated CO_2 concentration significantly enhances the carbonation rate of C-S-H, which produces silica gel, coarsens the pore structure, and facilitates further carbonation (Castellote et al., 2009; Auroy et al., 2015). As such, results from accelerated carbonation are deemed unreliable for modelling long-term carbonation behaviour of concrete. A possible approach to this problem would be to expose concrete specimens to natural carbonation for a relatively short period and then extrapolate the results to long-term exposure by predictive modelling. However, this would require accurate measurement of the shallow carbonation depth (e.g. several mm), which remains challenging to achieve with existing techniques.

The pH indicator spray test is the most widely used method to determine the carbonation depth of concrete. It involves spraying a freshly broken surface with a pH indicator (e.g. phenolphthalein or thymolphthalein) and measuring the depth at which a colour change takes place (Yu et al., 2010). Several measurements are taken at different locations to obtain an average carbonation depth. However, as this method is based on visual judgment of colour boundary, the accuracy of the measurement is often found to be impaired by the insignificant colouration (Lo & Lee, 2002). Furthermore, the method is often said to 'underestimate' the true carbonation depth due to the fact that the colouration change occurs only when the pH of the pore solution is < 9.8 for phenolphthalein (Vogler et al., 2020) and < 10.5 for thymolphthalein (Jung et al., 2003).

To improve the accuracy in determining carbonation depth, more sophisticated profile-grinding analysis techniques including thermogravimetry (TGA), X-ray diffraction (XRD) and Fourier transform infrared spectroscopy (FTIR) are applied. These techniques are believed to be more accurate because of the ability to directly measure $CaCO_3$ and $Ca(OH)_2$ by detecting the mass loss due to thermal decomposition (TGA), diffraction patterns when interacting with X-ray (XRD) and molecular vibrations using infrared light (FTIR). Profile-grinding analysis techniques involve sampling powder at increasing depths from the exposure surface to determine the contents of $CaCO_3$ and $Ca(OH)_2$ (Matsushita et al., 2000; Villain et al., 2007; Shah et al., 2018). Powder is homogenised across individual sampling depth and the carbonation depth is defined as the depth beyond which the content of $CaCO_3$ plateaus to the level in the non-carbonated zone (Chang & Chen, 2006; Belda Revert et al., 2016). Results demonstrate that the carbonation front is not sharp but gradual, which is known as the partially carbonated zone (Parrott & Killoh, 1989; Rahman & Glasser, 1989).

However, the carbonation depth determined by the profile-grinding analysis techniques can be significantly different compared with the pH indicator spray test. Table 6.1 and Fig. 6.1 present a summary of 13 different studies published over the last three decades to highlight this inconsistency. Table 6.1 shows that the carbonation conditions (CO_2 concentration, temperature, and relative humidity (RH)), the profile-grinding method and sampling interval vary significantly between studies. The results collectively show that., the carbonation depths determined by profile-grinding analysis are generally larger than the carbonation depths measured using pH indicators (Fig. 6.1). The differences are mostly < 10 mm but can be as high as 23.9 mm. Furthermore, profile-grinding analysis is destructive and requires substantial sample preparation including cutting and powder grinding, which can be time-consuming and prone to errors. The process may also induce further carbonation and complicate analysis (Morandeau et al., 2014). Moreover, profile-grinding is impractical for measuring shallow carbonation depths (< 1 mm) due to the limited sampling precision. The presence of large aggregate particles can also interfere with analysis (Villain et al., 2007; Witkowski & Koniorczyk, 2018).

Table 6.1 Experimental studies using pH indicators and profile-grinding techniques to measure the carbonation depths of neat CEM I and blended cement. Technique: PHP: phenolphthalein, TYP: thymolphthalein, AYR: alizarin yellow R, TGA: thermogravimetry, XRD: X-ray diffraction, FTIR: Fourier transform infrared spectroscopy, PP: pH profile method, Gamma: gammadensimetry, OM: optical microscopy. Sample type: P: paste, M: mortar, C: concrete, SCC: self-compacting concrete. Binder: PC: Portland cement, LS: limestone filler, MK: metakaolin, LDHs: layered double hydroxides, CSA: calcium sulfoaluminate cement.

Reference	Technique	Sample (Binder)	Carbonation conditions*	Profile-grinding	
				Method	Sampling interval (mm)
Parrott & Killoh (1989)	PHP, TGA	C	Atmospheric CO_2 (36 years)	Drilling	5
Rahman & Glasser (1989)	PHP, TGA	P (PC)	Atmospheric CO_2, 20 and 40°C, 60% RH (80 d)	Slicing	1
Lo & Lee (2002)	PHP, FTIR	C (PC)	2% CO_2, 21°C (30, 60, 90 d)	n/a	1.5-3
Chang & Chen (2006)	PHP, TGA, XRD, FTIR, PP	C (PC)	20% CO_2, 23°C, 70% RH (56, 112 d)	n/a	5
Villain & Platret (2006)	PHP, TYP, TGA, Gamma	C (PC)	50% CO_2, 20°C, 53% RH (7, 14, 28 d)	Slicing	5
Villain et al. (2007)	PHP, TGA, Gamma	C (PC)	45% CO_2, 20°C, 53% RH (7, 14, 28 d)	Slicing	5-10
Herrera et al. (2015)	PHP, FTIR, PP	M (PC, PFA)	50% CO_2, 28°C, 61.7% RH (1-28 d)	Slicing	2
Phung et al. (2015)	PHP, TGA	P (PC, LS)	100% CO_2 at 6 bar, 21°C (28 d)	Drilling	3
Shi et al. (2016)	PHP, TGA	M (PC, LS, MK)	1% CO_2, 20°C, 57% RH (7 to -280d)	Slicing	1-2
Belda Revert et al. (2016)	PHP, TYP, TGA, OM,	M (PC, CEM II/B-V, LS, PFA)	1.5% CO_2, 20°C, 60% RH (4 weeks)	Slicing	1-2
Witkowski & Koniorczyk (2018)	PHP, FTIR	SCC (CEM II/B-M, PFA)	1% CO_2, 21°C, 60% RH (56, 112, 168d)	Drilling, scrapping	5
Duan et al. (2018)	PHP, TGA, FTIR	C (PC, PFA, LDHs)	20% CO_2, 20°C, 70% RH (56 d)	n/a	3
Drouet et al. (2019)	PHP, TGA, XRD	P (PC, CEM V/A, GGBS, PFA)	50% CO_2, 20 and 80°C, 26-76% RH (7 d)	Slicing	0.5-2
Bui et al. (2021)	PHP, TGA	M (PC, CSA)	4% CO_2, 20°C, 65% RH (12 weeks)	Grinding	2

* Information on temperature and relative humidity is unavailable for some studies

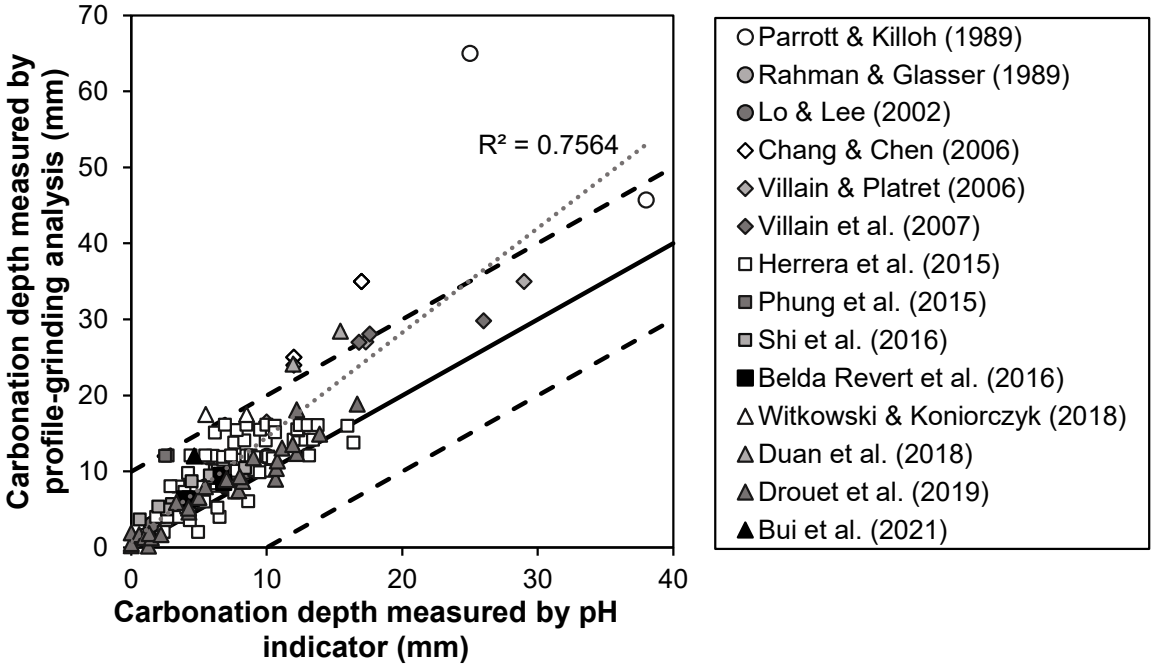


Figure 6.1 Carbonation depths measured using profile-grinding techniques (TGA, FTIR and XRD) vs. those measured using pH indicators from literature (Table 6.1). Solid and dashed lines mark 1:1 correspondence and ±10 mm boundaries respectively.

Raman spectroscopy (RS) is a powerful technique capable of providing chemical and structural information of organic and mineral phases. It is based on the detection of Raman scattering produced by the interaction between the incident laser and vibrating chemical bonds to provide fingerprint information of the chemical structure. Raman spectroscopy has been used to characterise various cements (Torréns-Martín et al., 2013), supplementary cementitious materials (Guedes et al., 2008; Yue et al., 2018), alkali-activated materials (Caggiani et al., 2021), corrosion (Larroumet et al., 2007; Criado et al., 2015) and carbonation products (Dubina et al., 2013; Mario et al., 2021). Combining Raman spectroscopy with confocal microscopy enables high-resolution chemical imaging of phase distribution. Confocal Raman micro-spectroscopy or microscopy (CRM) has been applied to image clinker remnants and aggregates in historic cement stone (Schmid & Dariz, 2013) and hydration of cement pastes (Higl et al., 2016; Mikhailova et al., 2019; Torres-Carrasco et al., 2019; Loh et al., 2021). Upon carbonation, CRM has also been used to map $CaCO_3$ polymorphs in lime paste (Ševčík et al., 2016), and naturally-weathered (Torres-Carrasco et al., 2017) and lab carbonated cement pastes (Corvisier et al., 2010; Mi et al., 2021). However, the reliability of CRM to determine carbonation depth is still not confirmed as the comparison with other well-characterised techniques (pH indicators and profile-grinding analysis techniques) has not been systematically studied. In addition, these literature works focused more on the hardened CEM I paste and the effect of other SCMs and aggregate still remains under-explored.

Following the measurement of early surface carbonation in Chapter 5, this study aims to investigate the feasibility of CRM for measuring the carbonation depth of cement-based materials using the optimised approach developed in Chapter 4. Neat CEM I and blended (CEM I + 30% fly ash, CEM I + 50% slag) cement pastes and mortars with water/binder ratios 0.45 and 0.60 exposed to accelerated (4% CO_2) and natural (440 ppm CO_2) carbonation for 1, 2 and 3 months were used for investigation. The carbonation depths measured with CRM were compared with those measured with phenolphthalein and profile-grinding analysis techniques including TGA, XRD, FTIR and RS. Porosity changes induced by carbonation were also evaluated using backscattered electron microscopy (BSE). A simple method was proposed to estimate the average carbonation depth from the profile-grinding analysis. Finally, CRM was applied to measure shallow carbonation depths (e.g. < 3 mm) induced by natural carbonation.

6.2 Experimental

6.2.1 Materials and sample preparation

The cementitious materials used in this study included CEM I 52.5 N, Class F Fly Ash (PFA), and ground granulated blastfurnace slag (GGBS). Their oxide compositions and physical properties are provided in Section 3.1. The mineralogical composition of CEM I was 62.4% C_3S, 10.3% C_2S, 10.6% C_3A, 2.2% C_4AF and 4.9% calcite as limestone filler, and the specific gravity was 3.06. For mortar samples, Thames Valley sand (< 5 mm) with specific gravity, 24-hour absorption, and moisture content of 2.54, 0.52%, 0.22% respectively was used. Tap water was used as batch water.

The mix proportions of pastes and mortars (Table 6.2) were calculated using the absolute volume method. Two water/binder ratios (w/b), i.e., 0.45 and 0.60 were used to investigate the effect of porosity on carbonation. The aggregate volume fraction for the mortar samples was set to 20% to allow faster Raman mapping of the carbonation front without the need to scan an excessively large area. The batch water was adjusted to account for aggregate absorption. Binders and aggregate were dry-mixed in a Hobart mixer for 3 min prior to the addition of water for further wet mixing of 3 min. Samples were compacted in two layers into steel moulds (50 × 50 × 50 mm) and then covered with plastic sheets and wet hessian to prevent water evaporation. After 24 h, the samples were demoulded and cured in a fog room at > 95% RH and 21 ºC for 3 days. For each mix, six replicates were prepared, half of them for natural carbonation and the other half for accelerated carbonation.

Table 6.2 Mix proportions.

Mix ID	Free w/b	Water (kg/m^3)	Binder (kg/m^3)			Sand (kg/m^3)
			CEM	PFA	GGBS	
P-0.45-PC	0.45	583	1294	-	-	0
P-0.6-PC	0.60	650	1084	-	-	0
M-0.45-PC	0.45	469	1036	-	-	517
M-0.6-PC	0.60	524	867	-	-	517
P-0.45-V	0.45	583	906	388	-	0
P-0.6-V	0.60	650	759	325	-	0
M-0.45-V	0.45	469	725	311	-	517
M-0.6-V	0.60	524	607	260	-	517
P-0.45-S	0.45	583	647	-	647	0
P-0.6-S	0.60	650	542	-	542	0
M-0.45-S	0.45	469	518	-	518	517
M-0.6-S	0.60	524	434	-	434	517

6.2.2 Conditioning and carbonation

After curing, the samples were conditioned in a climate chamber at 65% RH, 21°C until mass equilibrium (< 0.02%/day). The chamber contained saturated sodium nitrite to maintain the RH, soda lime to keep the CO_2 level at < 10 ppm and a motorised fan to circulate air. All except one cast surface were then sealed with two layers of water-proof tape to ensure unidirectional carbonation. Subsequently, half of the samples were transferred to an incubator with 4% CO_2 for accelerated carbonation and the other half to an incubator with 440 ppm CO_2 for natural carbonation (Section 3.2). The RH and temperature were maintained at 65% and 21°C respectively to achieve an optimum carbonation rate (Thiery et al., 2007).

Fig. 6.2 shows an overview of the experimental procedure. After 1, 2 and 3 months of carbonation, the samples were removed from the incubator and diamond-sectioned to produce two adjacent blocks of 6 × 21 × 50 mm^3 (Fig. 6.2a-b). Block A was surface-dried and then analysed directly under CRM (Section 6.2.3), followed by phenolphthalein spray test (Section 6.2.4). A smaller block of 6 × 10 × 15 to 21 mm^3 was then extracted for profile-grinding analysis (Section 6.2.5) (Fig. 6.2c-d). Block B was further dried at 33% RH, 21°C for 2 weeks, and then epoxy impregnated and finally surface polished following the procedure described in section 3.4.1 (Fig. 6.2e) for BSE imaging (Section 6.2.6).

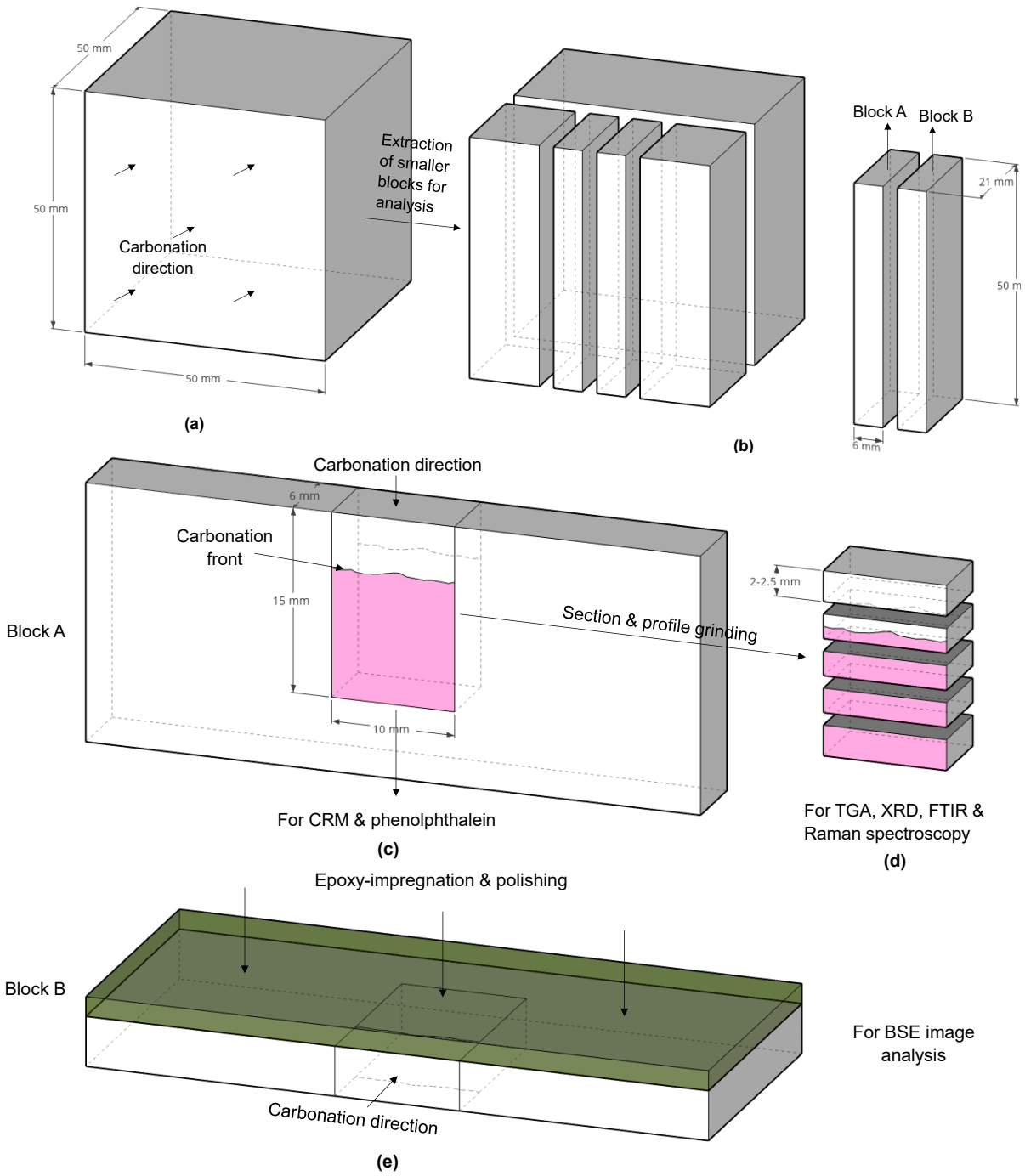


Figure 6.2 Overview of the experimental procedure. Extraction of two adjacent blocks (Blocks A and B) of 6 × 21 × 50 mm^3 from the main sample (a-b) for CRM and phenolphthalein spray test (c), profile-grinding analysis (d), and BSE image analysis (e) respectively.

6.2.3 Confocal Raman microscopy

The set-up of the confocal Raman microscope was specified in Section 3.3. Measurements were made using 532 nm laser, 2400 lines/mm grating, 50× long-working distance objective (NA = 0.5) and 1024

× 256 pixels charge-coupled device (CCD) array detector under ambient conditions (21ºC, 45% RH). Soda lime was placed in the microscope chamber to absorb atmospheric CO_2 to minimise additional carbonation during measurement. Raman shift calibration was carried out prior to each measurement using an internal silicon standard with a Raman shift of 520.2 ± 0.5 cm^{-1}. Based on the optimisation study performed in Chapter 4, the laser power at the sample surface and the exposure time were set to 4.15 mW and 0.5 s respectively to achieve a good balance between mapping time and signal-to-noise ratio. The spectral range was set to 143 to 1385 cm^{-1} to cover the main peaks of $CaCO_3$ polymorphs (1085 cm^{-1} for ν1 symmetric C-O stretching in calcite and aragonite, and a doublet of 1080 and 1090 cm^{-1} for the same vibration mode in vaterite) and $Ca(OH)_2$ (356 cm^{-1} for lattice vibration in portlandite).

A quick scan with a coarse step size of 1 mm was performed over a large area of 10 × 15 mm (width x depth) from the exposed surface to roughly determine the position of the carbonation front. This was followed by more precise imaging of the carbonation front using a finer step size of 25 μm over a smaller area of 10 × 15 mm in the StreamHR™ scan mode (Renishaw, 2022). A total of 241000 points were analysed for each map and this took approximately 1 d to complete. However, in other applications where such high resolution is not required, the testing duration can be significantly reduced, for example, to approximately 2 hours when using a coarser step size of 0.1 mm.

The Renishaw WiRE v.5.2 software was used for data acquisition. Spectral artefacts including cosmic rays and background were removed using the nearest neighbour method and least squares polynomial fit respectively. Raman maps of $CaCO_3$ polymorphs and $Ca(OH)_2$ were produced based on the intensity of their respective main peaks, i.e. 1085 + 1090 cm^{-1} and 356 cm^{-1}. The depth at which the peak intensities changed sharply on the Raman maps was taken as the carbonation front (Section 6.3.1). The carbonation depth was determined by precisely measuring the distance from the exposure surface to the carbonation front on the Raman map of $CaCO_3$ using Fiji (v.1.8.0). For each sample, both the front and rear surfaces were analysed to estimate the carbonation depth of the whole block for a fair comparison with the profile-grinding analysis. In total, 42 measurements were taken at an interval of 0.5 mm along the carbonation length and the results averaged.

6.2.4 Phenolphthalein spray method

After Raman mapping, both the front and rear surfaces of the sample were moistened with tap water and then sprayed with 1 wt.% phenolphthalein solution, prepared by mixing 1 g of phenolphthalein in a mixture of 30 ml deionised water and 70 ml ethyl alcohol. Once the colouration had stabilised, the surfaces were imaged with a stereomicroscope (Olympus SZX10) at a magnification of 0.63×. Similar to the CRM method, the carbonation depths were determined via image analysis using Fiji (v.1.8.0).

6.2.5 Profile-grinding analysis

Samples were sliced into layers at an interval of approximately 3 mm using a high precision cutter (Buehler IsoMet 1000) at a low speed of 100 rpm to ensure a good quality cut (Fig. 6.2d). The thickness of the sliced layers was 2-2.5 mm due to material loss caused by cutting, which is the thinnest slice that is practically feasible with this cutter to achieve consistent thickness without damaging. This interval was also corresponding to the average value used in the literature (Table 6.1). The slices were dried in a conditioning box (21°C, 33% RH) for 7 d in the presence of soda lime and then ground into powder in sealed plastic bags to minimise additional ambient carbonation during grinding. Prepared powders were then quickly sieved through a 0.3-mm mesh sieve, sealed again in plastic bags and stored in the conditioning box until testing. Only samples exposed to accelerated carbonation were analysed, because those exposed to natural carbonation mostly had very limited carbonation depths (< 3 mm), which were smaller than the interval used for profile-grinding.

TGA was performed using a Netzsch STA 449 F5 thermal analyser. Approximately 25 mg of powder was heated from 30 to 1050°C at a heating rate of 20°C/min in an alumina crucible under a continuous N_2 flow at 50 ml/min. The amount in moles (mol) of $Ca(OH)_2$ and $CaCO_3$ present were quantified by measuring the weight losses between 400 and 550°C, and 550 and 950°C, and multiplying the results by the molar mass of H_2O (18 g/mol), and CO_2 (44 g/mol) respectively.

FTIR analysis was performed using a Thermo Scientific Nicolet iS50 FTIR spectrometer equipped with an attenuated total reflectance (ATR) module. The wavelength range was set to 400 to 4000 cm^{-1} with a spectral resolution of 0.5 cm^{-1}. Approximately 1.2 mg of powder was used for analysis and 10 measurements were performed to obtain an average spectrum. The spectra collected were background corrected and the peak intensities at 858 and 877 cm^{-1} (ν2 asymmetric C-O bending), and 3640 cm^{-1} (ν1 symmetric O-H stretching) were used to evaluate the evolution of $CaCO_3$ polymorphs and $Ca(OH)_2$ (Diego Rodriguez-Blanco et al., 2011; Horgnies et al., 2013; Xu & Poduska, 2014).

XRD analysis was performed using a Malvern Panalytical Empyrean diffractometer equipped with a Cu X-ray source and a PIXcel3D detector. The powdered sample was backloaded into a sample holder of 8 mm diameter, mounted onto a spinning stage, and scanned using the Cu-Kα radiation (45 kV and 40 mA) with a fixed incident divergence slit size of 0.25º over a 2θ range of 5 to 80°. The step size was set to 0.013°. The peak intensities at 18.1°, 26.2°, 27.1° and 29.5° 2θ were used to evaluate $Ca(OH)_2$, aragonite, vaterite and calcite respectively (Hu et al., 2012; Esquivias et al., 2018).

Raman spectroscopic analysis was also performed on the ground powder. For ease of comparison with Raman mapping, the CRM with the same settings described in Section 6.2.3 was used. A small amount of powder was heaped on a glass slide and then flattened with a coverslip for analysis. Ten

random spots were analysed to obtain an average spectrum for each sample. The Raman peak intensities at 356, and 1085 + 1090 cm^{-1} were used to evaluate $Ca(OH)_2$ and all $CaCO_3$ polymorphs.

6.2.6 Backscattered electron microscopy

A Hitachi TM4000 Plus benchtop SEM equipped with an Oxford Instruments Aztec Advanced X-Act Compact energy dispersive X-ray detector (SEM-EDS) was used to observe carbonation-induced porosity changes in the epoxy-impregnated and surface-polished block (Section 6.2.2). The microscope was operated at 15 kV in the BSE mode and the working distance was set to 7 mm to achieve an optimal spatial resolution (Yio et al., 2016). Two hundred forty images (6 × 40 along the carbonation length and depth at intervals of 2 and 0.38 mm respectively) were captured per sample to observe the porosity changes along the carbonation depth. The magnification was set to 500× and the images were digitised to 1280 × 960 pixels with a spacing of 0.2 μm. Porosity was extracted from the images using the Overflow method (Wong et al., 2006).

6.3 Results

6.3.1 CRM vs. phenolphthalein spray method

Fig. 6.3 presents example Raman maps of $CaCO_3$ polymorphs and $Ca(OH)_2$, and corresponding phenolphthalein spray results for the neat CEM I systems (P-0.45-PC and M-0.45-PC) exposed to accelerated carbonation for 2 months. The pixel brightness of the Raman maps indicates the amount of $CaCO_3$ polymorphs and $Ca(OH)_2$ in the sample (Giridhar et al., 2017). Other phases including air void and aggregate particles appear dark but can be visually distinguished based on their defined shapes and boundaries. The aggregate particles, confirmed to be quartz from their Raman peak at 465 cm^{-1} (ν1 symmetric stretching) (Yadav & Singh, 2015), appear bright in the portlandite map due to the fact that the low-frequency distortion Raman peak of quartz (356 cm^{-1}) overlaps the lattice vibration peak (356 cm^{-1}) of portlandite (Lippincott et al., 1958; Loh et al., 2021).

It is evident from the Raman maps that there were two distinct zones in both the paste and mortar samples: a carbonated zone with a high content of $CaCO_3$ and an uncarbonated zone with a high content of $Ca(OH)_2$. The carbonation fronts appear distinct, as reflected by the sharp changes in the intensities of the $CaCO_3$ and $Ca(OH)_2$ maps. Importantly, the carbonation profiles appear to be in excellent agreement with those indicated by the colour change of phenolphthalein (Fig. 6.3c & g). The spatial distributions of $CaCO_3$ polymorphs and $Ca(OH)_2$ appear homogeneous in their respective regions and complement each other along the depth, thus confirming the consumption of portlandite during carbonation.

The pixel intensities of the Raman maps of all $CaCO_3$ polymorphs and $Ca(OH)_2$ were averaged across the image width and normalised to their respective lowest pixel values to produce one-dimensional carbonation profiles along the depth. The profiles can be divided into three zones: fully carbonated zone, transition zone or the so-called partially carbonated zone, and non-carbonated zone. The extent of the transition zone varies depending on the variation of the carbonation front, as indicated by the horizontal cyan lines drawn across the figure. The width of the transition zone was 1.4-4.1 mm for all CEM I samples exposed to 1-3 months accelerated carbonation (4% CO_2). The start of the transition zone marks the minimum carbonation depth, while the end marks the maximum carbonation depth.

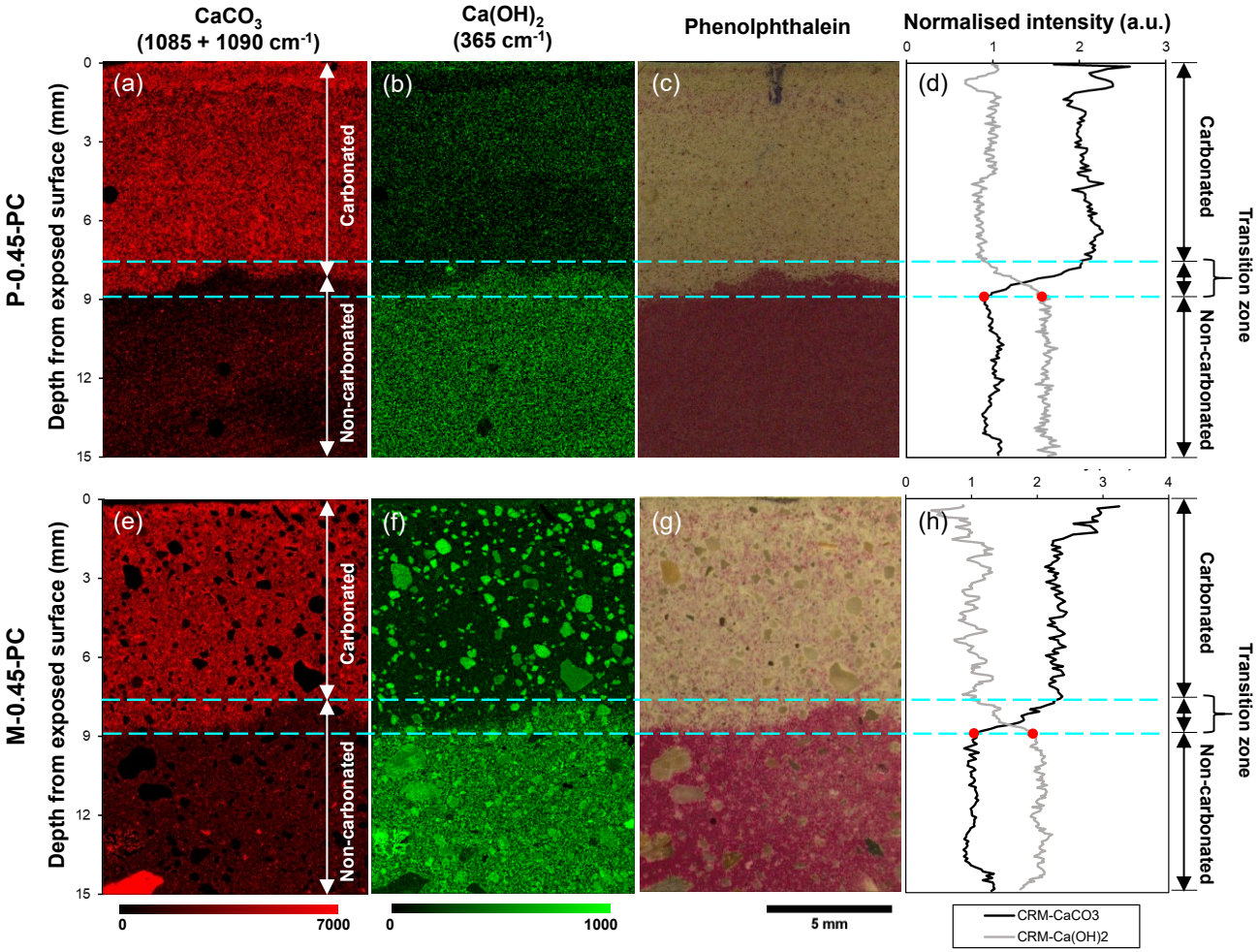


Figure 6.3 Raman maps of $CaCO_3$ polymorphs (1085 + 1090 cm^{-1}) (a, e) and $Ca(OH)_2$ (356 cm^{-1}) (b, f), and corresponding phenolphthalein spray results (c, g) and carbonation profiles (d, h) for P-0.45-PC and M-0.45-PC exposed to accelerated carbonation (4% CO_2) for 2 months. The horizontal cyan lines mark the width of the carbonation fronts.

Fig. 6.4 compares the average carbonation depths measured with Raman maps of $CaCO_3$ and with phenolphthalein for all CEM I samples exposed to 1-3 months accelerated carbonation. In general, the carbonation depths were consistently larger for w/b 0.6 due to higher porosity in the samples

facilitating the ingress of CO_2. When comparing the carbonation depths determined by the two techniques, a very good correlation with an average difference of 1.2% was observed. This confirms that the two techniques provide identical carbonation depths, despite the fact they measure different aspects of carbonation.

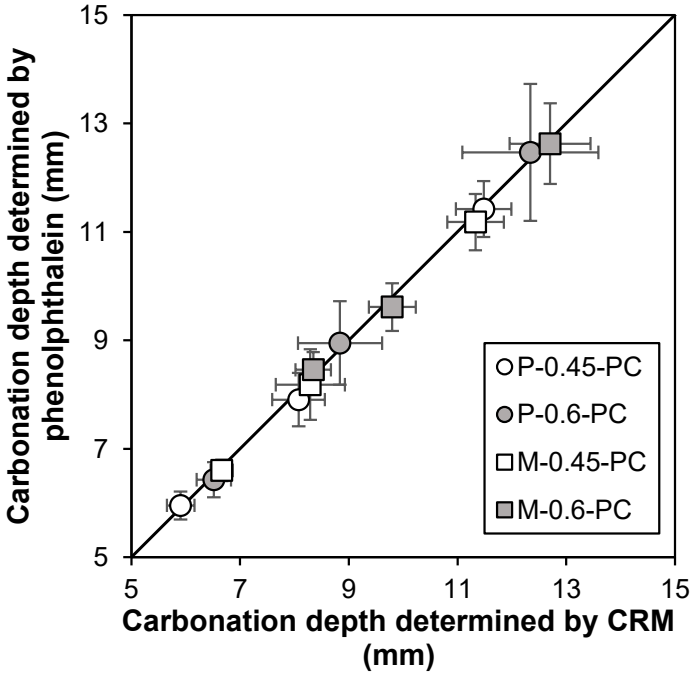


Figure 6.4 Comparison of the average carbonation depths measured with phenolphthalein and with Raman maps of $CaCO_3$ for all CEM I samples exposed to 1-3 months accelerated carbonation (4% CO_2). Error bars represent standard deviation. The solid line represents 1:1 correspondence.

6.3.2 CRM vs. profile-grinding analysis

Fig. 6.5 a-d present examples of differential thermogravimetry (DTG) curves, as well as XRD, FTIR and RS spectra of ground powders sampled at increasing depths from P-0.45-PC exposed to accelerated carbonation for 2 months. For all techniques, the peak intensity indicates the content of the phase present. In all cases, the peak intensities for $Ca(OH)_2$ remained insignificant between 0 and 5.5 mm depth but then increased and gradually stabilised between 6.5 mm and 15 mm depth. An opposite trend was observed for $CaCO_3$, suggesting that carbonation had occurred up to a depth of approximately 8.5 mm. Beyond this depth, a tiny amount of $CaCO_3$ from unreacted cement remained detectable, indicating the presence of limestone filler in the cement. As evident from the XRD and Raman spectra (from both RS and CRM), the main $CaCO_3$ polymorph formed was calcite. However, traces of aragonite and vaterite were also detected, suggesting that a small amount of C-S-H had carbonated under accelerated conditions (Morandeau et al., 2014). It is also clear from the spectra that

ettringite peak almost vanished near the exposed surface and appeared beyond 6.5 mm. Indeed, such phase can carbonate and form aragonite, gibbsite and gypsum (Auroy et al., 2018), however, the Raman peaks for the latter two were not distinct in the spectra.

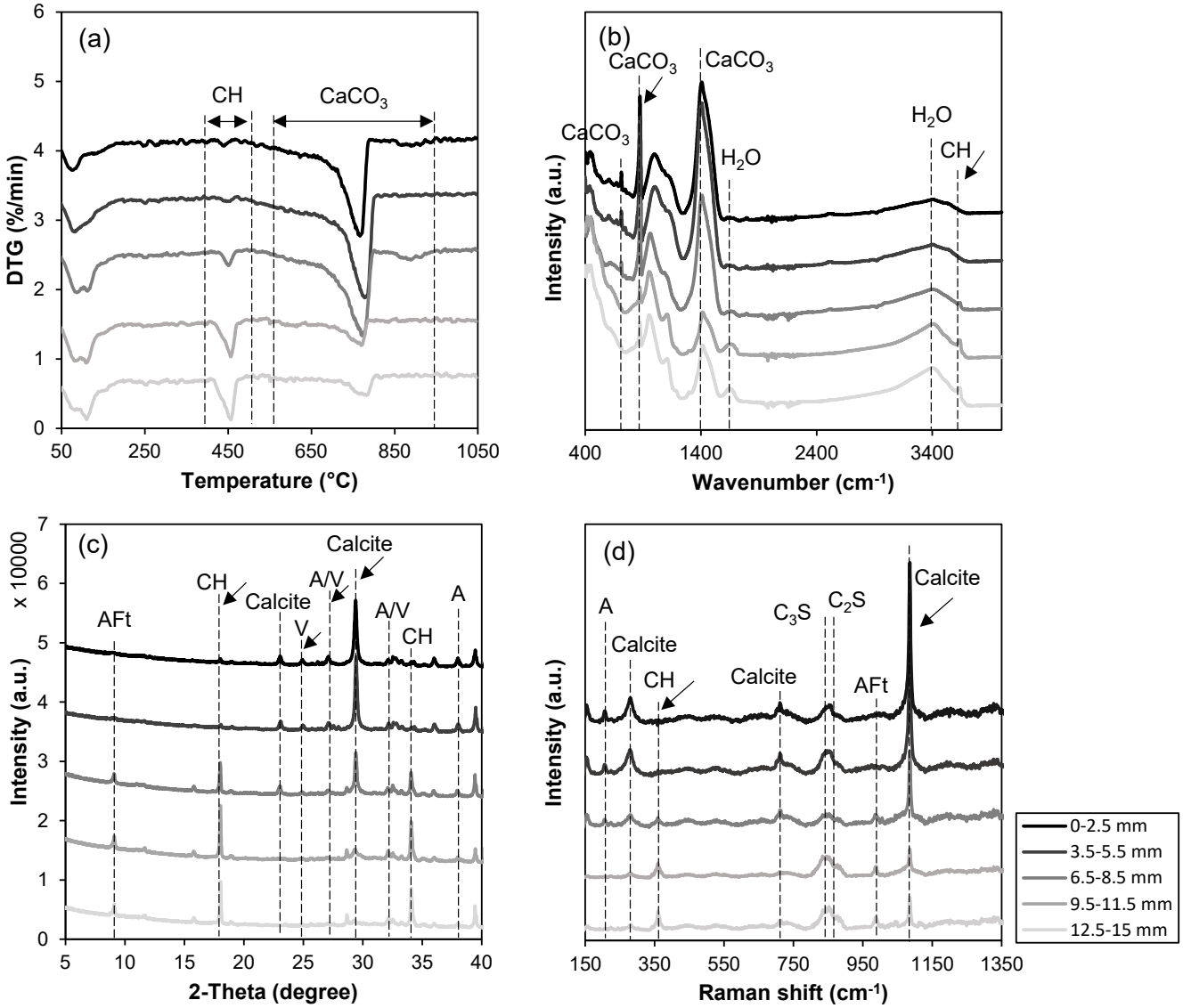


Figure 6.5 Example TGA-DTG curves (a), as well as FTIR (b), XRD (c) and RS (d) spectra of ground powders sampled at increasing depths from P-0.45-PC exposed to accelerated carbonation (4% CO_2) for 2 months. CH: portlandite, AFt: ettringite, A: aragonite, V: vaterite.

The amount of $CaCO_3$ and $Ca(OH)_2$ measured with TGA and their corresponding peak intensities from XRD, FTIR and RS (arrowed in Fig. 6.5) were plotted against the depth to observe their profile evolution (Fig. 6.6). All results were normalised to their corresponding smallest values for ease of comparison. Overall, the results show that the profiles obtained using different techniques agreed well for CEM I samples exposed to accelerated carbonation (4% CO_2).

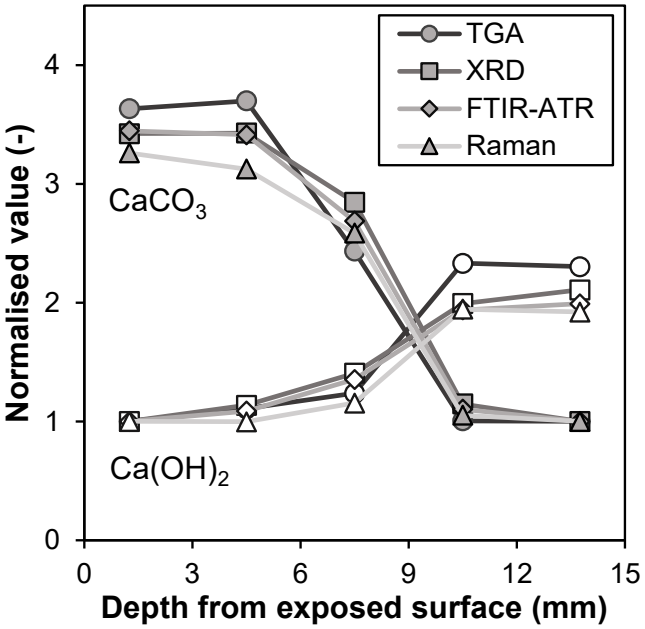


Figure 6.6 Carbonation profiles of $CaCO_3$ and $Ca(OH)_2$ produced by profile-grinding analysis with different techniques for P-0.45-PC exposed to accelerated carbonation (4% CO_2) for 2 months.

Fig. 6.7 plots the profiles of $CaCO_3$ and $Ca(OH)_2$ averaged from TGA, XRD, FTIR and RS analysis of ground powder together with the profiles from CRM and BSE image analysis for all CEM I samples exposed to 1-3 months accelerated carbonation (4% CO_2). In general, the carbonation depths determined by CRM image analysis (indicated by vertical red lines) were on average 3.4 mm smaller than the carbonation depths from profile-grinding analysis (indicated by black arrows, interval size 3 mm). This is because the carbonation depth measured from the profile-grinding analysis is only the 'apparent' maximum carbonation depth, intrinsically larger than the average carbonation depth determined by CRM image analysis. When comparing only the carbonation profiles, the evolution of porosity was in line with the trends of $Ca(OH)_2$ but opposite to the trends of $CaCO_3$ (both from CRM), confirming that pore densification had occurred in the CEM I system as a result of the formation of $CaCO_3$ in the carbonated zone (Arandigoyen et al., 2006). In all cases, a transition zone between fully carbonated and non-carbonated regions exists. However, due to the finer sampling intervals of CRM and BSE, the maximum carbonation depths measured with these techniques (marked by red arrows) were on average 2.2 mm (16.6%) smaller than those 'apparent' ones measured by profile-grinding. The coarser step size of profile-grinding analysis allowed only limited data points (5 to 7 compared to 600 in CRM) to be sampled along the carbonation depth and this significantly reduced the sensitivity of this method to detect the carbonation front accurately.

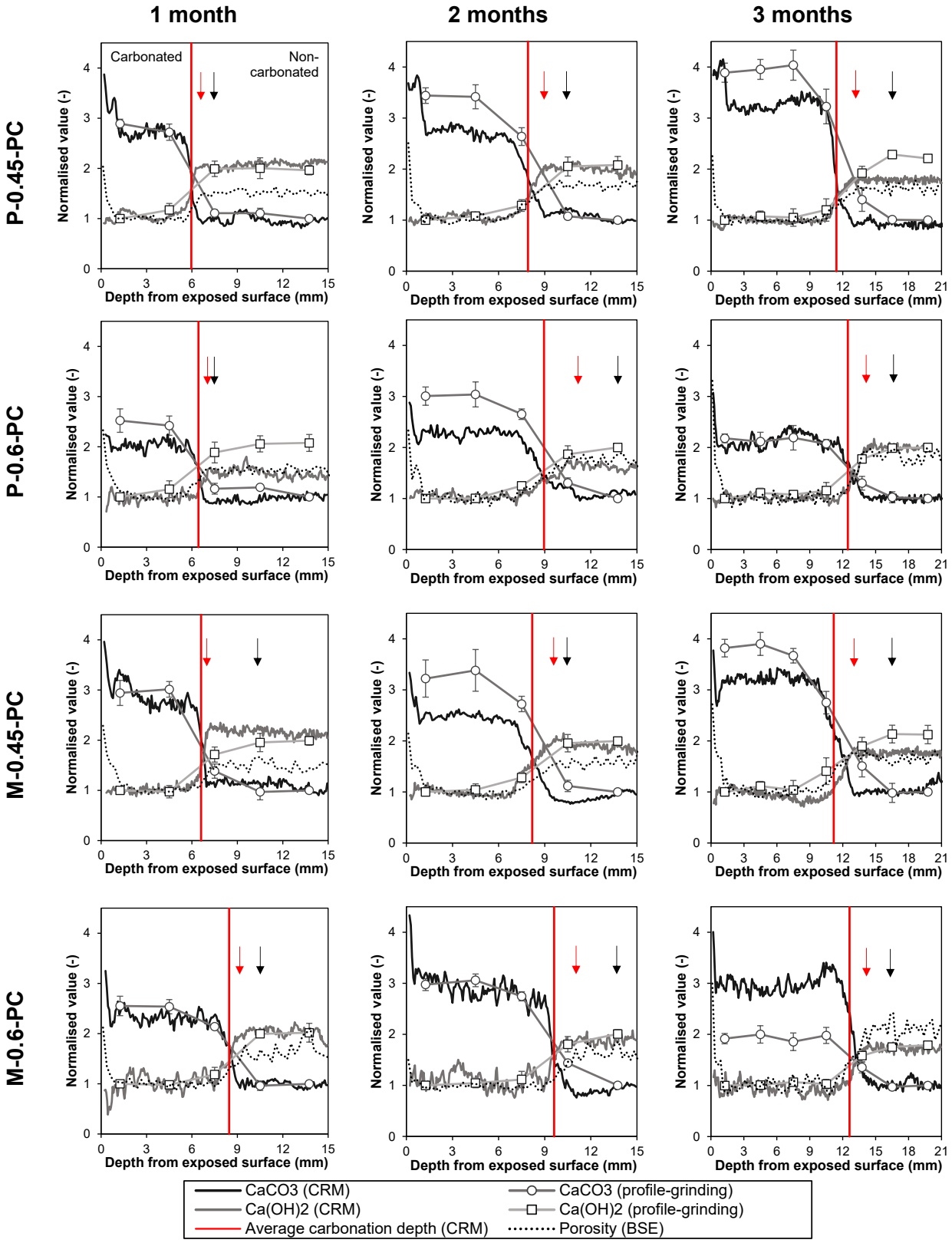


Figure 6.7 Profiles of $CaCO_3$, $Ca(OH)_2$ and porosity measured by CRM, profile-grinding analysis, and BSE for all CEM I samples after 1-3 months accelerated carbonation (4% CO_2). Vertical red lines represent the carbonation depth measured by CRM image analysis. Red and black arrows represent the carbonation depth measured from carbonation profile obtained with CRM and profile-grinding analysis respectively.

6.3.3 Spatial variation of carbonation front and sampling interval

The 'apparent' maximum carbonation depths determined using the profile-grinding techniques are highly dependent on the spatial variation of the carbonation front. Fig. 6.8 illustrates three scenarios where the 'apparent' maximum carbonation depth measured by profile-grinding (marked by white arrow) increases with the spatial variation or the heterogeneity of carbonation front and sampling position. The white dotted lines represent the $CaCO_3$ profiles measured by profile-grinding techniques, superimposed on the corresponding CRM maps of $CaCO_3$ divided into five equal-distanced sampling layers. In the first scenario (Fig. 6.8a), the carbonation front appears relatively homogenous across the image width and coincides with the edge of the 2nd sampling layer for profile grinding. However, the 'apparent' maximum carbonation depth is overestimated due to the fact that the profile plateaus only in the 3rd layer. In the second scenario (Fig. 6.8b), the carbonation front remains relatively constant but falls within the 3rd layer. This leads to a further overestimation of the 'apparent' maximum carbonation depth as the profile plateaus in the 4th layer. In the third scenario (Fig. 6.8c), the carbonation front spans from the 3rd to 4th layers and this exacerbates the overestimation even further, with the profile plateauing in the 5th layer.

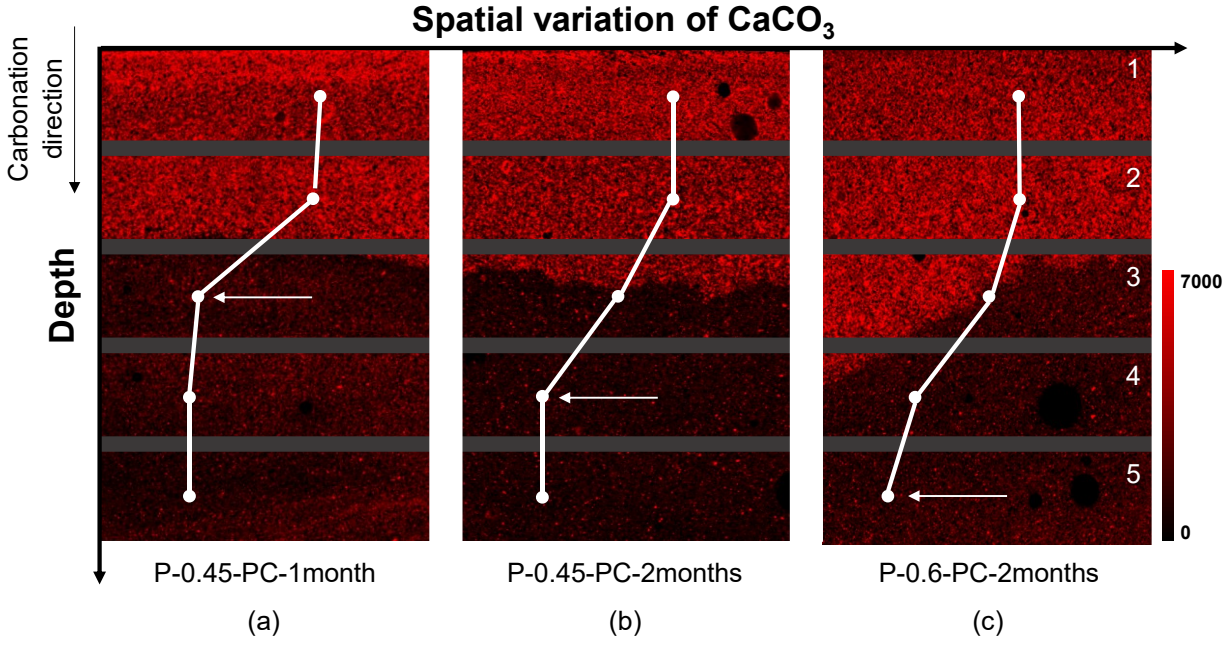


Figure 6.8 Illustration of three scenarios where 'apparent' maximum carbonation depth measured by profile-grinding increases with the variation of carbonation front and sampling position. White dotted lines represent profiles measured by profile-grinding, superimposed on CRM maps of $CaCO_3$ divided into five equal-distanced sampling layers. The right-hand side for each dotted line represents high $CaCO_3$ concentration.

Fig. 6.9 plots the overestimation of the 'apparent' maximum carbonation depths measured by profile-grinding analysis against the spatial variation of the carbonation front. The extent of spatial variation was specified by the width of the transition zone (Fig. 6.9a) and the standard deviation of the carbonation depths measured at 42 equally distanced locations (interval 0.5 mm) along the carbonation length by CRM image analysis (Fig. 6.9b). The results show that profile-grinding analysis overestimated the 'apparent' maximum carbonation depth in all cases and the overestimation increased with the extent of spatial variation of the carbonation front. The largest overestimation was approximately 3.8 mm, which is deemed significant considering that the measured maximum carbonation depth was only 12.8 mm.

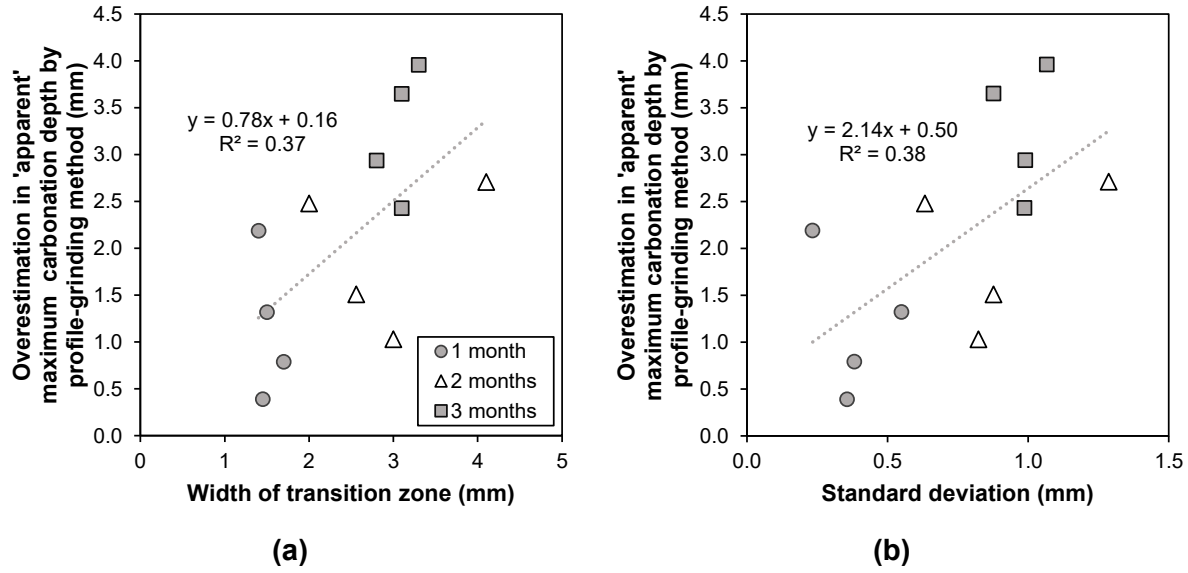


Figure 6.9 Effect of spatial variation of carbonation front indicated by the width of the transition zone (a) and standard deviation of the carbonation depths (b) on overestimation of 'apparent' maximum carbonation depths measured by profile-grinding for all CEM I samples exposed to 1-3 months accelerated carbonation (4% CO_2).

Another important factor that influences the results of profile-grinding analysis is the sampling interval. It would be expected that the smaller the sampling interval, the closer the estimated 'apparent' maximum carbonation depth would be to the actual value. The data from the Raman map of $CaCO_3$ of the neat CEM I pastes and mortars were resampled with successively larger sampling intervals (0.025 to 3.75 mm) to investigate the effect of sampling interval on the estimation of the 'apparent' maximum carbonation depth. Fig. 6.10 illustrates the results from M-0.6-PC after 1 month accelerated carbonation. As expected, the 'apparent' maximum carbonation depth (indicated by red dots) increases with the sampling interval and the deviation from the actual maximum carbonation depth becomes pronounced when the sampling interval is > 0.5 mm. When resampling with a 3 mm step size, the obtained apparent profile is comparable to those from the profile-grinding analysis.

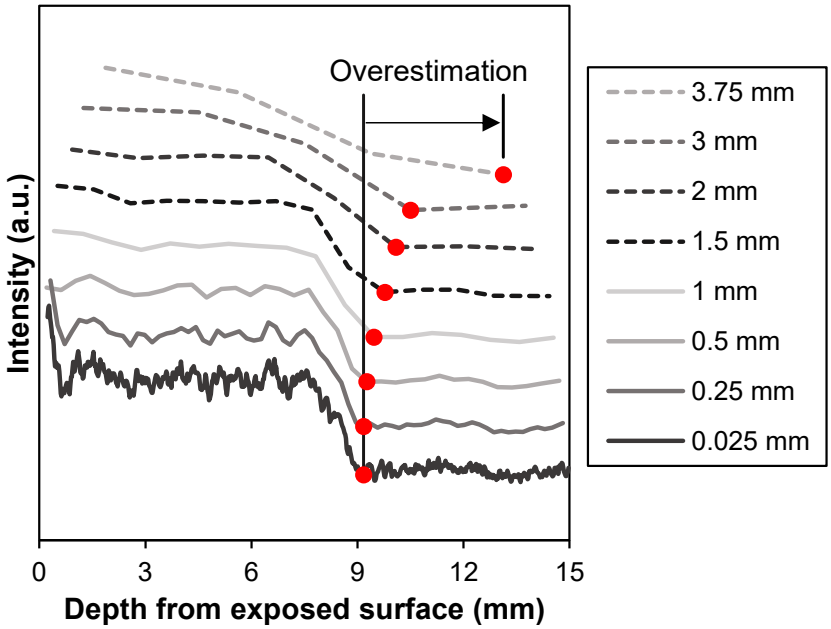


Figure 6.10 Evolution of $CaCO_3$ profiles with successively larger step size resampled from the Raman map of $CaCO_3$ for M-0.6-PC exposed to accelerated carbonation (4% CO_2) for 1 month. Red dots mark the 'apparent' maximum carbonation depths.

Fig. 6.11a plots the overestimation of the 'apparent' maximum carbonation depth obtained following the approach shown in Fig. 6.10 for all CEM I systems and carbonation durations as a function of increasing sampling interval. The overestimation is negligible for sampling interval ≤ 0.5 mm but increases exponentially with increase in sampling interval to an average 2.1 mm (21%) at a step size of 3 mm. As the sampling interval reaches 3.75 mm, the overestimations increase by 48.1% for P-0.45-PC to 64.2% for M-0.6-PC. A similar trend can be observed with the data extracted from literature findings (Fig. 6.11b). Here the y-axis represents the difference of carbonation depth measured by pH indicator and profile-grinding analysis, these results have suggested that a smaller step size (preferably < 0.5 mm) would provide a more accurate estimation of the actual maximum carbonation depth.

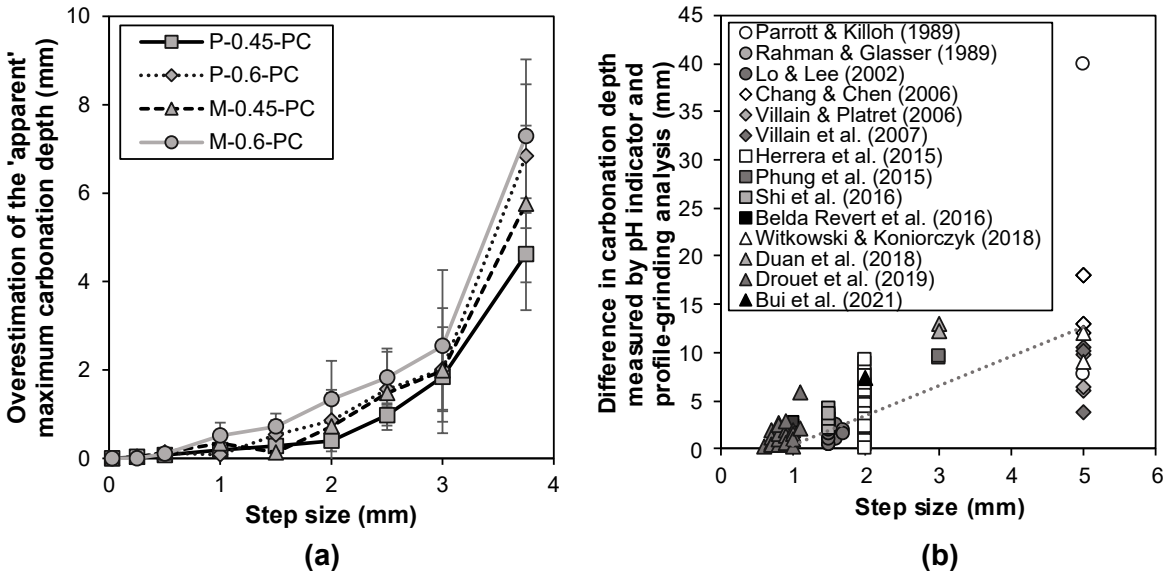


Figure 6.11 Effect of sampling interval on overestimation of 'apparent' maximum carbonation depth obtained following the approach shown in Figure 6.10 for all CEM I systems exposed to 1-3 months accelerated carbonation (4% CO_2) (a), and data extracted from the literature showing a similar trend (b).

6.3.4 Estimating average carbonation depth from profile analysis

The maximum carbonation depth may not be representative of the overall carbonation extent as it may occur only in a very localised area. A simple method to estimate the average carbonation depth from the carbonation profile is therefore proposed. Fig. 6.12a shows a random carbonation front with the carbonation depth of d_1, $d_2 \cdots d_n$ at different locations. The area of the carbonated zone (shaded) equals the sum of the depths when the interval is sufficiently small. The average carbonation depth (Fig. 6.12b), calculated by dividing the area with the number of locations, splits the original carbonation front into two parts with equal area (A_3, A_4). When assuming a homogeneous distribution of $CaCO_3$, with a concentration in the carbonated and non-carbonated zone of C_c and C_{nc} respectively, the $CaCO_3$ profile can then be plotted (Fig. 6.12c). The profile curve appears the same trend as the carbonation front and thus, by locating the depth at which the carbonation front is split into two equal areas, the average carbonation depth can be determined.

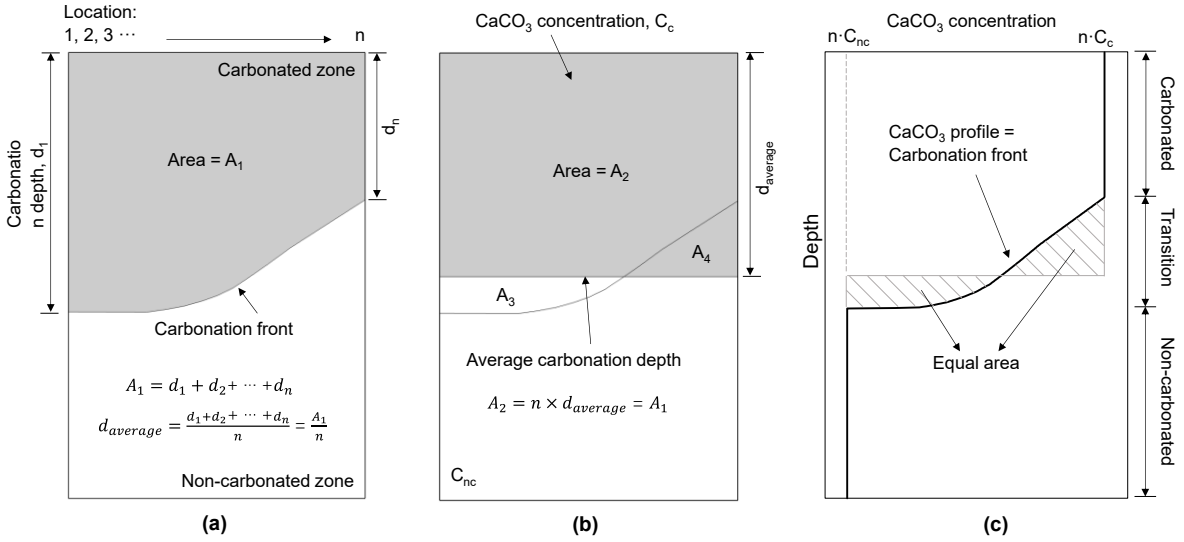


Figure 6.12 Proposed method to estimate average carbonation depth from profile analysis. The depth at which the carbonation front is split into two equal areas is taken as the average carbonation depth.

Fig. 6.13a demonstrates the application of the proposed method to determine the average carbonation depth of M-0.45-PC (3-month accelerated carbonation) from its $CaCO_3$ profile derived from the CRM map. The carbonation profile was smoothed by the moving average method (Schulze et al., 2012), and special care was made to avoid significant distortion of original features, especially the width of the transition region. This is followed by a simple regression to fit the transition zone, and since the main purpose is to obtain a best fit simplified plot for ease of calculation, this step is not exclusive to a certain type of regression, for example, linear regression as is exampled. The regression fit was then used in conjunction with the profile intensities at the start and end of the transition zone to determine the depth at which the zone is divided into two equal areas. This depth was taken as the average carbonation depth.

The proposed method was applied to estimate the average carbonation depths from the profiles of $CaCO_3$ obtained using CRM and profile-grinding analysis for all accelerated carbonated samples. Fig. 6.13b shows that the estimations were in excellent agreement with the average carbonation depths determined by CRM image analysis, with the average difference being only 0.1 mm for those estimated from CRM profiles, and 0.7 mm for those estimated from profile-grinding analysis. Overall, the results show that the proposed method is reliable for estimating the average carbonation depth from $CaCO_3$ profiles obtained either using CRM or profile-grinding analysis.

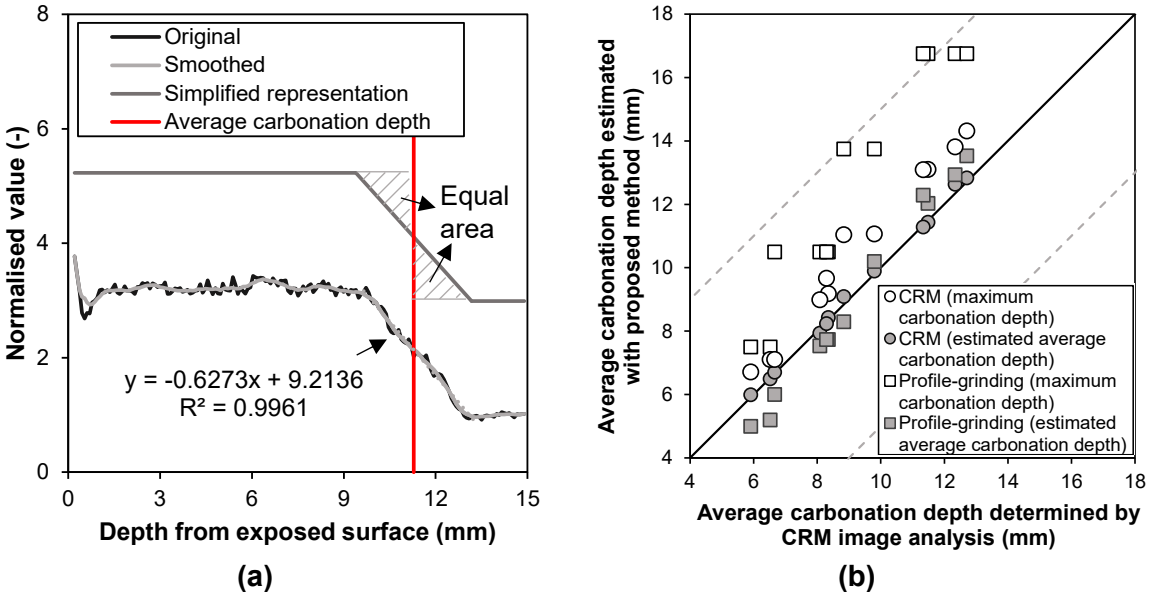


Figure 6.13 Determining the average carbonation depth of M-0.45-PC (3-month accelerated carbonation) from its $CaCO_3$ profile derived from CRM map (a), and average carbonation depths estimated with the proposed method vs. those measured by CRM image analysis for all accelerated carbonated samples (b). The solid and dashed lines represent 1:1 correspondence and ±5 mm boundaries respectively.

6.3.5 Application of CRM to measure short-term natural carbonation depth

Fig. 6.14 demonstrates the application of CRM to map the spatial distributions of $CaCO_3$ in w/b 0.45 pastes after short-term (1 - 3 months) natural carbonation. All samples exhibited a sharp and uniform carbonation front which advanced further into the samples with carbonation time. However, none of the exhibited carbonation fronts exceeded 3 mm from the exposed surface even after 3 months of carbonation. The smallest average carbonation depth observed was 0.71 mm in P-0.45-PC carbonated for 1 month. Such shallow carbonation depths would be impossible to measure accurately with profile-grinding techniques due to the limited sampling resolution.

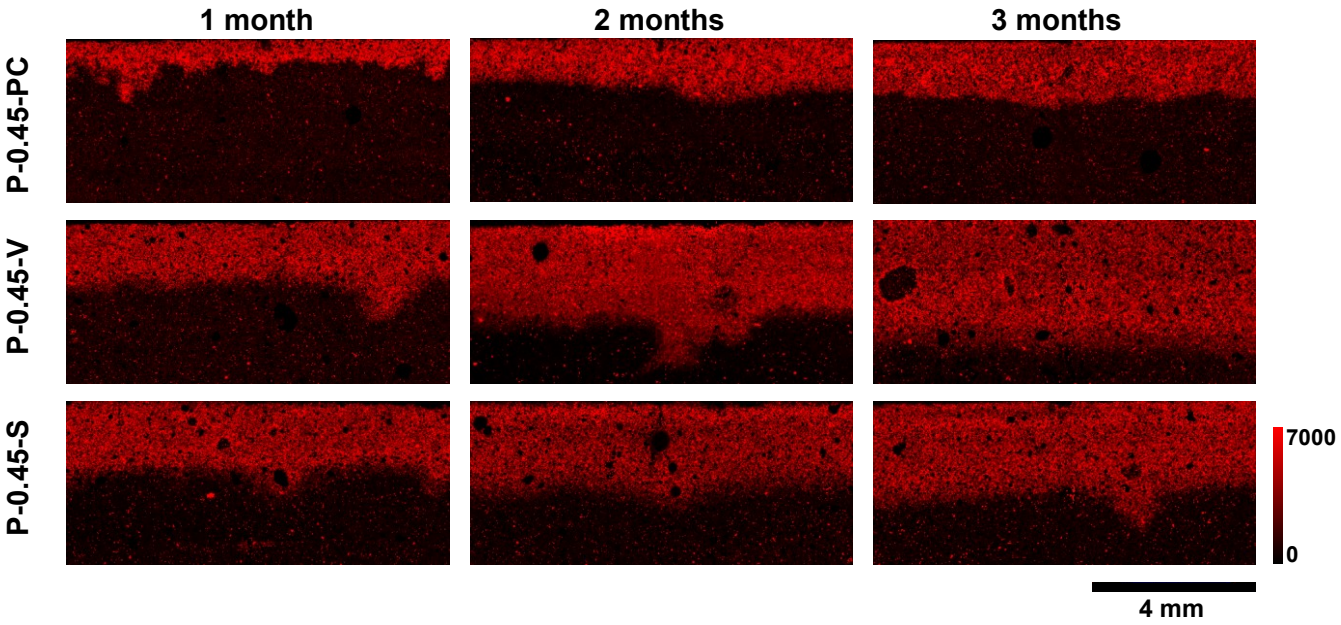


Figure 6.14 Example CRM-$CaCO_3$ images for w/b 0.45 paste containing different binder types after 1-3 months natural carbonation.

Fig. 6.15 summarises the average carbonation depths measured by CRM image analysis of all samples exposed to short-term natural carbonation. The average carbonation depths increased with the carbonation duration but were no more than 4 mm after 3 months of carbonation. As expected, the blended cement systems showed consistently higher carbonation depths than the neat CEM I systems. This was due to the lower portlandite content in the blended systems, which in turn reduced the pH buffer capacity against carbonation. Irrespective of the binders, the carbonation depths increased with w/b due to the higher capillary porosity in the systems which in turn facilitated the ingress of CO_2. The presence of aggregate particles, on the other hand, reduced the carbonation depth slightly due to increased tortuosity of the pore structure (Buenfeld & Okundi, 1998). Even though more porous 'interfacial transition zone' was introduced, the net effect on gas transport properties was found to be limited (Wong et al., 2009), so that the diluting effect of aggregate tends to predominate over the ITZ conductivity.

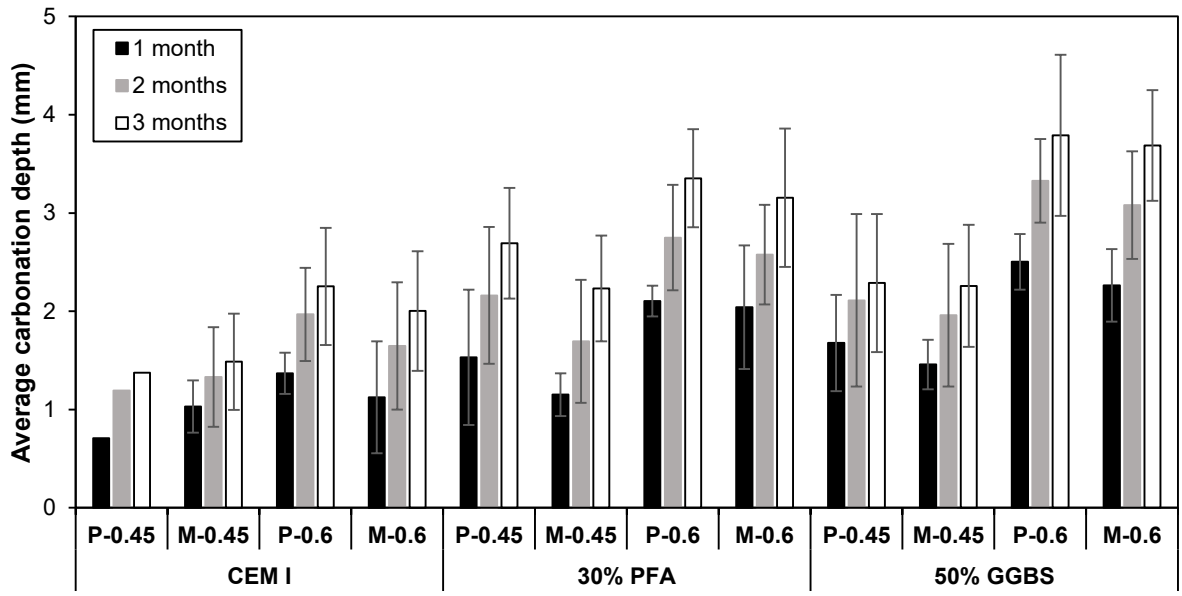


Figure 6.15 Average carbonation depths measured by CRM image analysis for all samples exposed to natural carbonation. Error bars represent standard deviation.

Fig. 6.16 compares the average carbonation depths measured with phenolphthalein against those measured with CRM image analysis after short-term natural carbonation. The results show a larger scatter. The average difference in carbonation depths measured with phenolphthalein and CRM image analysis was 14.3%, which is much larger than 1.2% for the case of accelerated carbonation (Fig. 6.4). Despite the good correlation for some of the results, the others (44% of the total population) for phenolphthalein were 10.6-63.7% lower than the corresponding ones for CRM. This is because in these samples, the colouration boundary after spraying phenolphthalein was ambiguous and difficult to detect, an example is shown in Fig. 6.17. This affects short-term natural carbonation with limited carbonation depth much more than accelerated carbonation. The problem of insignificant colour change for phenolphthalein spray test was also reported by Lo & Lee (2002), however, no reason was provided.

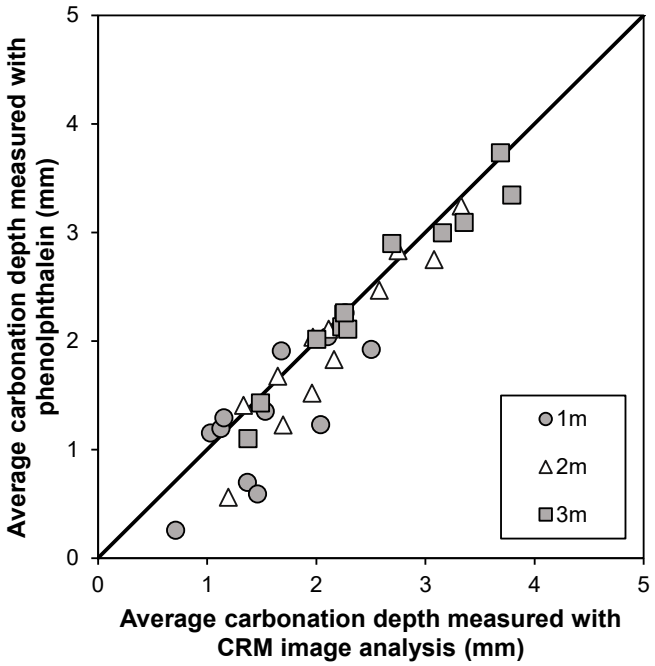


Figure 6.16 Comparison of the average carbonation depths measured with phenolphthalein and with CRM image analysis for all naturally carbonated samples.

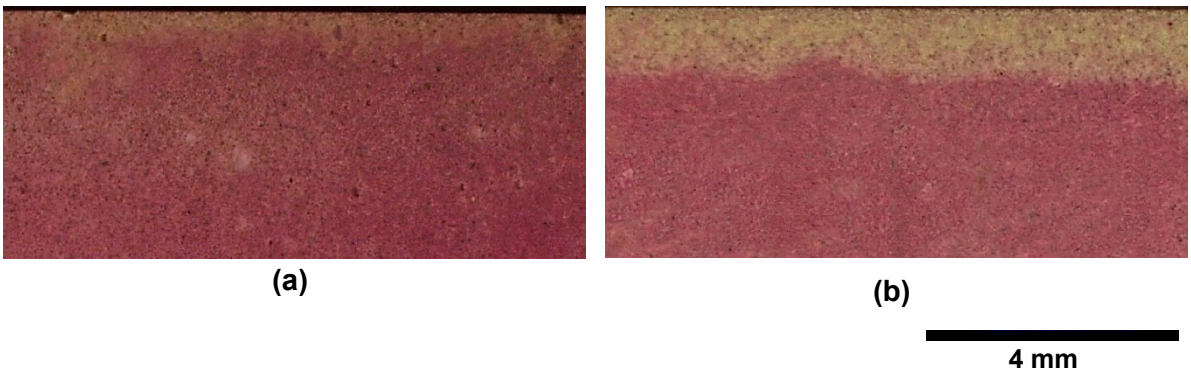


Figure 6.17 Images after spraying phenolphthalein for P-0.45-PC after 1 month (a) and 2 months (b) natural carbonation showing ambiguous coloration at the carbonation front.

6.4 Discussion

This chapter focuses on the measurement of carbonation depth using Raman maps of $CaCO_3$ polymorphs and $Ca(OH)_2$. Results show that calcite is the main $CaCO_3$ polymorph formed under both natural and accelerated carbonation. Other polymorphs, mainly aragonite, was found in the neat CEM I systems exposed to accelerated carbonation, likely due to the carbonation of C-S-H (Morandeau et al., 2014). These polymorphs were barely detected in the naturally carbonated CEM I samples. Amorphous calcium carbonate (ACC) and monohydrocalcite are two other possible $CaCO_3$ products.

However, ACC is known to form at early carbonation prior to the formation of crystalline $CaCO_3$ (Black et al., 2007) whereas monohydrocalcite is another hydrated form of $CaCO_3$ which exist only in high relative humidity (75 to 90%) (López-Arce et al., 2011). These phases were not observed in this study but they are readily detectable by CRM (Black et al., 2007; Coleyshaw et al., 2003) and hence can be included for analysis if necessary. This study demonstrates that CRM is a highly viable technique for understanding the mechanics of carbonation at high spatial resolution.

CRM maps of $CaCO_3$ polymorphs and $Ca(OH)_2$ have shown the distinct boundary between the carbonated and the non-carbonated zone. The spatial distributions of these phases in CRM maps appear almost homogeneous in the two regions, even in the area adjacent to the carbonation front. However, the carbonation profiles obtained by processing the CRM maps and profile-grinding analysis, show the existence of the transition zone with co-existing $CaCO_3$ and portlandite, which is the so-called partially carbonated zone. The width of this zone corresponds to the spatial variation of the carbonation front, with the start and end points marking the minimum and maximum carbonation depth respectively. The content of $CaCO_3$ and $Ca(OH)_2$ varies against depth in this region, but their actually spatial distribution is not affected. This study has also demonstrated that the carbonation front is sharp, instead of gradual as was reported by previous profile-grinding analysis (Thiery et al., 2007).

Although CRM and phenolphthalein provide different measures of carbonation, both give very consistent carbonation fronts produced under accelerated conditions. This is an interesting finding given that phenolphthalein is often said to underestimate the true carbonation depth due to the fact that it detects colouration change only when the pH of the pore solution is < 9.8. A recent study by Shi et al. (2016) has attempted to correlate phase changes with pH profiles in carbonated cementitious systems by thermodynamic modelling. The authors suggest that the carbonation depth indicated by phenolphthalein reflects the depletion of high-Ca C-S-H. Clearly, this is inconsistent with the findings derived from this study, which show that phenolphthalein colour change corresponds well with depletion of portlandite measured by CRM. Further work is therefore warranted to understand better the correlation between pH and phase changes under carbonation.

Profile-grinding techniques including TGA, FTIR, and XRD provide only the ‘apparent’ maximum carbonation depth which is dependent on the spatial variation of the carbonation front and the sampling interval used. Furthermore, as mentioned in the Introduction, profile-grinding is time-consuming and prone to sampling error. These techniques are also impractical for the analysis of concrete as the presence of large particle aggregates would interfere with the sampling process and complicate analysis. CRM, on the other hand, provides a detailed map of the spatial distribution of $CaCO_3$ products, from which the carbonation front can be profiled precisely, and both the maximum and average carbonation depth can be determined accurately. The presence of large aggregate

particles should also pose no problems as a larger area can be mapped to fully capture the carbonation front. The mapping step size can be adjusted to reduce the mapping time without compromising the spatial resolution, especially along the carbonation depth.

The carbonation depths induced by short-term natural carbonation can be too shallow (e.g. < 1.4 mm for P-0.45-PC after three months) to be measured accurately with profile-grinding analysis. The phenolphthalein method is also not ideal for measuring such shallow carbonation depths, as the colouration boundary can be ambiguous and sometimes undetectable, and hence difficult to ascertain. This problem can be exacerbated by the presence of aggregate in the case of concrete due to the small paste thickness between the adjacent aggregate particles. CRM does not have these issues as the carbonation front indicated by the distribution of $CaCO_3$ polymorphs remain distinct even at a carbonation depth of < 1 mm. This demonstrates a major advantage of CRM over other conventional techniques for measuring shallow carbonation depths.

This study proposed a simple method to estimate average carbonation depth from carbonation profiles. The average carbonation depth has been employed in the carbonation models to predict the long-term carbonation resistance, which is much more common than the maximum carbonation depth because the latter may not be representative of the overall carbonation extent as it may occur only in a localised area, and thus lead to a conservative prediction. Nevertheless, it is worthwhile noting that the maximum value should still be taken into consideration for carbonation modelling because this defines the worst-case scenario of carbonation induced corrosion. This is important because some previous studies have found corrosion initiation occurring before the average carbonation depth measured by phenolphthalein reaches the steel (Yoon et al., 2007; Hussain & Ishida, 2009; Hussain et al., 2011). Results in this study showed that the maximum carbonation depth can be 7-25% larger than the average value for CEM I samples exposed 1-3 months accelerated carbonation (4% CO_2) and the difference increased with the width of the transition zone and standard deviation of the measured carbonation depth.

The measured average carbonation depth by CRM after short-term natural carbonation can be used to rapidly assess the carbonation behaviour of cementitious materials. This could especially benefit the carbonation study of novel cements, for example, calcium sulphoaluminate/belite cements, alkali-activated cements, and magnesium silicate based binders. Such cements are fundamentally different from conventional Portland cement and the validity of accelerated carbonation tests to assess the carbonation mechanism are highly questionable when applied to novel cements. However, with the help of CRM, their carbonation resistance could be assessed with good reliability within a relatively short time, which could potentially reduce the introduction time for commercial adoption. Furthermore, these results can also be used in the service life prediction by fitting the results in the

carbonation models and predicting the long-term carbonation resistance. This could help the maintenance of existing structures and durability design of new structures. Results of such work will be presented in Chapter 8 by using artificial neural networks.

6.5 Conclusion

This study applies confocal Raman microscopy (CRM) to measure the carbonation depth of cement-based materials by mapping the spatial distributions of all three $CaCO_3$ polymorphs and $Ca(OH)_2$. Neat CEM I and blended (CEM I + 30% PFA, CEM I + 50% GGBS) cement pastes and mortars with w/b ratios 0.45 and 0.60 exposed to accelerated (4% CO_2) and natural (440 ppm CO_2) carbonation for 1, 2 and 3 months were used for the investigation. The carbonation depths measured with CRM combined with image analysis were compared with those measured with phenolphthalein spray method and profile-grinding analysis techniques including TGA, XRD, FTIR and RS. The key findings are:

a) Raman maps of $CaCO_3$ and $Ca(OH)_2$ show that the carbonation fronts in both paste and mortar samples are sharp and distinct, irrespective of the binder type, w/b ratio, and carbonation condition. CRM and phenolphthalein both reveal identical carbonation fronts (5.9-12.7 mm deep) produced under accelerated conditions with an average difference in carbonation depths of 1.2%. The average difference increased to 14.3% for short-term (1-3 months) natural carbonation due to the ambiguous colouration of phenolphthalein when measuring shallow carbonation depth (< 3 mm) in some samples.
b) Profile analysis of the Raman maps indicates the existence of three zones: fully carbonated zone, transition zone with co-existing $CaCO_3$ and portlandite and non-carbonated zone. The extent of the transition zone varies depending on the spatial variation of the carbonation front with the widths 1.4-4.1 mm for CEM I samples exposed to 1-3 months accelerated carbonation (4% CO_2). This accounts for 20 – 46 % of their respective carbonation depths. The maximum carbonation depth is indicated by the end of the transition zone where the content $CaCO_3$ returns to the level of the non-carbonated zone.
c) Profile-grinding analysis measures only the ‘apparent’ maximum carbonation depth, which increases with the spatial variation of the carbonation front and sampling interval adopted. With a sampling interval of 3 mm, the ‘apparent’ maximum carbonation depths observed in this chapter was on average 21% larger than the actual maximum carbonation depths measured by CRM profiles. This is due to the large spatial variation of the carbonation front and coarse sampling interval (3 mm) for profile-grinding analysis.

d) A simple method to estimate the average carbonation depth from carbonation profiles is proposed. The method involves fitting a regression to the transition zone to determine the depth at which the carbonation front is divided into two equal areas. The average carbonation depths estimated from profile-grinding analysis using the proposed method agreed well with those determined by CRM image analysis, with the average difference being only 1.1%.

e) CRM is ideal for measuring shallow carbonation depths (e.g. < 3 mm) induced by short-term natural carbonation, which are otherwise difficult or impossible to measure with profile-grinding analysis. The smallest average carbonation depth observed with CRM in this study was 0.71 mm in a CEM I cement paste naturally carbonated for 1 month.

f) Blended cement systems show consistently higher carbonation depths than neat CEM I systems. The carbonation depths increase with w/b and carbonation time, but reduce slightly with the presence of aggregate particles. None of the average natural carbonation depths observed in this study exceeded 4 mm even after 3 months.

7 Experimental investigation of natural carbonation and its influence on microstructure and transport properties

This chapter studies the evolution of average carbonation depth in paste, mortar and concrete samples after short-term (1-3 months) and longer-term (6-24 months) natural exposure, using confocal Raman microscopy image analysis method developed in Chapter 6 and phenolphthalein spray test. These experimental data were then employed to model the carbonation resistance of cement-based materials for up to 20 years in Chapter 8 using artificial neural networks (ANNs). Furthermore, the effects of four influential factors of carbonation involving water/binder ratio (w/b: 0.45 and 0.6), curing duration (3d and 122d), aggregate content (0% for paste, 20% and 50% for mortar, and 70% for concrete), and binder type (CEM I, CEM I + 30% fly ash and 50% slag) were studied, and the changes in mass transport properties and microstructure with the progress of carbonation were investigated. These understandings also contributed to the selection of essential variables that should be incorporated as input neurons in ANNs. Results show that the carbonation depths are larger in blended cement samples (0.98-11.29 mm) than CEM I samples (0.71-3.92 mm) after 1-24 months natural carbonation and are affected by the studied influential factors in different manners. Decreasing w/b from 0.6 to 0.45 is able to reduce the carbonation coefficient comparable to extending curing duration from 3d to 122d for CEM I samples, but the latter is more important for blended cements for improving carbonation resistance. The inclusion of more impermeable aggregate reduces the carbonation coefficient, but ITZ percolation can happen for high w/b samples with 50% aggregate fraction presumably due to more porous ITZ. Instead of using SCMs replacement level, the CO_2 binding capacity ($w/CaO_{reactive}$) is found to be a more reasonable indicator of carbonation resistance due to a good correlation with the carbonation coefficients after 122d curing ($R^2 > 0.88$) and the ability to make comparison between different materials. Furthermore, results show that the effect of natural carbonation on microstructure and mass transport properties are dependent on the binder type. Carbonation reduces the total porosity for all tested samples as shown by the water desorption measurements and BSE images. However, contrary to CEM I, blended systems showed an increased accessible porosity, O_2 diffusivity and sorptivity after carbonation. O_2 permeability is consistently increased for all tested samples due to the formation of carbonation-induced microcracking. The microcracking is more severe in blended cements indicating the importance of shrinkage caused by C-S-H carbonation.

7.1 Introduction

Hardened cement paste contains multiple different phases including hydration products, unreacted cement particles, and pores; these phases make up certain volumes resulting in a highly complex microstructure. When exposed to carbonation, calcium-bearing phases, particularly calcium hydroxide (CH) and calcium silicate hydrate (C-S-H), react with atmospheric CO_2 to form calcium carbonate ($CaCO_3$) (Slegers & Rouxhet, 1976). This process changes the phase assemblage in the carbonated zone, reduces the pH in the pore solution, and thereby triggers depassivation and corrosion in the steel reinforcement (Bentur et al., 1997). This, in turn, causes cracks in the concrete cover and exacerbates the deterioration of reinforced concrete by facilitating the ingress of CO_2 and other aggressive substances. Accurate assessment of the long-term carbonation resistance and understanding of the effect of carbonation on microstructure and transport properties are therefore necessary for reliable service life prediction of reinforced concrete structures.

Since natural carbonation of concrete is usually a very slow process, many experimental studies employed accelerated carbonation by carbonating cementitious samples in an unrealistic environment, for example, elevated CO_2 concentrations from 1% to 100% (Groves et al., 1991; Castellote et al., 2009; Bernal et al., 2012; Morandeau et al., 2014; Shi et al., 2016; Leemann et al., 2017). Although this reduces the testing time from years to months, the induced decalcification process and the formed carbonates under accelerated carbonation are reported to be different from those under natural carbonation (Chen et al., 2006; Galan et al., 2015; Šavija & Luković, 2016). For example, elevated CO_2 concentration from natural level to > 10% can significantly enhance the carbonation rate of not only C-S-H, but also other calcium-bearing phases like ettringite and unreacted cement (Castellote et al., 2009). Although accelerated carbonation at a relatively lower CO_2 concentration (e.g. 3%) was found to be somewhat representative of natural carbonation in terms of mineralogical and microstructural change in cement pastes (Castellote et al., 2009; Auroy et al., 2018), this is not applicable to all binding systems. For example, it was reported to underestimate the service life prediction for alkali-activated binders (Bernal et al., 2012) and mortars with 50% fly ash (Van Den Heede & De Belie, 2019) when exposed to 1% CO_2 concentration. As such, accelerated carbonation is not ideal for service life prediction for cement-based materials.

A possible approach to this problem would be to expose concrete specimens to natural carbonation for a relatively short period, characterise carbonation profile with time, and then extrapolate the results to long-term exposure by predictive modelling. One technical challenge is the ability to accurately measure the limited changes in the carbonation profile after short-term natural exposure, and confocal Raman microscopy (CRM) has been demonstrated as a reliable technique for this application in Chapter 5 and 6. The evolution of carbonation extent and depth can therefore be confidently studied in

different binding systems to assist the further predictive modelling for long-term carbonation resistance.

The aim of this chapter is to determine the average carbonation depths of cement-based materials exposed to short-term (1-3 months) and longer-term (6-24 months) natural carbonation to provide experimental results to the carbonation modelling study in Chapter 8. The effect of four internal material factors (water/binder ratio, binder type, aggregate content, and curing duration) on natural carbonation were analysed. Furthermore, this study also investigated the evolution of mass transport properties and porosity with carbonation duration, as well as the microstructural changes and damage induced by natural carbonation. These could assist the selection of essential variables that should be considered in the predictive models.

7.2 Experimental

7.2.1 Materials and sample preparation

The cementitious materials used were CEM I 52.5 N, Class F fly ash (PFA), and ground granulated blastfurnace slag (GGBS). The oxide compositions and the properties of materials are given in Section 3.1. The mineral composition of CEM I was 62.4% C_3S, 10.3% C_2S, 10.6% C_3A, 2.2% C_4AF and 4.9% calcite, and the specific gravity was 3.06. Thames Valley sand (< 5 mm) and gravel (< 10 mm) were used as fine and coarse aggregate, respectively. The particle size distribution, specific gravity at saturated and surface dry condition (SSD), 24-hour absorption, and moisture content of the sand and gravel are also given in Section 3.1.

The sample ID and mixture proportions are shown in Table 7.1. Paste, mortar and concrete samples were prepared at w/b ratios of 0.45 and 0.6 to obtain a low and high porosity material. The aggregate volume fractions were 20% and 50% for mortar, and 70% for concrete. The cementitious materials were dry mixed in a Hobart mixer for 3 min, followed by wet mixing with tap water for another 3 minutes. Mortar and paste samples were cast in cubes (50 × 50 × 50 mm^3) and concrete samples were cast in cylindrical discs (100Φ × 50 mm^3). Samples were compacted in two layers using a vibration table and each layer was compacted until little or no air bubbles escaped from the surface. Special care was made to pastes and mortars at low sand content to prevent significant bleeding and segregation caused by over-vibration. The compacted samples were covered by plastic sheets and wet hessian to prevent water evaporation for the first 24h. Afterwards, samples were demoulded and moist cured at > 95% RH, 21 ºC for 3 or 122 days.

Table 7.1 Mixture proportions for paste, mortar and concrete samples

Mix ID	Free w/b	Water (kg/m^3)	Binder (kg/m^3)			Sand		Gravel	
			CEM	PFA	GGBS	(kg/m^3)	(vol %)	(kg/m^3)	(vol %)
CEM I									
P-0.45-PC	0.45	582.5	1294.4	-	-	0	0	-	-
M-0.45-PC-20%	0.45	469.4	1035.5	-	-	516.6	20	-	-
M-0.45-PC-50%	0.45	299.7	647.2	-	-	1291.5	50	-	-
C-0.45-PC	0.45	200.3	388.3	-	-	617.4	24	1191.1	46
P-0.6-PC	0.60	650.3	1083.9	-	-	0	0	-	-
M-0.6-PC-20%	0.60	523.7	867.1	-	-	516.6	20	-	-
M-0.6-PC-50%	0.60	333.7	542	-	-	1291.5	50	-	-
C-0.6-PC	0.60	220.7	325.2	-	-	617.4	24	1191.1	46
CEM I + 30% PFA									
P-0.45-V	0.45	582.5	906.1	388.3	-	0	0	-	-
M-0.45-V-20%	0.45	469.4	724.8	310.6	-	516.6	20	-	-
M-0.45-V-50%	0.45	299.7	453	194.2	-	1291.5	50	-	-
C-0.45-V	0.45	200.3	271.8	116.5	-	617.4	24	1191.1	46
P-0.6-V	0.60	650.3	758.7	325.2	-	0	0	-	-
M-0.6-V-20%	0.60	523.7	607	260.1	-	516.6	20	-	-
M-0.6-V-50%	0.60	333.7	379.4	162.6	-	1291.5	50	-	-
C-0.6-V	0.60	220.7	227.6	97.6	-	617.4	24	1191.1	46
CEM I + 50% GGBS									
P-0.45-S	0.45	582.5	647.2	-	647.2	0	0	-	-
M-0.45-S-20%	0.45	469.4	517.7	-	517.7	516.6	20	-	-
M-0.45-S-50%	0.45	299.7	323.6	-	323.6	1291.5	50	-	-
C-0.45-S	0.45	200.3	194.2	-	194.2	617.4	24	1191.1	46
P-0.6-S	0.60	650.3	542	-	542	0	0	-	-
M-0.6-S-20%	0.60	523.7	433.6	-	433.6	516.6	20	-	-
M-0.6-S-50%	0.60	333.7	271	-	271	1291.5	50	-	-
C-0.6-S	0.60	220.7	162.6	-	162.6	617.4	24	1191.1	46

7.2.2 Conditioning and carbonation

After curing, all samples were transferred to several climate boxes for conditioning at 65% relative humidity (RH), 21 ºC until mass equilibrium (< 0.02%/day). These boxes contained saturated sodium nitrite to maintain the RH, soda lime to keep the CO_2 level at < 10 ppm and a motorised fan to circulate air. Once conditioned, for paste and mortar cubes, all except one cast surface were coated with two layers of water-proof tape to allow unidirectional carbonation. For concrete discs, the curved side surface was coated to allow unidirectional carbonation from the top and bottom surfaces.

Carbonation was carried out in a CO_2 incubator developed in Section 3.2.2 at the same humidity and temperature (65% RH, 21ºC) for 0, 1, 2, 3, 6, 9, 12, and 24 months. The environment inside the incubator was continuously refreshed using an air pump to maintain the CO_2 level at ~440 ppm. The relative humidity in the incubator was maintained at 65% to achieve a high carbonation rate (Thiery et al., 2007). Three duplicates for each mix were prepared for each carbonation duration to obtain averaged results. After the designated carbonation period, the paste and mortar samples were sectioned into two halves and surface-dried with paper towel for measuring the average carbonation depth (Section 7.2.3). For concrete discs, the samples were conditioned at 55% RH, 21 ºC for 4 months until mass equilibrium for mass transport tests and/or vacuum saturation (Section 7.2.4). 55% RH was selected to empty the capillary pores and cracks relevant to transport properties (Wong et al., 2007). Afterwards, the concrete discs were sectioned for average carbonation depth and BSE measurements (Section 7.2.5).

7.2.3 Average carbonation depth

Based on the findings in Chapter 6, CRM and phenolphthalein spray test were both employed to confidently measure the average carbonation depths of paste, mortar and concrete samples. CRM was mainly used to characterise the shallow carbonation depth (< 3 mm) due to its greater accuracy and reliability, and phenolphthalein was generally used for all samples also due to its simplicity and convenience.

The set-up of the CRM was introduced in Section 3.3 and measurement was conducted following the same procedure specified in Section 6.2.3. Raman scanning was performed with a larger step size of 50 μm over a wider but shallower area of 30 × 4 mm (width × depth) in the StreamHR^{TM} mode, allowing each scan to complete within approximately 5 hours. The regions near the top and bottom surfaces were not scanned to avoid any influence from edge effects. Raman maps of $CaCO_3$ polymorphs were produced based on the intensity of its main Raman peaks at 1085 + 1090 cm^{-1} (ν1 symmetric C-O stretching). The depths of carbonation front at 31 equally distanced locations (interval of 1 mm) were measured on the Raman maps using Fiji (v.1.8.0) and the results were averaged.

Parallel to CRM mapping, phenolphthalein solution was prepared by dissolving 1 g of phenolphthalein in a mixture of 30 ml deionised water and 70 ml ethyl alcohol, and was sprayed on the sectioned surface. Once the colouration had stabilised, the surfaces were imaged with a stereomicroscope (Olympus SZX10) at a magnification of 0.63×. Similar to the CRM method, the carbonation depths were determined via image analysis as is exampled in Fig. 7.1. In some samples where the colouration boundary was not distinct (Section 6.3.5), CRM mapping was also performed to provide accurate measurements.

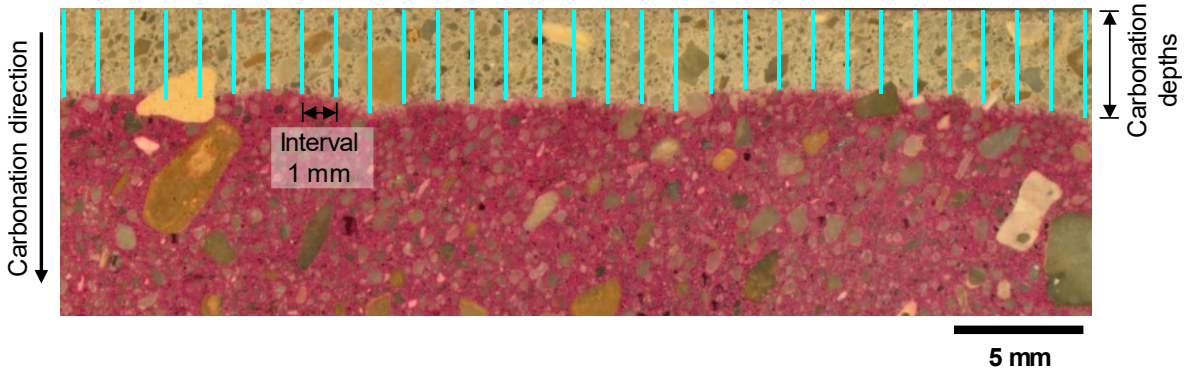


Figure 7.1 Measurement of carbonation depths (marked by the cyan bars) at 31 equally distanced (interval of 1 mm) locations on the surface sprayed with phenolphthalein of M-0.45-V-50% after 9 months of natural carbonation (average carbonation depth = 3.4 mm).

7.2.4 Mass transport tests and vacuum saturation

The conditioned concrete discs (at 55% RH, 21ºC) were tested following the sequence of O_2 diffusion, O_2 permeation and water absorption at 21 ºC as was specified in Wong et al. (2007) and described in Section 3.6. The diffusion and permeation tests can be completed within 0.6-2 hours. Significant drying in the samples due to the exposure to dry O_2 gas did not occur as was indicated by the limited mass loss (< 0.1%) at the end of each test. This allows the sorptivity tests to commence without requiring additional conditioning. Once completed, two of the three duplicates were transferred to a separate chamber to be saturated with tap water under vacuum for 6 hours and kept in water after the vacuum was released for an extra 18 hours. These duplicates were then oven-dried at 105 ºC for 1 month until mass equilibrium, and sectioned vertically to produce two halves for measuring carbonation depth. It should be noted that the conditioning, gas transport tests, water absorption test, and oven drying were not expected to cause further carbonation because care was taken to ensure that these procedures were carried out in zero CO_2 environments.

The total porosity φ_t and accessible porosity can be estimated with the water desorption measurements using the following equations:

$$\varphi_t = \left(\frac{m_s - m_d}{\rho V}\right) \times 100\% \qquad \text{Equation 7.1}$$

$$\varphi = \left(\frac{m_s - m}{\rho V}\right) \times 100\% \qquad \text{Equation 7.2}$$

where m_s, m_d, and m are the masses at the vacuum saturated state, oven-dried state at 105 ºC, and preconditioned state at 55% RH, 21 ºC, respectively. ρ is the density of water taken as 1 g/cm^3, and V is the sample volume.

7.2.5 Backscattered electron microscopy

After the sorptivity test, the third replicate sample for 0- and 24- months carbonation was sectioned vertically to produce two blocks of 50 × 21 × 6 mm^3. The blocks were pre-conditioned at 55% RH, 21 ºC in a conditioning chamber containing saturated magnesium chloride, soda lime and motorised fan for 2 weeks prior to impregnation with epoxy resin (Struers Epofix). The surface was then ground using silicon carbide (SiC) paper of grit sizes of 120, 220, 500, and 1000, and polished with and non-woven cloth applied with diamond abrasives from 6, 3, 1, to 0.25 μm to produce successively finer surfaces following the procedure described in Wong et al. (2009) and Section 3.4.1.

Microstructural characterisation and elemental analysis were performed via a Hitachi TM4000 Plus scanning electron microscope (SEM) equipped with an Oxford Instruments Aztec Advanced X-Act Compact energy dispersive X-ray detector (EDS). The SEM was operated at 15 kV in the backscattered electron (BSE) mode and the working distance was set to 7 mm to achieve an optimal spatial resolution according to Monte Carlo simulations (Yio et al., 2016). Images were captured at a magnification of 500× at a scan format of 1280 × 960 pixels to give pixel sizes of 0.2 μm. Porosity of each image was determined using the Overflow method (Wong et al., 2006). EDS spot analysis was performed on more than 20 locations per sample to characterise the elemental change after carbonation for different phases. Microcracking on over 20 BSE images in both the non-carbonated (0 month) and carbonated (24 months) samples were manually extracted in Fiji (Schindelin et al., 2012) to calculate the crack density (total crack length ÷ image area).

7.3 Results

7.3.1 Carbonation resistance

Fig. 7.2 a-c show the average carbonation depths of CEM I, CEM I blended with 30% PFA and 50% GGBS samples (3d curing) after 1-24 months of natural carbonation. The same y-axis scale was employed for meaningful comparison. In general, the carbonation rate was the highest at the beginning and decreased with time. Short-term natural exposure of 3 months was able to induce carbonation depths of on average 40.1% of those obtained after prolonged exposure of 24 months, but with 87.5% less carbonation duration. CEM I samples had the smallest carbonation depths with the majority being < 4 mm after 24 months, while this was significantly increased to ~11 mm for blended

cements samples. The average carbonation depths were consistently smaller at low w/b regardless of the binder type and aggregate content. Prolonged curing of 122d (not shown) decreased the carbonation depths by on average 44.8% compared with those for 3d curing samples. These results were then employed to predict the long-term carbonation resistance of cement-based materials for up to 20 years in Chapter 8.

To facilitate assessment of carbonation resistance, the average carbonation depths were further processed to calculate the carbonation coefficient following the square-root-of-time rule (Fig. 7.2 d-f). Results show a linear relationship with $R^2 > 0.84$.

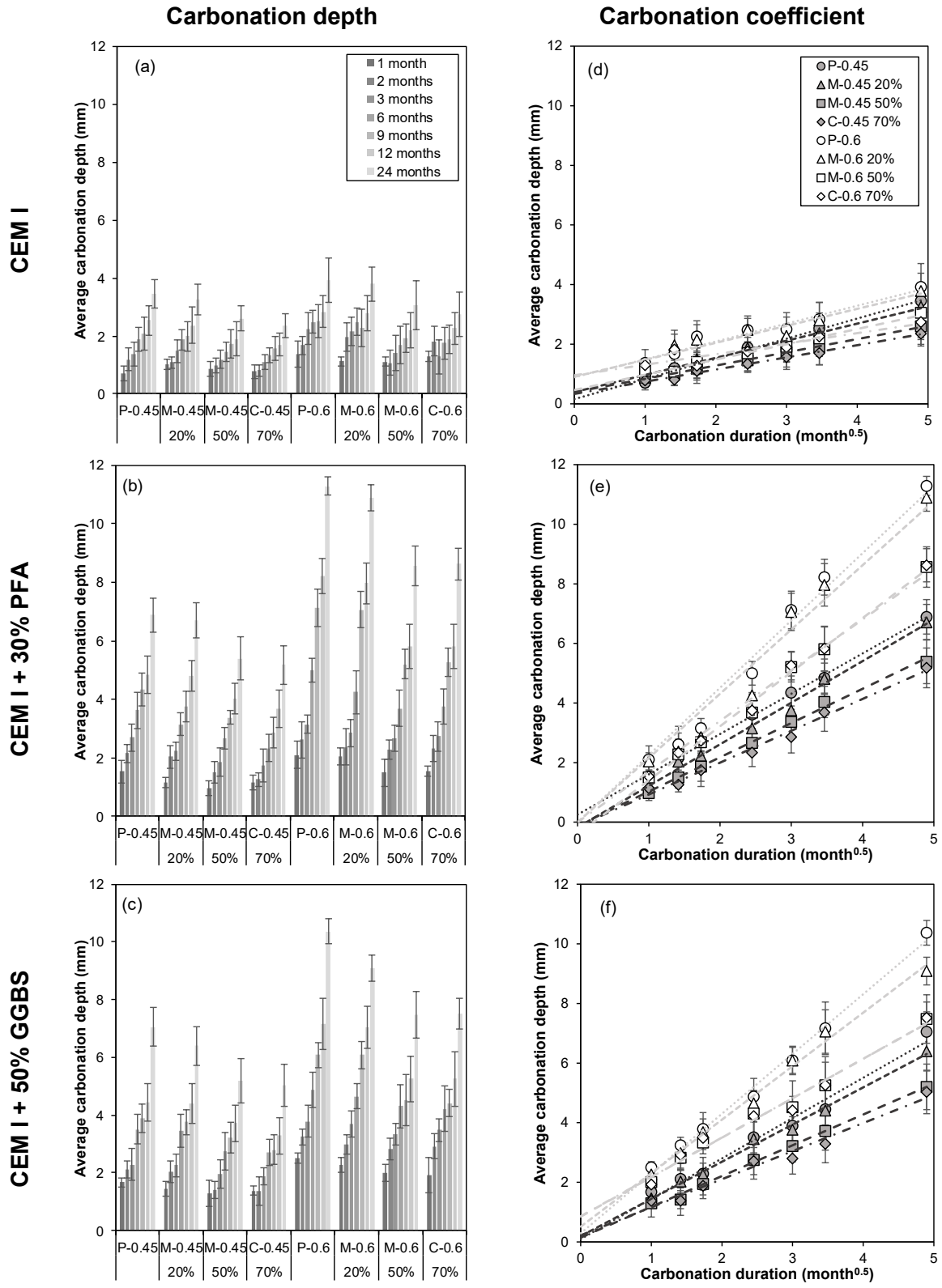


Figure 7.2 Average carbonation depth of CEM I (a), CEM I blended with 30% PFA (b) and 50% GGBS (c) samples (3d curing) after 1-24 months natural carbonation, and the corresponding plots against square-root-of-exposure duration (d-f). P, M and C represent paste, mortar and concrete respectively. The percentage values represent the aggregate volume fraction. Error bars represent standard deviation. The dotted lines represent the best fit linear regression ($R^2 > 0.84$).

Fig. 7.3 shows the carbonation coefficients for all tested samples after 3d and 122d curing respectively. Results show that the carbonation coefficients were consistently smaller at low w/b and long curing duration samples due to a denser microstructure which decreased the penetration of CO_2. When the results are normalised to their respective values at w/b 0.45 and 122d curing, Fig. 7.4 collectively shows that extending the curing duration from 3d to 122d was more efficient in reducing the carbonation coefficients than decreasing the w/b from 0.6 to 0.45. This observation was more profound for blended cements (reduced by on average 34.5%) compared to CEM I (13.1%), as prolonged curing is essential to promote pozzolanic reaction (Bouikni et al., 2009). However, the carbonation coefficients for blended cements were still on average 40.3% larger than CEM I after 122d because of the lower content of portlandite consumed by the pozzolanic reaction.

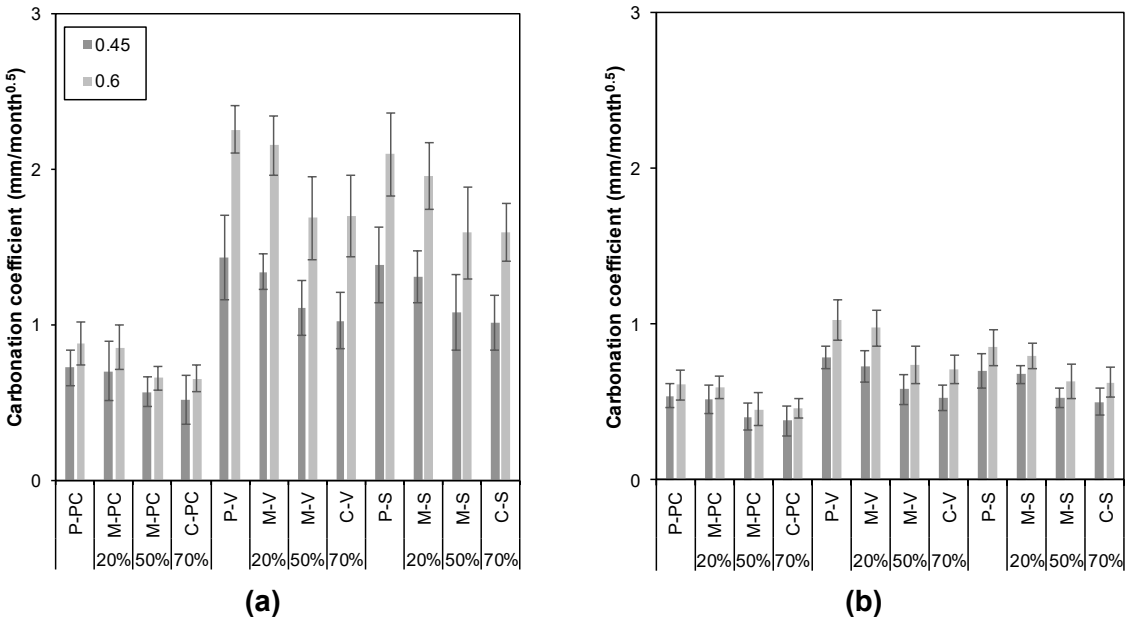


Figure 7.3 Carbonation coefficients of samples containing CEM I (PC), 30% PFA (V) and 50% GGBS (S) grouped according to the mix design and w/b after 3d (a) and 122d moist curing (b). Error bars represent standard deviation.

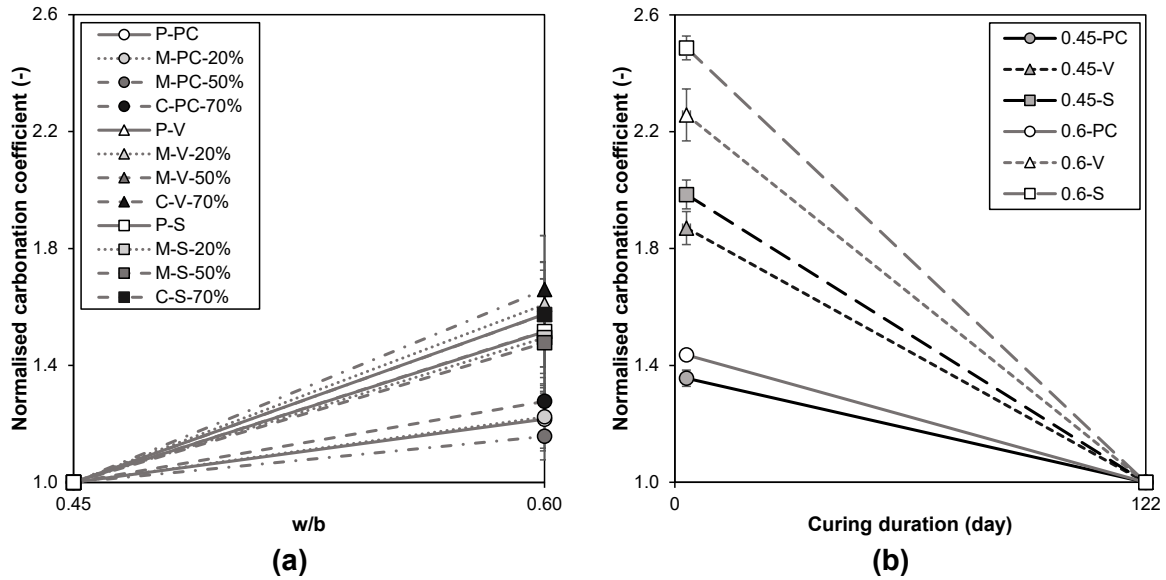


Figure 7.4 Normalised carbonation coefficients showing the effect of w/b (3d curing) (a) and curing duration (b). The same y-axis scale is used for better comparison. Error bars represent standard deviation. Note that the lines are indicative and do not represent a relationship, thus should not be used for interpolation or extrapolation.

The effect of aggregate content on the carbonation coefficients after 3d and 122d curing are presented in Fig. 7.5. The results were normalised to concrete with 70% aggregate volume fraction to facilitate comparison. Results show that the carbonation coefficients decreased consistently with aggregate content in w/b 0.45 mixes regardless of curing durations. This is because the aggregate employed in this study had low penetrability and acted as a local obstacle to penetration of the carbonation front. Even though more ITZ can be introduced, the dilution effect tends to predominate over the increased ITZ porosity. However, one remarkable observation was made for w/b 0.6 samples with 50% aggregate fraction where only limited changes in the carbonation coefficients were detected beyond this aggregate fraction. This is perhaps induced by the dominant ITZ percolation in high w/b samples due to more porous ITZ (Carcasses et al., 1998; Leemann & Moro, 2017).

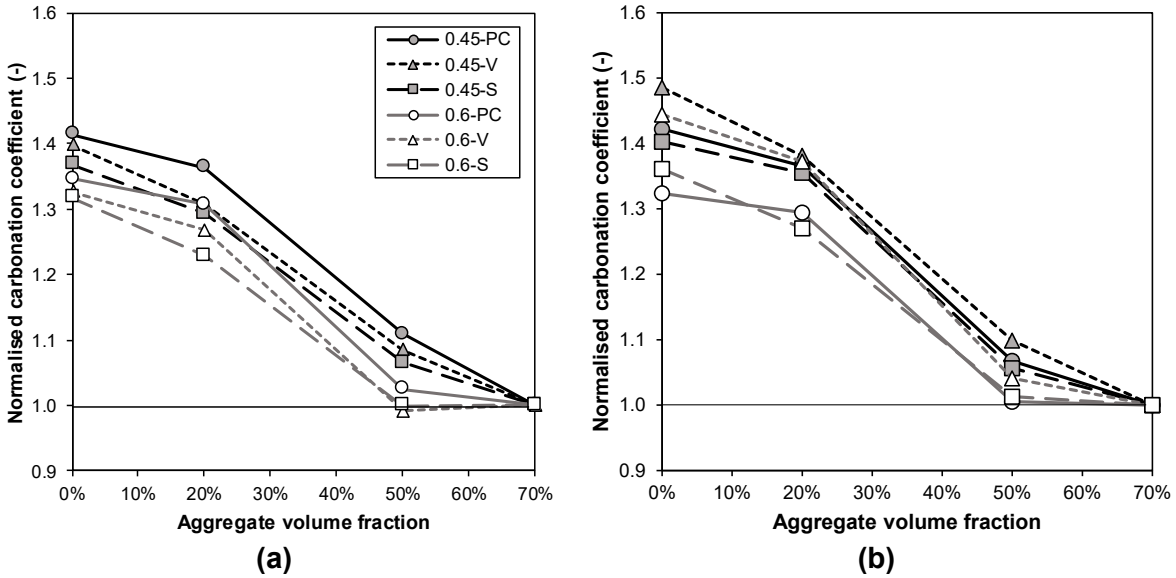


Figure 7.5 Normalised carbonation coefficients showing the effect of aggregate volume fraction on carbonation coefficients in samples moist cured for 3d (a) and 122d (b).

Fig. 7.6a shows the correlation of carbonation coefficients between blended cements and CEM I after 3d and 122d curing. Results show a linear relationship with $R^2 > 0.82$ and confirm that the blended cements were more vulnerable to carbonation than CEM I. The slopes were reduced after 122d curing indicating that blended cements are more sensitive to prolonged curing, which is in line with the observation in Fig. 7.4. When comparing the different SCMs, CEM I blended with 30% PFA samples had on average 9.3% larger carbonation coefficients than 50% GGBS even though at a lower replacement level. Since CO_2 is mainly combined with CaO from hydrates to form $CaCO_3$ during carbonation, the carbonation resistance is governed by the CO_2 buffer capacity, which can be expressed as the ratio between water and reactive CaO ($w/CaO_{reactive}$). The amount of reactive CaO is calculated from the oxide composition of the raw materials excluding any CaO in the form of $CaCO_3$, $CaSO_4$, unreacted cement clinker and SCMs (Leemann et al., 2015). However, since the degree of hydration in the samples was not known in this study, the entire amount of reactive CaO in the binders (exclude those present in $CaCO_3$ and $CaSO_4$) were implemented, assuming full hydration. Fig. 7.6b shows that the carbonation coefficients increased with the $w/CaO_{reactive}$ following a linear relationship. The R^2 values were relatively higher for 122d curing than 3d curing samples due to a higher degree of hydration.

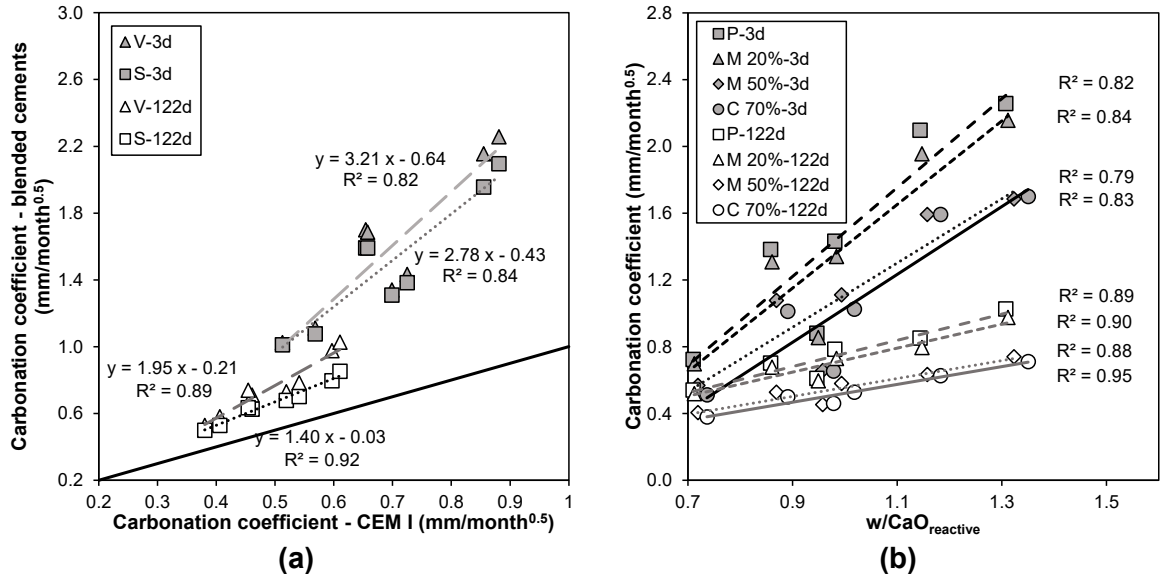


Figure 7.6 Correlation of carbonation coefficients between blended cements and CEM I (a), and correlation between carbonation coefficients and w/$CaO_{reactive}$ for all samples (b).

7.3.2 Mass transport properties and porosity after curing

Fig. 7.7 shows the O_2 diffusivity, O_2 permeability, sorptivity of concrete preconditioned at 55% RH, 21 ºC after 3d and 122d curing. Fig. 7.8 shows the total and accessible porosity estimated with water desorption measurements between vacuum-saturated state and preconditioned state at <3% RH, 105 ºC and 55% RH, 21 ºC, respectively. Similar to carbonation coefficients, the mass transport properties and porosities decreased with reduction in w/b and with prolonged curing. However, these two properties for blended concretes were on average 11% and 5% lower than CEM I after 122d curing due to the formation of additional C-S-H via pozzolanic reaction.

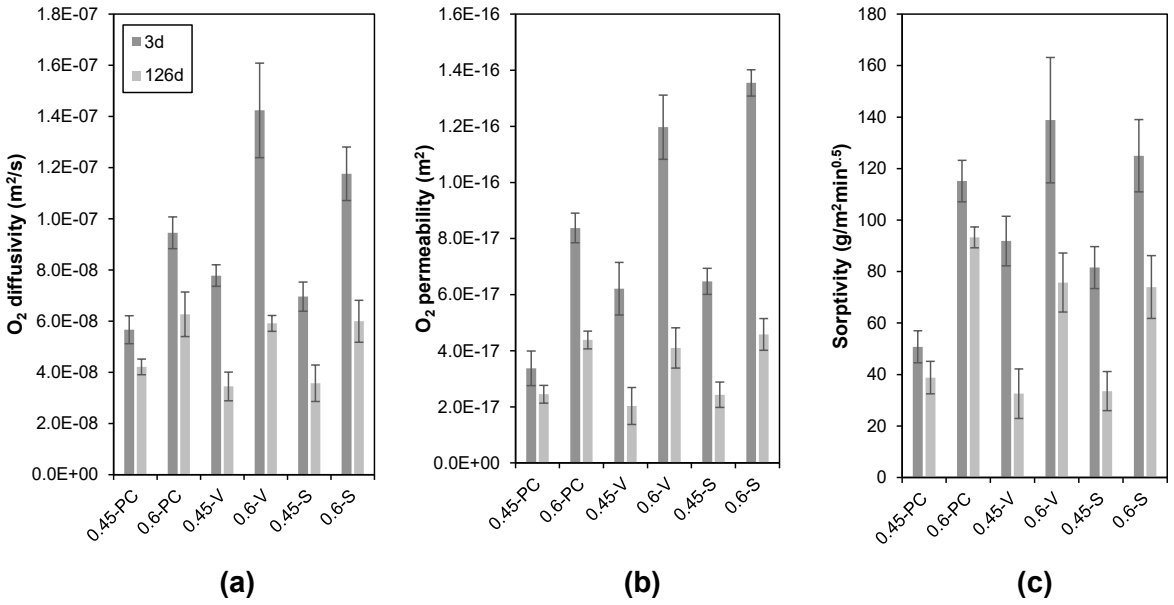


Figure 7.7 Mass transport properties: O_2 diffusivity (a), O_2 permeability (b), and sorptivity (c) of all concrete samples after 3d and 122d curing. Error bars represent standard deviation.

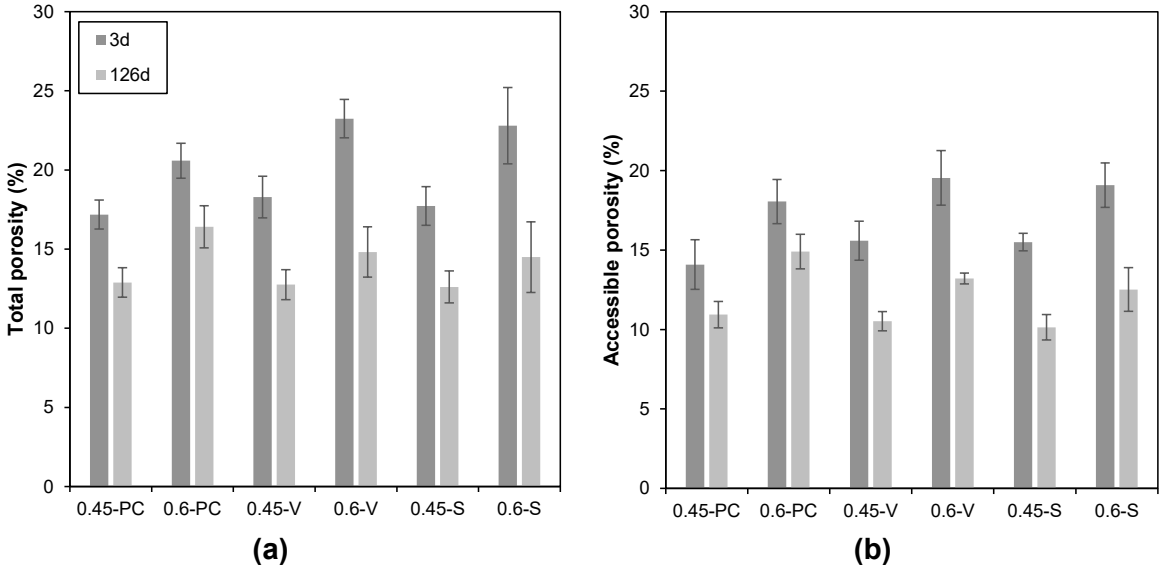


Figure 7.8 Changes of total (a) and accessible (b) porosity of all concrete samples after 3d and 122d curing. Error bars represent standard deviation.

Fig. 7.9 shows the correlation between mass transport properties and accessible porosity for all concrete samples. Despite the wide variation in mix composition and curing durations, strong correlations ($R^2 > 0.86$) were observed between all three transport properties and accessible porosity. This is not surprising as gas migration and water absorption occur in the open capillary pores and cracks that were sufficiently emptied when preconditioned at 55% RH (Wong et al., 2007). Among all the transport properties, the correlation was slightly weaker for permeation. This indicates that, even

though subjected to a gentle drying at 55% RH, some extent of microcracking might be induced during conditioning as they provide the paths of least resistance that are preferentially taken by the pressure-induced flow (Wu et al., 2015).

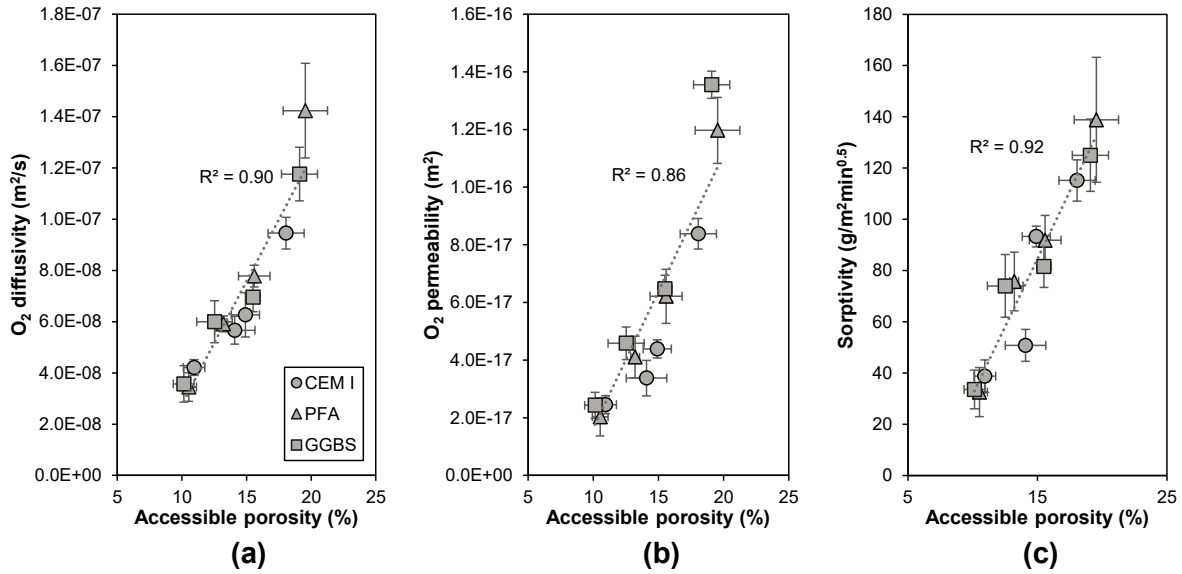


Figure 7.9 Correlation between accessible porosity and O_2 diffusivity (a), O_2 permeability (b), and sorptivity (c) for all concrete samples (3d and 122d curing). Error bars represent standard deviation. The dotted lines represent the best fit linear regression.

Fig. 7.10 shows the correlation between the carbonation coefficients and O_2 diffusivity. Irrespective of w/b and curing durations, there are stronger correlations between the carbonation coefficients and O_2 diffusivity for blended cements ($R^2 > 0.94$) than CEM I ($R^2 = 0.85$). This indicates that compared with CEM I, the carbonation rate of blended cements concretes is more dependent on the gas diffusivity. This is likely to do with the higher portlandite content in the hardened cement paste that acts as the pH buffer against carbonation.

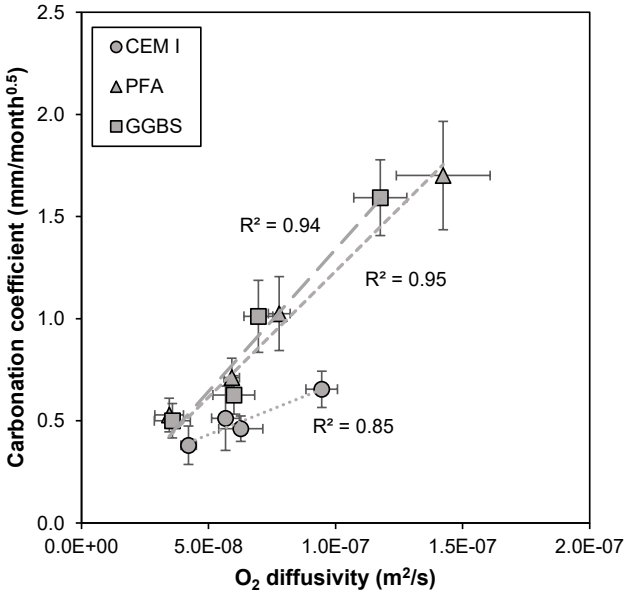


Figure 7.10 Correlations between carbonation coefficient and O_2 diffusivity for all concrete samples (3d and 122d curing). Error bars represent standard deviation.

7.3.3 Mass transport properties and porosity after carbonation

The evolution of mass transport properties with carbonation duration for 3d cured samples is shown in Fig. 7.11. Note that the 122d samples show a similar trend only with further reduced values compared with 3d curing samples, so they are not presented. Overall, the measured mass transport properties ranged over 1 order of magnitude and increased with increase in the w/b. Upon carbonation, these properties behaved in different manners for different binders. O_2 diffusivity and sorptivity continuously decreased with the progress of carbonation for CEM I concretes, but increased for blended concretes. However, O_2 permeability was increased for all samples, and was found to be more sensitive to blended cements as evident by the larger variation (increased by a factor of 2.4-3.9) than CEM I (1.5-1.6).

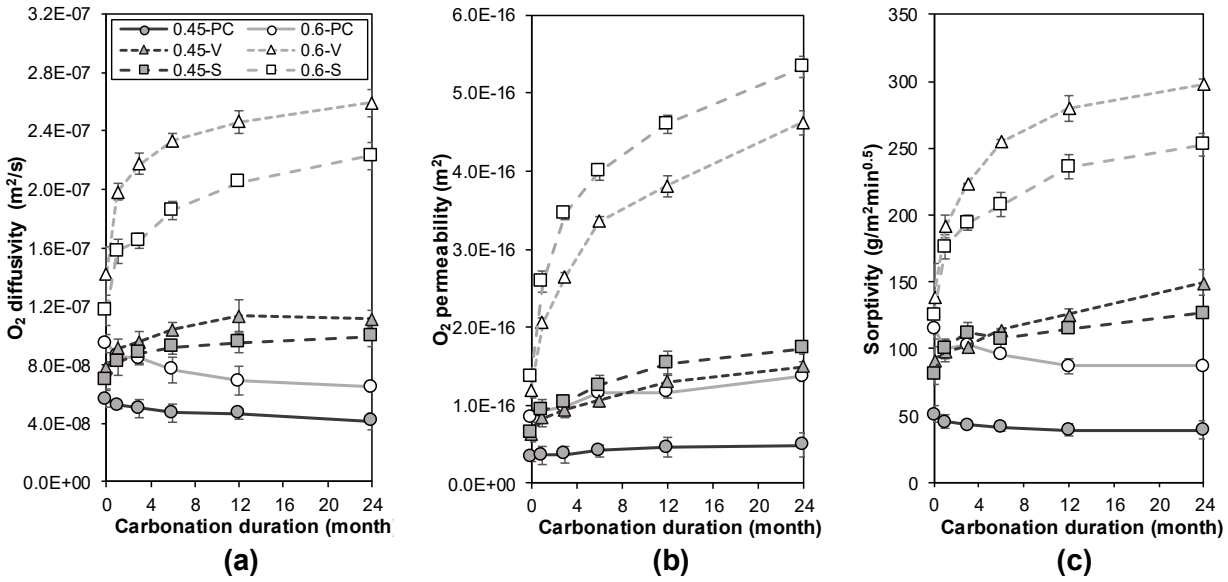


Figure 7.11 Evolution of mass transport properties: O_2 diffusivity (a), O_2 permeability (b), and sorptivity (c) with carbonation duration for 3d cured concrete samples. Error bars represent standard deviation.

Fig. 7.12 shows the evolution of total porosity and accessible porosity after natural carbonation. The total porosity was reduced for all samples with prolonged carbonation duration. This is due to the precipitation of $CaCO_3$ that increases the total volume of solid phases. The variation was stronger for CEM I samples (reduced by 12.8-14.4%) than blended cements (by 3.4-6.7%) because the latter had lower initial portlandite content, and carbonation of C-S-H would lead to coarsening of the pores. Indeed, the opposite trend was observed for blended cements where accessible porosity increased with carbonation duration. Although C-S-H carbonation also forms $CaCO_3$, this preferentially precipitates in gel pores < 2nm (Pham & Prince, 2014), which are not likely to be emptied when conditioned at 55% RH.

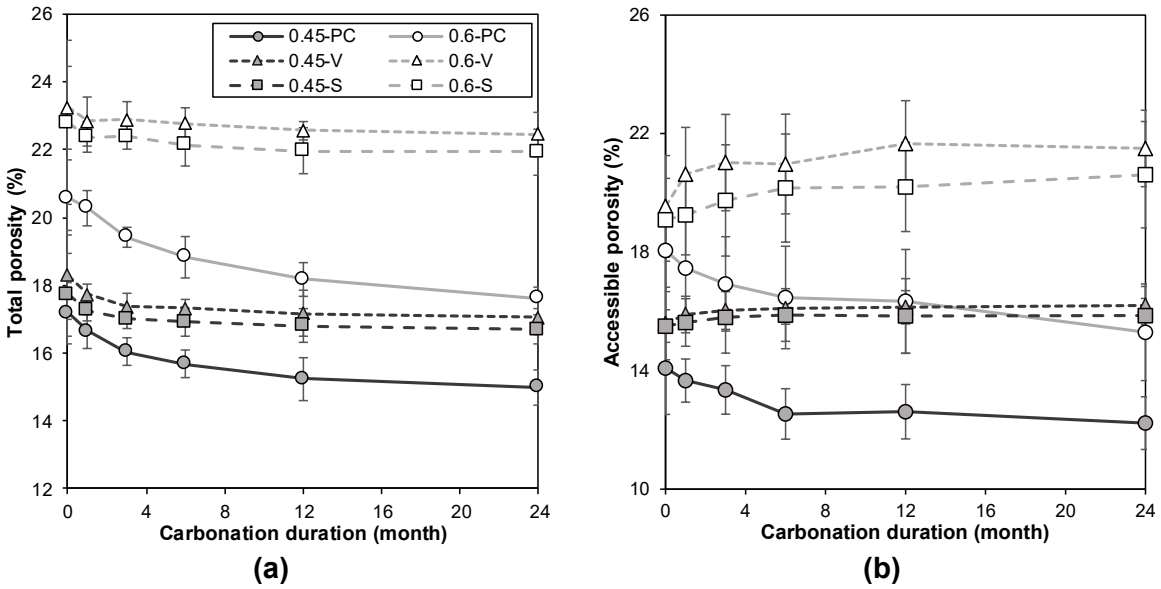


Figure 7.12 Evolution of total (a) and accessible (b) porosity with carbonation duration for 3d cured concrete samples. Error bars represent standard deviation.

Fig. 7.13a generally shows an increasing trend of O_2 diffusivity with total porosity ($R^2 = 0.65$), but the progress of carbonation (arrowed) for blended cements did not correlate well with total porosity. However, the correlation was better ($R^2 > 0.87$) when linking O_2 diffusivity and sorptivity to accessible porosity (Fig. 7.13 b, d), in line with the observation in Fig. 7.9 after curing. Similarly, the correlation was lower for permeability with a large scatter ($R^2 = 0.68$) presumably due to the formation of carbonation-induced microcracks. Considering that GGBS-containing mixes generally had lower diffusivity and sorptivity than PFA-containing mixes after carbonation, the relatively larger permeability in GGBS-containing mixes suggest a more severely microcracked paste after carbonation. This is due to the fact that pressure-induced flow (permeability) is highly sensitive to presence of microcracking, while diffusivity and sorptivity are relatively insensitive (Wu et al., 2015).

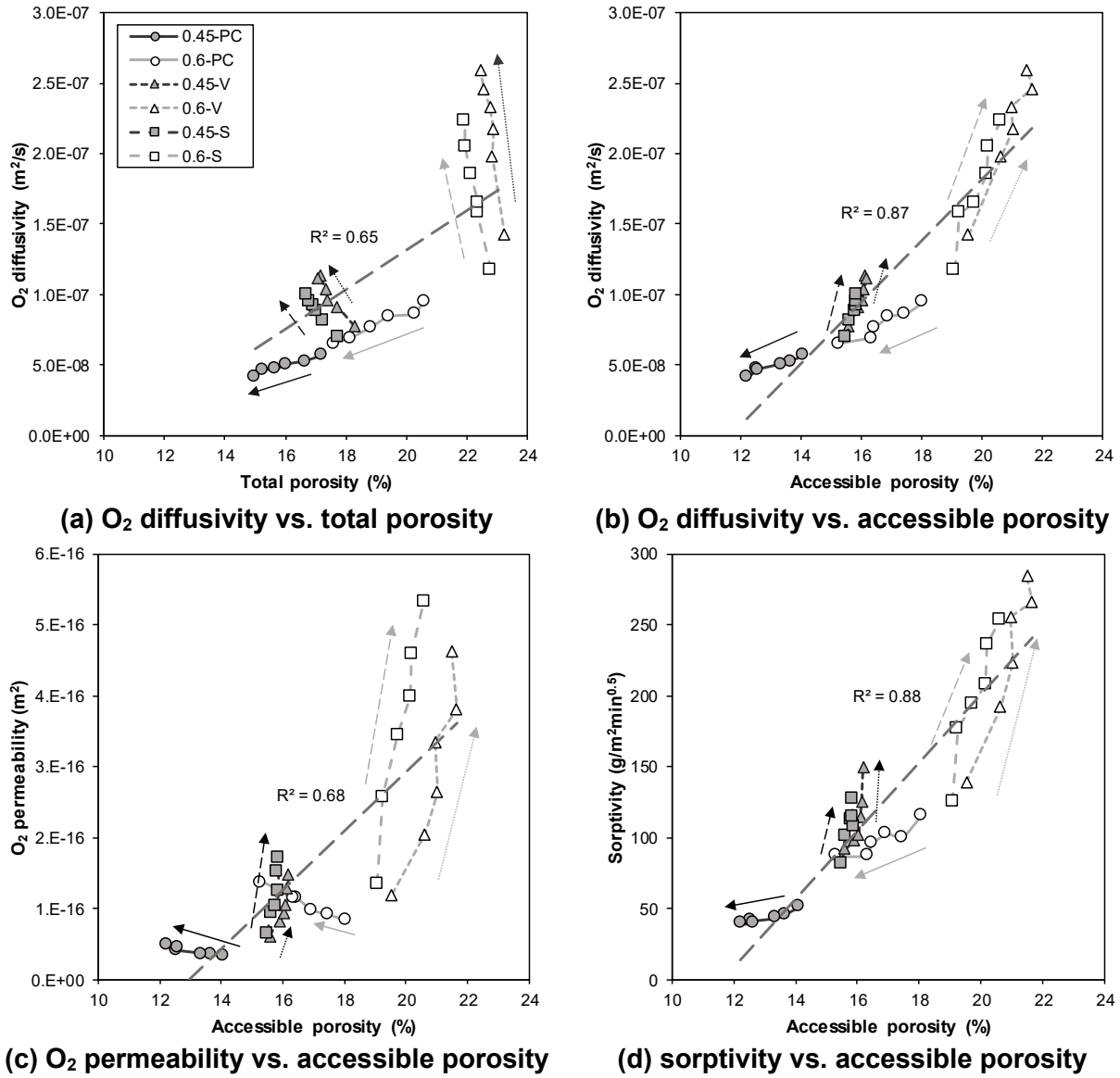


Figure 7.13 Correlation between O_2 diffusivity, O_2 permeability, sorptivity, total porosity and accessible porosity for 3d cured concrete samples after natural carbonation for up to 2 years. Arrows mark the progress of carbonation.

7.3.4 Effect of carbonation on microstructure

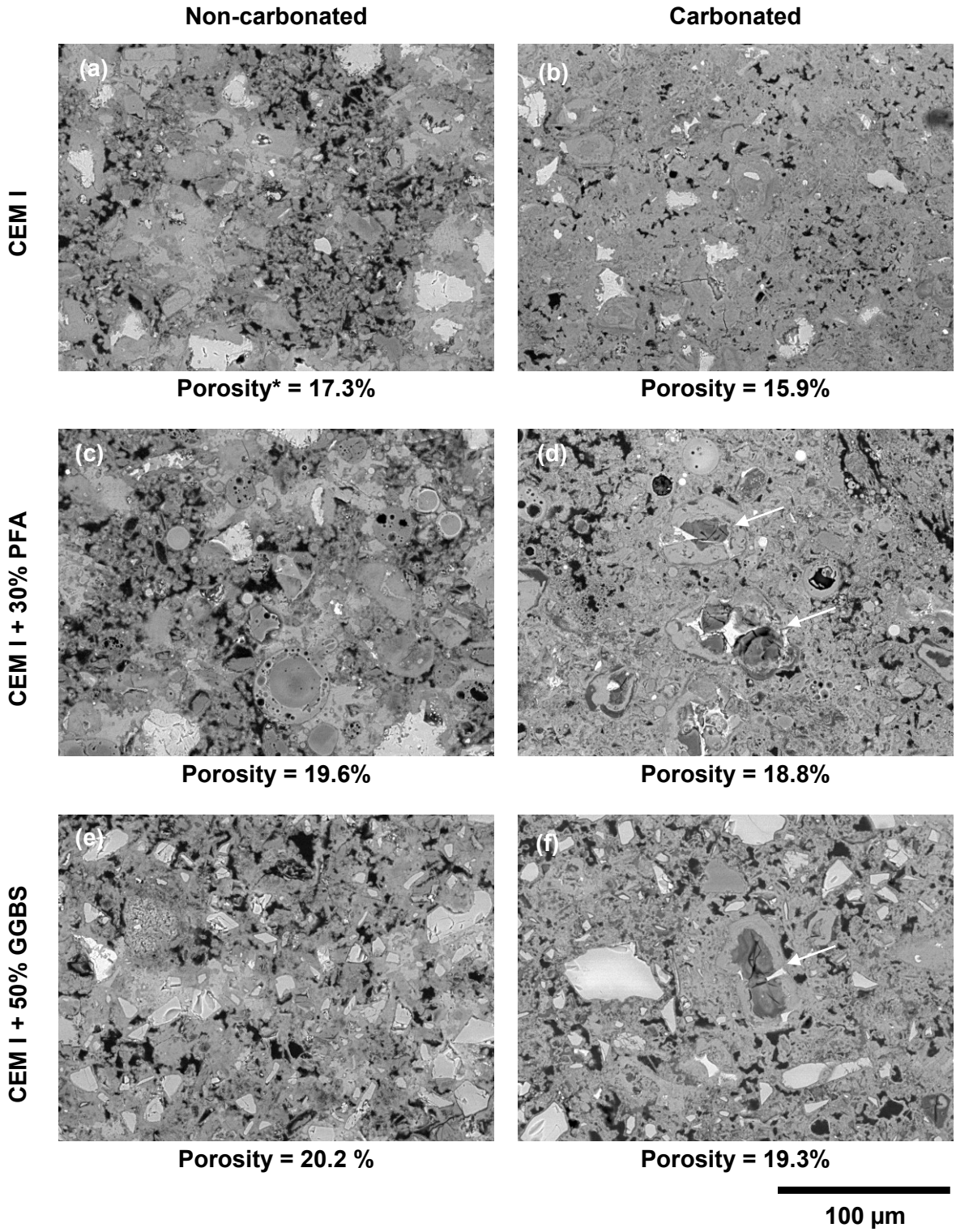
Fig. 7.14 presents example BSE images (500× magnification) showing the porosity change in carbonated and non-carbonated concrete of 3d curing samples (w/b 0.6) after 0- and 24-months natural carbonation. The different brightness is dependent on the average atomic number of the phase. The pores appear the darkest and the porosity for each image was calculated via the overflow method (Wong et al., 2006). In the non-carbonated zones, blended cements concretes had 13.3-16.8% higher porosity than CEM I concrete due to the lower clinker content and reaction rate at 3d. After carbonation, porosity reduction was observed regardless of the binder type and the reduction was

more significant for CEM I (8%) than blended cements (4.1-4.5%). These observations agree with the results obtained from water desorption measurements.

BSE-EDS also confirms changes in different phases after 24 months of carbonation. Portlandite can be observed as the lighter grey area in the outer product in all three non-carbonated mixes (Fig. 7.14 a, c, e) and EDS spot analysis confirms that these areas are high in Ca and O but low in Si. After carbonation, portlandite was no longer visually distinguishable in the carbonated paste (Fig. 7.14 b, d, f) as it is gradually consumed during carbonation (confirmed by the profile-grinding analysis results in Section 6.3.2) and intermixed with the precipitated $CaCO_3$. Decalcification in the hydration products was also observed after carbonation, especially for blended cements. These phases have been well characterised in the literature (Galan et al., 2015; Shah et al., 2018), so the changes of unreacted raw materials were given more focus in this chapter.

The unreacted cement grains appear the brightest and are surrounded by the darker inner and outer hydration products in the BSE image (Fig. 7.14a). The remaining unreacted cement grains are mainly belite due to a lower hydration rate. In the carbonated zones, some belite grains appear as dark relicts (arrowed in Fig. 7.14 d, f). EDS spot analysis shows a significantly reduced calcium intensity compared with typical unreacted belite grains, decreasing the Ca/Si ratio from approximately 2 in unreacted belite to on average 0.33 after decalcification. This reduces the mean atomic number and thus show a darker shade in the BSE image. Such observations were found in all carbonated samples but more frequently in blended cements.

A large number of unreacted PFA and slag particles can be observed (Fig. 7.14 c-f). The spherical unreacted PFA particles are readily detectable and are rich in Si, Al, and O but contain limited amount of Ca. Careful comparison between the carbonated and non-carbonated samples found no clear changes in the elemental composition for these particles. The unreacted slag particles appear more angular and smoother in a BSE image with higher Ca, Si, Al, Mg and O intensities. These particles are usually surrounded by a thin dark rim indicating the extent of reaction. The slag rim contains similar elements but reduced amount of Ca and Si, which are leached out to form the outer hydration product. After carbonation, EDS spot analysis shows no clear difference in unreacted slag particles, while decalcification in the rims was observed with a reduction of Ca/Si ratio from on average 1.41 to 0.8.



* The term 'porosity' in this subsection represents the area fraction of the epoxy-filled voids in the hardened paste including capillary pore, cracks, and hollow shells due to hydration and pozzolanic reaction.

Figure 7.14 Example BSE images of the non-carbonated and carbonated paste in CEM I, CEM I + 30% PFA, and CEM I + 50% GGBS concrete samples (w/b 0.6, 3d curing) after 0 and 24 months of natural carbonation. Arrows mark the belite grains appearing as dark relicts.

Microcracking caused by carbonation were traced on BSE images captured at 500× magnification in concretes exposed to 0- and 24-months natural carbonation. In general, two types of microcracks can be observed: bond cracks that occur along the aggregate-paste interface, and matrix cracks that propagate through the hardened cement paste. These cracks were distributed randomly across the entire sample, therefore over 20 images were captured at similar depths in the non-carbonated and carbonated samples. All detectable microcracks were extracted to produce binary images (exampled in Fig. 7.15) and to calculate the average crack density (Fig.7.16).

The matrix cracks in both carbonated and non-carbonated samples have similar morphology and appear scattered throughout the area with no preferred orientation. In the non-carbonated zones, only a limited number of microcracks (0.027-0.035 mm^{-1}) can be detected with widths between 0.5 and 6 μm. These microcracks tended to be short and isolated. More microcracks can be detected in carbonated zones, and the crack densities were increased by factors of 2.1, 2.8, and 2.7 for CEM I, 30% PFA and 50% GGBS concretes, respectively after carbonation. These microcracks are wider (~9 μm) and more interconnected, and some of them not only existed in the hydration product but also propagated through carbonated belite grains. When comparing different mixes, the non-carbonated CEM I and 30% PFA samples were microcracked to a similar extent, but 16-22% less than 50% GGBS sample. After carbonation, CEM I had the least microcracks, followed by 30% PFA samples. Some of the microcracks were also found to travel around the spherical PFA particles. 50% GGBS samples showed the most severe microcracking (0.092 mm^{-1}) and these were significantly longer than the other two mixes. Air voids can be detected in all mixes, and occasionally, these air voids appear to contribute to the propagation of microcracks.

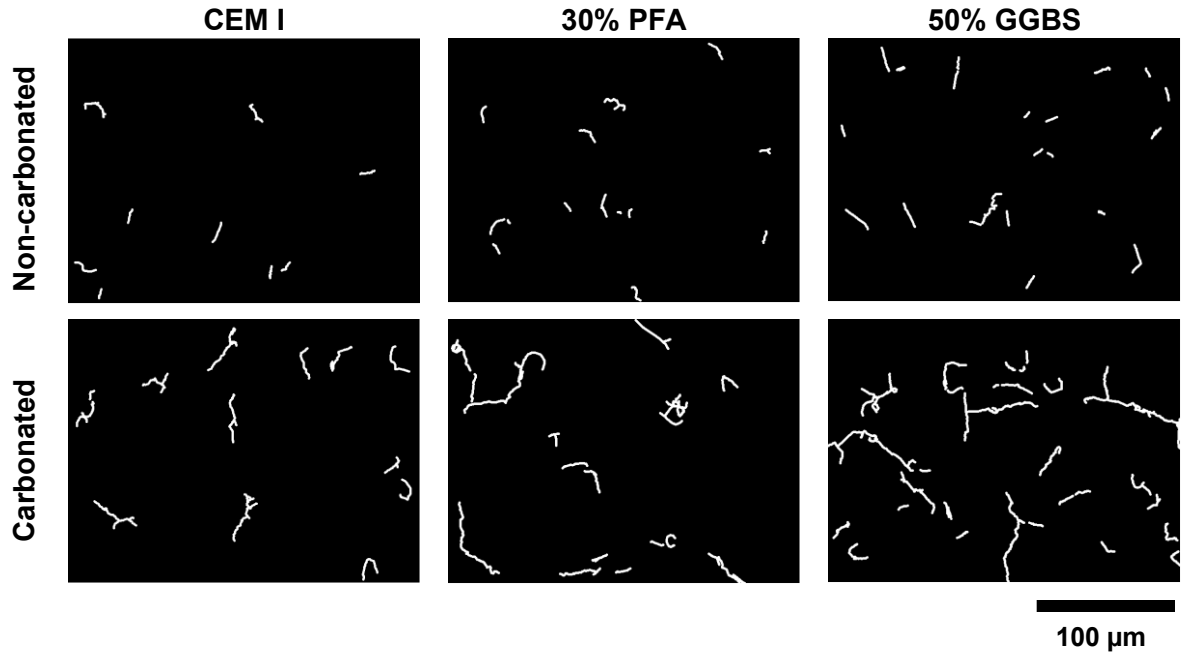


Figure 7.15 Example binary images showing the extent of detectable microcracks in the non-carbonated and 24-month naturally carbonated concrete samples (3d curing) containing different binder types. Microcracks were extracted for quantification via image analysis.

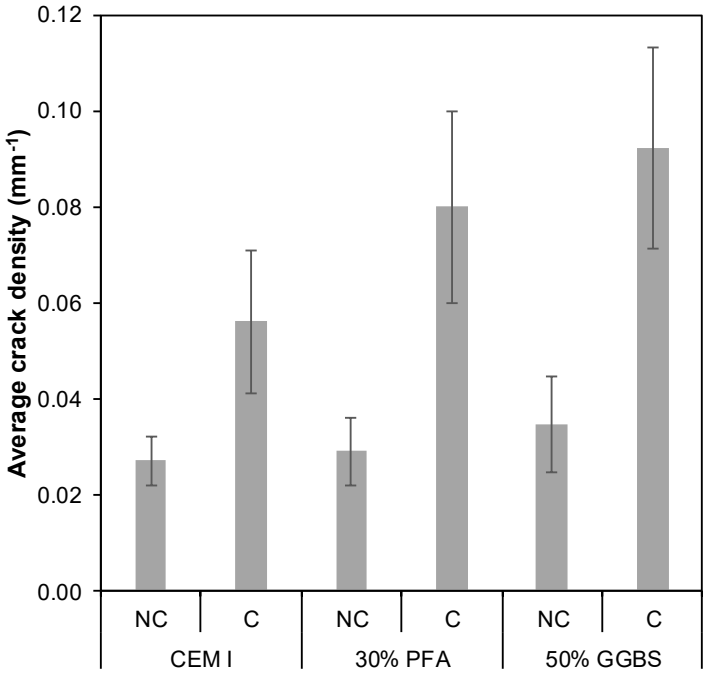


Figure 7.16 Average crack density observed in non-carbonated (NC) and 24-month naturally carbonated (C) concrete samples (3d curing) containing different binder types. Error bars represent standard deviation.

7.4 Discussion

7.4.1 Factors influencing carbonation resistance

Carbonation resistance was analysed using carbonation coefficients as an indicator, which is estimated with the square-root-of-time rule (Papadakis et al., 1991). This equation is based on Fick's first law assuming a steady state of diffusion and because the samples in this study were carbonated at a near constant environment (CO_2 level, RH, and temperature), a good correlation was achievable ($R^2 >$ 0.84). However, such stabile exposure conditions do not normally exist for real structures in service, so the carbonation process will be affected. For example, mortars exposed to sheltered and unsheltered conditions were reported to have significantly different carbonation coefficients due to the different moisture content (Leemann et al., 2018). Furthermore, the phase assemblage and pore structure evolve over time due to progress of hydration and carbonation, influencing the diffusion of CO_2 in concrete. All these could lead to a reduced precision when estimating the carbonation coefficient in samples carbonated in natural outdoor environments.

Carbonation is known as a diffusion-controlled process and the diffusion of CO_2 is closely relevant to the interconnected pore network (Fernández Bertos et al., 2004). The w/b and curing regime are critical factors that govern the pore structure of hardened cement paste and affect the carbonation process (Liu et al., 2017). This study shows decreased carbonation coefficients with reduced w/b and prolonged curing due to lower porosity and diffusivity. However, the importance of the two factors is different for different binder types. For blended cements, extending moist curing from 3d to 122d induced on average 34.5% higher reduction in carbonation coefficients than by decreasing the w/b from 0.6 to 0.45. This confirms the significance of good curing on the development of carbonation resistance for blended cements. For CEM I systems, decreasing w/b from 0.6 to 0.45 achieved carbonation coefficients comparable (on average 13.1% higher) to those obtained by extending curing from 3d to 122d.

Irrespective of w/b and curing duration, results show that CEM I samples had consistently lower carbonation rates than blended cements. Despite the fact that the addition of SCMs can somewhat increase the early hydration rate by prompting nucleation (Gruyaert et al., 2013), the higher content of clinker in the CEM I system tends to dominate the carbonation resistance at a young age (3d) and produce high content of portlandite, which acts as a pH buffer to slow down the progress of carbonation front. In blended cements, however, this buffer capacity is attenuated due to lower clinker content and continuous pozzolanic reaction, which reduces the pH from 12.7-13.8 to 12-13 (McPolin et al., 2009). The carbonation resistance is also affected by the lower reactive CaO content that the CO_2 cannot be readily depleted to form $CaCO_3$ before penetrating into a deeper area. Even though C-

S-H can decalcify to supply calcium to the pore solution, the pore structure is coarsened and this facilitates further penetration of CO_2 (Auroy et al., 2015). This explains the larger carbonation depth in blended cements after 122d curing even though they have a relatively lower total porosity than CEM I.

When comparing different SCMs, samples containing 30% PFA had higher carbonation rates than those containing 50% GGBS samples due to a larger w/$CaO_{reactive}$ ratio. This ratio was employed in Section 7.3.1 as an indicator for the CO_2 buffer capacity, allowing the comparison of carbonation resistance between different binding systems. In the calculation of reactive CaO, those present in the unreacted cement clinkers and SCMs are required to be excluded based on the assumption that CaO in these phases is not reactive with CO_2 (Leemann et al., 2015). However, it should be noted that belite carbonation can occur in all binder types, especially in blended cements even when the samples were carbonated naturally. Thus, a modification might be needed to address this observation.

Aggregate can have a twofold influence on carbonation. On one hand, aggregate with much lower porosity than cement paste can act as local obstacles to the carbonation process by decreasing the total porosity (i.e. dilution effect) and increasing the tortuosity of the transport path for CO_2. On the other hand, the 'interfacial transition zone' (ITZ) surrounding the aggregate surface generally contains more pores and portlandite, while fewer cement than the 'bulk' paste further away, which could facilitate the local transport for CO_2 (Scrivener et al., 2004). Results show that although more ITZ was introduced by increasing the aggregate fraction from 0% to 70%, a continuous reduction was observed in the carbonation coefficients for w/b 0.45 mixes. A similar trend was observed in Buenfeld & Okundi, (1998) who studied concrete (w/b 0.4 and 0.5) with increasing aggregate volume fraction from 60% to 75%. This is expected as the porous ITZs are balanced by a denser bulk paste that the overall paste matrix porosity is not affected as the w/b is conserved, so their net effect on the overall transport properties is only limited (Wong et al., 2009).

For w/b 0.6 samples, however, carbonation rates first decreased with aggregate content and then stabilised beyond 50% aggregate fraction. This seems to suggest that ITZ percolation could have occurred in the higher w/b sample due to a more porous ITZ. Similar observations were reported in Carcasses et al. (1998) who found a 40% critical percolation aggregate fraction for 0.5 w/c mortars, and Shen & Pan (2017) who found a 44% for w/c 0.53 mortar. However, it should be mentioned that the observation in this study might be affected by aggregate particle size as 70% aggregate in concrete contains not just sand, but also gravel. Despite that the inclusion of coarse aggregate at a constant total aggregate volume fraction is expected to reduce the fraction of ITZs due to reduced surface area, the net effect of ITZ on gaseous diffusivity is not likely to be significant (Wu et al., 2015).

7.4.2 Effect of natural carbonation on porosity and mass transport properties

Carbonation changes the phase assemblage in cementitious materials and thus alters the porosity due to differences in molar volume between hydration products and precipitated $CaCO_3$. The total porosity was estimated via water desorption measurements between the vacuum saturated state and oven dried state at 105°C. This temperature is commonly used in the literature to determine the content of all evaporable water (RILEM TC 116-PCD, 1999), although the bound water in some hydrates (e.g. ettringite, C-S-H) could also be removed. Therefore, a slight overestimation might be obtained in the calculated total porosity. As such, the preconditioned state at 55% RH, 21°C was used for measuring the accessible (capillary) porosity relevant to transport (Wong et al., 2007).

Results found a continuous reduction in total porosity for all samples after carbonation irrespective of w/b and curing duration, and the reduction was greater for CEM I than blended cements. These findings are in agreement with Papadakis (2000), Auroy et al. (2018) and Boumaaza et al. (2020). This is because lower portlandite content in blended cements, caused by either reduced clinker content or pozzolanic reaction, leads to more pronounced C-S-H carbonation. This decalcifies C-S-H and forms a porous silica gel (Chen et al., 2006). This problem tends to be worse for C-S-H with a low Ca/Si ratio due to a larger carbonation shrinkage for Ca/Si < 1.3 (Chen et al., 2006). Nevertheless, the precipitation of $CaCO_3$ from both CH and C-S-H carbonation increases the solids volume, therefore total porosity decreases despite the pore coarsening effect.

For CEM I systems, accessible porosity decreased continuously along the progress of carbonation due to the pronounced CH carbonation where $CaCO_3$ preferentially precipitates in capillary pores with size > 10 nm (Matsusato et al., 1992; Lawrence et al., 2007; Pham & Prince, 2014). In contrast, blended cements experienced an increase in accessible porosity with carbonation due to pore coarsening between 100-1000 nm caused by the formation of silica gel during C-S-H carbonation (Borges et al., 2010). Although C-S-H carbonation also forms $CaCO_3$, it precipitates outside of the original C-S-H and mainly in pores < 2 nm (Pham & Prince, 2014). Such small gel pores are emptied when dried at 105°C, but not at 55% RH, 21°C. This explains why total porosity decreased, but accessible porosity increased in blended concretes after carbonation. Similar observations were also reported in Papadakis (2000), Auroy et al. (2018), Boumaaza et al. (2020) and Justnes et al. (2020).

All three mass transport properties decreased with lower w/b and after prolonged curing due to reduction in porosity. Carbonation affects mass transport properties differently depending on the binder type. Irrespective of the w/b and curing duration, CEM I systems showed a reduction in diffusivity and sorptivity, while blended cement systems showed an increase. This is in line with the changes in accessible porosity (rather than total porosity) since gas migration and water absorption

occur only in empty pores (Wong et al., 2007). However, O_2 permeability increased for both CEM I and blended cement systems, due to carbonation-induced microcracking, which provide paths of least resistance that are preferentially taken by pressure-induced flow (Wong et al., 2009; Wu et al., 2017). A similar observation was reported in samples containing high GGBS content (~90%) in Borges et al. (2010).

7.4.3 Effect of natural carbonation on microstructure

Microstructural analysis via BSE microscopy has confirmed the reduction in total porosity after natural carbonation regardless of binder type. Furthermore, dark relicts of carbonated belite grains were more commonly observed in blended cements than CEM I presumably due to the lower portlandite content of the former. Shah et al. (2018) observed a dark inner rim located between unreacted cement particles and the inner C-S-H rim with reduced Ca content indicating decalcification, although this was not witnessed in this study. As has been mentioned above, the CO_2 buffer capacity of a mix as is indicated by the $w/CaO_{reactive}$ ratio does not consider the CaO from the unreacted cement and SCMs particles, based on the assumption that they are not reactive to CO_2 (Leemann et al., 2015). However, this might not be strictly true based on the observations in this study.

Carbonation increases the severity of microcracking. However, it should be noted that the microcracks detected in this study could be induced by a combination of drying (during preconditioning) and carbonation shrinkage. Indeed, previous studies by Wu et al. (2015) detected drying-induced microcracks even after gentle stepwise conditioning at 55% RH, 21° C. The drying-induced microcracking is more severe near the exposed surface (< 10 mm). Therefore, to decouple these from carbonation, concretes exposed to the same conditioning, but without carbonation were examined with BSE microscopy at similar depths and the results were used as reference. These showed that non-carbonated samples indeed experienced some drying-induced microcracking (0.027-0.035 mm^{-1}), but was clearly lower than the carbonated samples (0.056-0.092 mm^{-1}) confirming the effect of carbonation on microcracking.

The study also observed that carbonation increases the connectivity and width of microcracks, from 0.5-6 μm to ~9 μm. The characteristics of the detected microcracks are similar to those of drying-induced microcracks reported in Wong et al. (2009) and Wu et al. (2015). In carbonated systems, additional microcracks form as a result of shrinkage that occurs due to loss of water during portlandite carbonation. However, the degree of microcracking was more severe in blended cements than CEM I even though they had lower portlandite content. This can be ascribed to the shrinkage caused by decalcification of C-S-H and the formation of silica gel (Chen et al., 2006). These are consistent with

the increase in permeability observed for all samples, especially in blended concretes containing 50% GGBS.

7.5 Conclusion

This chapter studies the evolution of carbonation depth in paste, mortar and concrete samples after short-term (1-3 months) and longer-term (6-24 months) natural exposure, focusing on four major variables including w/b (0.45 and 0.6), curing duration (3d and 122d), aggregate content (0% for paste, 20% and 50% for mortar, and 70% for concrete), and binder type (CEM I, CEM I + 30% PFA and 50% GGBS). The effects of natural carbonation on mass transport properties and microstructure were investigated. Results derived from this chapter were then employed to model the long-term carbonation resistance for up to 20 years in Chapter 8. The key findings are:

a) The average carbonation depths are consistently larger in 3d-cured blended cement samples (0.98-11.29 mm) than CEM I samples (0.71-3.92 mm) after 1-24 months natural carbonation. Short-term natural exposure of 3 months was able to induce carbonation depths of on average 40.1% of those obtained after prolonged exposure of 24 months, but with 87.5% less carbonation duration.
b) Decreasing w/b from 0.6 to 0.45 is able to reduce the carbonation coefficient comparable to extending curing duration from 3d to 122d for CEM I samples, but the latter is more important for blended cements for improving carbonation resistance.
c) The inclusion of aggregate reduces carbonation coefficients due to the dilution effect dominating over the ITZ effect. However, ITZ percolation can occur with 50% aggregate fraction in the higher w/b (0.6) sample due to a more porous ITZ.
d) The addition of 30% PFA and 50% GGBS makes concrete more vulnerable to carbonation, even after prolonged curing of 122d. Samples containing 30% PFA has on average 9.3% larger carbonation coefficients than 50% GGBS due to the lower reactive CaO content. Water to reactive CaO ratio ($w/CaO_{reactive}$) is a promising indicator for estimating carbonation resistance in different systems, however, the contribution of CaO from unreacted cement particles should also be considered for better accuracy as they can decalcify during natural carbonation, especially in blended systems.
e) Water desorption measurements and BSE image analyses confirm the reduction of total porosity after carbonation for all samples due to $CaCO_3$ precipitation increasing the volume of the solid phases. However, the accessible porosity in blended cement increased after carbonation, indicating a coarsening of the pore structure due to carbonation of C-S-H.

f) The effect of carbonation on mass transport properties is dependent on the binder type. O_2 diffusivity and sorptivity decreased for CEM I but increased for blended cements. These properties agree well with the change in accessible porosity. However, O_2 permeability increased for all samples due to the formation of carbonation-induced microcracks.

g) Carbonation causes changes in the unreacted cementitious phases. BSE images confirm the carbonation of belite grains, which was more extensive in blended cements than CEM I. Unreacted PFA and slag particles do not experience significant elemental change, but decalcification was observed in the reacted slag rims after carbonation.

h) Carbonation induces microcracking. The microcracks are more severe in blended systems than CEM I, in agreement with the changes in permeability after carbonation.

8 Predicting carbonation with artificial neural network analyses

This chapter applied artificial neural networks (ANNs) to predict the long-term carbonation depths in concrete exposed to natural exposure for up to 20 years. Approximately 3300 pieces of data records were compiled from the literature (32 papers and Chapter 7) and 33 influential variables were selected as input neurons in the ANN model. Two critical parameters relating to the architecture of ANNs were optimised to reduce errors in the prediction. Results show a good correlation between the predicted and measured carbonation depths in the testing dataset with an average root mean squared error of 1.97 and an average percentage error of 19.2%. The accuracy of prediction is much higher for larger carbonation depths rendering ANN a suitable approach to model long-term carbonation-induced corrosion. The trained ANN model can replicate some well-established correlations between carbonation depths and certain variables, reinforcing the reliability of ANN in studying the carbonation process. Some less well-understood correlations, such as the influence of exposure conditions on carbonation rates, can also be revealed with the help of ANN. The advantages and limitations of this approach for predicting carbonation are discussed.

8.1 Introduction

Carbonation involves the ingress of atmospheric CO_2 in concrete and its reaction with calcium-bearing constituents, mainly calcium hydroxide and calcium silicate hydrates to form calcium carbonate. This is a neutralisation process that reduces the pH in the pore solution from 13.5 to 9 in the carbonated zone, and thus triggers depassivation and corrosion of embedded steel reinforcement (Bentur et al., 1997). This problem has led to a huge economic burden, estimated to account for 3–5% of the national gross domestic product (Ekolu, 2016). Therefore, a comprehensive understanding of the evolution of carbonation depth for modelling long-term carbonation resistance is required.

In the past decades, many mathematical models for concrete carbonation prediction have been developed (Kobayashi & Uno, 1990; Papadakis et al., 1991a; Papadakis et al., 1991b; Jiang et al., 2000; Khunthongkeaw et al., 2006; Hyvert et al., 2010; Zhang & Xiao, 2018; Carević et al., 2019). Most of these are semi-empirical and developed by fitting fundamental theory, for instance, Fick's first law, to experimental results to determine the required parameters. Despite good correlations reported in previous literature, majority of the proposed carbonation models are confined to the limited experimental data they were developed from. Therefore, these models are not implementable for service life prediction of concrete structures in real environments.

Another obstacle to their practical application is that these models are often based on and validated with results from accelerated carbonation with the assumption that the data can be directly transferred to natural carbonation (Wang & Lee, 2009; Zhang et al., 2013; Ta et al., 2016; Wang et al., 2020). However, this is not the case since accelerated exposure distorts the decalcification processes involved and the carbonates that formed in relation to natural carbonation (Castellote et al., 2009; Chen et al., 2006; Galan et al., 2015; Šavija & Luković, 2016). Such discrepancies would affect the accuracy when modelling long-term carbonation resistance in natural environments. Therefore, utilising natural carbonation data from long-term exposure trials and carbonation surveys would be a more rational approach for modelling carbonation. Unfortunately, such data are generally derived from a large number of variables, often containing missing information and non-linearity, which is difficult to be utilised in conventional modelling methods.

As such, models based on artificial neural networks (ANNs) are a promising alternative to describe the effect of multi factors on carbonation. This is due to their self-learning ability from available data and the convenience of not requiring predetermined assumptions or models. Indeed, previous attempts have shown the feasibility of ANNs in predicting carbonation depths. However, the majority of these were either based on limited number of inputs (Lu & Liu, 2009; Luo et al., 2014; Taffese et al., 2015; Akpinar & Uwanuakwa, 2020) or experimental data from accelerated carbonation (Lu & Liu, 2009; Kwon & Song, 2010; Felix et al., 2021; Londhe et al., 2021). Therefore, the feasibility of ANNs to model carbonation based on abundant natural carbonation data still has not been established.

This study aims to train ANNs to learn from a large amount of natural carbonation data and then to use it to predict the carbonation depth of cementitious materials. Approximately 3300 pieces of natural carbonation data compiled from 33 papers (including Chapter 7), classified into 33 concrete- and environmental-related input parameters, were used to train, validate and test the ANN model. The performance of the trained ANN to predict carbonation depths and the effects of several factors on carbonation resistance were investigated.

8.2 ANN model development

8.2.1 General

ANNs are biologically inspired computational systems composed of an input layer and an output layer, connected by one or more hidden layers (Fig. 8.1). Data are fed into the ANN algorithm through a number of artificial neurons, and then communicated to the nodes in the hidden layers where most of the processing occurs. The output of each node is calculated by multiplying the connected input data with their corresponding weight (connection strength, w_n) and summing up the

biases (b_n). The nodes then pass through an activation function for thresholding purposes and the results are transmitted to the next hidden or output layer. This is the so-called forward propagation process. The predicted and the expected results are compared to determine the direction (larger or smaller) and magnitude of error, which are then transferred backwards through the backpropagation process. Based on this, the weight assigned to each input is thus adjusted and the forward propagation is repeated again. In doing so, the prediction errors are expected to decrease with repeating epochs and the training is completed when the error reaches the target convergence.

To develop a carbonation model using ANN, the methodology was divided into several steps:

Step 1: Compilation of long-term natural carbonation data (Section 8.2.2).

Step 2: Definition of the input variables (Section 8.2.3).

Step 3: Parametric optimisation and ANN training (Section 8.2.4).

Step 4: Prediction of long-term carbonation depths (Section 8.3.2).

Step 5: Investigation of the effect of key variables on carbonation (Section 8.3.3).

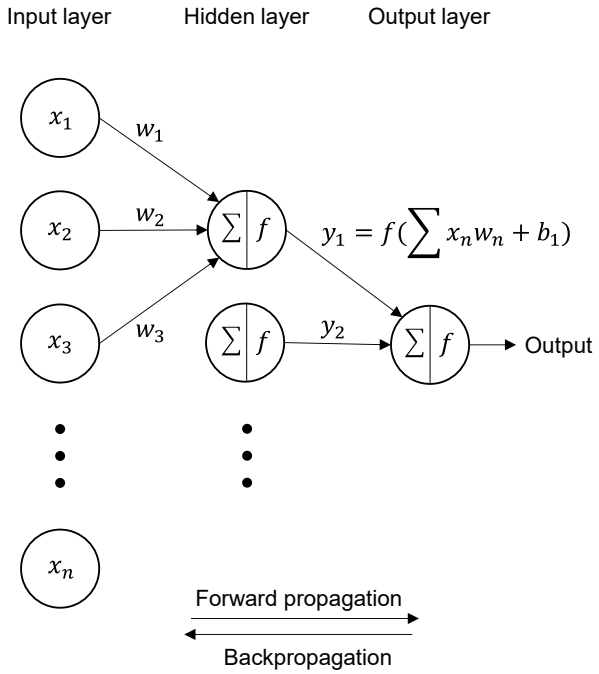


Figure 8.1 Schematic diagram of an ANN.

8.2.2 Data compilation

An extensive literature review was carried out to compile approximately 3300 pieces of data on long-term natural carbonation. These were compiled from 32 papers and Chapter 7 for modelling with ANNs. The summary of the data sources, testing regions and maximum carbonation durations are given in Table 8.1. In general, the literatures were published across a period of more than six decades at worldwide locations with the carbonation duration ranging from 1 months to 20 years. The majority of the data were for concrete specimens cast and cured in the laboratory and then exposed in natural exposure sites. Carbonation depths, determined by the phenolphthalein spray test in most literature, were recorded as the output. Despite this approach being criticised to 'underestimate' the carbonation depth due to the limited ability in determining the partially carbonated zone, results in Chapter 6 have shown this is not the case and its reliability for determining carbonation depth is as good as other techniques such as CRM. However, the carbonation front may not always be distinct and insignificant colouration of phenolphthalein occurred in samples with shallow natural carbonation depth (e.g. < 3 mm) can affect the measurement. Apart from carbonation depth, other concrete- and environmental-related variables were also compiled as inputs to ANNs, which are discussed in more detail in the next section.

The entire dataset was divided into three parts: 70% of the data was used for training, 15% for validating the ANN model (Section 8.2.4) and the remaining 15% was used for testing the trained ANN model (Section 8.3.2). Each subset involved randomly distributed data to be representative of the entire dataset and was completely independent from each other.

Table 8.1 Summary of the literature compiled in this study

Reference	Location	Maximum duration (months)	Data records			
			Total	Training (70%)	Validation (15%)	Testing (15%)
Soda & Yamazaki (1958)	Japan	240	108	76	16	16
Ludwig (1974)	Germany	60	44	31	7	6
Treadway et al. (1983)	Bahrain	9	68	48	10	10
Wierig (1984)	Germany	192	456	319	68	69
Byfors (1985)	Sweden	30	52	36	8	8
Nagataki et al. (1986)	Japan	180	144	101	22	21
Vennesland & Gjorv (1986)	Norway	14.5	18	13	3	2
De Fontenay & Skaarup (1987)	Bahrain	48	440	308	66	66
Ho & Lewis (1987a)	Australia	12	15	11	2	2
Hobbs (1988)	UK	36	71	50	11	10
Gebauer & Torrent (1989)	Switzerland	12	22	15	3	4
Ai-Amoudi et al. (1991)	Saudi Arabia	10	18	13	3	2
Hakkinen (1992)	Finland	22	14	10	2	2
Thomas & Matthews (1992)	UK	48	383	268	57	58
Parrott (1992)	UK	48	8	6	1	1
Haque & Kawamura (1992)	Australia	48	36	25	5	6
De Ceukelaire & Van Nieuwenburg (1993)	Belgium	18.9	3	2	0	1
Ewertson & Petersson (1993)	Sweden	24	36	25	5	6
Balayssac et al. (1995)	France	18	48	34	7	7
Jones et al. (2001)	UK	24	210	147	32	31
Houst & Wittmann (2002)	Switzerland	40.5	10	7	2	1
Sanjuán et al. (2003)	Spain	24	8	6	1	1
Khunthongkeaw et al. (2006)	Thailand	24	440	308	66	66
Roziere et al. (2009)	France	12	16	11	2	3
Kuosa (2010)	Finland	26	69	48	10	11
Valcuende & Parra (2010)	Spain	42.5	16	11	2	3
Hyvert et al. (2010)	France	10	21	15	3	3
Chatveera & Lertwattanaruk (2011)	Thailand	6	27	19	4	4
Jia et al. (2012)	China	23.7	288	202	43	43
Ribeiro et al. (2018)	Portugal	120	33	23	5	5
Sanjuán et al. (2018)	Spain	24	24	17	4	3
Kumar et al. (2018)	India	3.6	45	32	7	6
Chapter 7 (this thesis)	UK	24	84	59	13	12
Total			3275	2296	490	489

8.2.3 Input variables

The literature on the physical and chemical mechanisms of carbonation was reviewed to identify important variables that influence the diffusion-reaction process of carbonation. However, the number of potential variables is huge, and it is extremely rare to find studies that report on all of these variables. As such, the list of variables that will be considered for this study was reduced to 33, retaining those that are commonly found in the literature (at least 50% of the population). Nevertheless, the selected variables still outnumber those considered in previous carbonation models using ANNs. With the list of variables, their values were then picked from the abovementioned literature to act as inputs into the ANN model.

The concrete- and environment-related variables marked • in Table 8.2 were taken as neurons in the input layer of the ANNs. Variables relating to concrete can be further summarised into 4 categories covering cement composition, supplementary cementitious materials (SCMs), mix proportions and curing. The values in the right-hand column of Table 8.2 are the corresponding default values of the neurons employed to study the effect of each variable on carbonation depths (Section 8.3.3). Unless otherwise stated, these values were also assigned to the missing variables.

The oxide composition (%), mainly CaO and sodium oxide equivalent (Na_2O_{eq} = Na_2O + 0.658 K_2O), of the cement, were involved as two neurons. This is because CO_2 is mainly combined with reactive CaO to form $CaCO_3$ during carbonation, thus the CaO content in cement is closely linked to the CO_2 buffer capacity (Leemann et al., 2015). Na_2O_{eq} content is another important factor influencing the alkalinity of concrete pore solution (Kobayashi & Uno, 1989). In some papers, where the exact oxide compositions were not provided, information concerning the type of cement was used as an estimation. For example, if the unknown values were from a sulphate resisting cement, the oxide composition of the same type of cement were averaged and assigned to the unknown values.

SCMs involving fly ash (PFA), ground granulated blastfurnace slag (GGBS), microsilica (MS) and limestone filler (LS) were involved as neurons because these have been widely used to partially replace ordinary Portland cement both in practical application and in the compiled database. These were specified in terms of replacement level (%) and content (kg/m^3). Similar to cement, CaO composition (%) of PFA and GGBS were incorporated in the model. This input was also used to separate low and high lime PFA.

Clearly, mix proportions have a critical influence on carbonation. Water content and water/binder (w/b) ratio are closely relevant to the porosity of the concrete, and cement (binder) content determines the amount of carbonatable materials. These govern the microstructure and transport properties, which have been reported to change continuously during natural carbonation in Chapter 7. Nevertheless,

they were not incorporated as input neurons due to limited information in previous literature. The aggregate content was shown to affect the carbonation depth in Buenfeld & Okundi (1998) and also chapter 7, however, these values were not readily available in many papers, thus the coarse/fine aggregate ratio and maximum aggregate size were incorporated as two alternative neurons. Note that the aggregate involved were generally natural impermeable aggregate rather than lightweight aggregate.

Curing is another critical factor governing the development of pore structure and results from Chapter 7 have shown that good curing is important for blended cements for improving carbonation resistance. However, this variable can be especially difficult to justify due to the wide range of curing regimes applied in the literature, which were often composed of several curing regimes and durations. Generally, there are four curing types (water, moist, air and sealed curing) and each has three main features (the exposure moisture content, temperature, and duration). The moisture content was defined based on its relative impact on cement hydration; 0 for no curing and 10 for water curing. Moist curing occurs in a fog room with relative humidity (RH) > 90% to allow hydration to continue, while the RH for air curing is generally < 90% and hydration can effectively cease (Patel et al., 1988). Therefore, this RH value was used to categorise the intermediate curing regimes. Seal curing was taken as < 90% RH and was assigned a value of 4. The curing duration was entered as a logarithmic value because the benefit of curing at early stages clearly outweighs the benefit from the same duration at later ages. Therefore, the weighted duration, calculated by multiplying the assigned factors and the logarithmic duration, was involved as a neuron.

The exposure environment is another important factor, but ill-defined for natural environmental conditions. For instance, moisture content and temperature vary significantly with time for data records exposed to external carbonation. For these data, the annual average temperature and RH were collected from meteorology records. Three qualitative neurons were included to categorise whether the exposure is internal or external, sheltered or unsheltered from direct rainfall. In some climates, the temperature may vary only slightly while in some regions can fluctuate significantly even between day and night. To account for these aspects, another six qualitative neurons were involved to represent the geographical regions represented in the compiled data. CO_2 concentration was also incorporated as an input neuron. Considering the fact that the atmospheric CO_2 concentration rises with time (Prentice et al., 2001), 0.03% was assigned to papers published before the year 1950, 0.035% for those published between 1950 and 2000 and 0.04% after 2000.

Prior to ANN training, all data were scaled to the 0-1 range using the min-max normalisation method (Equation 8.1) to take advantage of the full range of the activation function. For example, none of the

maximum aggregate sizes in the database involved a value < 10 mm and hence these data were transformed by subtracting 10 prior to normalisation.

$$x' = \frac{x - \min(x)}{\max(x) - \min(x)} \qquad \text{Equation 8.1}$$

Table 8.2 Summary of input variables.

Input variables	Untransformed default values
Cement (2)	
● CaO (%)	60
● Na_2O_{eq} (%)	0.5
SCMs (10)	
● PFA CaO content (%)	0
● PFA replacement level (%)	0
● PFA content (kg/m3)	0
● GGBS CaO content (%)	0
● GGBS replacement level (%)	0
● GGBS content (kg/m3)	0
● MS replacement level (%)	0
● MS content (kg/m3)	0
● LS replacement level (%)	0
● LS content (kg/m3)	0
Mix proportions (5)	
● Water content (kg/m3)	180
● Cement content (kg/m3)	325
● Water/binder (ratio)	0.55
● Coarse/fine aggregate (ratio)	2
● Maximum aggregate size (mm)	20
Curing (2)	
Curing type – weight factors:	
No curing – 0	
Air curing (RH < 90%) – 4	
Seal curing - 4	
Moist curing (RH ≥ 90%) – 8	
Water curing –10	
● Weighted duration (weight factor × log(days))	3
● Temperature (ºC)	20
Natural exposure (14)	
● Internal (Yes/No)	No
● External sheltered (Yes/No)	Yes
● External unsheltered (Yes/No)	No
● Average RH (%)	65
● Average temperature (ºC)	20
● CO_2 concentration (%)	0.04
● Exposure duration (month)	240
● Exposure duration (√month)	15.49
Region:	
● UK (Yes/No)	Yes
● Gulf (Yes/No)	No
● Germany (Yes/No)	No
● Thailand (Yes/No)	No
● China (Yes/No)	No
● Japan (Yes/No)	No

8.2.4 Parametric optimisation and ANN training

The ANNs model was developed with Matlab v.2019a software and supervised with the 'feedforward backpropagation' method (Rumelhart et al., 1987). The performance of an ANN model can be affected by a number of hyperparameters, for instance, the number of hidden layers, the choice of activation functions, the number of epochs, learning rate, etc. To obtain a general overview of the effect of different hyperparameters, trials were performed on the entire training dataset with a combination of different values in these parameters. Results showed that the number of hidden layers and hidden layer neurons had a more profound influence and thus these were further optimised. The number of hidden layers neurons (1-50) and hidden layers (1-2) were studied. The other parameters were kept constant at 100 epochs, tansig as the activation functions, and 0.4 as the learning rate. The trained ANN for each optimisation stage was applied to both the training and validation datasets for prediction.

In this study, the difference between the predicted and actual result was calculated using root mean squared error (RMSE) (equation 8.2) and percentage of absolute error (equation 8.3) to meet the convergence criteria. These errors were expected to converge to a reasonably low level after optimisation. However, attempts to reduce the error too much may lead to the problem of overfitting where the ANN algorithm starts to learn from noise in the data, which would increase errors in the validation and testing datasets.

$$RMSE = \sqrt{\frac{\sum_{i=1}^{n}(y_i - t_i)^2}{n}} \qquad \text{Equation 8.2}$$

$$\text{Absolute error (\%)} = \frac{y_i - t_i}{y_i} \times 100\% \qquad \text{Equation 8.3}$$

where y_i and t_i are the correct and predicted results, and n is the number of data facts.

The optimised architecture of the ANN model was then applied to the testing dataset to predict the carbonation depths and the results are shown in Section 8.3.2.

8.3 Results

8.3.1 Parametric optimisation for ANN models

Fig. 8.2 ab show the evolution of average RMSE and average percentage error with the number of neurons in the (first and only) hidden layer. The input and output layers have 33 and 1 neurons respectively. Results show large errors when incorporating just 1 neuron and the errors decrease with increase in neuron number (~15) indicating an improvement of performance in the ANN model. The curves for training and validation datasets agree well until 15 neurons, after which the two curves diverge. The error for the training set keeps decreasing, while the one for validation shows an increasing trend. This indicates that overfitting starts to occur, and the ANN algorithm begins to learn from noise in the data.

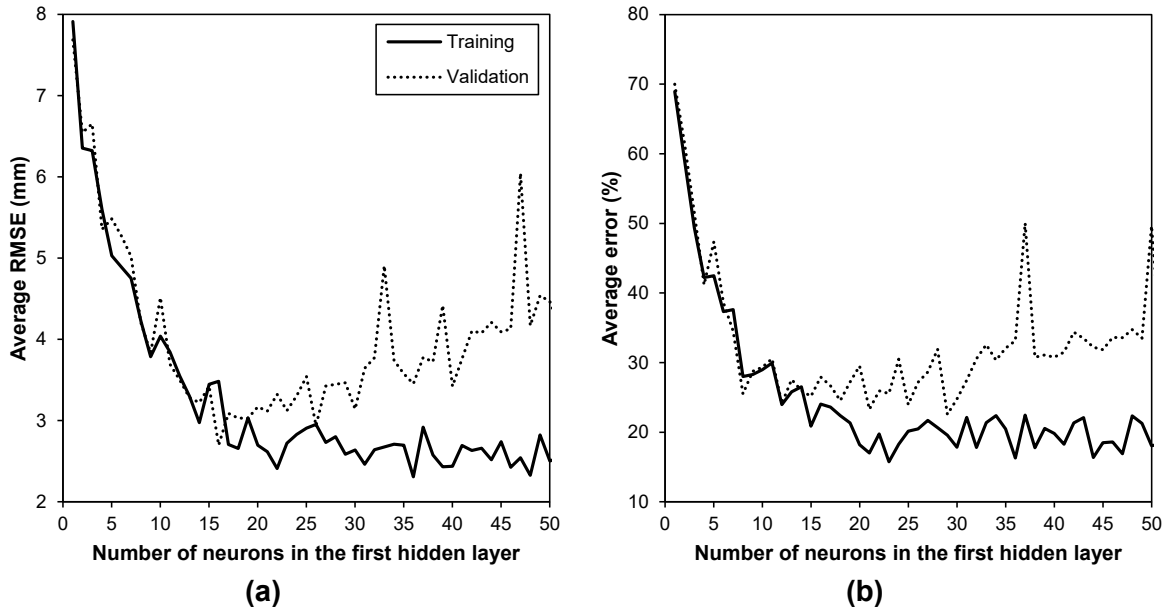


Figure 8.2 Effect of the number of neurons in the (first and only) hidden layer on the average RMSE (a) and average percentage error (b).

Fig. 8.3 shows the errors from training and validation datasets when increasing the number of neurons in the second hidden layer. 15 neurons were incorporated in the first hidden layer. A similar trend was observed, however, the overall errors are significantly lower. Again, beyond 10 neurons, overfitting starts to occur and the errors in the validation set increased. The incorporation of a second hidden layer in addition to 15 neurons in the first hidden layer, does not reduce errors in the training set but decreases errors by on average 29% in the validation set. The lowest errors were 2.1 mm for RMSE and 20.3% for percentage error when using 10 neurons. Therefore, it is beneficial to incorporate 10

neurons in the second hidden layer for a better performing ANN. This architecture was then applied to the testing datasets to predict carbonation depths.

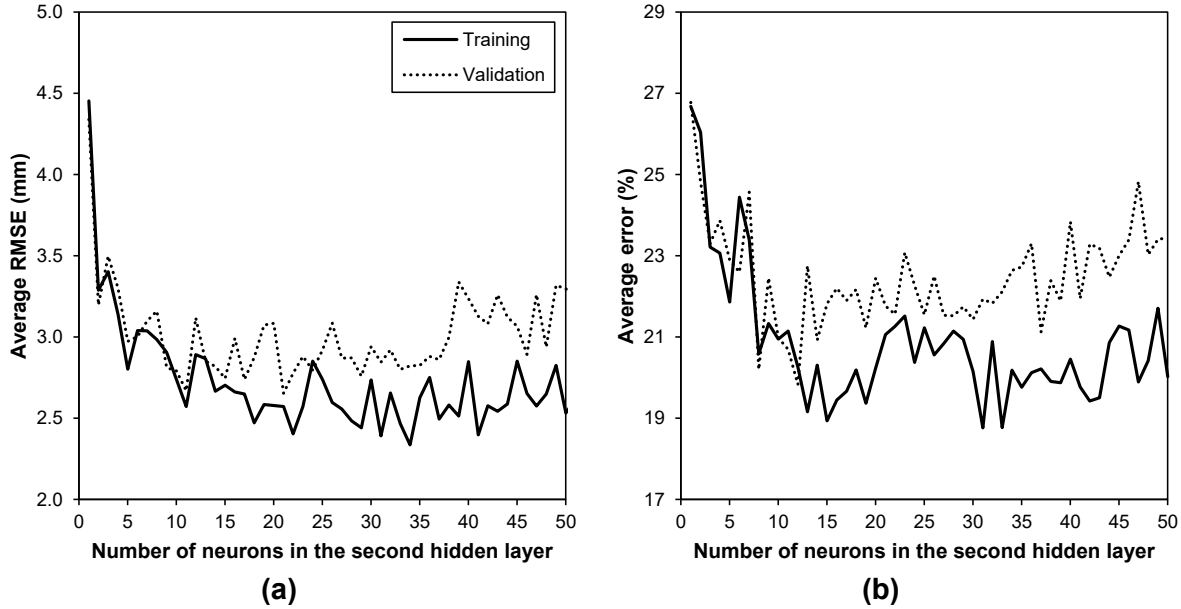


Figure 8.3 Effect of the number of neurons in the second hidden layer on the average RMSE (a) and percentage error (b).

8.3.2 Prediction of carbonation depth

Fig. 8.4 shows the correlation between predicted carbonation depth and measured carbonation depth for training, validation and testing datasets. The predicted results were obtained with the trained ANN model with an architecture of 33-15-10-1 (indicating the number of neurons in the input, first and second hidden, and output layer respectively). Results show that the majority of the results were located near the 1:1 line within ±5 mm boundaries with a few points scattering in the validation set. A similar observation was made in the testing set (Fig. 8.4c), with average errors being 1.97 mm and 19.2% for RMSE and percentage error respectively. These obtained errors were very close to those obtained from the validation dataset after optimisation (2.09 and 20.3%) indicating a good reliability of the trained ANN model. It is also remarkable to find good predictions for large carbonation depths, e.g. 50 mm predicted with an accuracy of 95.7% (arrowed in Fig. 8.4c).

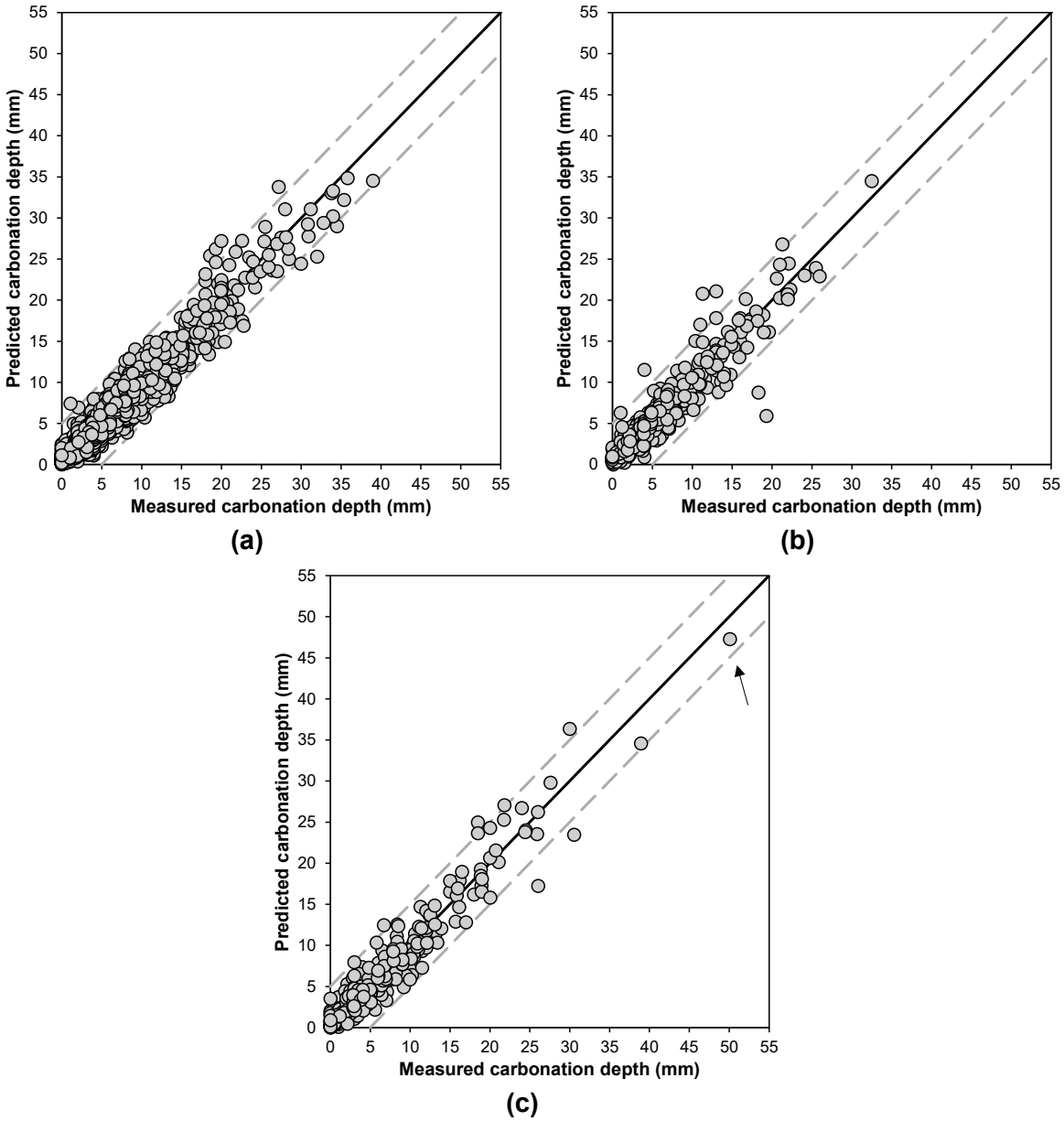


Figure 8.4 Correlation between predicted and measured carbonation depths for the training (a), validation (b), and testing (c) datasets. Solid and dashed lines represent 1:1 and ±5 mm boundaries respectively.

The correlation between absolute error and the measured carbonation depth for each data record is presented in Fig. 8.5a. Results show that the majority of the absolute error was < 4 mm, which is deemed reasonable considering the huge number of variables involved and the fact that the presence of aggregate in concrete can significantly affect the carbonation front. However, considering that most of the measured carbonation depths were < 10 mm, the errors are not necessarily regarded as small. Indeed, when comparing the percentage error with the measured carbonation depths for each data record (Fig. 8.5b), the error can be up to 120% when the measured carbonation depth was < 3 mm. Nevertheless, the percentage error decreases significantly with the measured carbonation depth and is

only 4.3% for 50 mm depth (arrowed). This is encouraging because the main application of the model is to predict long-term carbonation depth and a large carbonation depth is a necessary condition for the carbonation-induced corrosion. This is also deemed suitable for blended concretes due to their higher vulnerability to carbonation than CEM I concrete. Therefore, the trained ANN model is believed to be reliable for predicting long-term natural carbonation exposure.

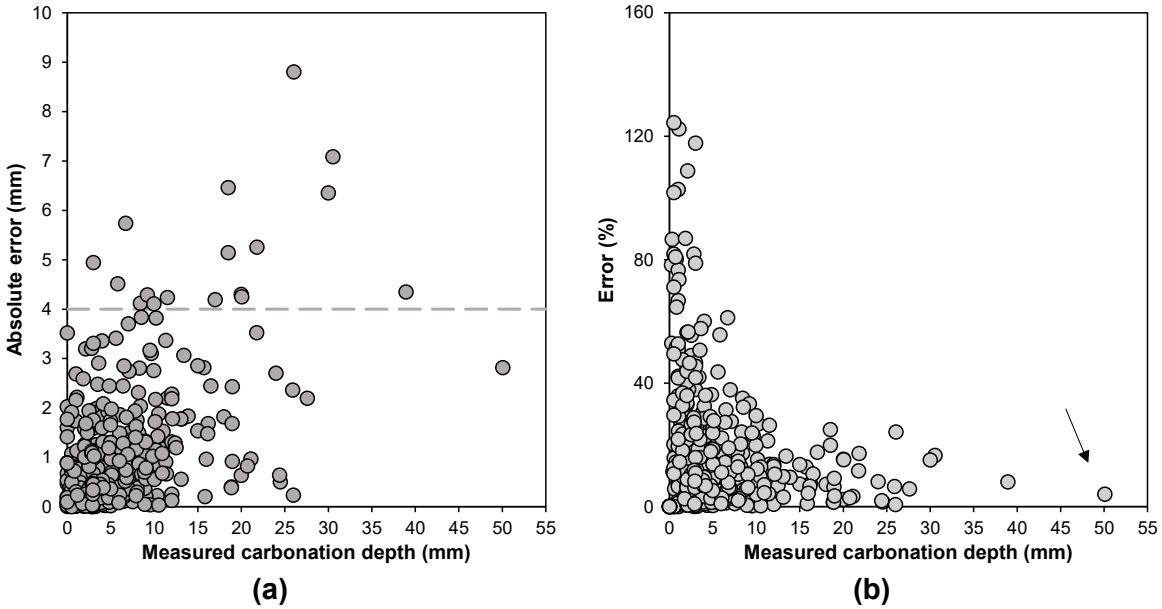


Figure 8.5 Correlation of absolute error (a) and percentage error (b) with the measured carbonation depth.

The entire database was also analysed using the square-root-of-time model. Fig. 8.6a shows a wide scatter of the carbonation depth and a very poor correlation with the square-root-of-carbonation duration ($R^2 = 0.13$). The calculated carbonation coefficient and initial carbonation depth were used to predict the carbonation depth and an average error percentage of 121.9% was obtained (Fig. 8.6b). This is perhaps not surprising considering the large amount of data for linear regression and distinct carbonation conditions involved.

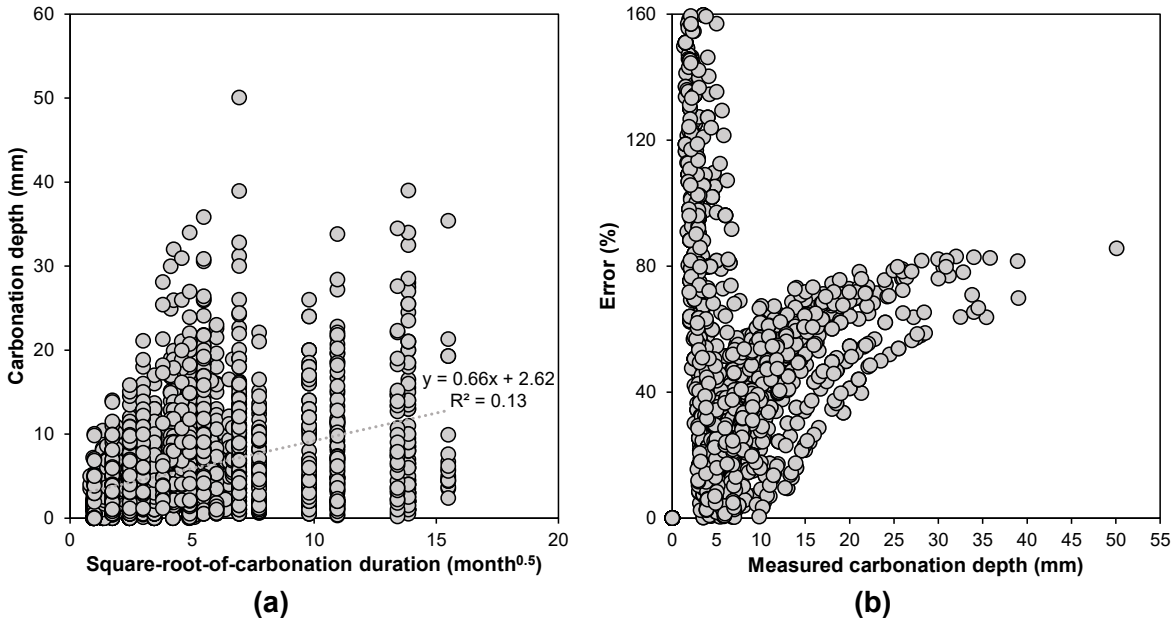


Figure 8.6 Correlation of measured carbonation depth and square-root-of-carbonation duration for the entire dataset (a), and percentage error obtained with the prediction (b).

8.3.3 Effect of variables on carbonation

The trained ANN model was used to study the effect of specific input variables on carbonation depth. This was conducted by running the ANN model with all the variables set as the default values listed in Table 8.2, while the variable of interest was held constant. Their effect on carbonation depth can then be investigated by employing a range of values. Although the effects of some variables are already well-established in the literature, for instance, w/b and RH, these were still studied in this chapter to reinforce the reliability of the ANN model in revealing hidden correlations between the carbonation process and the input variables. To be specific, the following simulations were made by changing the tested variables while controlling the other variables as CEM I cement with 60% CaO, 0.5% Na_2O_{eq} and no SCMs addition, water and cement content of 180 and 325 kg/m^3, w/b of 0.55, coarse/fine aggregate ratio of 2, maximum aggregate size of 20mm, curing factor of 3, curing temperature of 20ºC, external carbonation sheltered from rainfall at an average RH, temperature, and CO_2 concentration of 65%, 20ºC and 0.04% for 2 years in the UK.

Fig. 8.7a shows the predicted carbonation depths as a function of duration for internal, external sheltered and unsheltered exposures for up to 20 years (240 months). Results clearly show that internal exposure has the largest carbonation depth, followed by external sheltered and external unsheltered. This is unsurprising because unsheltered concretes are directly exposed to rainfall, and the pores are often water-filled, which significantly retards the diffusion of CO_2 (Wierig, 1984). The effect of Na_2O_{eq} in cement on carbonation depth is shown in Fig. 8.7b and increasing the alkali

content is predicted to increase the carbonation rate irrespective of the exposure conditions. A similar observation was also reported in Kobayashi & Uno (1989) stating that the carbonation rate can be enhanced with increased pH in the pore solution.

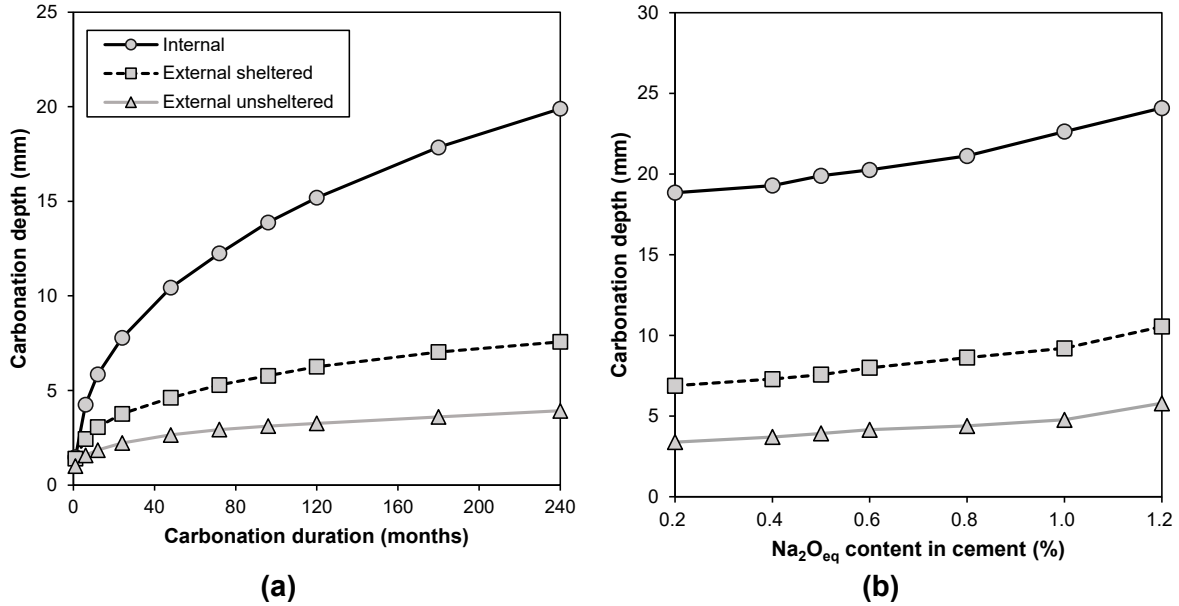


Figure 8.7 Effect of different exposure types (a) and Na_2O_{eq} content in cement (b) on carbonation depth.

The effect of the PFA replacement level is illustrated in Fig. 8.8a and this shows increasing carbonation depths with PFA content. This observation is in agreement with Ho & Lewis (1983) and Ogha & Nagataki (1989). Substituting CEM I with 10% PFA has only limited effect on the carbonation rate, which agrees with Khunthongkeaw et al. (2006), while increasing to 50% PFA is predicted to double the carbonation depth regardless of the exposure conditions. However, it should be noted that this prediction is based on 3 days of moist curing, and therefore the degree of pozzolanic reaction is expected to be low. The effect of the PFA replacement level is envisaged to be smaller for concretes with prolonged curing. When comparing different SCMs (Fig. 8.8b), CEM I with 30% PFA is found to have the largest carbonation depth, followed by 50% GGBS, which is in line with the findings in Chapter 7. However, the additions of 10% microsilica (MS) and limestone (LS) only marginally increase the carbonation rate. This could be associated with the lower replacement level and their very fine particle size that prompts nucleation of hydration and densifying the microstructure at an early age (De Weerdt et al., 2011).

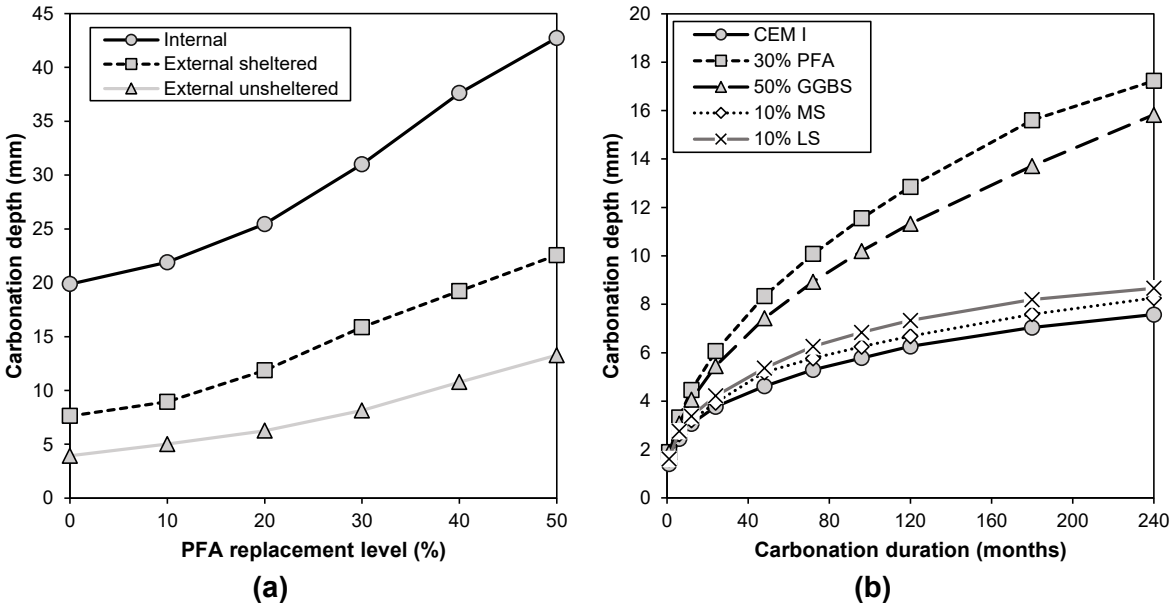


Figure 8.8 Effect of PFA replacement level (a) and different SCMs (b) on carbonation depth.

Fig. 8.9a shows that increasing the cement content at constant w/b reduces the carbonation rate. This is expected because cement content defines the amount of carbonatable material in concrete. When keeping water content constant and changing w/b, an increasing trend is observed in Fig. 8.9b. The effect of w/b is found to be significant as the carbonation depths are almost quadrupled when increasing the w/b from 0.25 to 1. The w/b controls the pore structure and total porosity in concrete, the larger the w/b, the higher the total porosity, favouring the transport of CO_2. Curing is another critical factor that governs the development of pore structure. Fig. 8.9c shows that extending moist curing duration from 3 to 28 days is predicted to reduce carbonation depth by on average 43%.

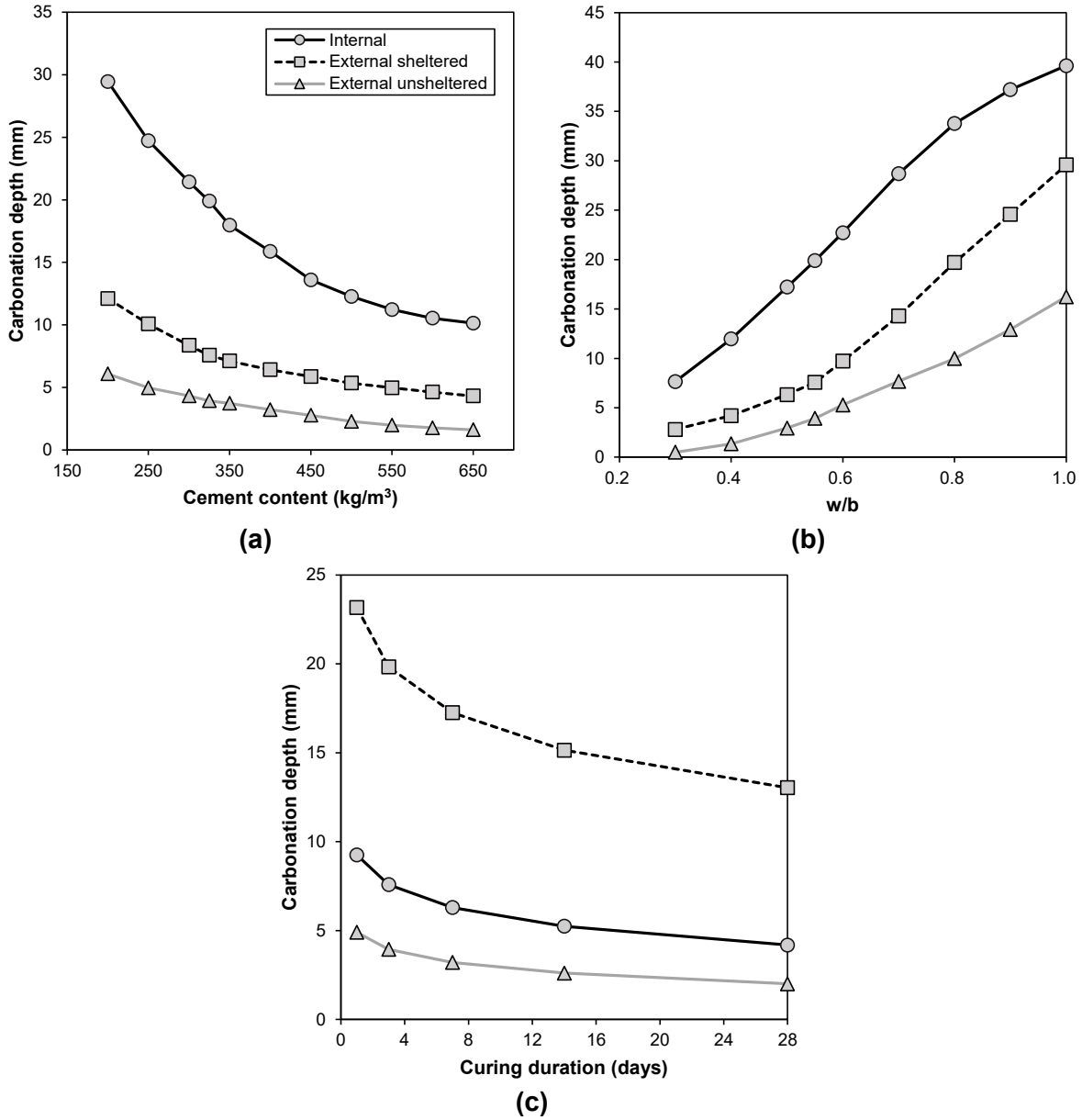


Figure 8.9 Effect of cement content (a), w/b (b), and durations for moist curing (c) on carbonation depth.

The effect of RH and temperature in the exposure environment on carbonation depth is shown in Fig. 8.10a. The carbonation rate is found to be the highest between 55% and 65% RH, which is in line with the optimum RH for carbonation reported in Wierig (1984) and Saeki et al. (1991). These well-established correlations were replicated by the trained ANN model reinforcing the reliability of ANN in studying the carbonation process. The model can then be utilised to predict the effect of less well-understood variables.

Fig. 8.10b illustrates the evolution of carbonation depths with duration in six worldwide regions: London (UK, 71% RH, 12 ºC), Manama (Bahrain, 63% RH, 28 ºC), Berlin (Germany, 71% RH, 10

ºC), Bangkok (Thailand, 66% RH, 30 ºC), Beijing (China, 51% RH, 13ºC), and Tokyo (Japan, 71% RH, 17 ºC). The annual average RH and temperature were all collected from meteorology records. For the same concretes, the carbonation rates are predicted to be the highest in Manama due to the high temperature, moderate moisture content, and high CO_2 level from the oil industry, larger in Bangkok, and Tokyo than Beijing, London, and Berlin. The utilisation of ANNs enables the comparison of carbonation rates between different regions, which is otherwise difficult for the conventional modelling approach due to the different cements, mix proportions and exposure conditions.

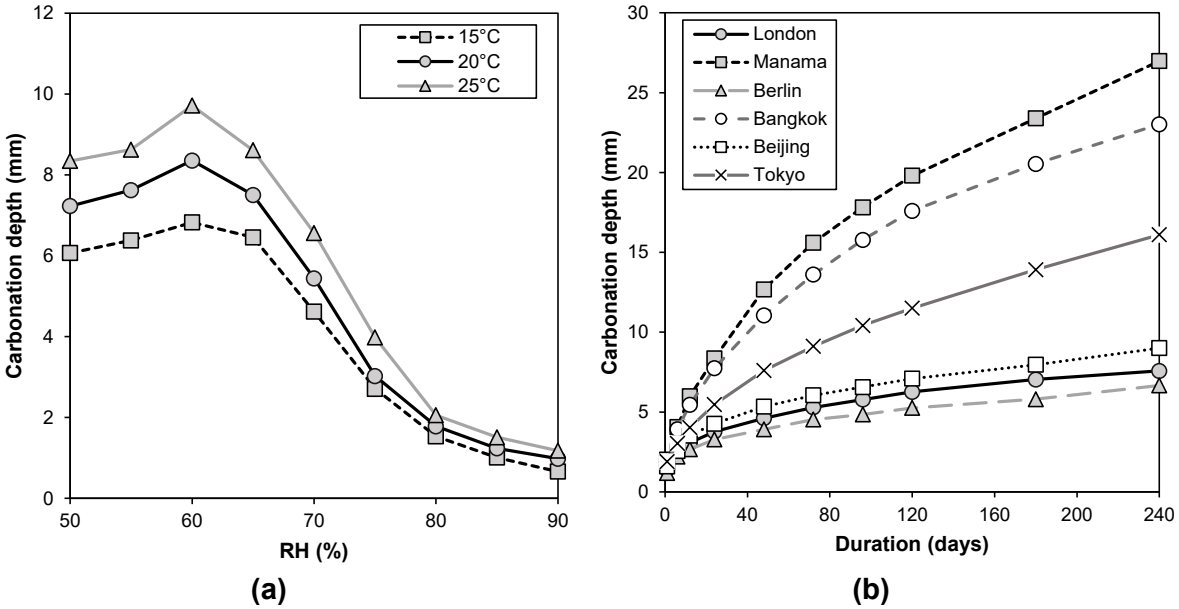


Figure 8.10 Effect of RH and temperature in the exposure environment (a), and exposure locations (b) on carbonation depth.

8.4 Discussion

Results show that it is necessary to perform a parametric optimisation to increase the performance of ANN models and to avoid overlearning from the noise in the dataset. However, even though some of the parameters have been optimised before applying to the testing dataset, the percentage error is still larger than 19%. It is almost certain that this error can be further reduced with additional optimisation and more reliable training facts. The possible sources of the errors from ANN prediction can be associated with the following factors:

- A number of data records have poor reliability. Assigning the missing data in some of the key input variables with assumed values could distort the true relationship.

- Concrete is a heterogeneous material and the studied area or number of replicates in some papers could be insufficient to be truly representative.
- The measurement of carbonation depth using phenolphthalein cannot always yield a distinct colouration boundary. This was rarely specified in the previous papers and can be interpreted in different manners for different researchers. For example, there are a number of zero values of carbonation depth in Jia et al. (2012) even after a natural internal exposure of 11.8 months.
- Another possible source of error could arise from the disturbance of chloride as some of the exposure regions could suffer from the airborne chlorides carried by sea wind, for instance, Bahrain (Treadway et al., 1983; De Fontenay & Skaarup, 1987) and Bangkok (Khunthongkeaw et al., 2006; Chatveera & Lertwattanaruk, 2011). Such data can take up around 30% of the total number of data records.

The predicted carbonation depths from the testing dataset correlate well with the measured carbonation depths indicating the reliability of the trained ANN algorithm to cope with a large amount of data when predicting natural carbonation depths. This is further reinforced with the fact that some of the well-established nonlinear correlations between variables and carbonation depths can be replicated with the ANN model. The results demonstrate a much better accuracy for larger carbonation depth rendering the trained ANN algorithm a suitable approach for modelling carbonation-induced corrosion after long-term natural carbonation. The trained ANN can then be used to predict the carbonation of samples that are not included in the compiled database as long as the required variables are provided. However, further studies are still needed to confirm the reliability of the ANN algorithm trained with the current database when predicting the carbonation of new cementitious materials such as calcium sulphoaluminate/belite cements, alkali-activated cements, and magnesium silicate based binders. Furthermore, since the compiled data only extended to 20 years, it would be unwise to attempt to predict directly to longer periods, thus the prediction of using this ANN model is limited to 20 years, though this is still not enough when compared with the 50- or 120-year design service life of typical concrete structures. This could be somewhat mitigated by learning more precise correlations between carbonation depth and duration within the scope of 20 years and then extrapolating these to longer-term performance. Future attempts should be conducted to cover this work.

8.5 Conclusions

This study applied artificial neural networks (ANNs) to predict long-term natural carbonation depths for up to 20 years based on approximately 3300 pieces of natural carbonation data records compiled from 32 studies. The ability of ANNs to cope with a large amount of data was utilised to learn from

33 input variables and study the effects of some of the key variables on carbonation depth. The ANN model was trained and validated with an architecture of 33-15-10-1 and then applied to the testing dataset. The main findings are:

a) The predicted carbonation depths correlate well with the measured carbonation depths in the testing dataset with an average root mean squared error of 1.97 and an average percentage error of 19.2%. The square-root-of-time model however, is not capable of dealing with such a large database, which derived an average percentage error of 121.9%.
b) The majority of the absolute errors from prediction are smaller than 4 mm and the prediction accuracy is much higher for larger carbonation depths, which is an essential condition for carbonation-induced corrosion. This indicates that ANNs based modelling is a promising approach for modelling long-term carbonation depths.
c) The trained ANN model can reveal well-established correlations between carbonation depth and some variables, reinforcing the reliability of ANNs in studying nonlinear carbonation behaviour.
d) The utilisation of an ANN model can explore some less well-understood effects of certain variables that are otherwise difficult for other modelling techniques, for example, the comparison of carbonation rates at different exposure regions.

9 Conclusions and further research

9.1 Conclusions

Accelerated carbonation distorts the overall carbonation mechanism in relation to natural carbonation, providing results that affect the accuracy of the carbonation prediction models. This flaw can be especially significant for blended cements due to the lower portlandite content and thus the lower CO_2 binding capacity. As such, this thesis aims to develop a reliable alternative methodology to assess the carbonation resistance of cement-based materials. This is based on short-term exposure to natural carbonation, high-resolution characterisation of carbonation profile with time, and extrapolation to longer-term carbonation resistance. The main technical challenge is the ability to detect and measure the limited changes in properties due to the short-term natural carbonation, which is difficult for the most widely used techniques for measuring carbonation depth, i.e., phenolphthalein spray test and various profile-grinding analysis techniques such as thermogravimetry, X-ray diffraction and Fourier transform infrared spectroscopy. Therefore, an alternative technique, confocal Raman microscopy (CRM), was optimised first to explore its feasibility for this application. The main conclusions related to the original objectives of the thesis are as follows:

Objective 1: Optimise and validate CRM for studying carbonation in cement-based materials.

A parametric optimisation for CRM was carried out in Chapter 4 to study the effect of various operating parameters on data quality. The use of short laser wavelength (532 nm) is advantageous over 785 nm for cement-based materials as it yields a higher signal-to-noise ratio (SNR) in the collected spectrum at the same parametric input and can avoid photoluminescence bands. The SNR of the collected spectrum increases with increase in laser power, exposure time and accumulation scan following a power law trend ($R^2 > 0.95$). The optimisation work showed that a 4.15 mW laser power, 2s exposure time and scan accumulation of 2 with a 532 nm laser represent a good operating condition for Raman analysis of cement-based materials. This yields an SNR of > 10 for all investigated phases at a relatively short testing time and low risk of laser-induced damage.

The effect of sample preparation on Raman scanning was also investigated. Freshly cut specimens can be analysed as-is without drying, however, the presence of residual surface moisture can obscure phase detection. This problem is mitigated by short gentle drying prior to Raman analysis. For example, drying at 45% RH, 21ºC for several minutes improves SNR significantly, achieving values that are equivalent to those obtained after long-term drying (1 month) at 33% RH. Surface grinding and polishing prior to analysis increases peak intensities, improves spatial resolution of Raman maps

and enables detection of finer features. Repeated spot laser irradiation up to 1000 accumulations at 4.5 mW did not cause detectable Raman peak shifts or formation of new peaks, suggesting no changes to the chemical structure or composition of the analysed phases. However, closely spaced laser irradiation (< 20 μm step size) during Raman mapping can cause extensive microcracking due to localised heating, especially for carbonated systems. This effect can be mitigated by using a step size > 20 μm or by epoxy impregnating the specimen prior to mapping.

CRM has huge potential for high-resolution chemical mapping to characterise the composition and spatial distribution of various phases (e.g. unreacted cement, portlandite and calcite) in cement-based materials. The obtained maps can be further processed by image analysis to extract quantitative information to complement results from BSE microscopy.

Objective 2: Characterise phase evolution of cementitious materials in real-time when exposed to natural and accelerated carbonation.

The feasibility of CRM to trace the evolution of various cementitious phases (calcium carbonate polymorphs, portlandite, unreacted cement) subjected to early (< 7 days) surface carbonation under both natural and accelerated conditions was investigated in Chapter 5. Results show that surface carbonation completed within 1 d of accelerated carbonation, but the formation of calcite is expected to continue beyond 7d for natural carbonation. Portlandite and ettringite decreased rapidly under accelerated carbonation but much more gradually under natural carbonation. Unreacted cement particles remained relatively unaffected throughout the 7d exposure to carbonation. Overall, this study demonstrated that Raman microscopy is a powerful tool for non-destructive real-time monitoring the evolution of various cementitious phases of surface carbonation after short-term exposure.

Objective 3: Determine the reliability of CRM for measuring shallow carbonation depth after relatively short-term natural exposure.

The reliability of CRM in determining carbonation depth was studied by comparing with the widely used phenolphthalein and profile-grinding analysis techniques in Chapter 6. Results show that the carbonation fronts observed with CRM were distinct and matched well with those observed with the phenolphthalein method under accelerated conditions. The average difference in the carbonation depths measured with these two methods was 1.2% for accelerated carbonation. This increased to 14.3% for short-term (1-3 months) natural carbonation due to the ambiguous colouration of phenolphthalein when measuring shallow carbonation depth in some samples. The profile-grinding analysis measures only the ‘apparent’ maximum carbonation depth, which increases with the degree of variation of the carbonation front and sampling interval adopted. With a sampling interval of 3 mm,

the ‘apparent’ maximum carbonation depths observed in this chapter was on average 16.6% larger than the actual maximum carbonation depths measured by CRM image analysis.

A simple method was proposed to estimate the average carbonation depth from the carbonation profile. The method involves fitting a regression to the transition zone to determine the depth at which the carbonation front is divided into two equal areas. The average carbonation depths estimated from profile-grinding using the proposed method agreed well with those determined by CRM image analysis, with the average difference being only 0.7 mm.

CRM is demonstrated as a reliable technique for measuring the true carbonation depth of cement-based materials and is especially powerful for measuring shallow carbonation depths (e.g. < 3 mm) induced by short-term natural carbonation, which are otherwise difficult or impossible to measure with either phenolphthalein or profile-grinding analysis. The smallest average carbonation depth observed with CRM in this study was 0.71 mm in a CEM I cement paste naturally carbonated for 1 month.

Objective 4: Investigate the evolution of natural carbonation in cement-based materials containing SCMs; examine the effect of different influential factors of carbonation (water/binder ratio, curing duration, aggregate content, and binder type), and the influence of natural carbonation on microstructure and transport properties.

CRM, together with phenolphthalein spray test, was therefore applied to study the evolution of carbonation depth in different binding materials for both short-term (1-3 months) and longer-term (6 months - 2 years) carbonation in Chapter 7, focusing on four important influential factors of carbonation involving water/binder ratio (w/b: 0.45 and 0.6), curing duration (3d and 122d), aggregate content (0% for paste, 20% and 50% for mortar, and 70% for concrete), and supplementary cementitious materials (SCMs: CEM I, CEM I + 30% fly ash and 50% slag). Results show that decreasing w/b from 0.6 to 0.45 is able to reduce the carbonation coefficient comparable to extending curing duration from 3d to 122d for CEM I samples, but the latter is more important for blended cements in enhancing carbonation resistance. The inclusion of more impermeable aggregate reduces the carbonation coefficient, but ITZ percolation can happen for high w/b samples with 50% aggregate fraction presumably due to more porous ITZ. Instead of using SCMs replacement level, the CO_2 binding capacity ($w/CaO_{reactive}$) is found to be a more reasonable indicator of carbonation resistance due to a good correlation with the carbonation coefficients after 122d curing ($R^2 > 0.88$) and the ability to make comparisons between different materials.

The effects of natural carbonation on mass transport properties and microstructure were also investigated. Results show that the effect of natural carbonation on microstructure and mass transport

properties are dependent on the binder type. Carbonation reduces the total porosity for all tested samples as shown by water desorption measurements and BSE imaging. However, contrary to CEM I, blended cements show increase in accessible porosity, O_2 diffusivity and sorptivity after carbonation. O_2 permeability is consistently increased for all tested samples due to the formation of carbonation-induced microcracks. The microcracking problem is more severe in blended cements indicating the importance of shrinkage caused by C-S-H carbonation.

Objective 5: Establish a database for natural carbonation of cement-based materials and model long-term carbonation resistance from short-term measurements.

Carbonation modelling was performed using artificial neural networks (ANNs) in Chapter 8 to predict the long-term carbonation depth of cement-based materials. Approximately 3300 pieces of natural carbonation data were compiled from 33 studies (including Chapter 7), and were classified into 33 concrete- and environmental-related input parameters to train, validate and test the ANN model. By fitting the required input variables to the trained ANN algorithm, prediction of carbonation depths can be obtained for up to 20 years. Results show a good correlation between the predicted and measured carbonation depths in the test dataset with an average root mean squared error of 1.97 and an average percentage error of 19.2%. The prediction accuracy is much higher for larger carbonation depths and the obtained error was reduced to merely 4.3% when predicting a carbonation depth of 50 mm. Since larger carbonation depth is usually detected in blended cements due to their higher vulnerability to carbonation, ANNs are thus deemed especially suitable for rapidly assessing the long-term carbonation resistance of blended cements with good accuracy. Furthermore, the trained ANN model can replicate some well-established correlations between carbonation depths and certain variables, reinforcing the reliability of ANNs in studying the carbonation process. Some less well-understood correlations, such as the comparison of carbonation rates at different exposure regions, can also be revealed with the help of ANNs.

9.2 Recommendations for further research

CRM parametric optimisation was made on CEM I cements focusing on unreacted cement particles, calcium carbonate ($CaCO_3$), and portlandite, and the optimised parameters were found to be applicable for studying the carbonation behaviour in blended cements. In future, detailed optimisation needs to be extended to other phases, such as unreacted slag, PFA particles. This is important because most blended cements used in real structures are not exposed to adequate curing and such unreacted phases can be abundant in the hardened cement paste. Furthermore, the reaction rates of such phases are closely relevant to the other apparent physical properties in concrete, e.g., compressive strength and mass transport properties. Parametric optimisation on such phases could aid more detailed

research on their hydration and carbonation processes when combined with the real-time in situ characterisation capability of CRM.

In addition, a range of novel cements have been proposed as low-carbon or even negative carbon alternatives to Portlandite cements, e.g., calcium sulphoaluminate/belite cements, alkali-activated cements, and magnesium silicate-based binders. These novel cements hold much promise but have yet to see widespread use beyond small scale demonstrations, niche products and non-structural applications. Their acceptance in the construction industry has been hindered by a lack of understanding of their long-term properties, performances, and independent unbiased evaluation. This thesis has shown the ability of CRM in studying the carbonation process of conventional Portland and blended cements, while more research is still needed to assess the carbonation behaviour in such novel cements.

Real-time study on early surface carbonation is focused on calcite, unreacted cement particle and portlandite. Some other phases, involving the hydrated form of $CaCO_3$ such as amorphous $CaCO_3$ and monohydrocalcite, as well as the other crystalline $CaCO_3$ polymorphs, should also be studied, especially in blended and novel systems. This will help better understand the carbonation process to compare the mineralogical changes induced by natural and accelerated carbonation. It could potentially allow to set a maximum CO_2 level to be used in accelerated tests that can be at least comparable to natural carbonation. This can also help assess the rate of carbonation of novel cement-based materials if combined with transport measurements in an appropriate carbonation depth model.

CRM has been compared with phenolphthalein and four profile-grinding analysis techniques to determine carbonation depth. However, since phenolphthalein is classified as carcinogenic, some other pH indicators should be studied, such as thymolphthalein as it has been reported as the best substitute for phenolphthalein (Yu et al., 2010). Additionally, other techniques are also required to provide supporting evidence. One possible technique is thin-section optical microscopy in cross-polar mode. This technique could distinguish $CaCO_3$ from the other cementitious phases due to its opaline and brighter appearance and thus obtain its spatial distribution. Such technique has been commonly used in the past, but the main challenge is the ability to produce the required thin section within a relatively short time to enable many measurements. Another possible technique is the indentation to characterise profiles in mechanical properties induced by carbonation. This is made possible because of the different hardness of different cementitious phases. Samples with impregnated and polished surfaces for BSE and CRM can be used for complementary results.

This study shows that CRM and phenolphthalein provide identical carbonation depths, despite the fact they measure different aspects of carbonation. Considering that CRM directly maps the spatial

distribution of $CaCO_3$ and portlandite, the determined carbonation depth is deemed the true reflection of the carbonation reaction. However, due to the discrepancy between the phenolphthalein colouration pH (8.2-9.8) and the threshold value for steel corrosion (11.5), the relationship between the carbonation of different phases and the change of pH in the pore solution needs to be further studied. Furthermore, the relationship between the measured carbonation depth and the corrosion of steel also needs more investigation because some researchers have observed corrosion initiation occurring before the carbonation depth measured by phenolphthalein reaches the reinforcement (Yoon et al., 2007; Hussain & Ishida, 2009). This could be caused by the spatial variation of carbonation fronts in their samples but could also be ascribed to the kinetics of carbonation when steel reinforcement is present. Several aspects should be considered in future investigations, for example, (1) the effect of steel reinforcement on the progress of carbonation depth, (2) the change of corrosion rate with the progress of carbonation, (3) the effect of the rebar size on the carbonation depth.

Carbonation modelling using an ANN model has shown its ability to predict long-term carbonation resistance of cement-based materials. By fitting with the required variables, the long-term carbonation depth for up to 20 years can be predicted with an average root mean squared error of 1.97 mm and an average percentage error of 19.2%. These could be further reduced by increasing the reliability of the data facts, and incorporating other carbonation-related variables, such as the porosity and transport properties. In addition, natural carbonation data for more than 20 years are also needed to help extrapolate the prediction to an even longer term.

References

Ai-Amoudi, O. S., Rasheeduzzafar, & Maslehuddin, M. (1991). Carbonation and Corrosion of Rebars in Salt Contaminated OPC/PFA Concretes. *Cement and Concrete Research*, *21*, 38–50.

Akpinar, P., & Uwanuakwa, I. D. (2020). Investigation of the parameters influencing progress of concrete carbonation depth by using artificial neural networks. *Materiales de Construcción*, *70*(337). https://materconstrucc.revistas.csic.es/index.php/materconstrucc/article/view/2271/2988

Al Omari, M. M. H., Rashid, I. S., Qinna, N. A., Jaber, A. M., & Badwan, A. A. (2016). Calcium Carbonate. In Harry G. Brittain (Ed.), *Profiles of Drug Substances, Excipients and Related Methodology* (Vol. 41, pp. 31–132). Academic Press.

Allaoui, A., & El Bounia, N.-E. (2009). How carbon nanotubes affect the cure kinetics and glass transition temperature of their epoxy composites?-A review. *Express Polymer Letters*, *3*(9), 588–594. https://doi.org/10.3144/expresspolymlett.2009.73ï

Anstice, D. J., Page, C. L., & Page, M. M. (2005). The pore solution phase of carbonated cement pastes. *Cement and Concrete Research*, *35*(2), 377–383. https://doi.org/10.1016/J.CEMCONRES.2004.06.041

Arandigoyen, M., Bicer-Simsir, B., Alvarez, J. I., & Lange, D. A. (2006). Variation of microstructure with carbonation in lime and blended pastes. *Applied Surface Science*, *252*(20), 7562–7571. https://doi.org/10.1016/j.apsusc.2005.09.007

Ashraf, W., & Olek, J. (2016). Carbonation behavior of hydraulic and non-hydraulic calcium silicates : potential of utilizing low-lime calcium silicates in cement-based materials. *Journal of Materials Science*, *51*(13), 6173–6191. https://doi.org/10.1007/s10853-016-9909-4

ASTM E579-04. (2015). *Standard Test Method for Limit of Detection of Fluorescence of Quinine Sulfate in Solution*. https://compass.astm.org/EDIT/html_annot.cgi?E579+04(2015)

Auroy, M., Poyet, S., Le Bescop, P., Torrenti, J. M., Charpentier, T., Moskura, M., & Bourbon, X. (2015). Impact of carbonation on unsaturated water transport properties of cement-based materials. *Cement and Concrete Research*, *74*, 44–58. https://doi.org/10.1016/J.CEMCONRES.2015.04.002

Auroy, M., Poyet, S., Le Bescop, P., Torrenti, J. M., Charpentier, T., Moskura, M., & Bourbon, X. (2018). Comparison between natural and accelerated carbonation (3% CO2): Impact on mineralogy, microstructure, water retention and cracking. *Cement and Concrete Research*, *109*, 64–80. https://doi.org/10.1016/J.CEMCONRES.2018.04.012

Balayssac, J. P., Detriche, C. H., & Grandet, J. (1995). Effect of curing upon carbonation of concrete. *Construction and Building Materials*, *9*(2), 91–95.

Belda Revert, A., De Weerdt, K., Hornbostel, K., & Geiker, M. R. (2018). Carbonation-induced corrosion: Investigation of the corrosion onset. *Construction and Building Materials*, *162*, 847–856. https://doi.org/10.1016/j.conbuildmat.2017.12.066

Belda Revert, A., Weerdt, K. De, Hornbostel, K., & Geiker, M. R. (2016). Carbonation Characterization of Mortar with Portland Cement and Fly Ash, Comparison of Techniques. *Nordic Concrete Research*, *54*, 60–76.

Bensted, J. (1976). Uses of Raman Spectroscopy in Cement Chemistry. *Journal of the American Ceramic Society*, *59*(3–4), 140–143. https://doi.org/10.1111/j.1151-2916.1976.tb09451.x

Bentur, A., Berke, N., & Diamond, S. (1997). *Steel Corrosion in Concrete: Fundamentals and civil engineering practi*. E&FN Spon. https://www.routledge.com/Steel-Corrosion-in-Concrete-Fundamentals-and-civil-engineering-practice/Bentur-Berke-Diamond/p/book/9780367863715

Bernal, S. A., Provis, J. L., Brice, D. G., Kilcullen, A., Duxson, P., & Van Deventer, J. S. J. (2012). Accelerated carbonation testing of alkali-activated binders significantly underestimates service life: The role of pore solution chemistry. *Cement and Concrete Research*, *42*(10), 1317–1326. https://doi.org/10.1016/j.cemconres.2012.07.002

Bernard, S., Beyssac, O., & Benzerara, K. (2008). Raman Mapping Using Advanced Line-Scanning Systems: Geological Applications. *Applied Spectroscopy*, *62*(11), 1180–1188. https://www.osapublishing.org/abstract.cfm?uri=as-62-11-1180

Bertin, M., Baroghel-Bouny, V., Huet, B., Wong, H. S., & Omikrine Metalssi, O. (2018). *Impact of carbonation on transport properties of cement pastes*.

Black, L., Breen, C., & Yarwood, J. (2007). Structural Features of C–S–H(I) and Its Carbonation in Air—A Raman Spectroscopic Study. Part II: Carbonated Phases. *Journal of the American Ceramic Society*, *917*(21881), 908–917. https://doi.org/10.1111/j.1551-2916.2006.01429.x

Bonen, D., Johnson, T. J., & Sarkar, S. L. (1994). Characterization of principal clinker minerals by FT-Raman microspectroscopy. *Cement and Concrete Research*, *24*(5), 959–965. https://doi.org/10.1016/0008-8846(94)90016-7

Borges, P. H. R., Costa, J. O., Milestone, N. B., Lynsdale, C. J., & Streatfield, R. E. (2010). Carbonation of CH and C-S-H in composite cement pastes containing high amounts of BFS. *Cement and Concrete Research*, *40*(2), 284–292. https://doi.org/10.1016/j.cemconres.2009.10.020

Bouikni, A., Swamy, R. N., & Bali, A. (2009). Durability properties of concrete containing 50% and 65% slag. *Construction and Building Materials*, *23*(8), 2836–2845. https://doi.org/10.1016/j.conbuildmat.2009.02.040

Boumaaza, M., Turcry, P., Huet, B., & Aït-Mokhtar, A. (2020). Influence of carbonation on the microstructure and the gas diffusivity of hardened cement pastes. *Construction and Building Materials*, *253*, 119227. https://doi.org/10.1016/J.CONBUILDMAT.2020.119227

Branch, J. L., Kosson, D. S., Garrabrants, A. C., & He, P. J. (2016). The impact of carbonation on the microstructure and solubility of major constituents in microconcrete materials with varying alkalinities due to fly ash replacement of ordinary Portland cement. *Cement and Concrete Research*, *89*, 297–309. https://doi.org/10.1016/j.cemconres.2016.08.019

BS 1881-210. (2013). *Testing hardened concrete: Determination of the potential carbonation resistance of concrete. Accelerated carbonation method*.

BS EN 13295:2004. (2004). *Products and systems for the protection and repair of concrete structures.Test methods. Determination of resistance to carbonation*. https://shop.bsigroup.com/ProductDetail?pid=000000000030105144

Buenfeld, N. R., & Okundi, E. (1998). Effect of cement content on transport in concrete. *Magazine of Concrete Research*, *50*(4), 339–351. https://doi.org/10.1680/macr.2000.52.1.73

Bui, H., Boutouil, M., Levacher, D., & Sebaibi, N. (2021). Evaluation of the influence of accelerated carbonation on the microstructure and mechanical characteristics of coconut fibre-reinforced cementitious matrix. *Journal of Building Engineering*, *39*, 102269. https://doi.org/10.1016/J.JOBE.2021.102269

Byfors, K. (1985). Carbonation of concrete with silica fume and fly ash. *Nordic Concrete Reseaerch*, *4*, 26–35.

Caggiani, M. C., Coccato, A., Barone, G., Finocchiaro, C., Fugazzotto, M., Lanzafame, G., Occhipinti, R., Stroscio, A., & Mazzoleni, P. (2021). Raman spectroscopy potentiality in the study of geopolymers reaction degree. *Journal of Raman Spectroscopy*, 1–13. https://doi.org/10.1002/JRS.6167

Carcasses, M., Petit, J. Y., & Olliver, J. P. (1998). Gas Permeability of Mortars in Relation with the Microstructure of Interfacial Transition Zone (ITZ). In A. Katz, M. Bentur, G. Alexander, & Arliguie (Eds.), *Interfacial Transition Zone in Cementitious Composites: Vol. RILEM Proc* (pp. 85–92). E & FN Spon.

Carević, V., Ignjatović, I., & Dragaš, J. (2019). Model for practical carbonation depth prediction for high volume fly ash concrete and recycled aggregate concrete. *Construction and Building Materials*, *213*, 194–208. https://doi.org/10.1016/J.CONBUILDMAT.2019.03.267

Castellote, M., Fernandez, L., Andrade, C., & Alonso, C. (2009). Chemical changes and phase analysis of OPC pastes carbonated at different CO2concentrations. *Materials and Structures/Materiaux et Constructions*, *42*(4), 515–525. https://doi.org/10.1617/s11527-008-9399-1

Chakrabarty, D., & Mahapatra, S. (1999). Aragonite crystals with unconventional morphologies. *Journal of Materials Chemistry*, *9*(11), 2953–2957. https://doi.org/10.1039/a905407c

Chang, C. F., & Chen, J. W. (2006). The experimental investigation of concrete carbonation depth. *Cement and Concrete Research*, *36*(9), 1760–1767. https://doi.org/10.1016/j.cemconres.2004.07.025

Chatveera, B., & Lertwattanaruk, P. (2011). Durability of conventional concretes containing black rice husk ash. *Journal of Environmental Management*, *92*, 59–66. https://doi.org/10.1016/j.jenvman.2010.08.007

Chen, J. J., Thomas, J. J., & Jennings, H. M. (2006). Decalcification shrinkage of cement paste. *Cement and Concrete Research*, *36*(5), 801–809. https://doi.org/10.1016/j.cemconres.2005.11.003

Chindaprasirt, P., & Rukzon, S. (2009). Pore Structure Changes of Blended Cement Pastes Containing Fly Ash, Rice Husk Ash, and Palm Oil Fuel Ash Caused by Carbonation. *Journal of Materials in Civil Engineering*, *21*(11), 666–671. https://doi.org/10.1061/(ASCE)0899-1561(2009)21:11(666)

Chong, K. Y., Chia, C. H., & Zakaria, S. (2014). Polymorphs calcium carbonate on temperature reaction. *AIP Conference Proceedings*, *1614*(1), 52–56. https://doi.org/10.1063/1.4895169

Coleyshaw, E. E., Crump, G., & Griffith, W. P. (2003). Vibrational spectra of the hydrated carbonate minerals ikaite, monohydrocalcite, lansfordite and nesquehonite. *Spectrochimica Acta Part A: Molecular and Biomolecular Spectroscopy*, *59*(10), 2231–2239. https://doi.org/10.1016/S1386-1425(03)00067-2

Çopuroğlu, O. (2016). Revealing the dark side of portlandite clusters in cement paste by circular polarization microscopy. *Materials*, *9*(3). https://doi.org/10.3390/ma9030176

Corvisier, J., Brunet, F., Fabbri, A., Bernard, S., Findling, N., Rimmelé, G., Barlet-Gouédard, V., Beyssac, O., & Goffé, B. (2010). Raman mapping and numerical simulation of calcium carbonates distribution in experimentally carbonated Portland-cement cores. *European Journal of Mineralogy*, *22*(1), 63–74. https://doi.org/10.1127/0935-1221/2010/0022-1977

Criado, M., Martínez-Ramirez, S., & Bastidas, J. M. (2015). A Raman spectroscopy study of steel corrosion products in activated fly ash mortar containing chlorides. *Construction and Building Materials*, *96*, 383–390. https://doi.org/10.1016/J.CONBUILDMAT.2015.08.034

Cui, H., Tang, W., Liu, W., Dong, Z., & Xing, F. (2015). Experimental study on effects of CO2 concentrations on concrete carbonation and diffusion mechanisms. *Construction and Building Materials*, *93*, 522–527. https://doi.org/10.1016/J.CONBUILDMAT.2015.06.007

Cultrone, G., Sebastián, E., & Huertas, M. O. (2005). Forced and natural carbonation of lime-based mortars with and without additives: Mineralogical and textural changes. *Cement and Concrete Research*, *35*(12), 2278–2289. https://doi.org/10.1016/j.cemconres.2004.12.012

Dang, V. H., François, R., L'Hostis, V., & Meinel, D. (2015). Propagation of corrosion in pre-cracked carbonated reinforced mortar. *Materials and Structures*, *48*, 2575–2595. https://doi.org/10.1617/S11527-014-0338-Z/FIGURES/18

De Ceukelaire, L., & Van Nieuwenburg, D. (1993). Accelerated Carbonation of a Blast-Furnace Cement Concrete. *Cement and Concrete Research*, *23*, 442–452.

De Fontenay, C., & Skaarup, J. (1987). The influence of exposure conditions on the rates of carbonation of different concretes in Bahrain. *Proceedings of the Second International Conference on Deterioration and Repair of Reinforced Concrete*, 203–223.

De Weerdt, K., Haha, M. Ben, Le Saout, G., Kjellsen, K. O., Justnes, H., & Lothenbach, B. (2011). Hydration mechanisms of ternary Portland cements containing limestone powder and fly ash. *Cement and Concrete Research*, *41*(3), 279–291. https://doi.org/10.1016/J.CEMCONRES.2010.11.014

DeCarlo, T. M. (2018). Characterizing coral skeleton mineralogy with Raman spectroscopy. *Nature Communications 2018 9:1*, *9*, 1–3. https://doi.org/10.1038/s41467-018-07601-3

Dewaele, P. J., Reardon, E. J., & Dayal, R. (1991). Permeability and porosity changes associated with cement grout carbonation. *Cement and Concrete Research*, *21*(4), 441–454. https://doi.org/10.1016/0008-8846(91)90092-V

Diego Rodriguez-Blanco, J., Shaw, S., & Benning, L. G. (2011). The kinetics and mechanisms of amorphous calcium carbonate (ACC) crystallization to calcite, via vaterite. *Nanoscale*, *3*, 265–271. https://doi.org/10.1039/c0nr00589d

Drouet, E., Poyet, S., Le Bescop, P., Torrenti, J. M., & Bourbon, X. (2019). Carbonation of hardened cement pastes: Influence of temperature. *Cement and Concrete Research*, *115*, 445–459. https://doi.org/10.1016/J.CEMCONRES.2018.09.019

Duan, P., Yan, C., & Zhou, W. (2018). Effects of calcined layered double hydroxides on carbonation of concrete containing fly ash. *Construction and Building Materials*, *160*, 725–732. https://doi.org/10.1016/J.CONBUILDMAT.2017.11.099

Dubina, E., Korat, L., Black, L., Strupi-Šuput, J., & Plank, J. (2013). Influence of water vapour and carbon dioxide on free lime during storage at 80 °C, studied by Raman spectroscopy. *Spectrochimica Acta. Part A, Molecular and Biomolecular Spectroscopy*, *111*, 299–303. https://doi.org/10.1016/J.SAA.2013.04.033

Dullien, F. A. L. (1992). Porous Media: Fluid Transport and Pore Structure. In *Porous Media* (2nd ed.). Academic Press, London. https://doi.org/10.1016/C2009-0-26184-8

DuraCrete. (1999). *Compliance testing for probabilistic design purposes (DuraCrete project document BE95-1347/R8)*. Netherlands: The European Union-Brite EuRam III. https://www.amazon.co.uk/Compliance-Testing-Probabilistic-Design-Purposes/dp/B001ABPSZK

Dyer, C. D., Hendra, P. J., & Forsling, W. (1993). The Raman spectroscopy of cement minerals under 1064 nm excitation. *Spectrochimica Acta Part A: Molecular Spectroscopy*, *49*(5–6), 715–722. https://doi.org/10.1016/0584-8539(93)80094-Q

Dyer, C., & Smith, B. J. E. (1995). Application of continuous extended scanning techniques to the simultaneous detection of Raman scattering and photoluminescence from calcium disilicates using visible and near-infrared excitation. *Journal of Raman Spectroscopy*, *26*(8–9), 777–785. https://doi.org/10.1002/JRS.1250260827

Ekolu, S. O. (2016). A review on effects of curing, sheltering, and CO2concentration upon natural carbonation of concrete. *Construction and Building Materials*, *127*, 306–320. https://doi.org/10.1016/j.conbuildmat.2016.09.056

Ekolu, S. O. (2018). Model for practical prediction of natural carbonation in reinforced concrete: Part 1-formulation. *Cement and Concrete Composites*, *86*, 40–56. https://doi.org/10.1016/j.cemconcomp.2017.10.006

Erlin, B., & Stark, D. (1990). Petrography applied to concrete and concrete aggregates — STP 1061. In *Cement and Concrete Composites* (Vol. 13, Issue 1). https://doi.org/10.1016/0958-9465(91)90048-m

Esquivias, L., Morales-Flórez, V., & Santos, A. (2018). Carbon dioxide sequestration by phosphogypsum based procedure. In *Carbon Dioxide Sequestration in Cementitious Construction Materials* (pp. 199–223). Woodhead Publishing. https://doi.org/10.1016/B978-0-08-102444-7.00009-5

Ewertson, C., & Petersson, P. E. (1993). The influence of curing conditions on the permeability and durability of concrete. Results from a field exposure test. *Cement and Concrete Research*, *23*, 683–692.

Fabbri, A., Corvisier, J., Schubnel, A., Brunet, F., Goffé, B., Rimmele, G., & Barlet-Gouédard, V. (2009). Effect of carbonation on the hydro-mechanical properties of Portland cements. *Cement and Concrete Research*, *39*(12), 1156–1163. https://doi.org/10.1016/j.cemconres.2009.07.028

Felix, E. F., Carrazedo, R., & Possan, E. (2021). Carbonation model for fly ash concrete based on artificial neural network: Development and parametric analysis. *Construction and Building Materials*, *266*. https://doi.org/10.1016/j.conbuildmat.2020.121050

Feng, X., Garboczi, E. J., Bentz, D. P., Stutzman, P. E., & Mason, T. O. (2004). Estimation of the degree of hydration of blended cement pastes by a scanning electron microscope point-counting procedure. *Cement and Concrete Research*, *34*, 1787–1793. https://doi.org/10.1016/j.cemconres.2004.01.014

Fernández Bertos, M., Simons, S. J. R., Hills, C. D., & Carey, P. J. (2004). A review of accelerated carbonation technology in the treatment of cement-based materials and sequestration of CO2. *Journal of Hazardous Materials*, *112*(3), 193–205. https://doi.org/10.1016/j.jhazmat.2004.04.019

FIB 34. (2006). *Model code for service-life design, fib bulletin 34*. Federation International Du Beton, Lausanne, Nitherland. https://www.researchgate.net/publication/308016422_fib_bulletin_34_Model_Code_for_Service_Life_Design

Fukushima, T., Yoshizaki, Y., Tomosawa, F., & Takahashi, K. (1998). Relationship Between Neutralization Depth and Concentration Distribution of CaCO3 -Ca(OH)2 in Carbonated Concrete. *Advances in Concrete Technology*, *ACI SP-179*, 347–363. https://doi.org/10.14359/6049

Galan, I., Glasser, F. P., Baza, D., & Andrade, C. (2015). Assessment of the protective effect of carbonation on portlandite crystals. *Cement and Concrete Research*, *74*, 68–77. https://doi.org/10.1016/j.cemconres.2015.04.001

Garbev, K., Stemmermann, P., Black, L., Breen, C., Yarwood, J., & Gasharova, B. (2007). Structural

features of C-S-H(I) and its carbonation in air-A Raman spectroscopic study. Part I: Fresh phases. *Journal of the American Ceramic Society*, *90*(3), 900–907. https://doi.org/10.1111/j.1551-2916.2006.01428.x

Gartner, E. (2004). Industrially interesting approaches to “low-CO2” cements. *Cement and Concrete Research*, *34*(9), 1489–1498. https://doi.org/10.1016/j.cemconres.2004.01.021

GB/T 50082-2009. (2010). *Standard for test methods of long-term performance and durability of ordinary concrete*.

Gebauer, J., & Torrent, R. J. (1989). Effect of Curing on Some Pore Structure-Dependent Properties of Concrete. *Material Research Society Symposium*, *137*(301–309). https://doi.org/10.1557/proc-137-301

Gierlinger, N., Keplinger, T., & Harrington, M. (2012, September 23). Imaging of plant cell walls by confocal Raman microscopy. *Nature Protocols*, *7*(9), 1694–1708. https://doi.org/10.1038/nprot.2012.092

Giridhar, G., Manepalli, R. R. K. N., & Apparao, G. (2017a). Confocal Raman Spectroscopy. In S. Thomas, R. Thomas, A. K. Zachariah, & R. Kumar Mishra (Eds.), *Spectroscopic Methods for Nanomaterials Characterization* (Vol. 2, pp. 141–161). Elsevier. https://doi.org/10.1016/B978-0-323-46140-5.00007-8

Giridhar, G., Manepalli, R. R. K. N., & Apparao, G. (2017b). Confocal Raman Spectroscopy. In *Spectroscopic Methods for Nanomaterials Characterization* (Vol. 2, pp. 141–161). Elsevier. https://doi.org/10.1016/B978-0-323-46140-5.00007-8

Goñi, S., Gaztañaga, M. T., & Guerrero, A. (2002). Role of cement type on carbonation attack. *Journal of Materials Research*, *17*(7), 1834–1842. https://doi.org/10.1557/JMR.2002.0271

Groves, G. W., Brough, A., Richardson, I. G., & Dobson, C. M. (1991). Progressive Changes in the Structure of Hardened C_3S Cement Pastes due to Carbonation. *Journal of American Ceramic Society*, *74*(11), 2891–2896.

Groves, G. W., Rodway, D. I., & Richardson, I. G. (1990). The carbonation of hardened cement pastes. *Advances in Cement Research*, *3*(11), 117–125. https://doi.org/10.1680/ADCR.1990.3.11.117

Gruyaert, E., Van Den Heede, P., & De Belie, N. (2013). Carbonation of slag concrete: Effect of the cement replacement level and curing on the carbonation coefficient - Effect of carbonation on the pore structure. *Cement and Concrete Composites*, *35*(1), 39–48. https://doi.org/10.1016/j.cemconcomp.2012.08.024

Guedes, A., Valentim, B., Prieto, A. C., Sanz, A., Flores, D., & Noronha, F. (2008). Characterization of fly ash from a power plant and surroundings by micro-Raman spectroscopy. *International Journal of Coal Geology*, *73*(3–4), 359–370. https://doi.org/10.1016/J.COAL.2007.09.001

Hakkinen, T. (1992). The permeability of high strength blast furnace slag concrete. *Nordic Concrete Research*, *11*(1), 55–66.

Hall, C., & Hoff, W. D. (2012). *Water transport in brick, stone and concrete*. Spon Press, London.

Haque, M. N., & Kawamura, M. (1992). Carbonation and Chloride-Induced Corrosion of Reinforcement in Fly Ash Concretes. *ACI Materials Journal*, *89*(1), 41–48.

Herrera, R. (2011). *Comparison of methods to determine the carbonation depth in fly ash blended cement mortars*. Lakehead University.

Herrera, R., Kinrade, S. D., & Catalan, L. J. J. (2015). A Comparison of Methods for Determining Carbonation Depth in Fly Ash-Blended Cement Mortars. *Materials Journal*, *112*(2), 287–294.

https://doi.org/10.14359/51687452

Heukamp, F. H., Ulm, F. J., & Germaine, J. T. (2003). Poroplastic properties of calcium-leached cement-based materials. *Cement and Concrete Research*, *33*, 1155–1173. https://doi.org/10.1016/S0008-8846(03)00024-3

Higl, J., Köhler, M., & Lindén, M. (2016). Confocal Raman microscopy as a non-destructive tool to study microstructure of hydrating cementitious materials. *Cement and Concrete Research*, *88*, 136–143. https://doi.org/10.1016/J.CEMCONRES.2016.07.005

Ho, D. W. S., & Lewis, R. K. (1987a). Carbonation of concrete incorporating fly ash or a chemical admixture. *Fly Ash, Silica Fume, Slag & Other Mineral By-Products in Concrete I (ACI SP-79)*, 333–346.

Ho, D. W. S., & Lewis, R. K. (1987b). Carbonation of concrete and its prediction. *Cement and Concrete Research*, *17*(3), 489–504. https://doi.org/10.1016/0008-8846(87)90012-3

Hobbs, D. W. (1988). Carbonation of concrete containing pfa. *Magazine of Concrete Research*, *40*(143), 69–78. https://doi.org/10.1680/macr.1988.40.143.69

Horgnies, M., Chen, J. J., & Bouillon, C. (2013). Overview about the use of fourier transform infrared spectroscopy to study cementitious materials. *WIT Transactions on Engineering Sciences*, *77*, 251–262. https://doi.org/10.2495/MC130221

Houst, Y. F. (1996). The Role of Moisture in the Carbonation of Cementitioiis Materials. *International Journal for Restoration of Buildings and Monuments*, *2*, 49–66.

Houst, Y. F., & Wittmann, F. H. (1994). Influence of porosity and water content on the diffusivity of CO2 and O2 through hydrated cement paste. *Cement and Concrete Research*, *24*(6), 1165–1176.

Houst, Y. F., & Wittmann, F. H. (2002). Depth profiles of carbonates formed during natural carbonation. *Cement and Concrete Research*, *32*(12), 1923–1930. https://doi.org/10.1016/S0008-8846(02)00908-0

Hu, Q., Zhang, J., Teng, H., & Becker, U. (2012). Growth process and crystallographic properties of ammonia-induced vaterite. *American Mineralogist*, *97*, 1437–1445. https://doi.org/10.2138/AM.2012.3983

Huijgen, W. J. J., Witkamp, G. J., & Comans, R. N. J. (2005). Mineral CO2 sequestration by steel slag carbonation. *Environmental Science and Technology*, *39*(24), 9676–9682. https://doi.org/10.1021/es050795f

Hussain, R R, Ishida, T., & Wasim, M. (2011). Experimental investigation of time dependent non-linear 3D relationship between critical carbonation depth and corrosion of steel in carbonated concrete. *Corrosion Engineering, Science and Technology*, *46*(5), 657–660. https://doi.org/10.1179/147842210X12659647007086

Hussain, Raja Rizwan, & Ishida, T. (2009). Critical carbonation depth for initiation of steel corrosion in fully carbonated concrete and development of electrochemical carbonation induced corrosion model. *International Journal of Electrochemical Science*, *4*(8), 1178–1195.

Hyvert, N., Sellier, A., Duprat, F., Rougeau, P., & Francisco, P. (2010). Dependency of C-S-H carbonation rate on CO2 pressure to explain transition from accelerated tests to natural carbonation. *Cement and Concrete Research*, *40*(11), 1582–1589. https://doi.org/10.1016/j.cemconres.2010.06.010

Ibáñez, J., Artús, L., Cuscó, R., López, Á., Menéndez, E., & Andrade, M. C. (2007). Hydration and carbonation of monoclinic C2S and C3S studied by Raman spectroscopy. *Journal of Raman Spectroscopy*, *38*(1), 61–67. https://doi.org/10.1002/jrs.1599

Ji, Y. S., Wu, M., Ding, B., Liu, F., & Gao, F. (2014). The experimental investigation of width of semi-carbonation zone in carbonated concrete. *Construction and Building Materials*, *65*, 67–75. https://doi.org/10.1016/j.conbuildmat.2014.04.095

Jia, Y., Yan, P., & Aruhan, B. (2012). Natural and accelerated carbonation of concrete containing fly ash and GGBS after different initial curing period. *Magazine of Concrete Research*, *64*(2), 143–150.

Jiang, L., Lin, B., & Cai, Y. (2000). A model for predicting carbonation of high-volume fly ash concrete. *Cement and Concrete Research*, *30*(5), 699–702. https://doi.org/10.1016/S0008-8846(00)00227-1

Jones, M. R., Newlands, M. D., Abbas, A. M. O., & Dhir, R. K. (2001). Comparison of 2 year carbonation depths of common cement concretes using the modified draft CEN test. *Materials and Structures/Matdriaux et Constructions*, *34*, 396–403.

Jung, W., Yoon, Y. S., & Sohn, Y. M. (2003). Predicting the remaining service life of land concrete by steel corrosion. *Cement and Concrete Research*, *33*(5), 663–677. https://doi.org/10.1016/S0008-8846(02)01034-7

Justnes, H., Skocek, J., Østnor, T. A., Engelsen, C. J., & Skjølsvold, O. (2020). Microstructural changes of hydrated cement blended with fly ash upon carbonation. *Cement and Concrete Research*, *137*, 106192. https://doi.org/10.1016/J.CEMCONRES.2020.106192

Kashef-Haghighi, S., & Ghoshal, S. (2013). Physico-chemical processes limiting CO2 uptake in concrete during accelerated carbonation curing. *Industrial and Engineering Chemistry Research*, *52*(16), 5529–5537. https://doi.org/10.1021/ie303275e

Khan, M. S. H., Castel, A., & Noushini, A. (2017). Carbonation of a low-calcium fly ash geopolymer concrete. *Magazine of Concrete Research*, *69*(1), 24–34. https://doi.org/10.1680/jmacr.15.00486

Khunthongkeaw, J., Tangtermsirikul, S., & Leelawat, T. (2006). A study on carbonation depth prediction for fly ash concrete. *Construction and Building Materials*, *20*(9), 744–753. https://doi.org/10.1016/j.conbuildmat.2005.01.052

Klinkenberg, L. J. (1941). The permeability of porous media to liquids and gases, drilling and production practice. In *undefined* (Vol. 2012, Issue 2). Oil Gas Scientific Research Project Institute. https://doi.org/10.5510/OGP20120200114

Kobayashi, K., & Uno, Y. (1989). Influence of alkali on carbonation of concrete, part I. Preliminary tests with mortar specimens. *Cement and Concrete Research*, *19*(5), 821–826. https://doi.org/10.1016/0008-8846(89)90053-7

Kobayashi, K., & Uno, Y. (1990). Mechanism of carbonation of concrete. *Concrete Library of JSCE*, *16*(12), 139–151. http://library.jsce.or.jp/jsce/open/00670/No16/CLI-16-0139.pdf

Kobayashl, K., & Shuttoh, K. (1991). Oxygen diffusivity of various cementitious materials. *Cement and Concrete Research*, *21*, 273–284.

Köliö, A., Niemelä, P. J., & Lahdensivu, J. (2016). Evaluation of a carbonation model for existing concrete facades and balconies by consecutive field measurements. *Cement and Concrete Composites*, *65*, 29–40. https://doi.org/10.1016/J.CEMCONCOMP.2015.10.013

Kontoyannis, C. G., & Vagenas, N. V. (2000). Calcium carbonate phase analysis using XRD and FT-Raman spectroscopy. *Analyst*, *125*(2), 251–255. https://doi.org/10.1039/a908609i

Kumar, M., Malay, N., & Kujur, J. (2018). Study of natural carbonation of concrete incorporating marble dust. *Proceedings of the Institution of Civil Engineers - Construction Materials*, *January*, 1–8. https://doi.org/10.1680/jcoma.17.00001

Kuosa, H. (2010). *Concrete durability field testing Field and Laboratory results 2007-2010 in DuraInt-project*.

Kwon, S. J., & Song, H. W. (2010). Analysis of carbonation behavior in concrete using neural network algorithm and carbonation modeling. *Cement and Concrete Research*, *40*(1), 119–127. https://doi.org/10.1016/j.cemconres.2009.08.022

Larroumet, D., Greenfield, D., Akid, R., & Yarwood, J. (2007). Raman spectroscopic studies of the corrosion of model iron electrodes in sodium chloride solution. *Journal of Raman Spectroscopy*, *38*(12), 1577–1585. https://doi.org/10.1002/JRS.1810

Lawrence, R. M., Mays, T. J., Rigby, S. P., Walker, P., & D'Ayala, D. (2007). Effects of carbonation on the pore structure of non-hydraulic lime mortars. *Cement and Concrete Research*, *37*(7), 1059–1069. https://doi.org/10.1016/J.CEMCONRES.2007.04.011

Lee, H. J., Kim, D. G., Lee, J. H., & Myoung Suk Cho. (2012). A Study for Carbonation Degree on Concrete using a Phenolphthalein Indicator and Fourier-Transform Infrared Spectroscopy. *World Academy of Science, Engineering and Technology*, *6*(2), 2–25.

Lee, J. H., Kim, D. G., & Seo, E. A. (2017). Semi-quantitative Evaluation of Concrete Carbonation by XRD Analysis. *International Journal of Advanced Research in Science, Engineering and Technology*, *4*(11), 4832–4844. www.ijarset.com

Leemann, A., Loser, R., Münch, B., & Lura, P. (2017). Steady-state O2 and CO2 diffusion in carbonated mortars produced with blended cements. *Materials and Structures/Materiaux et Constructions*, *50*(6). https://doi.org/10.1617/s11527-017-1118-3

Leemann, A., & Moro, F. (2017). Carbonation of concrete: the role of CO 2 concentration, relative humidity and CO 2 buffer capacity. *Materials and Structures*, *50*(30), 1–14. https://doi.org/10.1617/s11527-016-0917-2

Leemann, A., Nygaard, P., Kaufmann, J., & Loser, R. (2015). Relation between carbonation resistance, mix design and exposure of mortar and concrete. *Cement and Concrete Composites*, *62*, 33–43. https://doi.org/10.1016/J.CEMCONCOMP.2015.04.020

Leemann, A., Pahlke, H., Loser, R., & Winnefeld, F. (2018). Carbonation resistance of mortar produced with alternative cements. *Materials and Structures/Materiaux et Constructions*, *51*(5), 1–12. https://doi.org/10.1617/S11527-018-1239-3/FIGURES/9

Leng, Y. (2013). *Materials Characterization: Introduction to Microscopic and Spectroscopic Methods* (2nd ed.). John Wiley & Sons.

Lin, Y., Zhu, D., Zeng, D., Yang, Y., Shi, T., Deng, K., Ren, C., Zhang, D., & Wang, F. (2013). Experimental studies on corrosion of cement in CO2 injection wells under supercritical conditions. *Corrosion Science*, *74*, 13–21. https://doi.org/10.1016/j.corsci.2013.03.018

Ling, T. C., Balachandran, C., Munoz, J. F., & Youtcheff, J. (2018). Chemical evolution of alkali–silicate reaction (ASR) products: a Raman spectroscopic investigation. *Materials and Structures*, *51*(23). https://doi.org/10.1617/S11527-018-1151-X/FIGURES/9

Lippincott, E. R., Van Valkenburg, A., Weir, C. E., & Bunting, E. N. (1958). Infrared Studies on Polymorphs of Silicon Dioxide and Germanium Dioxide. *Journal of Research of the National Bureau of Standards*, *61*(1), 61–70.

Litvan, G. G., & Meyer, A. (1986). Carbonation of Granulated Blast Furnace Slag Cement Concrete During Twenty Years of Field Exposure. *ACI Special Publication*, *91*, 1445–1462. https://doi.org/10.14359/10130

Liu, F., Sun, Z., & Qi, C. (2015). Raman spectroscopy study on the hydration behaviors of portland

cement pastes during setting. *Journal of Materials in Civil Engineering*, *27*(8), 1–10. https://doi.org/10.1061/(ASCE)MT.1943-5533.0001189

Liu, J., Qiu, Q., Chen, X., Xing, F., Han, N., He, Y., & Ma, Y. (2017). Understanding the interacted mechanism between carbonation and chloride aerosol attack in ordinary Portland cement concrete. *Cement and Concrete Research*, *95*, 217–225. https://doi.org/10.1016/j.cemconres.2017.02.032

Liu, W., Cui, H., Dong, Z., Xing, F., Zhang, H., & Lo, T. Y. (2016). Carbonation of concrete made with dredged marine sand and its effect on chloride binding. *Construction and Building Materials*, *120*, 1–9. https://doi.org/10.1016/j.conbuildmat.2016.05.011

Liu, W., Li, Y. Q., Tang, L. P., & Dong, Z. J. (2019). XRD and 29Si MAS NMR study on carbonated cement paste under accelerated carbonation using different concentration of CO2. *Materials Today Communications*, *19*, 464–470. https://doi.org/10.1016/j.mtcomm.2019.05.007

Lo, Y., & Lee, H. M. (2002a). Curing effects on carbonation of concrete using a phenolphthalein indicator and Fourier-transform infrared spectroscopy. *Building and Environment*, *37*, 507–514. https://doi.org/10.1016/S0360-1323(01)00052-X

Lo, Y., & Lee, H. M. (2002b). Curing effects on carbonation of concrete using a phenolphthalein indicator and Fourier-transform infrared spectroscopy. *Building and Environment*, *37*(5), 507–514. https://doi.org/10.1016/S0360-1323(01)00052-X

Loh, H.-C., Kim, H.-J., Ulm, F.-J., & Masic, A. (2021). Time-Space-Resolved Chemical Deconvolution of Cementitious Colloidal Systems Using Raman Spectroscopy. *Langmuir*, *37*(23), 7019–7031. https://doi.org/10.1021/ACS.LANGMUIR.1C00609

Londhe, S. N., Kulkarni, P. S., Dixit, P. R., Silva, A., Neves, R., & de Brito, J. (2021). Predicting carbonation coefficient using Artificial neural networks and genetic programming. *Journal of Building Engineering*, *39*. https://doi.org/10.1016/j.jobe.2021.102258

López-Arce, P., Gómez-Villalba, L. S., Martínez-Ramírez, S., Álvarez de Buergo, M., & Fort, R. (2011). Influence of relative humidity on the carbonation of calcium hydroxide nanoparticles and the formation of calcium carbonate polymorphs. *Powder Technology*, *205*(1–3), 263–269. https://doi.org/10.1016/J.POWTEC.2010.09.026

Lu, C., & Liu, R. (2009). Predicting Carbonation Depth of Prestressed Concrete under Different Stress States Using Artificial Neural Network. *Advances in Artificial Neural Systems*, *2009*, 1–8. https://doi.org/10.1155/2009/193139

Ludwig, U. (1974). Durability of Cement Mortars and Concretes. In *Durability of Building Materials and Components, ASTM STP-691* (pp. 269–281).

Luo, D., Niu, D., & Dong, Z. (2014). Application of Neural Network for Concrete Carbonation Depth Prediction. *4th International Conference on the Durability of Concrete Structures*, 24–26.

Marcotte, T. D., & Hansson, C. M. (2007). Corrosion products that form on steel within cement paste. *Materials and Structures*, *40*, 325–340. https://doi.org/10.1617/S11527-006-9170-4

Mario, M., Jean-Michel, M., Cécile, D., Mohamed-Nadjib, B., Romain, T., André, L., & Patrice, B. (2021). Portable quantitative confocal Raman spectroscopy: Non-destructive approach of the carbonation chemistry and kinetics. *Cement and Concrete Research*, *139*, 106280. https://doi.org/10.1016/J.CEMCONRES.2020.106280

Martin, G. R. (1986). A method for determining the relative permeability of concrete using gas. *Http://Dx.Doi.Org/10.1680/Macr.1986.38.135.90*, *38*(135), 90–94. https://doi.org/10.1680/MACR.1986.38.135.90

Martinez-Ramirez, S., Sanchez-Cortes, S., Garcia-Ramos, J. V., Domingo, C., Fortes, C., & Blanco-Varela, M. T. (2003). Micro-Raman spectroscopy applied to depth profiles of carbonates formed in lime mortar. *Cement and Concrete Research*, *33*(12), 2063–2068. https://doi.org/10.1016/S0008-8846(03)00227-8

Martinez-Ramirez, Sagrario, Diaz, L., & Camacho, J. J. (2013). CW CO2-Laser-Induced Formation of Fulgurite on Lime–Pozzolan Mortar. *Journal of the American Ceramic Society*, *96*(9), 2824–2830. https://doi.org/10.1111/jace.12515

Martys, N. S., & Ferraris, C. F. (1997). Capillary transport in mortars and concrete. *Cement and Concrete Research*, *27*(5), 747–760. https://doi.org/10.1016/S0008-8846(97)00052-5

Masilamani, V., Ghaithan, H. M., Aljaafreh, M. J., Ahmed, A., Al Thagafi, R., Prasad, S., & Alsalhi, M. S. (2017). Using a Spectrofluorometer for Resonance Raman Spectra of Organic Molecules. *Journal of Spectroscopy*. https://doi.org/10.1155/2017/4289830

Matsusato, H., Ogawa, K., Funato, M., & Sato, T. (1992). Studies on the carbonation of hydrated cement and its effect on microstructure and strength. *9th International Congress on the Chemistry of Cement, Performance and Durability of Concrete and Cement Systems*, 363–369.

Matsushita, F., Aono, Y., & Shibata, S. (2000). Carbonation degree of autoclaved aerated concrete. *Cement and Concrete Research*, *30*(11), 1741–1745. https://doi.org/10.1016/S0008-8846(00)00424-5

McPolin, D. O., Basheer, P. A., & Long, A. E. (2009). Carbonation and pH in Mortars Manufactured with Supplementary Cementitious Materials. *Journal of Materials in Civil Engineering*, *21*(5), 217–225. https://doi.org/10.1061/(ASCE)0899-1561(2009)21:5(217)

Mi, T., Li, Y., Liu, W., Li, W., Long, W., Dong, Z., Gong, Q., Xing, F., & Wang, Y. (2021). Quantitative evaluation of cement paste carbonation using Raman spectroscopy. *Npj Materials Degradation*, *5*(35), 1–7. https://doi.org/10.1038/s41529-021-00181-6

Mikhailova, O., del Campo, A., Rovnanik, P., Fernández, J. F., & Torres-Carrasco, M. (2019). In situ characterization of main reaction products in alkali-activated slag materials by Confocal Raman Microscopy. *Cement and Concrete Composites*, *99*, 32–39. https://doi.org/10.1016/J.CEMCONCOMP.2019.02.004

Morandeau, A., Thiéry, M., & Dangla, P. (2014). Investigation of the carbonation mechanism of CH and C-S-H in terms of kinetics, microstructure changes and moisture properties. *Cement and Concrete Research*, *56*, 153–170. https://doi.org/10.1016/j.cemconres.2013.11.015

Morandeau, A., Thiéry, M., & Dangla, P. (2015). Impact of accelerated carbonation on OPC cement paste blended with fly ash. *Cement and Concrete Research*, *67*, 226–236. https://doi.org/10.1016/j.cemconres.2014.10.003

Nagataki, S., Ogha, H., & Kim, E. K. (1986). Effect of curing conditions on the carbonation of concrete with fly ash and the corrosion of reinforcement in long term tests. *Proceedings of the Second International Conference on Fly Ash, Silica Fume, Slag and Other Natural Pozzolans in Concrete*, *ACI-SP91*, 521–539. https://www.google.com/search?q=Prediction+of+carbonation+depth+of+concrete+with+fly+ash.+In%3A+Third+international+conference+on+fly+ash%2C+silica+fume%2C+slag+and+natural+pozzolans+in+concrete&oq=Prediction+of+carbonation+depth+of+concrete+with+fly+ash.

Neville, A. M. (2011). *Properties of Concrete* (5th Edition). Pearson Education Limited. https://www.engbookspdf.com/download/Concrete/properties-of-concrete-5th-edition

Newlands, M. D. (2001). *Development of a simulated natural carbonation test and durability of selected CEM II concretes*.

Ngala, V. T., & Page, C. L. (1997). Effects of carbonation on the pore structure and diffusional properties of hydrated cement paste. *Cement and Concrete Research*, *27*(7), 995–1007. https://doi.org/10.1016/S0008-8846(97)00102-6

Nishikawa, T., & Suzuki, K. (1994). Chemical conversion of C-S-H in concrete. *Cement and Concrete Research*, *24*, 176–182.

Ogino, T., Suzuki, T., & Sawada, K. (1987). The formation and transformation mechanism of calcium carbonate in water. *Geochimica et Cosmochimica Acta*, *51*(10), 2757–2767.

Omikrine Metalssi, O., Aït-Mokhtar, A., & Turcry, P. (2020). A proposed modelling of coupling carbonation-porosity-moisture transfer in concrete based on mass balance equilibrium. *Construction and Building Materials*, *230*, 116997. https://doi.org/10.1016/J.CONBUILDMAT.2019.116997

Papadakis, V. G. (2000). Effect of supplementary cementing materials on concrete resistance against carbonation and chloride ingress. *Cement and Concrete Research*, *30*(2), 291–299. https://doi.org/10.1016/S0008-8846(99)00249-5

Papadakis, V. G., Vayenas, C. G., & Fardis, M. N. (1991a). Experimental Investigation and Mathematical-Modeling of the Concrete Carbonation Problem. *Chemical Engineering Science*, *46*(5–6), 1333–1338. https://doi.org/10.1016/0009-2509(91)85060-b

Papadakis, V. G., Vayenas, C. G., & Fardis, M. N. (1991b). Fundamental Modeling and Experimental Investigation of Concrete Carbonation. *ACI Materials Journal*, *88*(4), 363–373. https://doi.org/10.14359/1863

Parrott, L. J. (1987). *A Review of Carbonation in Reinforced Concrete*. https://trid.trb.org/view/280156

Parrott, L. J. (1992). Variations of water absorption rate and porosity with depth from an exposed concrete surface: Effects of exposure conditions and cement type. *Cement and Concrete Research*, *22*(6), 1077–1088. https://doi.org/10.1016/0008-8846(92)90038-W

Parrott, L. J., & Killoh, D. C. (1989). Carbonation in a 36 year old, in-situ concrete. *Cement and Concrete Research*, *19*, 649–656. https://doi.org/10.1190/segam2013-0137.1

Patel, R. G., Killoh, D. C., Parrott, L. J., & Gutteridge, W. A. (1988). Influence of curing at different relative humidities upon compound reactions and porosity in Portland cement paste. *Materials and Structures*, *21*(123), 192–197. https://doi.org/10.1007/BF02473055

Pham, S. T., & Prince, W. (2014). Effects of Carbonation on the Microstructure of Cement Materials: Influence of Measuring Methods and of Types of Cement. *International Journal of Concrete Structures and Materials*, *8*(4), 327–333. https://doi.org/10.1007/s40069-014-0079-y

Phung, Q. T., Maes, N., Jacques, D., Bruneel, E., Van Driessche, I., Ye, G., & De Schutter, G. (2015). Effect of limestone fillers on microstructure and permeability due to carbonation of cement pastes under controlled CO2pressure conditions. *Construction and Building Materials*, *82*, 376–390. https://doi.org/10.1016/j.conbuildmat.2015.02.093

Poole, A. B., & Sims, I. (2016). *Concrete petrography : a handbook of investigative techniques* (2nd ed.). CRC Press, London.

Pourchez, J., Valdivieso, F., Grosseau, P., Govin, A., & Guilhot, B. (2006). Kinetic modelling of the thermal decomposition of ettringite into metaettringite. *Cement and Concrete Research*, *36*(11), 2054–2060. https://doi.org/10.1016/J.CEMCONRES.2006.06.007

Prentice, L. C., Farquhar, G. D., Fasham, M. J. R., Goulden, M. L., Heimann, M., Jaramillo, V. J., Kheshgi, H. S., Le Quéré, C., Scholes, R. J., & Wallace, D. W. R. (2001). The Carbon Cycle and

Atmospheric Carbon Dioxide. In *TAR Climate Change 2001: The Scientific Basis* (pp. 183–237).

Rafiq, M., Tsioulou, O., & Al-Ameeri, A. (2018, July 20). Influence of cracks on the carbonation resistance of concrete structures. *Sixth International Conference on the Durability of Concrete Structures*.

Rahman, A. A., & Glasser, F. P. (1989). Comparative studies of the carbonation of hydrated cements. *Advances in Cement Research*, *2*(6), 49–54. https://doi.org/10.1680/adcr.1989.2.6.49

Renishaw. (2022). *StreamHR™: generate high resolution chemical images*. https://www.renishaw.com/en/streamhr-generate-high-resolution-chemical-images--25501

Ribeiro, A. B., Santos, T., & Gonçalves, A. (2018). Performance of concrete exposed to natural carbonation: Use of the k-value concept. *Construction and Building Materials*, *175*, 360–370. https://doi.org/10.1016/j.conbuildmat.2018.04.206

Richardson, I. G., Skibsted, J., Black, L., & Kirkpatrick, R. J. (2010). Characterisation of cement hydrate phases by TEM, NMR and Raman spectroscopy. *Advances in Cement Research*, *22*(4), 233–248. https://doi.org/10.1680/adcr.2010.22.4.233

RILEM Committee CPC-18. (1988). Measurement of hardened concrete carbonation depth. *Materials and Structures*, *21*(6), 453–455. https://doi.org/10.1007/BF02472327

RILEM TC 116-PCD. (1999). Permeability of concrete as a criterion of its durability. *Materials and Structures*.

Rimmelé, G., Barlet-Gouédard, V., Porcherie, O., Goffé, B., & Brunet, F. (2008). Heterogeneous porosity distribution in Portland cement exposed to CO2-rich fluids. *Cement and Concrete Research*, *38*(8–9), 1038–1048. https://doi.org/10.1016/j.cemconres.2008.03.022

Roziere, E., Loukili, A., & Cussigh, F. (2009). A performance based approach for durability of concrete exposed to carbonation. *Construction and Building Materials*, *23*, 190–199. https://doi.org/10.1016/j.conbuildmat.2008.01.006

Rumelhart, D. E., Hinton, G. E., & Williams, R. J. (1987). Learning Internal Representations by Error Propagation. In *Parallel Distributed Processing: Explorations in the Microstructure of Cognition: Foundations* (pp. 318–362). MIT Press. https://ieeexplore.ieee.org/document/6302929

Saeki, T., Ohga, H., & Nagataki, S. (1991). Mechanism of carbonation and prediction of carbonation process of concrete. *Concrete Library of JSCE*, *414*(12), 99–108. https://doi.org/10.2208/JSCEJ.1990.414_99

Sahu, S., Beyene, M., & Meininger, R. (2019). Characterization of carbonated calcium silicate cement-based concrete. *17th EMABM*, 214–219.

Sanjuán, M. A., Andrade, C., & Cheyrezy, M. (2003). Concrete carbonation tests in natural and accelerated conditions. *Advances in Cement Research*, *15*(4), 171–180. https://doi.org/10.1680/adcr.2003.15.4.171

Sanjuan, M. Á., Estévez, E., Argiz, C., & Bario, D. D. (2018). Effect of curing time on granulated blast-furnace slag cement mortars carbonation. *Cement and Concrete Composites*, *90*(February), 257–265. https://doi.org/10.1016/j.cemconcomp.2018.04.006

Šavija, B., & Luković, M. (2016). Carbonation of cement paste: Understanding, challenges, and opportunities. *Construction and Building Materials*, *117*(August), 285–301. https://doi.org/10.1016/j.conbuildmat.2016.04.138

Schindelin, J., Arganda-Carreras, I., Frise, E., Kaynig, V., Longair, M., Pietzsch, T., Preibisch, S.,

Rueden, C., Saalfeld, S., Schmid, B., Tinevez, J.-Y., White, D. J., Hartenstein, V., Eliceiri, K., Tomancak, P., & Cardona, A. (2012). Fiji: an open-source platform for biological-image analysis. *Nature Methods*, *9*(7), 676–682. https://doi.org/10.1038/nmeth.2019

Schmid, T., & Dariz, P. (2013). Determination and imaging of binder remnants and aggregates in historic cement stone by Raman microscopy. *Journal of Raman Spectroscopy*, *44*(6), 882–891. https://doi.org/10.1002/JRS.4296

Schulze, H. G., Foist, R. B., Okuda, K., Ivanov, A., & Turnera, R. F. B. (2012). A small-window moving average-based fully automated baseline estimation method for Raman spectra. *Applied Spectroscopy*, *66*(7), 757–764. https://doi.org/10.1366/11-06550

Scrivener, K. L., Lyon, A. K. C., & Laugesen, F. P. (2004). The Interfacial Transition Zone (ITZ) Between Cement Paste and Aggregate in Concrete. *INTERFACE SCIENCE*, *12*, 411–421.

Ševčík, R., & Mácová, P. (2018). Localized quantification of anhydrous calcium carbonate polymorphs using micro-Raman spectroscopy. *Vibrational Spectroscopy*, *95*, 1–6. https://doi.org/10.1016/J.VIBSPEC.2017.12.005

Ševčík, R., Mácová, P., Sotiriadis, K., Pérez-Estébanez, M., Viani, A., & Šašek, P. (2016). Micro-Raman spectroscopy investigation of the carbonation reaction in a lime paste produced with a traditional technology. *Journal of Raman Spectroscopy*, *47*(12), 1452–1457. https://doi.org/10.1002/jrs.4929

Shah, V., Scrivener, K., Bhattacharjee, B., & Bishnoi, S. (2018). Changes in microstructure characteristics of cement paste on carbonation. *Cement and Concrete Research*, *109*(April), 184–197. https://doi.org/10.1016/j.cemconres.2018.04.016

Shen, Q. Z., & Pan, G. H. (2017). The Carbonation of Cement-Based Materials with Different Aggregate Content. *Materials Science Forum*, *902*. https://doi.org/10.4028/www.scientific.net/MSF.902.74

Shi, Z., Lothenbach, B., Geiker, M. R., Kaufmann, J., Leemann, A., Ferreiro, S., & Skibsted, J. (2016). Experimental studies and thermodynamic modeling of the carbonation of Portland cement, metakaolin and limestone mortars. *Cement and Concrete Research*, *88*, 60–72. https://doi.org/10.1016/j.cemconres.2016.06.006

Siddique, S., Naqi, A., & Jang, J. G. (2020). Influence of water to cement ratio on CO2 uptake capacity of belite-rich cement upon exposure to carbonation curing. *Cement and Concrete Composites*, *111*, 103616. https://doi.org/10.1016/j.cemconcomp.2020.103616

Sisomphon, K., & Franke, L. (2007). Carbonation rates of concretes containing high volume of pozzolanic materials. *Cement and Concrete Research*, *37*(12), 1647–1653. https://doi.org/10.1016/J.CEMCONRES.2007.08.014

Slegers, P. A., & Rouxhet, P. G. (1976). Carbonation of the hydration products of tricalcium silicate. *Cement and Concrete Research*, *6*(3), 381–388. https://doi.org/10.1016/0008-8846(76)90101-0

Soda, T., & Yamazaki, K. (1958). Long Time Study (20 Years) on the Neutralization of Concrete and the Rusting of Reinforcing Bars. *Journal of the Japan Society for Testing Materials*, *7*(63), 680–690. https://doi.org/10.2472/jsms1952.7.680

Song, H. W., & Kwon, S. J. (2007). Permeability characteristics of carbonated concrete considering capillary pore structure. *Cement and Concrete Research*, *37*(6), 909–915. https://doi.org/10.1016/J.CEMCONRES.2007.03.011

Stemmermann, P., Schweike, U., & Garbev, G. (2010). Celitement - A sustainable prospect for the cement industry. *Cement International*, *8*(5), 52–56.

Ševula, L., Madej, J., Kozánková, J., & Madejová, J. (1994). Hydration products at the blastfurnace slag aggregate - cement paste interface. *Cement and Concrete Research*, *24*(3), 413–423. https://doi.org/10.1016/0008-8846(94)90128-7

Stutzman, P. (2004). Scanning electron microscopy imaging of hydraulic cement microstructure. *Cement and Concrete Composites*, *26*(8), 957–966. https://doi.org/10.1016/j.cemconcomp.2004.02.043

Stutzman, P. E., Feng, P., & Bullard, J. W. (2016). Phase Analysis of Portland Cement by Combined Quantitative X-Ray Powder Diffraction and Scanning Electron Microscopy. *Journal of Research of the National Institute of Standards and Technology*, *121*(April), 47. https://doi.org/10.6028/jres.121.004

Sufian Badar, M., Kupwade-Patil, K., Bernal, S. A., Provis, J. L., & Allouche, E. N. (2014). Corrosion of steel bars induced by accelerated carbonation in low and high calcium fly ash geopolymer concretes. *Construction and Building Materials*, *61*, 79–89. https://doi.org/10.1016/J.CONBUILDMAT.2014.03.015

Swenson, E. G., & Sereda, P. J. (1968). Mechanism of the carbonatation shrinkage of lime and hydrated cement. *Journal of Applied Chemistry*, *18*(4), 111–117. https://doi.org/10.1002/jctb.5010180404

Ta, V. L., Bonnet, S., Senga Kiesse, T., & Ventura, A. (2016). A new meta-model to calculate carbonation front depth within concrete structures. *Construction and Building Materials*, *129*, 172–181. https://doi.org/10.1016/j.conbuildmat.2016.10.103

Taffese, W. Z., Sistonen, E., & Puttonen, J. (2015). CaPrM: Carbonation prediction model for reinforced concrete using machine learning methods. *Construction and Building Materials*, *100*, 70–82. https://doi.org/10.1016/J.CONBUILDMAT.2015.09.058

Tarrida, M., Madon, M., Le Rolland, B., & Colombet, P. (1995). An in-situ Raman spectroscopy study of the hydration of tricalcium silicate. *Advanced Cement Based Materials*, *2*(1), 15–20. https://doi.org/10.1016/1065-7355(95)90035-7

Thiery, M., Baroghel-Bouny, V., Morandeau, A., & Dangla, P. (2012). *Impact of carbonation on the microstructure and transfert properties of cement-based materials*.

Thiery, M., Faure, P., Morandeau, A., Platret, G., Bouteloup, J.-F., Dangla, P., & Baroghel-Bouny, V. (2011). Effect of carbonation on the microstructure and the moisture properties of cement-based materials. *International Conference on Durability of Building Materials and Components*, 1–8. https://doi.org/10.1117/1.OE.55.1.XXXXXX

Thiery, M., Villain, G., Dangla, P., & Platret, G. (2007). Investigation of the carbonation front shape on cementitious materials: Effects of the chemical kinetics. *Cement and Concrete Research*, *37*(7), 1047–1058. https://doi.org/10.1016/j.cemconres.2007.04.002

Thomas, M. (2013). *Supplementary Cementing Materials in Concrete* (1st ed.). CRC Press. https://www.routledge.com/Supplementary-Cementing-Materials-in-Concrete/Thomas/p/book/9781138075658

Thomas, M. D. A., & Matthews, J. D. (1992). Carbonation of fly ash concrete. *Magazine of Concrete Research*, *44*(160), 217–228.

Torréns-Martín, D., Fernández-Carrasco, L., Martínez-Ramírez, S., Ibáñez, J., Artús, L., & Matschei, T. (2013). Raman spectroscopy of anhydrous and hydrated calcium aluminates and sulfoaluminates. *Journal of the American Ceramic Society*, *96*(11), 3589–3595. https://doi.org/10.1111/jace.12535

Torres-Carrasco, M., del Campo, A., de la Rubia, M. A., Reyes, E., Moragues, A., & Fernández, J. F.

(2017). New insights in weathering analysis of anhydrous cements by using high spectral and spatial resolution Confocal Raman Microscopy. *Cement and Concrete Research*, *100*, 119–128. https://doi.org/10.1016/j.cemconres.2017.06.003

Torres-Carrasco, M., Del Campo, A., Rubia, M. de la, Reyes, E., Moragues, A., & Fernández, J. F. (2017). Confocal Raman Microscopy : new perspective on the weathering of anhydrous cement. *IOP Conference Series: Materials Science and Engineering, Volume 251, 3rd International Conference on Innovative Materials, Structures and Technologies (IMST 2017)*, *251*. https://doi.org/10.1088/1757-899X/251/1/012035

Torres-Carrasco, M., Campo, A., Rubia, M. A., Reyes, E., Moragues, A., & Fernández, J. F. (2019). In situ full view of the Portland cement hydration by confocal Raman microscopy. *Journal of Raman Spectroscopy*, *50*(5), 720–730. https://doi.org/10.1002/jrs.5574

Treadway, K. W. ., Macmillan, G., De Fontenay, C., & Hawkins, P. (1983). The influence of concrete quality on carbonation in middle eastern conditions, a preliminary study. In *Corrosion of reinforcement in concrete construction* (pp. 102–118).

Vagenas, N. V., Gatsouli, A., & Kontoyannis, C. G. (2003). Quantitative analysis of synthetic calcium carbonate polymorphs using FT-IR spectroscopy. *Talanta*, *59*(4), 831–836. https://doi.org/10.1016/S0039-9140(02)00638-0

Valcuende, M., & Parra, C. (2010). Natural carbonation of self-compacting concretes. *Construction and Building Materials*, *24*(5), 848–853. https://doi.org/10.1016/j.conbuildmat.2009.10.021

Valenti, G. L., & Cioffi, R. (1985). Quantitative determination of calcium hydroxide in the presence of calcium silicate hydrates. Comparison between chemical extraction and thermal analysis. *Journal of Materials Science Letters*, *4*(4), 475–478. https://doi.org/10.1007/BF00719749

Van Den Heede, P., & De Belie, N. (2019). Difference in carbonation behavior at 0.04%, 1% and 10% CO2 for High-Volume Fly Ash (HVFA) mortar: effect on internal humidity and resistivity. *Proceedings of the International Conference on Sustainable Materials Systems and Structures (SMSS2019) Durability, Monitoring and Repair of Structures*, 317–324.

Vennesland, O., & Gjorv, O. E. (1986). Silica concrete - protection against corrosion of embedded steel. *Proceedings of the Second International Conference on the Durability of Concrete*, 721–725.

Villain, G., & Platret, G. (2006). Two Experimental Methods to Determine Carbonation Profiles in Concrete. *ACI Materials Journal*, *103*(4), 265–271.

Villain, G., & Thiery, M. (2006). Gammadensimetry: A method to determine drying and carbonation profiles in concrete. *NDT and E International*, *39*(4), 328–337. https://doi.org/10.1016/j.ndteint.2005.10.002

Villain, G., Thiery, M., & Platret, G. (2007). Measurement methods of carbonation profiles in concrete: Thermogravimetry, chemical analysis and gammadensimetry. *Cement and Concrete Research*, *37*(8), 1182–1192. https://doi.org/10.1016/j.cemconres.2007.04.015

Visser, J. H. M. (2012). Accelerated carbonation testing of mortar with supplementary cementing materials - Limitation of the acceleration due to drying. *HERON*, *57*(3), 231–247. https://www.researchgate.net/publication/279929718_Accelerated_carbonation_testing_of_mortar_with_supplementary_cementing_materials_-Limitation_of_the_acceleration_due_to_drying

Vogler, N., Lindemann, M., Drabetzki, P., & Kühne, H. C. (2020). Alternative pH-indicators for determination of carbonation depth on cement-based concretes. *Cement and Concrete Composites*, *109*, 103565. https://doi.org/10.1016/J.CEMCONCOMP.2020.103565

Walker, H. N., Lane, D. S., & Stutzman, P. E. (2006). *Petrographic Methods of Examining Hardened*

Concrete: A Petrographic Manual. Revised 2004. https://doi.org/10.21949/1404099

Wang, H., Alfredsson, V., Tropsch, J., Ettl, R., & Nylander, T. (2013). Formation of CaCO3 deposits on hard surfaces - Effect of bulk solution conditions and surface properties. *ACS Applied Materials and Interfaces*, *5*(10), 4035–4045. https://doi.org/10.1021/am401348v

Wang, X. H., Val, D. V., Zheng, L., & Jones, M. R. (2020). Carbonation of loaded RC elements made of different concrete types: Accelerated testing and future predictions. *Construction and Building Materials*, *243*, 118259. https://doi.org/10.1016/J.CONBUILDMAT.2020.118259

Wang, X. Y., & Lee, H. S. (2009). A model for predicting the carbonation depth of concrete containing low-calcium fly ash. *Construction and Building Materials*, *23*(2), 725–733. https://doi.org/10.1016/J.CONBUILDMAT.2008.02.019

Wierig, H. J. (1984). Long time Studies on the Carbonation on Concrete under Normal Outdoor Exposure. *Proceedings of Seminar on Durability of Concrete Structures under Normal Outdoor Exposure*, *08*(04), 239–249.

Witkowski, H., & Koniorczyk, M. (2018). New sampling method to improve the reliability of FTIR analysis for Self-Compacting Concrete. *Construction and Building Materials*, *172*, 196–203. https://doi.org/10.1016/J.CONBUILDMAT.2018.03.216

Wolery, T. J. (1992). *EQ3NR, A Computer Program for Geochemical Aqueous Speciation-Solubility Calculations: Theoretical Manual, User 's Guide, and Related Documentation (Version 7 . 0)* (Issue February). https://doi.org/10.2172/138643

Wong, H. S. (2006). *Quantifying the pore structure of cement-based materials using backscattered electron microscopy* (Issue May).

Wong, H. S., & Buenfeld, N. R. (2006). Patch microstructure in cement-based materials: Fact or artefact? *Cement and Concrete Research*, *36*(5), 990–997. https://doi.org/10.1016/J.CEMCONRES.2006.02.008

Wong, H. S., & Buenfeld, N. R. (2009). Determining the water–cement ratio, cement content, water content and degree of hydration of hardened cement paste: Method development and validation on paste samples. *Cement and Concrete Research*, *39*(10), 957–965. https://doi.org/10.1016/j.cemconres.2009.06.013

Wong, H. S., Buenfeld, N. R., Hill, J., & Harris, A. W. (2007). Mass transport properties of mature wasteform grouts. *Advances in Cement Research*, *19*(1), 35–46. https://doi.org/10.1680/adcr.2007.19.1.35

Wong, H. S., Head, M. K., & Buenfeld, N. R. (2006). Pore segmentation of cement-based materials from backscattered electron images. *Cement and Concrete Research*, *36*(6), 1083–1090. https://doi.org/10.1016/j.cemconres.2005.10.006

Wong, H. S., Matter, K., & Buenfeld, N. R. (2013). Estimating the original cement content and water–cement ratio of Portland cement concrete and mortar using backscattered electron microscopy. *Magazine of Concrete Research*, *65*(11), 693–706. https://doi.org/10.1680/macr.12.00201

Wong, H. S., Pappas, A. M., Zimmerman, R. W., & Buenfeld, N. R. (2011). Effect of entrained air voids on the microstructure and mass transport properties of concrete. *Cement and Concrete Research*, *41*(10), 1067–1077. https://doi.org/10.1016/j.cemconres.2011.06.013

Wong, H. S., Poole, A. B., Wells, B., Eden, M., Barnes, R., Ferrari, J., Fox, R., Yio, M. H. N., Copuroglu, O., Guðmundsson, G., Hardie, R., Jakobsen, U. H., Makoubi, K., Mitchinson, A., Raybould, P., Strongman, J., & Buenfeld, N. R. (2020). Microscopy techniques for determining water–cement (w/c) ratio in hardened concrete: a round-robin assessment. *Materials and Structures*, *53*(25), 1–19. https://doi.org/10.1617/S11527-020-1458-2/TABLES/5

Wong, H. S., Zobel, M., Buenfeld, N. R., & Zimmerman, R. W. (2009). Influence of the interfacial transition zone and microcracking on the diffusivity, permeability and sorptivity of cement-based materials after drying. *Magazine of Concrete Research*, *61*(8), 571–589. https://doi.org/10.1680/macr.2008.61.8.571

Wu, B., & Ye, G. (2017). Development of porosity of cement paste blended with supplementary cementitious materials after carbonation. *Construction and Building Materials*, *145*, 52–61. https://doi.org/10.1016/j.conbuildmat.2017.03.176

Wu, Z., Wong, H. S., & Buenfeld, N. R. (2015). Influence of drying-induced microcracking and related size effects on mass transport properties of concrete. *Cement and Concrete Research*, *68*, 35–48. https://doi.org/10.1016/J.CEMCONRES.2014.10.018

Wu, Z., Wong, H. S., & Buenfeld, N. R. (2017). Transport properties of concrete after drying-wetting regimes to elucidate the effects of moisture content, hysteresis and microcracking. *Cement and Concrete Research*, *98*(December 2016), 136–154. https://doi.org/10.1016/j.cemconres.2017.04.006

Wu, Z., Wong, H. S., Chen, C., & Buenfeld, N. R. (2019). Anomalous water absorption in cement-based materials caused by drying shrinkage induced microcracks. *Cement and Concrete Research*, *115*, 90–104. https://doi.org/10.1016/j.cemconres.2018.10.006

Xu, B., & Poduska, K. M. (2014). Linking crystal structure with temperature-sensitive vibrational modes in calcium carbonate minerals. *Physical Chemistry Chemical Physics*, *16*(33), 17634–17639. https://doi.org/10.1039/c4cp01772b

Yadav, A. K., & Singh, P. (2015). A Review of Structure of Oxide Glasses by Raman Spectroscopy. *RSC Advances*, *5*, 67583–67609. https://doi.org/10.1039/c0xx00000x

Yio, M. H.N., Phelan, J. C., Wong, H. S., & Buenfeld, N. R. (2014). Determining the slag fraction, water/binder ratio and degree of hydration in hardened cement pastes. *Cement and Concrete Research*, *56*, 171–181. https://doi.org/10.1016/j.cemconres.2013.12.002

Yio, M. H.N., Wong, H. S., & Buenfeld, N. R. (2016). 3D Monte Carlo simulation of backscattered electron signal variation across pore-solid boundaries in cement-based materials. *Cement and Concrete Research*, *89*, 320–331. https://doi.org/10.1016/J.CEMCONRES.2016.09.008

Yio, Marcus Heo Nong. (2017). *Characterising the microstructure of cement-based materials using laser scanning confocal microscopy*. Imperial College London.

Yoon, I.-S., Çopuroğlu, O., & Park, K.-B. (2007). Effect of global climatic change on carbonation progress of concrete. *Atmospheric Environment*, *41*(34), 7274–7285. https://doi.org/10.1016/j.atmosenv.2007.05.028

Yoon, I. S., Çopuroğlu, O., & Park, K. B. (2007). Effect of global climatic change on carbonation progress of concrete. *Atmospheric Environment*, *41*(34), 7274–7285. https://doi.org/10.1016/j.atmosenv.2007.05.028

Yu, M.-Y., Lee, J.-Y., & Chung, C.-W. (2010). The Application of Various Indicators for the Estimation of Carbonation and pH of Cement Based Materials. *Journal of Testing and Evaluation*, *38*(5), 102382. https://doi.org/10.1520/JTE102382

Yue, Y., Wang, J. J., & Bai, Y. (2018). Tracing the status of silica fume in cementitious materials with Raman microscope. *Construction and Building Materials*, *159*, 610–616. https://doi.org/10.1016/J.CONBUILDMAT.2017.11.015

Zeng, Q., Li, K., Fen-Chong, T., & Dangla, P. (2012). Pore structure characterization of cement pastes blended with high-volume fly-ash. *Cement and Concrete Research*, *42*(1), 194–204. https://doi.org/10.1016/j.cemconres.2011.09.012

Zhang, J. S., Cheng, M., & Zhu, J. H. (2020). Carbonation Depth Model and Prediction of Hybrid Fiber Fly Ash Concrete. *Advances in Civil Engineering*, *2020*. https://doi.org/10.1155/2020/9863963

Zhang, Kai, Yio, M., Wong, H., & Buenfeld, N. (2022). Real-time monitoring of carbonation of hardened cement pastes using Raman microscopy. *Journal of Microscopy*.

Zhang, Kaijian, & Xiao, J. (2018). Prediction model of carbonation depth for recycled aggregate concrete. *Cement and Concrete Composites*, *88*, 86–99. https://doi.org/10.1016/J.CEMCONCOMP.2018.01.013

Zhang, X., Zhou, X., Zhou, H., Gao, K., & Wang, Z. (2013). Studies on forecasting of carbonation depth of slag high performance concrete considering gas permeability. *Applied Clay Science*, *79*, 36–40. https://doi.org/10.1016/J.CLAY.2013.02.020

Zhou, Q., & Glasser, F. P. (2001). Thermal stability and decomposition mechanisms of ettringite at <120°C. *Cement and Concrete Research*, *31*(9), 1333–1339. https://doi.org/10.1016/S0008-8846(01)00558-0

Appendix - Publications arising from this research

Journal papers

1. Zhang, Kai, Yio, M., Wong, H., & Buenfeld, N. (2022). Real-time monitoring of carbonation of hardened cement pastes using Raman microscopy. *Journal of Microscopy*, 286(2), 126-133. https://doi.org/10.1111/jmi.13084

2. Zhang, Kai, Yio, M., Wong, H., & Buenfeld, N. (2022). Optimising confocal Raman microscopy for spectral mapping of cement-based materials. *Materials and Structures*, 55. https://doi.org/10.1617/s11527-022-01979-9

3. Zhang, Kai, Yio, M., Wong, H., & Buenfeld, N. (2022). Confocal Raman microscopy for measuring carbonation depth in cement-based materials: a comparison with other techniques. (In preparation).

4. Zhang, Kai, Wong, H., & Buenfeld, N. (2022). Effect of natural carbonation on microstructure and transport properties. (In preparation).

5. Zhang, Kai, Wong, H., & Buenfeld, N. (2022). Predicting carbonation with artificial neural network analyses. (In preparation).